Generalized finite-volume micromechanics theory for heterogeneous materials

---

A Dissertation

Presented to

the faculty of the School of Engineering and Applied Science

University of Virginia

---

in partial fulfillment

of the requirements for the degree

Doctor of Philosophy

by

Marcio Andre Araujo Cavalcante

December

2012

APPROVAL SHEET

The dissertation

is submitted in partial fulfillment of the requirements

for the degree of

Doctor of Philosophy

Márcio Cunbré C. Cavalcante.
AUTHOR

The dissertation has been read and approved by the examining committee:

Marek-Jerzy Pindera

Advisor

Thomas T. Baber

James G. Simmonds

Sean R. Agnew

Alexey Volkov

Accepted for the School of Engineering and Applied Science:

James H. Ay

Dean, School of Engineering and Applied Science

December

2012

To my wife, Maysa,

and my mother, Genilda,

for all the support and blessings.

In memory of my father, Totonho.

Abstract

In the last decades, new generations of advanced materials have been designed and manufactured for specific applications. Micromechanics of heterogeneous materials plays an important role in the development of these materials, enabling efficient analyses of composite materials with complex geometries, circumventing the traditional trial-and-error approach, producing substantial cost savings. The unit cell problem generic to the analysis of periodic heterogeneous media is explored in this dissertation, with emphasis initially on the well-established 0th order version of the finite-volume method called finite-volume direct averaging micromechanics (FVDAM) theory. Differences and similarities with the finite element method are highlighted using newly introduced stress measures, and the resulting tangible advantages of the finite-volume approach are discussed and illustrated. A recent attempt to develop an alternative version of this technique is also discussed, illustrating shortcomings intrinsic to the 0th order and alternative versions, setting the stage for further development of this theory in order to enhance its predictive capability and efficiency.

Towards this end, a generalized finite-volume theory is constructed for two-dimensional linear elasticity problems on rectangular domains. The generalization is based on a higher-order displacement field representation within individual subvolumes of a discretized analysis domain, in contrast with the second-order expansion employed in the 0th order theory. The higher-order displacement field is expressed in terms of elasticity-based surface-averaged kinematic variables which are subsequently related to corresponding static variables through a local stiffness matrix derived in closed form. Satisfaction of subvolume equilibrium equations in an integral sense, a defining feature of finite-volume techniques, provides the required additional equations for the local stiffness matrix construction. The theory is constructed in a manner which enables systematic specialization through reductions to lower-order versions. Comparison of predictions by the generalized theory with its predecessor, analytical and finite element results illustrates substantial improvement in the satisfaction of interfacial continuity conditions at adjacent subvolume faces, producing smoother stress distributions and good interfacial conformability.

Given these very promising results, the generalized finite-volume theory is further extended to accommodate finite deformations of periodic materials with complex microstructures. This is accomplished by embedding the generalized finite-volume theory with newly incorporated finite-deformation features into the 0th order homogenization framework, and introducing parametric mapping to enable efficient mimicking of complex microstructural details, producing a parametric version of the new approach named generalized finite-volume direct averaging micromechanics (FVDAM) theory. As in the case of the linear theory, the higher-order fluctuating displacement field representation within subvolumes of the discretized unit cell microstructure, expressed in terms of elasticity-based surface-averaged kinematic variables, substantially improves interfacial conformability and pointwise traction and non-traction stress continuity between adjacent subvolumes. This improvement is particularly important in the finite-deformation domain wherein large differences in adjacent subvolume face rotations may lead to the loss of mesh integrity. The nonlinear theory is also constructed in a manner which enables systematic specialization through reductions to lower-order versions with the 0th order corresponding to the standard FVDAM theory. The advantages of the generalized FVDAM theory are illustrated through examples based on a known analytical solution and finite element results generated with a recently constructed finite element formulation that mimics the generalized theory's framework. An application of the generalized FVDAM theory involving the response of wavy multilayers confirms previously generated results with the 0th order theory that revealed microstructural effects in this class of materials applicable to bio-inspired material architectures that mimic certain biological tissues.

Acknowledgments

I would like to sincerely thank Professor Marek-Jerzy Pindera for his guidance and support during these three years as a PhD student at the University of Virginia. I also would like to thank the members of the examining committee for serving and providing constructive comments. My thanks also go to the collaborators and co-authors of the developed research and published papers essential to this dissertation, Dr. Hamed Khatam, Prof. Dr. Eduardo Nobre and Prof. Dr. Severino Marques.

My special thanks to Prof. Dr. Glaucio Paulino for being a close witness of my development at the University of Virginia, and also responsible for my first contact with Professor Marek-Jerzy Pindera in 2006, making possible the beginning of our collaboration and publication of five archival journal papers using the parametric version of the finite-volume theory.

The author gratefully acknowledges the Brazilian Federal Research Agency CNPq, the National Science Foundation, and the Engineering Materials Concepts, LCC for providing the necessary funding supports and fellowships.

Contents

Chapter 1

Introduction

1.1. Motivation

In light of the myriad of combinations and permutations of both geometric and material properties that may be realized in modern advanced materials, the field of micromechanics plays a key role in their development and design. Benefits from the use of micromechanical modeling are realized in the rapid identification and selection of candidate materials for a given application, development of engineered materials with desired thermo-mechanical and other physical properties, and design/optimization of composite structural components in a multiscale analysis setting. Well-conceived micromechanical theories lead to better understanding how local properties of constituent phases and their arrangement influence the macroscopic structural levels, including localized plastic flow, damage or failure rooted in different deformation mechanisms operative at different scales. Successful coupling of micromechanics theories with optimization algorithms has the potential to contribute in a significant way towards the development of materials and structural components with targeted performance

characteristics. Through the use of micromechanics, material development and implementation cycle time can be significantly reduced by circumventing the traditional trial-and-error approach, producing substantial cost savings.

1.2. Micromechanics Modeling Approaches

Micromechanics of heterogeneous materials has a rich history with scientific origins rooted in the early attempts to predict the response of polycrystalline metals in 1980's. The development of composite materials in the 1960's for aerospace applications has given rise to intense activity in the area of micromechanics, producing a variety of approaches and models in the past fifty years. This effort continues today, often spurred by the development of new materials with previously undocumented properties, such as nano and smart materials. The construction of new micromechanical approaches for the ever-developing applications is often characterized by the use of interchangeable terminology to describe the different types of material microstructures that dictate the chosen modeling approach. A very extensive literature exists on the different approaches employed in modeling the response of heterogeneous materials, recently reviewed and critically examined by Pindera et al. (2009) and Charalambakis (2010).

In particular, Pindera et al. (2009) describe a convenient framework for classifying the different micromechanics approaches developed during the past 50 years based on three categories, Table 1.1. The microstructural detail-free schemes encompass the classical approaches that do not explicitly consider the actual geometric details of the constituent phases. They are, in fact, constructs that allow the calculation of so-called Hill's

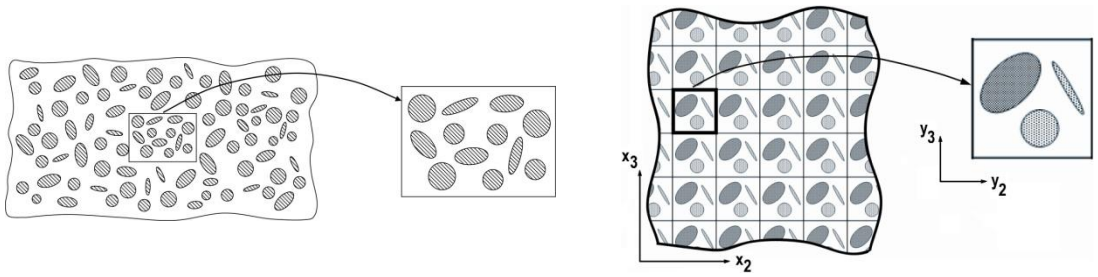

(a) (b)

Figure 1.1. Two geometric representations of heterogeneous materials with macroscopically uniform microstructure and the concomitant smallest subdomains representative of the material-at-large: (a) statistically homogeneous microstructure characterized by an RVE; (b) periodic microstructure characterized by an RUC.

concentration tensors, Hill (1963), needed in the determination of macroscopic or homogenized stiffness tensors based on simplified geometric models that do not capture the actual microstructural details. The remaining two categories are based on different geometric representations of heterogeneous materials with macroscopically uniform microstructures, which may be modeled using either the concepts of statistical homogeneity based on Representative Volume Element (RVE) or periodicity based on Repeating Unit Cell (RUC), Figure 1.1. In either case, these are the smallest possible volume elements which contain the necessary microstructural details such that the response of these elements under appropriate boundary conditions is identical to that of the material-at-large. The representative volume element concept is based on the equivalence of homogeneous displacement and traction boundary conditions, Pindera et al. (2009), while the repeating unit cell concept is employed in the analysis of periodic materials, characterized by the repetition of a basic configuration and the use of periodic boundary conditions, Drago and Pindera (2007). Periodic arrays are technologically important given current manufacturing capabilities, allowing precise placement of ceramic fibers and laser drilling of micron-size porosities, Drago and Pindera (2007). A

very extensive literature exists on the different approaches employed in modeling the response of this class of heterogeneous materials based on the above two concepts, recently reviewed and critically examined by Pindera et al. (2009) and Charalambakis (2010).

Table 1.1. Classification of the micromechanics modeling approaches (Pindera et al., 2009).

Microstructural Detail-Free Schemes
• Voigt and Reuss Estimates • Self-Consistent and Generalized Self-Consistent Schemes • Mori-Tanaka Scheme • Three-Phase Model
Statistically Homogeneous Materials
• Composite Sphere/Cylinder Assemblage Model
Periodic Materials
• Approximate models: Achenbach's Cell Model, Aboudi's Method of Cells and Generalized Method of Cells • Fourier series/transform solutions • Asymptotic Homogenization Theory ✓ Finite element method based solutions of the unit cell boundary-value problem ✓ High-Fidelity Generalized Method of Cells - HFGMC ✓ **Finite-volume based solutions of the unit cell boundary-value problem: FVDAM**

In practice, the equivalence of homogeneous displacement and traction boundary conditions is difficult to achieve exactly. This provides an explanation for the present trend to model statistically homogeneous materials as periodic, Table 1.1, given that periodic boundary conditions do not depend on the unit cell's content in contrast with the representative volume element representation of material microstructure. Amongst the different micromechanics approaches for determining the response of periodic materials,

the homogenization theory provides a systematic framework for formulating and solving the unit cell boundary-value problem required for the determination of homogenized moduli and post-elastic response. Historically, the solution had been obtained using the finite element method, but new approaches had evolved as attractive alternatives which have gained prominence.

The finite-volume direct averaging micromechanics (FVDAM) theory is one such approach which has its roots in the so-called High-Fidelity Generalized Method of Cells proposed by Aboudi et al. (2002) in a sequence of papers based, in turn, on the Higher-Order Theory for Funtionally Graded Materials, Aboudi et al. (1999), as discussed in the following section. The FVDAM theory has been shown to be an attractive alternative to the finite element based solution of unit cell problems, and due to its demonstrated advantages continues to evolve. The present contribution is a continuation of, and significant contribution to, this effort as discussed in the sequel.

1.3. A Brief History of Finite-Volume Methods

The finite-volume method is a well-established numerical technique for the solution of boundary-value problems in fluid mechanics governed by parabolic and hyperbolic equations, cf. Leveque (2002), Versteeg and Malalasekera (2007). Satisfaction of the governing (transport or equilibrium) field equations within control volumes of the discretized domain of interest in an integral sense is a key feature of the finite-volume method which distinguishes it from variational techniques such as the finite element method (Cavalcante et al., 2012b).

The simplicity and demonstrated stability of the finite-volume method in fluid mechanics applications has motivated the implementation of this technique in solid mechanics problems during the past 25 years as an alternative to the finite element approach. Three versions of this technique can be identified in the analysis of solid mechanics problems. The first two have been developed originally for homogeneous materials and structures, while the third version evolved independently and nearly in parallel for applications involving heterogeneous materials.

The cell centered and cell vertex finite-volume techniques originally developed for homogeneous materials were motivated by the established finite-volume technique for fluid mechanics problems and elements of the finite element method. An excellent comparison of the two methods can be found in the paper by Fallah (2004) in the context of solution to plate problems based on the Mindlin-Reissner plate theory.

The cell centered finite-volume method is similar to the original fluid mechanics version and employs control volumes which are centered around grid points at which field variables are defined. Initially, structured meshes based on rectangular or cylindrical control volumes had been used for domain discretization, which were subsequently generalized to unstructured meshes with arbitrary control volume topology based on polyhedral shapes, Figure 1.2(a). In the early developments, Taylor series expansion was employed to approximate surface variables in terms of the control volume-center variables needed in the local satisfaction of equilibrium equations in an integral sense (volume or surface averaged), Demirdzic et al. (1988), Demirdzic and Martinovic (1993), Demirdzic and Muzaferija (1994). Linear displacement field approximation along control volume faces was successfully used by Wheel (1996, 1999) in the solution of

axisymmetric linear and incompressible elasticity problems. Applications of this approach continue to problems involving anisotropic materials, extrusion, and incompressible elasticity amongst others, cf. Demirdzic et al. (2000), Basic et al. (2005), Bijelonja et al. (2006). In order to better approximate variation of unknown variables across control volume faces, which in turn facilitate calculation of interfacial stress resultants, shape functions have been introduced recently into the cell centered finite-volume framework in conjunction with parametric mapping in the solution of plate problems based on the Mindlin-Reissner plate theory, Fallah (2006, 2008).

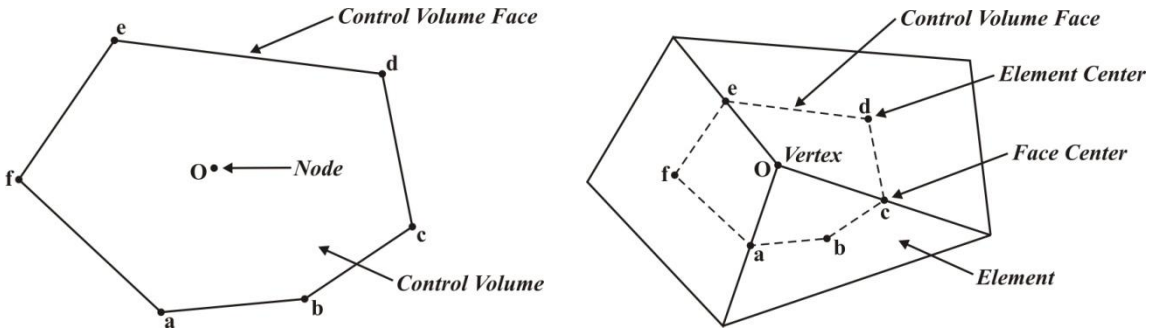

(a) Cell centered control volume (b) Vertex based control volume

Figure 1.2. Control volumes employed in cell centered and vertex based finite-volume analyses of homogeneous material and structural problems in solid mechanics.

The cell vertex, or vertex based, finite-volume approach leverages elements of the finite element method in domain discretization and displacement field approximation. The domain is first discretized into finite elements, and the common vertices of adjacent elements provide grid points at which field variables are defined using shape functions borrowed from the finite element approach. Control volumes centered around grid points are then constructed taking contributions from elements with common vertices and using element and face centers as control volume corners, Figure 1.2(b). Thus the control volume geometry and displacement field approximation are directly linked to element

discretization and employed shape functions. Satisfaction of the local equilibrium equations is carried out over all control volumes containing every common vertex shared by adjacent elements forming grid points. Arbitrarily shaped polygonal control volumes may thus be constructed based on the chosen element type used to mesh the analysis domain.

The use of shape functions in the context of vertex based finite-volume method was proposed by Fryer et al. (1991) for the analysis of two-dimensional elasticity problems, which was subsequently extended to three-dimensional problems by Bailey and Cross (1995), and then applied by Taylor et al. (1995, 2003) and also Fallah et al. (2000). Applications and further development of this approach continue, characterized by different control volume displacement field representations. For instance, Wenke and Wheel (2003) proposed the use of shape functions with rotational degrees of freedom based on six-noded triangular element discretization used in the construction of control volumes. Applications of this approach were subsequently carried out for micropolar media and incompressible materials, Wheel (2008), Pan et al. (2010).

The above contributions based on cell centered and vertex based approaches in the analysis domain discretization have demonstrated that the finite-volume method is a very viable alternative to the finite element approach in the solution of structural and solid mechanics boundary-value problems involving at least homogeneous materials.

The third version has evolved independently of the above approaches to model materials with heterogeneous microstructures, including periodic and functionally graded materials, cf. Suquet (1987), Charalambakis and Murat (2006), Buryachenko (2007), Birman and Byrd (2007), Chatzigeorgiou et al. (2008), and Paulino et al. (2008). The structural finite-

volume theory has its roots in the so-called Higher-Order Theory for Functionally Graded Materials (HOTFGM), developed in a sequence of papers in the 1990's and summarized in Aboudi et al. (1999). This theory provided the main framework for the construction of its homogenized counterpart initially named the Higher-Order Theory for Periodic Multiphase Materials by Aboudi et al. (2001). The homogenized version was subsequently renamed the High-Fidelity Generalized Method of Cells (HFGMC) by Aboudi et al. (2002) although predictions of HFGMC generally do not reduce to those of the Generalized Method of Cells (GMC), Paley and Aboudi (1992), as expected of theories related to each other through similar names.

The structural and homogenized versions of these so-called higher-order theories were subsequently re-constructed in a sequence of papers by Bansal and Pindera (2003, 2005) and Zhong et al. (2004) by simplifying the discretization of analysis domain which, in turn, facilitated implementation of the efficient local/global stiffness matrix approach, Bufler (1971), Pindera (1991). This significant re-construction revealed the above higher-order approaches to be in fact finite-volume theories, which in turn motivated corresponding name changes in order to correctly reflect the fundamental character of these re-constructed theories. The version of the finite-volume theory developed for periodic materials within the homogenization framework was subsequently named finite-volume direct averaging micromechanics (FVDAM) theory, Bansal and Pindera (2006).

The re-constructed finite-volume theories are similar to the cell centered techniques that evolved in parallel for homogeneous materials and structures during roughly the same period. However, in contrast with the early cell centered techniques, the re-constructed theories employ explicit displacement field approximation within individual subvolumes

of the discretized analysis domain, and follow an elasticity-based approach in satisfying interfacial displacement and traction continuity conditions in a surface-averaged sense, following the original idea proposed by Achenbach (1975). This is consistent with the satisfaction of equilibrium equations in a surface-averaged sense and leads to the explicit construction of local stiffness matrix for the individual subvolumes.

These re-constructed theories were further extended by incorporating parametric mapping to enable efficient modeling of complex microstructures. This mapping was first introduced by Cavalcante (2006) and Cavalcante et al. (2007a,b) into the structural version of the finite-volume theory originally developed by Bansal and Pindera (2003) and Zhong et al. (2004). Subsequently, the homogenized (FVDAM) version had been constructed by Gattu et al. (2008) and Khatam and Pindera (2009a,b) who, following Cavalcante et al. (2007a,b), introduced parametric mapping into the rectangular subvolume-based version of the FVDAM theory originally developed by Bansal and Pindera (2005, 2006). Both the structural and homogenized versions of the parametric finite-volume theory have proved to be attractive alternatives to the finite element analysis of heterogeneous materials whose predictive capability has been verified both analytically, numerically and experimentally.

We note that independent of the above finite-volume approaches to the analysis of functionally graded and periodic materials, parametric mapping was also introduced by Fallah (2005a, 2006) into the cell centered finite-volume formulation of the Mindlin-Reissner plate theory, and by Fallah (2005b, 2008) into two-dimensional stress analysis of solids. While the parametric mapping employed by Fallah (2006) contains no simplifications, the mapping proposed by Cavalcante (2006) employs the concept of

volume-average Jacobian as its defining feature consistent with the surface-averaging framework of the parametric finite-volume theory. Quadrilateral subvolumes were also introduced into the original FVDAM framework by Gao et al. (2009) based on direct geometric (rather than parametric mapping) approach.

The rapidly developing finite-volume approach to the solution of unit cell boundary-value problems of periodic materials is an attractive alternative to the prevalent finite element based solutions of such problems. This approach may also be profitably used in modeling the response of statistically homogeneous materials based on the representative volume element concept through relaxation of the homogenization-based displacement field representation and the replacement of periodicity boundary conditions by homogeneous displacement or traction boundary conditions.

1.4. Objectives

The parametric finite-volume direct averaging micromechanics (FVDAM) theory has been shown to be a well-suited method for the analysis of heterogeneous materials with complex periodic microstructures. Comparison of results generated using this theory with analytical solutions, the finite element method and experimental results has provided rigorous verifications and validations of this approach, Gattu et al. (2008), Khatam at el. (2009), and Cavalcante et al. (2011b). The satisfaction of equilibrium equations at the subvolume level and the concomitant displacement and traction continuities enforced in an average-sense between common faces of distinct subvolumes reveal the strength of this approach, providing a stable and suitable theory for the analysis of heterogeneous materials, Cavalcante et al. (2012b). However, interfacial interpenetration and

discontinuity of the non-traction stress components are shortcomings which remained to be addressed in the current version of the theory (Cavalcante et al., 2012a). Nonetheless, the subvolume average values of both traction and non-traction stress components are reliable (Cavalcante et al., 2008, 2011b), reported by Katham and Pindera in their papers dealing with the parametric version of the FVDAM theory.

With the main goal of overcoming the above shortcomings of the current parametric FVDAM theory, a generalized finite-volume theory has been constructed on rectangular subdomains and implemented within the framework of elastic stress analysis in solid mechanics with a profitable outcome, Cavalcante and Pindera (2012a,b). The very promising results indicated that the implementation of the developed generalized finite-volume approach within a homogenization framework which accounts for finite-deformation effects would enable accurate analysis of heterogeneous materials with periodic microstructures subjected to large deformations, thereby overcoming the limitations intrinsic to the standard theory (Katham and Pindera, 2012).

To achieve this goal, it was necessary to incorporate parametric mapping capability and the homogenized approach into this generalized finite-volume theory, subsequently named generalized finite-volume direct averaging micromechanics (FVDAM) theory, with the additional complications introduced by the finite deformation formulation. This generalized FVDAM theory can be applied to the analysis of periodic heterogeneous materials with linear and nonlinear elastic phases, allowing the investigation of different phenomena occurring at the microstructure level. Comparison and verification with analytical and finite element method results provide a good understanding of the main features and advantages of the generalized FVDAM theory.

Specifically, this dissertation has the following objectives:

- **incorporation of parametric mapping capability into the generalized finite-volume theory;**
- **incorporation into the generalized finite-volume theory of the homogenized approach to the analysis of periodic heterogeneous materials;**
- **implementation of solution techniques and constitutive models for the analysis of periodic heterogeneous materials subjected to large deformations;**
- **comparison and verification of the results obtained by the generalized FVDAM theory with analytical solutions and those obtained by the finite element method;**
- **analysis of the main features and advantages of the generalized FVDAM theory in comparison with the standard approach and the finite element method;**
- **independent verification of the microstructure effect in wavy-multilayers undergoing finite-deformation.**

The development of the above-described computational technology facilitates accurate and efficient analyses of a new generation of materials of interest to several strategic areas.

1.5. Outline of the Dissertation

The dissertation is organized as follows. In Chapter 2, the emphasis is placed on the parametric finite-volume direct averaging micromechanics (FVDAM) theory developed for the infinitesimal analysis of elastic-plastic materials, Gattu et al. (2008) and Khatam and Pindera (2009a,b). For the first time a direct comparison of the parametric FVDAM theory and the finite element method is presented on equal footing, highlighting the

differences and some particular features of both methods, Cavalcante et al. (2011b). Analyses of perforated metallic sheets and wavy multilayers are also performed using both techniques. In the last section, shortcomings of the parametric FVDAM theory are discussed, pointing out possible solutions. In Chapter 3, the generalized finite-volume theory is presented in the context of elastic stress analysis in solid mechanics, showing the main features and advantages of this higher-order theory in relation to the standard approach and the finite element method through the analyses of three problems with different geometries and boundary conditions. This was the first step in generalizing our finite-volume theory without introducing the complication of parametric mapping. The generalized finite-volume theory for two-dimensional linear elasticity problems on rectangular domains is further extended in Chapter 4 to accommodate finite deformations of periodic materials with complex microstructures, and subsequently named generalized finite-volume direct averaging micromechanics (FVDAM) theory. This is accomplished by embedding the generalized finite-volume theory with newly incorporated finite-deformation features into the 0th order homogenization framework, and introducing parametric mapping capability to enable efficient mimicking of complex microstructural details. Chapter 5 presents a finite element formulation applied to the analysis of periodic materials subjected to large deformations, in order to verify the generalized FVDAM theory by independent means. Comparison with available analytical solutions demonstrates the capability of this numerical approach to predict the homogenized response and the local fields in the finite-deformation domain with excellent accuracy. In Chapter 6, the advantages of the generalized FVDAM theory are illustrated through examples based on a known analytical solution and results generated by the finite-

element approach developed in the previous chapter. An application of the generalized FVDAM theory involving the response of wavy multilayers confirms previously generated results with the 0th order theory that revealed microstructural effects in this class of materials that are important in bio-inspired material architectures that mimic certain biological tissues (Katham and Pindera, 2012). Summary, conclusions and proposed future work are presented in Chapter 7.

Chapter 2

Infinitesimal Elasto-Plastic Analysis of Periodic Materials

2.1. Introduction

In this chapter, we present for the first time direct comparison of the parametric FVDAM and finite element approaches in the context of infinitesimal elasto-plastic analysis of periodic materials within the same computational framework, using practically the same unit cell discretization, comparable displacement field representation and the same solution method for the implicitly nonlinear equations governing the unit cell response. Comparison of the predictions of local stress and plastic strain fields, and homogenized response, for problems involving different unit cell architectures which have revealed interesting plasticity-driven phenomena reported by Khatam and Pindera (2010, 2011), is performed, highlighting the differences and some particular features of both methods, such as the manner of satisfying the equilibrium equations, examined herein using a new measure introduced by Cavalcante et al. (2011b). Finally, shortcomings of the parametric FVDAM theory are discussed, pointing out possible solutions.

2.2. Homogenization of Periodic Materials

The central problem in the micromechanics of heterogeneous materials with statistically homogeneous, Figure 1.1(a), or periodic, Figure 1.1(b), microstructures is the determination of localization relations for the subdomains into which the smallest domain representative of the material's response is subdivided for analysis purposes,

$$\bar{\varepsilon}^{(q)} = \mathbb{A}^{(q)}\bar{\varepsilon} + \mathbb{D}^{(q)} \tag{2.1}$$

where $\mathbb{A}^{(q)}$ are elastic strain concentration tensors calculated just once for every qth subdomain, Hill (1963), and vectors $\mathbb{D}^{(q)}$ represent inelastic contributions repeatedly determined at each point along the loading path. Using these relations in the definition for the volume-average stress expressed in terms of subdomain stresses

$$\bar{\sigma} = \frac{1}{V}\int_V \sigma(x)\, dV = \frac{1}{V}\sum_{q=1}^{N_q}\int_{V_q} \sigma^{(q)}(x) dV_q = \sum_{q=1}^{N_q} c_{(q)}\bar{\sigma}^{(q)} \tag{2.2}$$

which in turn are given in terms of subdomain strains through local constitutive equations, $\sigma^{(q)} = \boldsymbol{C}^{(q)}\left(\varepsilon^{(q)} - \varepsilon^{p(q)}\right)$. The homogenized Hooke's law for the material-at-large is then constructed in the form

$$\bar{\sigma} = \boldsymbol{C}^*(\bar{\varepsilon} - \bar{\varepsilon}^p) \tag{2.3}$$

where the homogenized stiffness matrix $\boldsymbol{C}^*$ and plastic strain $\bar{\varepsilon}^p$ are given by,

$$\boldsymbol{C}^* = \sum_{q=1}^{N_q} c_{(q)}\boldsymbol{C}^{(q)}\,\mathbb{A}^{(q)}, \quad \bar{\varepsilon}^p = [\boldsymbol{C}^*]^{-1}\sum_{q=1}^{N_q} c_{(q)}\boldsymbol{C}^{(q)}\left(\bar{\varepsilon}^{p(q)} - \mathbb{D}^{(q)}\right) \tag{2.4}$$

$\bar{\varepsilon}^{p(q)}$ are volume-averaged plastic strains in the qth subdomain, and $c_{(q)}$ is the corresponding volume fraction.

Herein, we consider periodic materials characterized by the basic building block called the repeating unit cell which is replicated in two or three dimensions, depending on the

material's microstructure, to generate the periodically repeating material microstructure, Figure 1.1(b). Hence the response of the periodic material is characterized by the response of a single unit cell subjected to periodic boundary conditions. Such problems are typically treated using the asymptotic homogenization theory, Bensoussan et al. (1978), which in its simplest or 0-th order form leads to the displacement field representation in the *q*th subdomain in terms of two-scale expansion in global and local coordinates, (x_1, x_2, x_3) and (y_1, y_2, y_3), respectively, involving macroscopic and microstructure-induced fluctuating components,

$$u_i^{(q)}(\boldsymbol{x}, \boldsymbol{y}) = \bar{\varepsilon}_{ij} x_j + u'^{(q)}_i(\boldsymbol{y}), \quad (i = 1,2,3) \tag{2.5}$$

where $\bar{\varepsilon}_{ij}$ are the specified macroscopic or average strains applied to the entire material, and thus the unit cell. Consequently, the strain field is also partitioned into average and fluctuating contributions induced by the heterogeneous microstructure, $\varepsilon_{ij}^{(q)} = \bar{\varepsilon}_{ij} + \varepsilon'^{(q)}_{ij}$. Solution of the unit cell problem for the unknown fluctuating displacement components enables determination of the localization relations, Equation (2.1), and hence the homogenized Hooke's law.

Given the complicated state of stress induced by heterogeneous material microstructure in conjunction with inelastic effects, sufficient discretization of the unit cell is required to accurately capture the field variable distributions in the individual constituents. This limits the choice of techniques capable of capturing field variable distribution details with sufficient fidelity to variational-based, transform or finite-volume techniques.

2.3. Parametric FVDAM Theory

The parametric version of the FVDAM theory is based on microstructural dicretization of the unit cell into quadrilateral subvolumes. This is a paradigm shift in the evolution of the FVDAM theory as it provides the capability to mimic microstructural details with much better fidelity and efficiency. The use of quadrilateral subvolumes facilitates efficient modeling of microstructures with arbitrarily shaped heterogeneities, and eliminates artificial stress concentrations produced by the rectangular subvolumes employed in the standard version. The use of quadrilateral subvolumes is accomplished through mapping of square subvolume in reference coordinate system onto a quadrilateral subvolume in the actual microstructure as described in the sequel.

This homogenized version of the finite-volume theory has been developed explicitly for the analysis of periodic materials characterized by the basic building blocks called unit cells, rather than statistically homogeneous materials, cf. Drago and Pindera (2007), and Pindera et al. (2009). The response of periodic materials with differently-shaped porosities embedded in various arrays, Khatam et al. (2009), and layered materials with wavy microstructures, Khatam and Pindera (2010), has been investigated efficiently using FVDAM, and new effects discovered. Most recent investigation into the response of perforated metallic sheets has revealed characteristic plastic deformation modes which produce distinct branches of the macroscopic yield and limit surfaces of hexagonal arrays of circular porosities in elastic-perfectly plastic sheets in plane stress state, Khatam and Pindera (2011). The ability of the parametric FVDAM theory to accurately capture homogenized response of perforated sheets has been verified by comparison with both the finite element analysis and experimental data reported by Fedele et al. (2006).

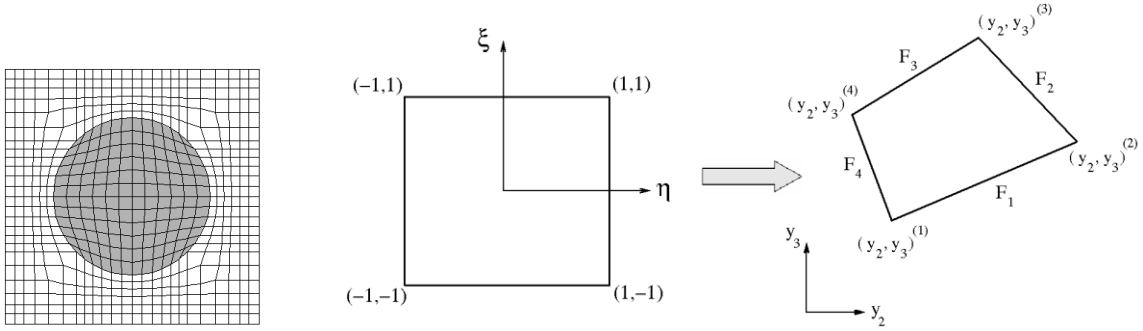

(a) (b)

Figure 2.1. Discretization of a unit cell with a circular inclusion using quadrilateral subvolumes, and the corresponding mapping transformation employed in the parametric FVDAM theory.

In the parametric FVDAM theory, the microstructure of a periodic material is discretized into quadrilateral subvolumes designated by the bracketed index (q) whose locations are specified by the vertices $\left(y_2^{(p,q)}, y_3^{(p,q)}\right)$ referred to a fixed coordinate system, Figure 2.1. Following the convention of Cavalcante et al. (2007a), the vertices are numbered counterclockwise starting from lower left corner, and the faces are also numbered counterclockwise with the *pth* face defined by the endpoints of two adjacent vertices. The *qth* quadrilateral subvolume resident in the actual microstructure is an image of the reference square subvolume in the $\eta - \xi$ plane bounded by $-1 \leq \eta \leq +1$ and $-1 \leq \xi \leq +1$. Its vertices correspond to the vertices of the *qth* subvolume in the actual discretized microstructure, Figure 2.1. The mapping of the point (η, ξ) in the reference subvolume to the corresponding point in the *qth* subvolume is given by

$$y_i^{(q)}(\eta, \xi) = \sum_{p=1}^{4} N_p\,(\eta, \xi) y_i^{(p,q)}, \quad i = 2,3 \tag{2.6}$$

where $N_1(\eta, \xi) = \frac{1}{4}(1-\eta)(1-\xi)$, $N_2(\eta, \xi) = \frac{1}{4}(1+\eta)(1-\xi)$,

$N_3(\eta, \xi) = \frac{1}{4}(1+\eta)(1+\xi)$ and $N_4(\eta, \xi) = \frac{1}{4}(1-\eta)(1+\xi)$.

The displacement field in the *qth* subvolume is represented by the two-scale expansion involving macroscopic and fluctuating components

$$u_i^{(q)}\big(\boldsymbol{x}, \boldsymbol{y}(\eta,\xi)\big) = \bar{\varepsilon}_{ij}x_j + u'^{(q)}_i(\eta,\xi) \tag{2.7}$$

where the fluctuating displacement components are given in terms of the reference subvolume coordinates (η, ξ),

$$u'^{(q)}_i = W^{(q)}_{i(00)} + \eta W^{(q)}_{i(10)} + \xi W^{(q)}_{i(01)} + \frac{1}{2}(3\eta^2 - 1)W^{(q)}_{i(20)} + \frac{1}{2}(3\xi^2 - 1)W^{(q)}_{i(02)} \tag{2.8}$$

The local strains are then obtained in terms of the macroscopic and fluctuating strain components upon use of the strain-displacement relations

$$\varepsilon^{(q)}_{ij} = \bar{\varepsilon}_{ij} + \frac{1}{2}\left(\frac{\partial u'^{(q)}_i}{\partial y_j} + \frac{\partial u'^{(q)}_j}{\partial y_i}\right) \tag{2.9}$$

Subsequently, local stiffness matrix for the *qth* subvolume is constructed by relating the surface-averaged fluctuating displacements to the surface-averaged tractions on each face of the subvolume. The integration of interfacial displacements is done in the $\eta - \xi$ plane in light of Equation (2.6), while interfacial tractions are integrated along quadrilateral subvolume faces of length l_p in the actual microstructure taking into account the coordinate transformation given by Equation (2.13) in the sequel. The surface-averaged displacements on the *pth* face of the *qth* subvolume are defined by

$$\hat{u}'^{(1,3)}_i = \frac{1}{2}\int_{-1}^{+1} u'_i(\eta, \mp 1)d\eta, \quad \hat{u}'^{(2,4)}_i = \frac{1}{2}\int_{-1}^{+1} u'_i(\pm 1, \xi)d\xi \tag{2.10}$$

Similarly, the corresponding surface-averaged tractions are given in terms of stresses through the Cauchy's relations $t_i^{(p)} = \sigma_{ji}^{(p)} n_j^{(p)}$,

$$\hat{t}_i^{(p)} = \frac{1}{l_p}\int t_i^{(p)} dl_p = \frac{1}{l_p}\int \sigma_{ji}^{(p)} n_j^{(p)} dl_p, \quad p = 1,2,3,4 \tag{2.11}$$

The stresses associated with each surface are expressed in terms of the corresponding strains through Hooke's law for the *qth* subvolume,

$$\sigma_{ij}^{(q)} = C_{ijkl}^{(q)} \varepsilon_{kl}^{(q)} - 2\mu^{(q)} \varepsilon_{ij}^{p(q)} \tag{2.12}$$

where the plastic behavior is currently limited to isotropic subvolumes, whereas strictly elastic subvolumes may be orthotropic or (transversely) isotropic. The surface-averaged strains on the faces of quadrilateral subvolumes in the actual microstructure are generated using the following relations between surface-averaged partial derivatives of the displacement field in the two coordinate systems

$$\begin{bmatrix} \dfrac{\partial u'_i}{\partial y_2} \\ \dfrac{\partial u'_i}{\partial y_3} \end{bmatrix}^{(p)} = \hat{\boldsymbol{J}} \begin{bmatrix} \dfrac{\partial u'_i}{\partial \eta} \\ \dfrac{\partial u'_i}{\partial \xi} \end{bmatrix}^{(\hat{p})} \quad for \quad \hat{\boldsymbol{J}}^{-1} = \bar{\boldsymbol{J}} = \frac{1}{4} \int_{-1}^{+1} \int_{-1}^{+1} \boldsymbol{J} d\eta \, d\xi \tag{2.13}$$

where $\boldsymbol{J}$ is the Jacobian of the transformation. The superscripts p and $\hat{p}$ denote the faces of quadrilateral and reference subvolumes, respectively, with the following correspondence $\hat{p} = 1,3 \rightarrow \xi = \mp 1$ and $\hat{p} = 2,4 \rightarrow \eta = \pm 1$.

The surface-averaged strains are obtained in terms of the unknown coefficients in the subvolume displacement representation which are then expressed explicitly in terms of the surface-averaged fluctuating displacement components upon use of the definitions given in Equation (2.10) and the application of equilibrium equations in the large (which provide the remaining two equations)

$$\int_S \boldsymbol{t} dS = \sum_{p=1}^{4} \int_{l_p} \boldsymbol{t}^{(p)} dl_p = \sum_{p=1}^{4} l_p \, \hat{\boldsymbol{t}}^{(p)} = \boldsymbol{0} \tag{2.14}$$

This leads to the relationship between the surface-averaged tractions and surface-averaged fluctuating displacements given in terms of the local stiffness matrix $\boldsymbol{K}$ for the *qth* subvolume

$$\hat{\boldsymbol{t}} = \boldsymbol{N}\boldsymbol{C}\bar{\boldsymbol{\varepsilon}} + \boldsymbol{K}\hat{\boldsymbol{u}}' + \bar{\boldsymbol{A}}\boldsymbol{N}\boldsymbol{\Phi}^{-1}\boldsymbol{Z}^{p} - \boldsymbol{N}\hat{\boldsymbol{\sigma}}^{\boldsymbol{p}} \tag{2.15}$$

where $\hat{\boldsymbol{t}} = \left[\hat{\boldsymbol{t}}^{(1)}\ \hat{\boldsymbol{t}}^{(2)}\ \hat{\boldsymbol{t}}^{(3)}\ \hat{\boldsymbol{t}}^{(4)}\right]^{T}$, $\hat{\boldsymbol{u}} = \left[\hat{\boldsymbol{u}}^{(1)}\ \hat{\boldsymbol{u}}^{(2)}\ \hat{\boldsymbol{u}}^{(3)}\ \hat{\boldsymbol{u}}^{(4)}\right]^{T}$, $\boldsymbol{N} = \left[\boldsymbol{n}^{(1)}\ \boldsymbol{n}^{(2)}\ \boldsymbol{n}^{(3)}\ \boldsymbol{n}^{(4)}\right]^{T}$, $\hat{\boldsymbol{\sigma}}^{\boldsymbol{p}}$ contains surface-averaged components of plastic strains along subvolume faces, and the matrices $\bar{\boldsymbol{A}}$, $\boldsymbol{\Phi}$ have been given in explicit form in Khatam and Pindera (2009b). The plastic vector $\boldsymbol{Z}^{p}$ comprises the elements

$$Z_i^p = \sum_{p=1}^{4} l_p\left(n_2\hat{\sigma}_{i2}^p + n_3\hat{\sigma}_{i3}^p\right)^{(p)}/(12|\bar{\boldsymbol{J}}|)\,, \qquad i = 1,2,3 \tag{2.16}$$

with

$$\hat{\sigma}_{ij}^{p(1,3)} = \int_{-1}^{+1}\sigma_{ij}^p(\eta, \mp 1)d\eta, \qquad \hat{\sigma}_{ij}^{p(2,4)} = \int_{-1}^{+1}\sigma_{ij}^p(\pm 1, \xi)d\xi \tag{2.17}$$

The surface-averaged plastic strains are calculated using a collocation procedure given in Khatam and Pindera (2009b).

Imposition of interfacial traction and displacement continuity conditions at the common subvolume faces, together with periodic boundary conditions, produces the global system of equations for the determination of the common surface-averaged fluctuating displacements,

$$\mathbb{K}\widehat{\boldsymbol{U}}' = \Delta\boldsymbol{C}\bar{\boldsymbol{\varepsilon}} + \boldsymbol{G} \tag{2.18}$$

where the global $\Delta\boldsymbol{C}$ matrix is comprised of the differences in the material stiffness matrices of adjacent subvolumes, and the vector $\boldsymbol{G}$ represents surface-averaged plastic contributions. The global stiffness matrix singularity is eliminated by constraining external faces of selected boundary subvolumes in order to remove rigid body

displacements. The remaining interfacial surface-averaged displacements are then determined by solving the reduced system of equations iteratively at each load increment, given that vector $\boldsymbol{G}$ contains surface-averaged plastic strains which depend implicitly on surface-averaged displacements. This yields the localization relations, Equation (2.1), used to construct the homogenized Hooke's law in the form given by Equation (2.3).

At each load increment, the surface plastic strains are calculated iteratively using the technique of successive elastic solutions proposed by Mendelson (1986), wherein the point-wise plastic strains within the reference subvolume are decomposed into converged contributions from the previous load step plus increments that result from the imposed load increment

$$\varepsilon_{ij}^{p(q)}(\eta,\xi) = \varepsilon_{ij}^{p(q)}(\eta,\xi)\Big|_{previous} + d\varepsilon_{ij}^{p(q)}(\eta,\xi) \tag{2.19}$$

Plastic strain increments are calculated using the classical plasticity theory with isotropic hardening based on the Prandtl-Reuss equations reformulated in terms of so-called modified total strain deviators e'_{ij}, rather than deviatoric stresses, Mendelson (1986), as follows

$$d\varepsilon_{ij}^{p} = \frac{e'_{ij}}{e_{eff}} d\varepsilon_{eff}^{p} \tag{2.20}$$

where $e'_{ij} = \varepsilon_{ij} - 1/3\varepsilon_{kk}\delta_{ij} - \varepsilon_{ij}^{p}\big|_{previous}$, $e_{eff} = \sqrt{2/3 e'_{ij} e'_{ij}}$, and the effective plastic strain increment is given in terms of e_{eff} and effective stress σ_{eff} as follows $d\varepsilon_{eff}^{p} = e_{eff} - \sigma_{eff}/3\mu$. The implementation of the reformulated equations is made very efficient by the plastic loading condition $1 - \sigma_{eff}/3\mu e_{eff} > 0$, Williams and Pindera (1997).

2.4. Finite Element Method applied to Periodic Materials with Elastoplastic Phases

In order to compare the FVDAM theory with the FEM (applied to periodic materials with elastoplastic phases) on as equal footing as possible, we have chosen an element which mimics both the displacement field and the domain discretization of the FVDAM theory. The Q4 element employs the same mapping as that used in the FVDAM mesh discretization, leading to quadrilateral elements with straight sides in the actual microstructure. However, the concomitant bilinear displacement field representation produces inferior stress fields, Cavalcante et al. (2008). Conversely, the Q8 element based on a quadratic displacement field representation along the element sides reproduces the local stress field with somewhat higher fidelity than the FVDAM theory, while retaining a nearly quadrilateral geometry with sufficiently small discretization. This enables mesh construction with the same vertex coordinates.

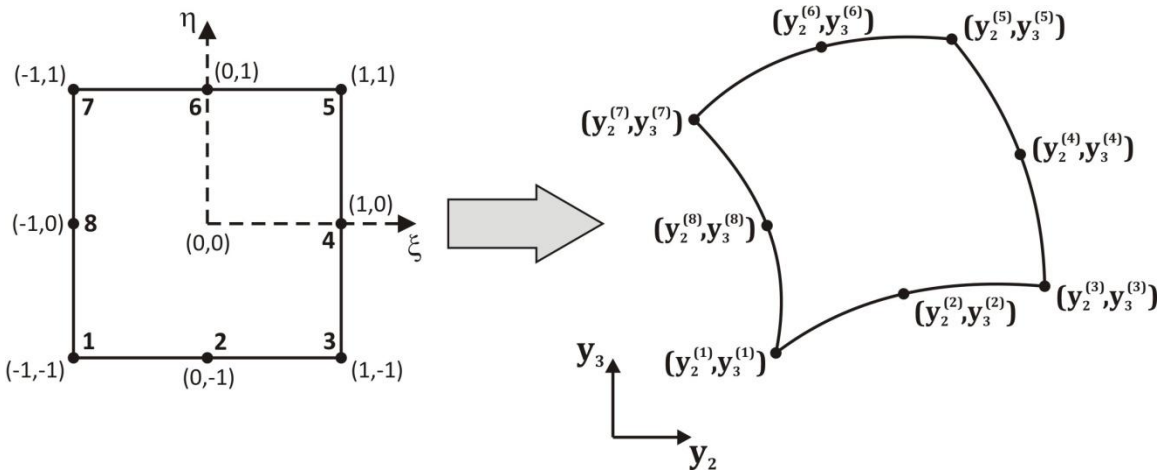

Figure 2.2. Parametric mapping employed in the Q8 element.

Strictly speaking, Q8 elements yield sides that vary quadratically with spatial coordinates, in contrast with the linear-sided FVDAM quadrilateral subvolumes.

Nonetheless, this is the closest approximation of the local displacement field and domain discretization that can be attained with both methods, and imposes a demanding comparison standard for the FVDAM theory.

The mapping of the point (η, ξ) in the reference element to the corresponding point in the *qth* element used in the mesh construction (Figure 2.2) and displacement field representation is given by $y_i^{(q)}(\eta,\xi) = \sum_{p=1}^{8} N_p(\eta,\xi) y_i^{(p,q)}$ $(i = 2,3)$ where

$$\begin{aligned} N_1(\eta,\xi) &= -\frac{1}{4}(1-\eta)(1-\xi)(1+\eta+\xi), \quad N_2(\eta,\xi) = \frac{1}{2}(1-\eta^2)(1-\xi), \\ N_3(\eta,\xi) &= -\frac{1}{4}(1+\eta)(1-\xi)(1-\eta+\xi), \quad N_4(\eta,\xi) = \frac{1}{2}(1+\eta)(1-\xi^2), \\ N_5(\eta,\xi) &= -\frac{1}{4}(1+\eta)(1+\xi)(1-\eta-\xi), \quad N_6(\eta,\xi) = \frac{1}{2}(1-\eta^2)(1+\xi), \\ N_7(\eta,\xi) &= -\frac{1}{4}(1-\eta)(1+\xi)(1+\eta-\xi), \quad N_8(\eta,\xi) = \frac{1}{2}(1-\eta)(1-\xi^2). \end{aligned} \tag{2.21}$$

A fundamental difference between the FVDAM and finite element based solutions of the unit cell problem is rooted in the manner of satisfying local, and thus global, equilibrium equations. While the FVDAM approach enforces equilibrium in the integral sense for every subvolume at each level of mesh refinement (Equation 2.14), the minimization of the total potential energy (this one deduced in Appendix A) of the unit cell problem within the finite element framework,

$$\begin{aligned} \Pi = \frac{1}{2}\int_V \bar{\boldsymbol{\varepsilon}}^T \boldsymbol{C} \bar{\boldsymbol{\varepsilon}} dV + \frac{1}{2}\int_V \boldsymbol{\varepsilon}'^T \boldsymbol{C} \boldsymbol{\varepsilon}' dV + \int_V \boldsymbol{\varepsilon}'^T \boldsymbol{C} \bar{\boldsymbol{\varepsilon}} dV - \int_V \boldsymbol{\varepsilon}'^T \boldsymbol{C} \boldsymbol{\varepsilon}^p dV \\ - \int_V \bar{\boldsymbol{\varepsilon}}^T \boldsymbol{C} \boldsymbol{\varepsilon}^p dV + \frac{1}{2}\int_V \boldsymbol{\varepsilon}^{pT} \boldsymbol{C} \boldsymbol{\varepsilon}^p dV - \bar{\boldsymbol{\sigma}}^T \bar{\boldsymbol{\varepsilon}} V \end{aligned} \tag{2.22}$$

leads to ultimate satisfaction of the unit cell's global equilibrium with sufficient mesh refinement.

In the sequel, we outline the solution of the unit cell problem based on the finite element approach within the 0-th order homogenization framework, which reduces to the determination of the fluctuating displacement components $u'^{(q)}_i$.

As in the FVDAM theory, the displacement field in each element is decomposed into average and fluctuating components following Equation (2.7). For direct comparison with the FVDAM theory, the functional form of the fluctuating displacement components for the Q8 elements is

$$u'^{(q)}_i = U^{(q)}_{i(00)} + \eta U^{(q)}_{i(10)} + \xi U^{(q)}_{i(01)} + \eta\xi U^{(q)}_{i(11)} + \eta^2 U^{(q)}_{i(20)} + \xi^2 U^{(q)}_{i(02)} + \eta^2\xi U^{(q)}_{i(21)} + \eta\xi^2 U^{(q)}_{i(12)} \tag{2.23}$$

The displacement-based finite element method minimizes total potential energy of the unit cell with respect to the unknown nodal fluctuating displacements. Hence, the fluctuating displacement field is expressed in terms of interpolation functions and nodal fluctuating displacements

$$u'^{(q)}_i = \sum_{p=1}^{8} N_p(\eta,\xi) u_i^{o(p,q)} \tag{2.24}$$

where $u_i^{o(p,q)}$ are the nodal fluctuating displacements at the four corners and four midpoints of the reference element starting at the lower left corner and progressing counterclockwise as shown in Figure 2.2. The nodal fluctuating displacements are linearly related to the unknown coefficients $U_{i(00)}, \ldots, U_{i(12)}$ through an invertible matrix based solely on kinematic considerations. This is in contrast with the FVDAM theory where both local kinematic and equilibrium equations are needed to find the relationship between the unknown surface-averaged displacements and the coefficients in the subvolume fluctuating displacement field approximation. The interpolation functions

$N_p(\eta,\xi)$ which generate quadratic displacement variations along the reference element's sides are the same as those used in the mapping of the reference element onto the actual discretized domain, Equation (2.21). The above displacement field representation can be contrasted with the quadratic representation employed in the parametric FVDAM theory, Equation (2.8), where the product terms $\eta\xi$, $\eta^2\xi$ and $\eta\xi^2$ are absent.

Applying the differential operator $\partial = (\partial/\partial \boldsymbol{y})_{sym}$ to the fluctuating displacement components expressed in terms of the nodal fluctuating displacements using the matrix notation $\boldsymbol{u'}^{(q)} = \boldsymbol{N}^{(q)}\boldsymbol{u}_o^{(q)}$, the strain field due to the fluctuating displacement field is obtained in the form

$$\boldsymbol{\varepsilon'}^{(q)} = \partial \boldsymbol{N}^{(q)}\boldsymbol{u}_o^{(q)} = \boldsymbol{B}^{(q)}\boldsymbol{u}_o^{(q)} \tag{2.25}$$

which is used to construct the potential energy integral at the element level following Equation (2.22). Assembly of the individual contributions through the enforcement of nodal force equilibrium and displacement continuity, together with periodic boundary conditions, produces the total potential energy of the unit cell in the form,

$$\begin{aligned}\Pi = \frac{1}{2}\int_V \bar{\boldsymbol{\varepsilon}}^T \boldsymbol{C}\bar{\boldsymbol{\varepsilon}} dV + \frac{1}{2}\boldsymbol{U}_o^T\left(\int_V \boldsymbol{B}^T\boldsymbol{C}\boldsymbol{B}dV\right)\boldsymbol{U}_o + \boldsymbol{U}_o^T\left(\int_V \boldsymbol{B}^T\boldsymbol{C}dV\right)\bar{\boldsymbol{\varepsilon}} \\ -\boldsymbol{U}_o^T\left(\int_V \boldsymbol{B}^T\boldsymbol{C}\boldsymbol{\varepsilon}^p dV\right) - \int_V \bar{\boldsymbol{\varepsilon}}^T\boldsymbol{C}\boldsymbol{\varepsilon}^p dV + \frac{1}{2}\int_V \boldsymbol{\varepsilon}^{pT}\boldsymbol{C}\boldsymbol{\varepsilon}^p dV - \bar{\boldsymbol{\sigma}}^T\bar{\boldsymbol{\varepsilon}}V\end{aligned} \tag{2.26}$$

where $\boldsymbol{U}_o = \left[\boldsymbol{u}_o^{(1)},\dots,\boldsymbol{u}_o^{(N)}\right]^T$ and the global matrix $\boldsymbol{B}$ contains contributions from all the elements. Minimization of the total potential energy with respect to the nodal fluctuating displacements, $\partial\Pi/\partial\boldsymbol{U}_o$, produces the global system of equations for the unknown nodal fluctuating displacements

$$\boldsymbol{K}\boldsymbol{U}_o = \bar{\boldsymbol{f}} + \boldsymbol{f}_p \tag{2.27}$$

where

$$\boldsymbol{K} = \int_V \boldsymbol{B}^T \boldsymbol{C}\boldsymbol{B} dV\,, \quad \bar{\boldsymbol{f}} = -\left(\int_V \boldsymbol{B}^T \boldsymbol{C} dV\right)\bar{\boldsymbol{\varepsilon}}, \quad \boldsymbol{f_p} = \int_V \boldsymbol{B}^T \boldsymbol{C}\boldsymbol{\varepsilon}^p dV \tag{2.28}$$

We note that there are two differences between the finite element and FVDAM approaches in the manner of applying periodicity conditions. In the former case, the periodicity conditions are enforced only on the external nodal displacements of the unit cell, while in the latter case the periodicity conditions are applied on both the external surface-averaged tractions and displacements. In the finite element approach the periodic displacement boundary conditions are implemented in point-wise rather than surface-average sense, which ensures implicit enforcement of point-wise periodic tractions.

The use of Q8 elements requires numerical calculation of the local stiffness matrix elements, based herein on complete 9-point Gaussian quadrature, in contrast with the closed-form expressions developed for the parametric FVDAM framework. The procedure shown in Chen et al. (1996) is used to evaluate the stress field within an element. In this approach, the least-squares method is employed to evaluate the extrapolation surface compounded by the interpolation functions $N_p(\eta, \xi)$, to extrapolate stress and plastic strain fields from their values at Gauss points.

The same iterative procedure for the solution of the global elastic-plastic system of equations (Equation 2.27) was implemented into the finite element approach as that used in the parametric FVDAM theory, based on the technique of successive elastic solutions proposed by Mendelson (1986). Both the FVDAM and finite element codes have been written in MATLAB.

2.5. Equilibrium Aspects of FVDAM and FEM Approaches

As mentioned in the foregoing, the manner of satisfying equilibrium equations in the discretized domain of the unit cell is fundamentally different for the FVDAM and finite element approaches. The minimization of total potential energy within the finite element framework requires sufficient mesh refinement to achieve global equilibrium, and hence equilibrium at the element level. In contrast, the FVDAM approach directly enforces equilibrium in the integral sense for every subvolume at each level of mesh refinement. The extent to which equilibrium of an element is satisfied at each level of mesh refinement within the finite element framework may be gauged by defining an unbalanced average stress based on the Average Stress Theorem.

The above theorem states that, for an arbitrary body in equilibrium regardless of its composition, the average stress $\hat{\boldsymbol{\sigma}}$ may be calculated from the integral of the surface tractions as follows,

$$\hat{\sigma}_{ij} = \frac{1}{V}\int_S t_i x_j dS = \frac{1}{V}\int_S \sigma_{ik} n_k x_j dS \tag{2.29}$$

Converting the surface integral to volume integral using Gauss Theorem, we obtain

$$\hat{\sigma}_{ij} = \frac{1}{V}\int_S \sigma_{ik} n_k x_j dS = \frac{1}{V}\int_V \frac{\partial}{\partial x_k}(\sigma_{ik} x_j) dV = \frac{1}{V}\int_V \left(\sigma_{ij} + \frac{\partial \sigma_{ik}}{\partial x_k} x_j\right) dV \tag{2.30}$$

When the local equilibrium equations are satisfied in a point-wise sense, that is when in the absence of body forces $\partial \sigma_{ik}/\partial x_k = 0$, the above integral reduces to the standard definition for the volume-averaged stress. This occurs in the case of the FVDAM theory in the elastic region in light of the employed quadratic displacement field and the use of the volume-averaged Jacobian in the displacement gradient relations given in Equation (2.13). In the case of the finite element method, however, the local equilibrium

equations are satisfied only in the limit with increasing mesh discretization, thereby allowing to define an unbalanced average stress in any subdomain of the unit cell as follows

$$\Delta\bar{\sigma}_{ij} = \hat{\sigma}_{ij} - \frac{1}{V}\int_V \sigma_{ij}dV = \hat{\sigma}_{ij} - \bar{\sigma}_{ij} = \frac{1}{V}\int_V \frac{\partial \sigma_{ik}}{\partial x_k}x_j dV \tag{2.31}$$

At the element or subvolume level, the unbalanced average stress components are calculated from the formula

$$\Delta\bar{\sigma}_{ij}\big|^q = \left(\hat{\sigma}_{ij} - \bar{\sigma}_{ij}\right)^q \tag{2.32}$$

while for the entire unit cell domain we employ the weighted sum of positive local unbalanced stress contributions in order to avoid artificial cancellations due to sign changes

$$\Delta\bar{\sigma}_{ij} = \sum_{q=1}^{N} c_{(q)}\big|\Delta\bar{\sigma}_{ij}\big|^q \tag{2.33}$$

where $c_{(q)} = V_q/V$ is the volume fraction of the *qth* element or subvolume, and $V = \sum_{q=1}^{N} V_q$.

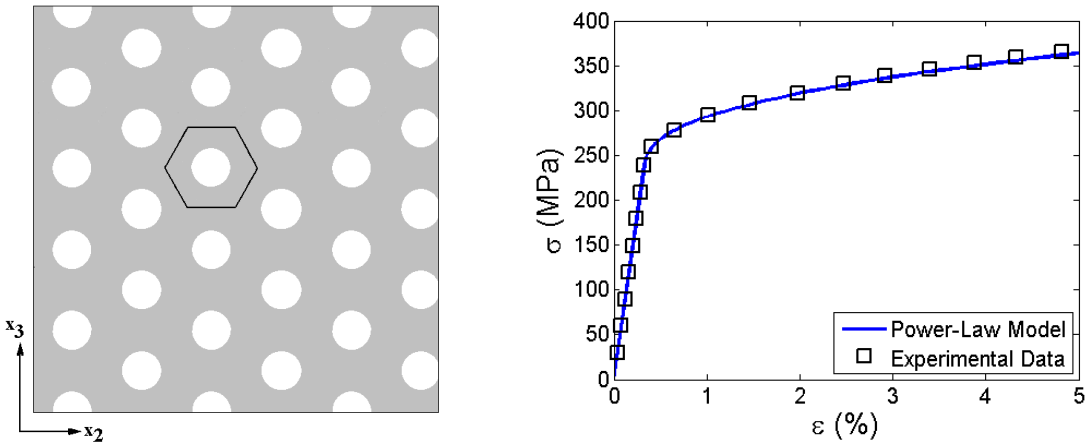

Figure 2.3. Hexagonal array of circular holes in a power-law hardening aluminum matrix showing a highlighted unit cell (left), and stress-strain response of the matrix (right).

To illustrate the degree to which local equilibrium is satisfied by the parametric FVDAM and finite element methods as a function of mesh refinement, we examine the response of a hexagonal array of circular porosities in a thin metallic sheet in plane stress under inplane loading, Figure 2.3. Power-law aluminum matrix characterized by the effective stress-strain response,

$$\sigma_{eff} = \sigma_y + H_p\left(\varepsilon_{eff}^p\right)^n \tag{2.34}$$

included in the figure, is used in the simulations based on properties given in Table 2.1. Three unit cell discretizations were employed, namely 18x3, 30x5 and 60x10 Q8 elements or subvolumes shown in Figure 2.4.

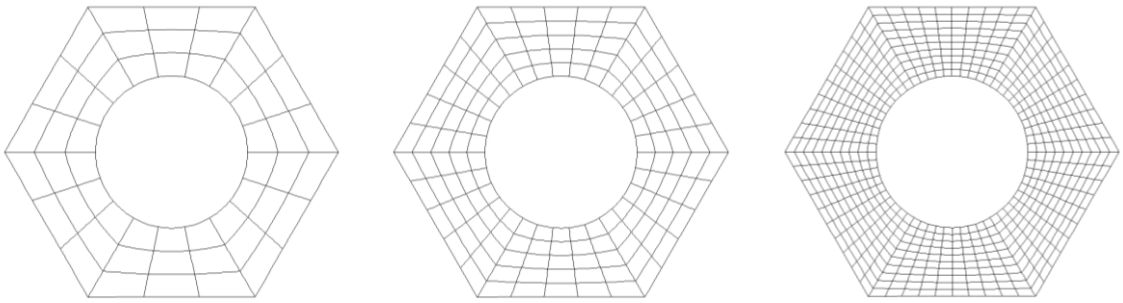

Figure 2.4. Unit cells of the hexagonal array of circular holes with the porosity volume fraction of 0.25 discretized into 18x3, 30x5 and 60x10 Q8 elements or subvolumes.

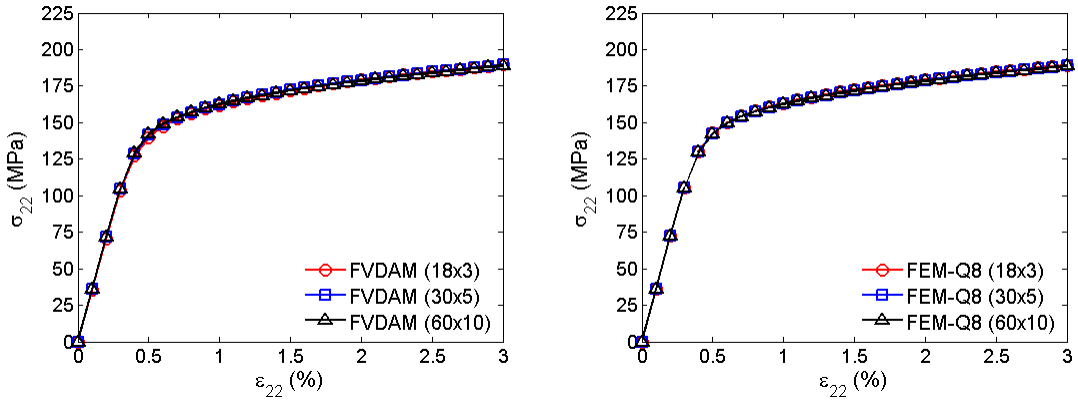

Figure 2.5. Homogenized stress-strain response under loading by $\bar{\sigma}_{22} \neq 0$ only as a function of unit cell discretization. Comparison between FVDAM and FEM simulations.

Table 2.1. Elastic and plastic properties of the power-law hardening aluminum matrix.

$E(MPa)$	ν	$\sigma_y(MPa)$	$H_p(MPa)$	n
72,700	0.34	240	457.6	0.4218

Figure 2.5 illustrates the homogenized transverse normal responses under pure normal loading defined by $\bar{\sigma}_{22} \neq 0$. The corresponding local transverse normal stress $\sigma_{22}(y_2, y_3)$ distributions for the three discretizations obtained using the two approaches are compared in Figure 2.6 at the terminal $\bar{\varepsilon}_{22}$ strain of 3%. As observed, both approaches produce macroscopically converged responses with as few as 18x3 elements/subvolumes. The local stress fields, however, are better approximated at small unit cell discretizations by the FVDAM theory. This feature is important in multiscale analyses. The reason for this is illustrated in Figure 2.7 which compares local distributions of the unbalanced average stress components $|\Delta\bar{\sigma}_{22}|^q$ normalized by the average unit cell value $\bar{\sigma}_{22}$ for the three unit

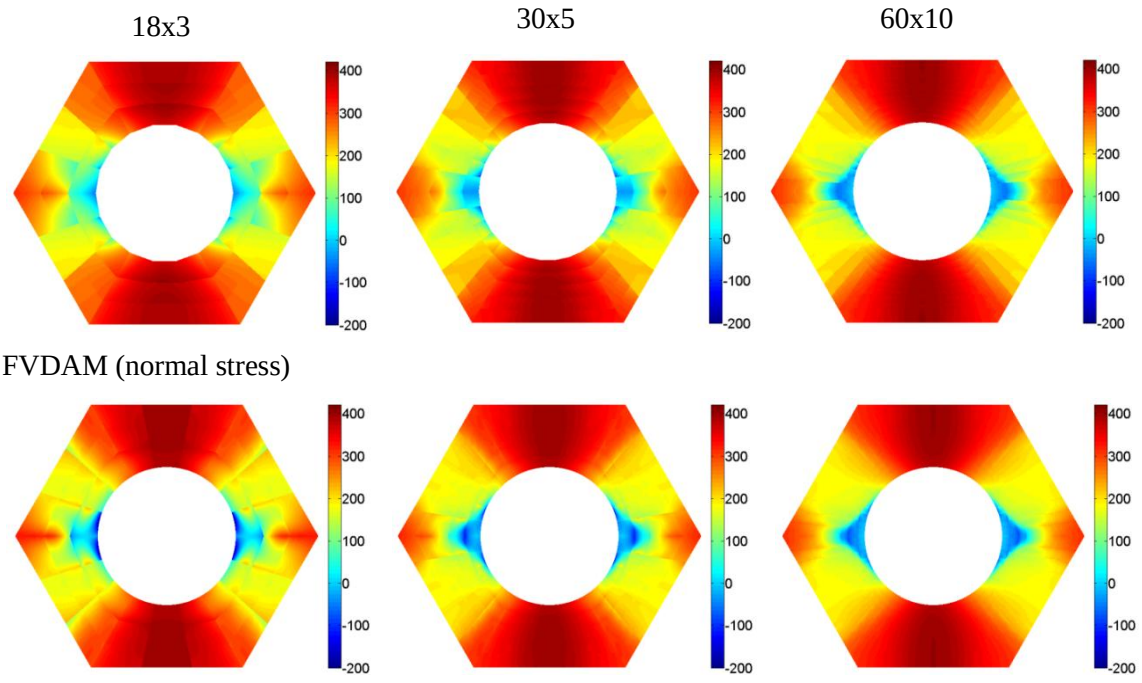

FVDAM (normal stress)

FEM (normal stress)

Figure 2.6. Normal σ_{22} stress distributions at the homogenized strain $\bar{\varepsilon}_{22} = 3\%$ for three unit cell discretizations. Comparison between FEM and FVDAM predictions.

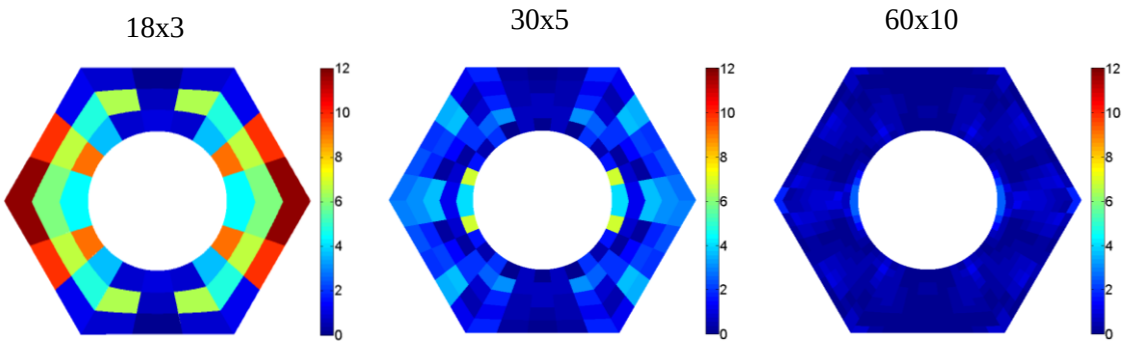

FEM (unbalanced normal stress)

(a) $\bar{\varepsilon}_{22} = 0.1\%$

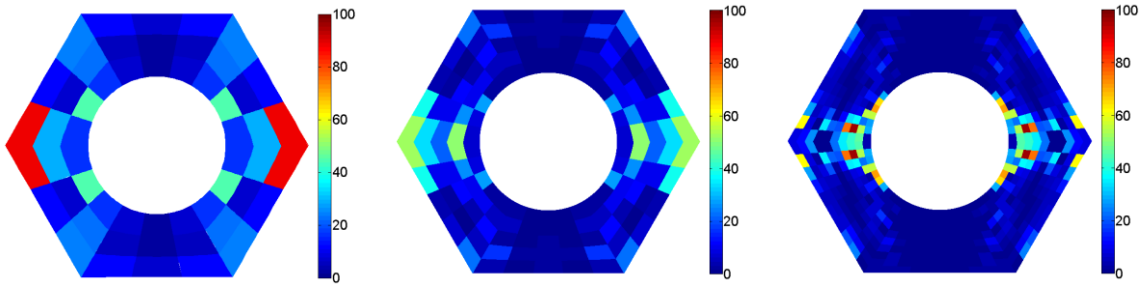

FEM (unbalanced normal stress)

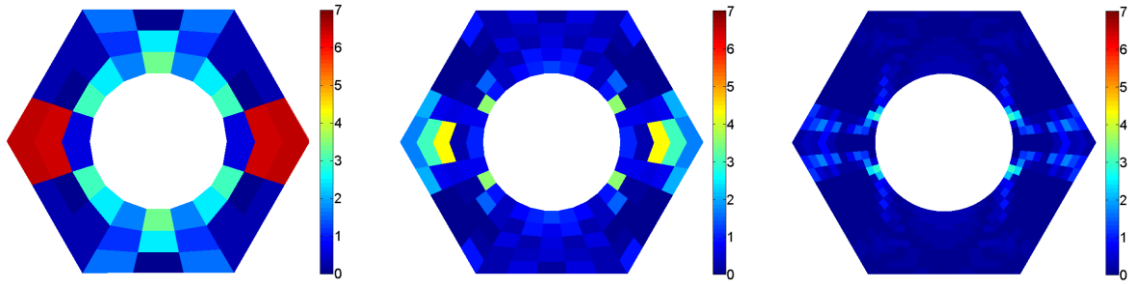

FVDAM (unbalanced normal stress)

(b) $\bar{\varepsilon}_{22} = 3.0\%$

Figure 2.7. Unbalanced normalized $\left|\Delta\bar{\sigma}_{22}^{q}/\bar{\sigma}_{22}\right|$ (%) stress distributions at two homogenized strain levels in the elastic and elastic-plastic regions for three unit cell discretizations. Comparison between FEM and FVDAM predictions.

cell discretizations at the applied strain levels of $\bar{\varepsilon}_{22} = 0.1\%$ and 3.0%. The first strain level produces elastic fields only, while substantial plastic fields develop at the second strain level. In the absence of plasticity, the unbalanced average stress $|\Delta\bar{\sigma}_{22}|^{q}$ decreases to a small fraction of the homogenized stress $\bar{\sigma}_{22}$ with increasing mesh refinement

relatively fast for the finite element method, Figure 2.7(a). In contrast, this occurs much slower as plasticity develops, it is only with increasing mesh refinement, greater than 60x10 in this case, that the finite element distributions of the unbalanced average stress become comparably small to those predicted by the parametric FVDAM theory, Figure 2.7(b).

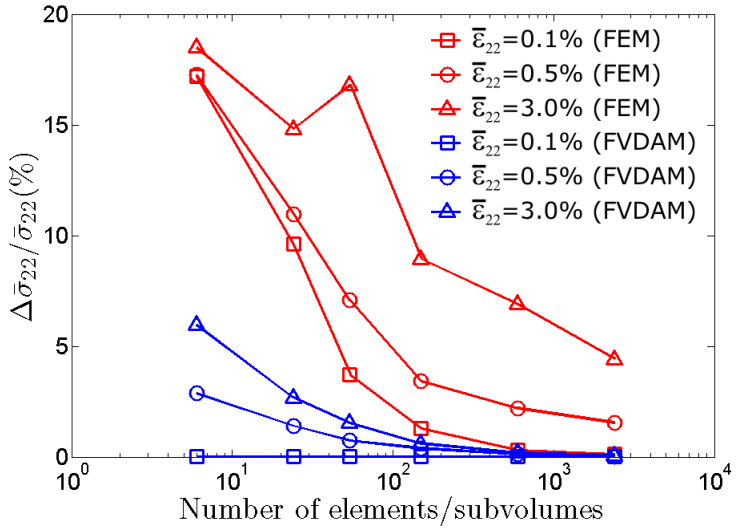

Figure 2.8. Convergence of the unbalanced average stress $\Delta\bar{\sigma}_{22}/\bar{\sigma}_{22}$ with mesh size at three homogenized strain levels in the elastic and elastic-plastic regions. Comparison of finite element method and FVDAM results.

Figure 2.8 presents the global unbalanced stress $\Delta\bar{\sigma}_{22}$ as a function of mesh refinement at three applied strain levels which produce purely elastic ($\bar{\varepsilon}_{22} = 0.1\%$) and increasingly greater plastic strain fields ($\bar{\varepsilon}_{22} = 0.5\%$ and 3.0%), illustrating the global aspects of the equilibrium behavior of the finite element method and parametric FVDAM theory. These results reinforce the observation in Figure 2.7 that plasticity requires greater mesh refinement for the satisfaction of local equilibrium by the finite element method. In contrast, the corresponding global convergence in the presence of plasticity is much faster for the FVDAM theory.

2.6. Multi-Axial Loading of Perforated Metallic Sheets

The macroscopic response of multiphase materials with unidirectional reinforcement under combined multi-axial loading can be generated using just one unit cell discretization, which is valid for any combination of all six components of macroscopic stresses or strains. As observed in Equations (2.18) and (2.27), the solution of the unit cell boundary-value problem is obtained for any combination of specified macroscopic strains $\bar{\boldsymbol{\varepsilon}}$. In order to simulate loading by specified stress components, the strain components are adjusted accordingly using the homogenized constitutive equation $\bar{\boldsymbol{\sigma}} = \boldsymbol{C}^*(\bar{\boldsymbol{\varepsilon}} - \bar{\boldsymbol{\varepsilon}}^p)$. In the absence of plasticity, constant strain ratios that correspond to fixed stress ratios are obtained in terms of the homogenized moduli $\boldsymbol{C}^*$. In the presence of plasticity, the incremental version of the homogenized constitutive equations,

$$d\bar{\boldsymbol{\sigma}} = \boldsymbol{C}^*(d\bar{\boldsymbol{\varepsilon}} - d\bar{\boldsymbol{\varepsilon}}^p) \tag{2.35}$$

is employed, and strain increment ratios are adjusted iteratively at each load increment to generate the desired load path specified in terms of macroscopic stresses. This is required in applications involving generations of yield, limit or failure surfaces in the macroscopic stress space as well as in multiscale algorithms where the local response at a material or structural point is obtained from microscopic considerations.

An illustration of the multi-axial loading capability is shown in Figure 2.9 for a hexagonal array of circular holes in an elastic-plastic strain hardening matrix (see Table 2.1) with 10% porosity loaded in the macroscopic $\bar{\sigma}_{22} - \bar{\sigma}_{33}$ and $\bar{\sigma}_{22} - \bar{\sigma}_{23}$ stress spaces along constant stress paths defined by fixed angles β with respect to the $\bar{\sigma}_{22}$ axis in both instances. Unit cells discretized into 198x25 subvolumes and Q8 elements were

employed which produced converged homogenized response generated using both parametric FVDAM theory and finite element method.

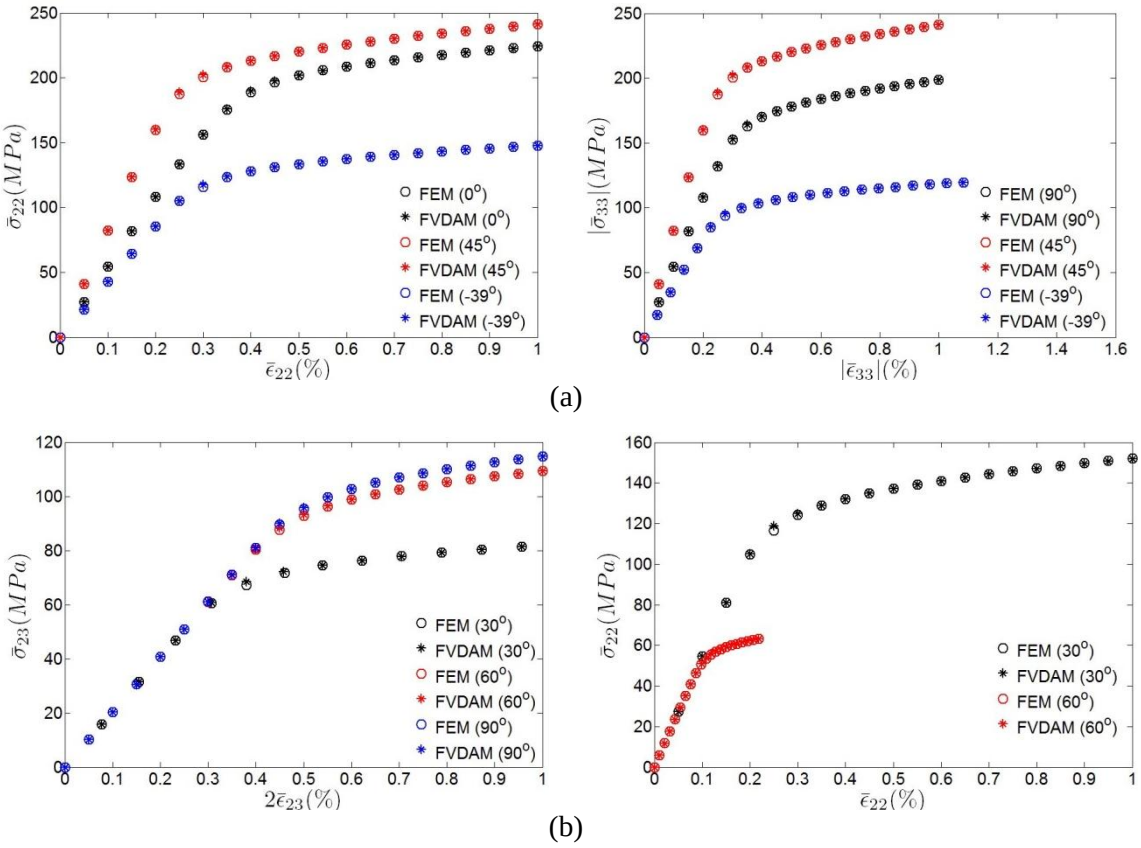

Figure 2.9. Homogenized response of hexagonal arrays with 10% porosity in homogenized $\bar{\sigma}_{22} - \bar{\sigma}_{33}$ (a) and $\bar{\sigma}_{22} - \bar{\sigma}_{23}$ (b) stress spaces. Note that in each case, the angle in the figure legends denotes the inclination of the radial load vector relative to the horizontal $\bar{\sigma}_{22}$ stress axis.

The local σ_{22} stress and the effective plastic strain distributions predicted by the two methods at the applied terminal strain $\bar{\varepsilon}_{22}(\bar{\varepsilon}_{33}) = 1.0\%$ are compared in Figures 2.10 and 2.11 for radial paths oriented at $\beta = 90^o, 45^o, 0^o, -39^o$ in the $\bar{\sigma}_{22} - \bar{\sigma}_{33}$ stress space. No observed differences in the results generated using the FVDAM theory and finite element method are evident. Figures 2.12 and 2.13 present comparisons of the local σ_{23} stress and the corresponding effective plastic strain distributions along three radial loading paths oriented at $\beta = 90^o, 60^o, 30^o$ in the $\bar{\sigma}_{22} - \bar{\sigma}_{23}$ stress space, at the applied terminal strain

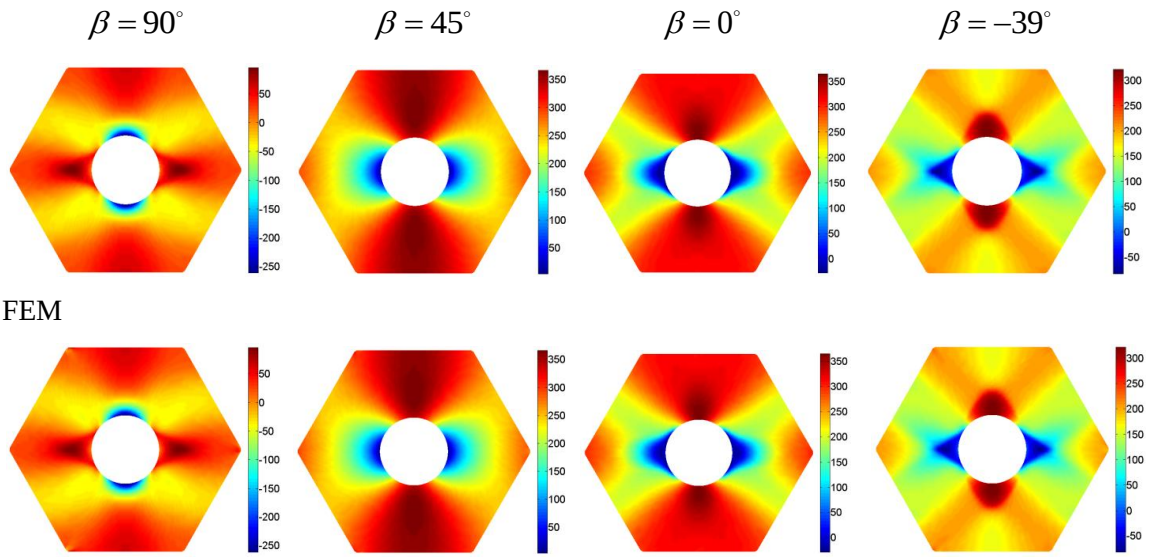

Figure 2.10. Comparison of σ_{22} stress fields in radially loaded hexagonal array with 10% porosity in the $\bar{\sigma}_{22} - \bar{\sigma}_{33}$ stress space ($\bar{\varepsilon}_{22} = 1.0\%\ for\ \beta = 90^o, 45^o, 0^o, -39^o$ and $\bar{\varepsilon}_{33} = 1.0\%\ for\ \beta = 90^o$).

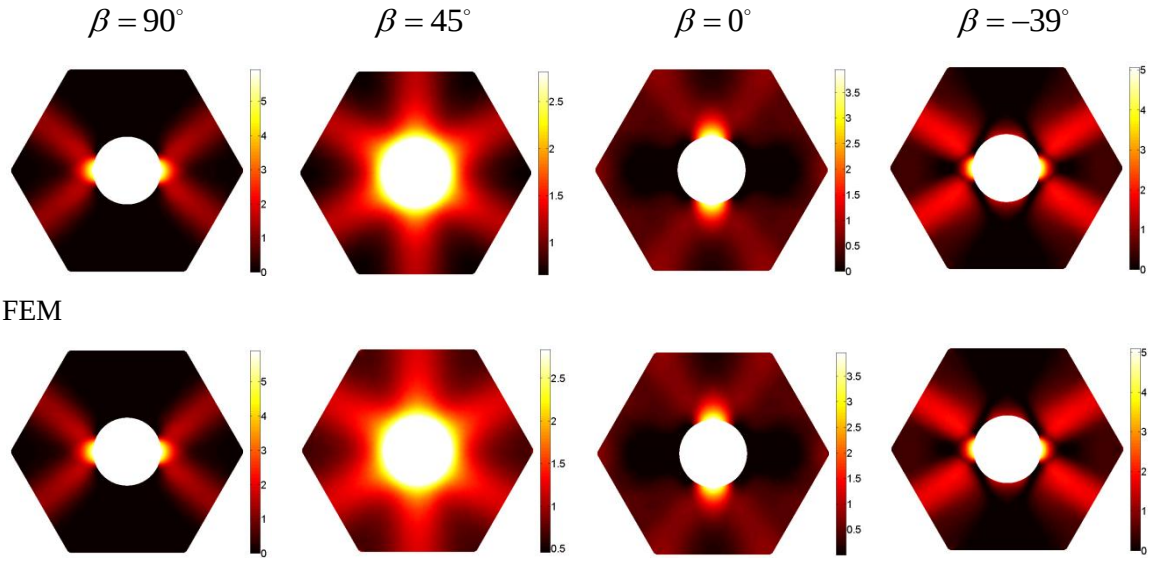

Figure 2.11. Comparison of full-field effective plastic strains in radially loaded hexagonal array with 10% porosity in the $\bar{\sigma}_{22} - \bar{\sigma}_{33}$ stress space ($\bar{\varepsilon}_{22} = 1.0\%\ for\ \beta = 90^o, 45^o, 0^o, -39^o$ and $\bar{\varepsilon}_{33} = 1.0\%\ for\ \beta = 90^o$).

$2\bar{\varepsilon}_{23} = 1.0\%$ in the case of $\beta = 90^o, 60^o$ and $\bar{\varepsilon}_{22} = 1.0\%$ in the case of $\beta = 30^o$. No observable differences between the FVDAM and finite element predictions can be readily

noted. This comparison provides further evidence of the FVDAM theory's excellent predictive capability under multiaxial loading paths vis-à-vis the finite element method.

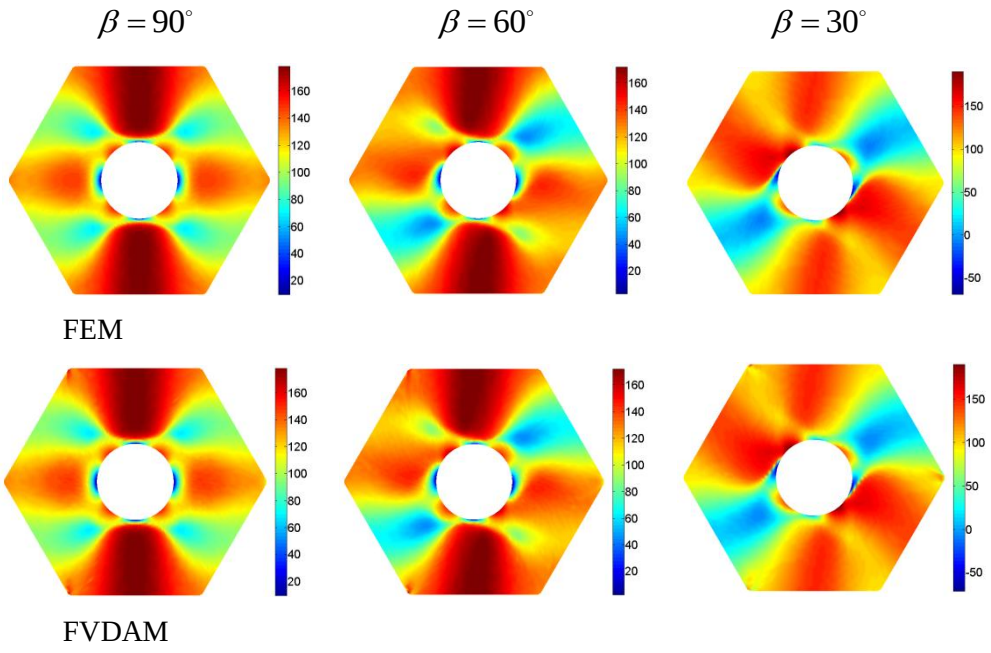

Figure 2.12. Comparison of σ_{23} stress fields in radially loaded hexagonal array with 10% porosity in the $\bar{\sigma}_{22} - \bar{\sigma}_{23}$ stress space ($2\bar{\varepsilon}_{23} = 1.0\%\ for\ \beta = 90^{o}, 60^{o}$ and $\bar{\varepsilon}_{22} = 1.0\%\ for\ \beta = 30^{o}$).

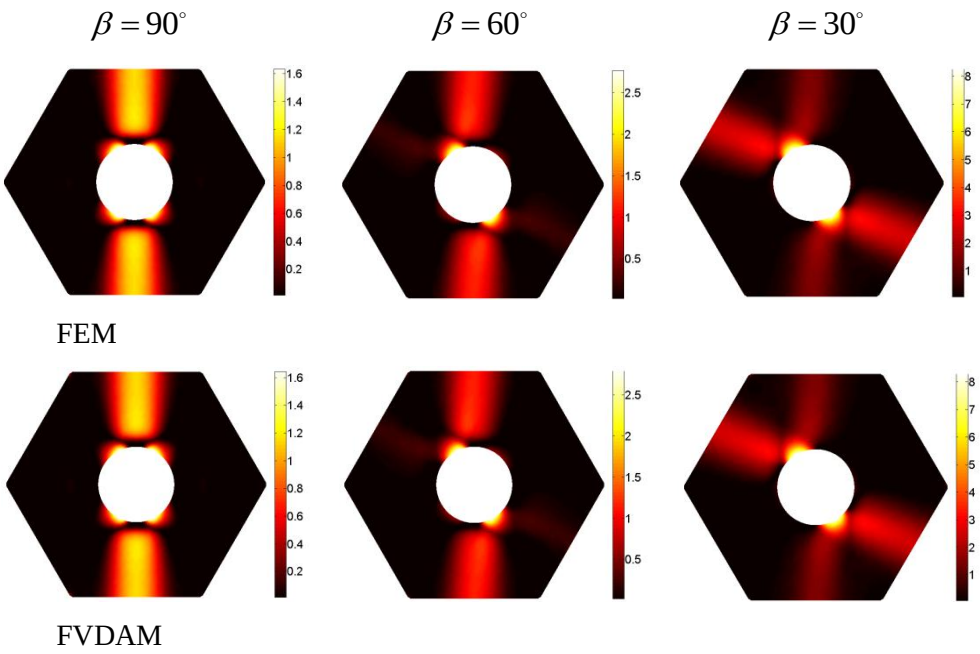

Figure 2.13. Comparison of full-field effective plastic strains in radially loaded hexagonal array with 10% porosity in the $\bar{\sigma}_{22} - \bar{\sigma}_{23}$ stress space ($2\bar{\varepsilon}_{23} = 1.0\%\ for\ \beta = 90^{o}, 60^{o}$ and $\bar{\varepsilon}_{22} = 1.0\%\ for\ \beta = 30^{o}$).

Using the multidimensional loading capability of the parametric FVDAM theory, Khatam and Pindera (2011) generated homogenized yield and limit surface data for use in the construction of a homogenized plasticity theory based on underpinning microlevel plastic fields for this class of periodic materials.

2.7. Microstructural Effects in Wavy Multilayers

The parametric FVDAM theory has also been employed to investigate thermo-elastic, elastic-plastic and nonlinearly elastic responses of emerging periodic materials consisting of wavy multilayers with soft and hard phases, Figure 2.14. Thermo-elastic moduli of such materials were obtained as a function of phase volume fraction, amplitude-to-wavelength ratio and waveform shape by Khatam and Pindera (2009a). This investigation was subsequently extended to the elastic-plastic domain and interesting plastic localization effects illustrated, demonstrating the major role that the plastic strain controlled stress transfer between elastic-plastic and elastic layers plays in affecting the macroscopic post-yield response, Khatam and Pindera (2009b). The most recent study has revealed the important role that the layer thickness plays in the plastic strain localization process at a fixed amplitude-to-wavelength ratio and volume fraction of the hard phase, Khatam and Pindera (2010). In this investigation, unit cells with progressively thinner layers were generated by subdividing a thick ceramic layer within a unit cell of fixed geometry into progressively thinner ones and redistributing the thinner layers uniformly in a manner that preserved the vertical layer spacing relative to unit cells with the thick layers. Such subdivision of flat multilayers produces no changes in the homogenized response due to the preservation of geometric similitude of the unit cell. In

the presence of layer waviness, however, this is no longer true. The effect of this subdivision on the elastic response in the infinitesimal strain region is very small. In contrast, the homogenized elastic-plastic response is affected to a surprisingly greater extent.

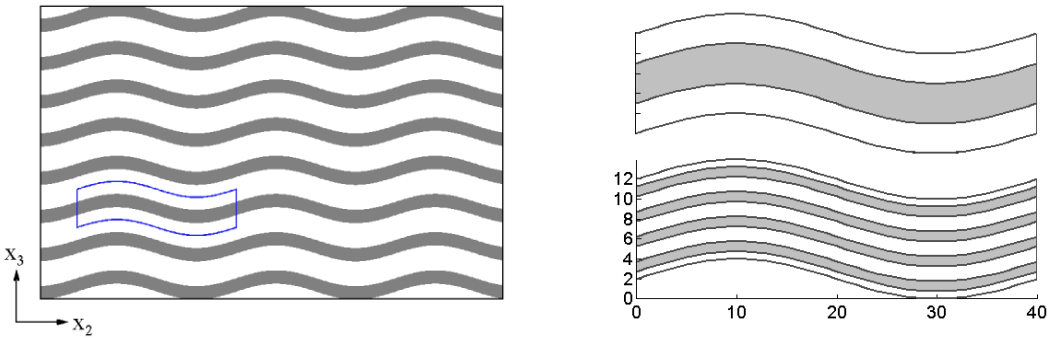

Figure 2.14. (left) A wavy multilayer with a highlighted unit cell of the periodic microstructure; (right) unit cells with increasingly refined microstructures with the amplitude-to-wavelength ratio of 0.05 and hard-phase volume fraction of 0.40.

Table 2.2. Elastic and plastic parameters of the materials employed in the wavy multilayers study.

Layer	$\boldsymbol{E(MPa)}$	$\boldsymbol{\nu}$	$\boldsymbol{\sigma_y(MPa)}$	$\boldsymbol{H_p(MPa)}$	$\boldsymbol{n}$
Elastic Ceramic	420,000	0.25	-	-	-
Softer Aluminum Matrix	72,400	0.33	286.67	1.396	1.0

This recently discovered effect is illustrated, and verified herein using an independent finite element analysis, for wavy periodic multilayers comprised of elastic ceramic-like layers embedded in much softer nearly elastic-perfectly plastic aluminum-like matrix (see Table 2.2 for the elastic and plastic parameters of these materials based on the power-law model shown in Equation 2.34), where the amplitude-to-wavelength ratio of a sinusoidal unit cell waveform is 0.05 and the ceramic phase volume fraction is fixed at 0.40 and 0.60 while the unit cell microstructure is refined from a single thick ceramic layer to four equally-spaced thinner ones for both volume fractions. Figure 2.15 shows the unit cells

discretized into 120x80 subvolumes and Q8 elements which produced converged homogenized response using the FVDAM theory and the finite element method.

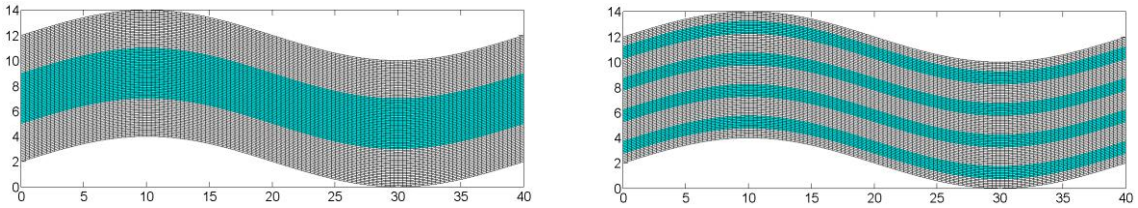

Ceramic phase with volume fraction of 0.40 (green region)

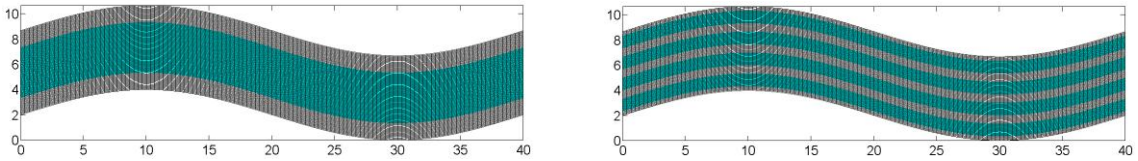

Ceramic phase with volume fraction of 0.60 (green region)

Figure 2.15. Unit cells of the lamellar material comprised of sinusoidally varying single and multiple stiff layers with the amplitude-to-wavelength ratio of 0.05, discretized into 120×80 quadrilateral subvolumes and Q8 elements.

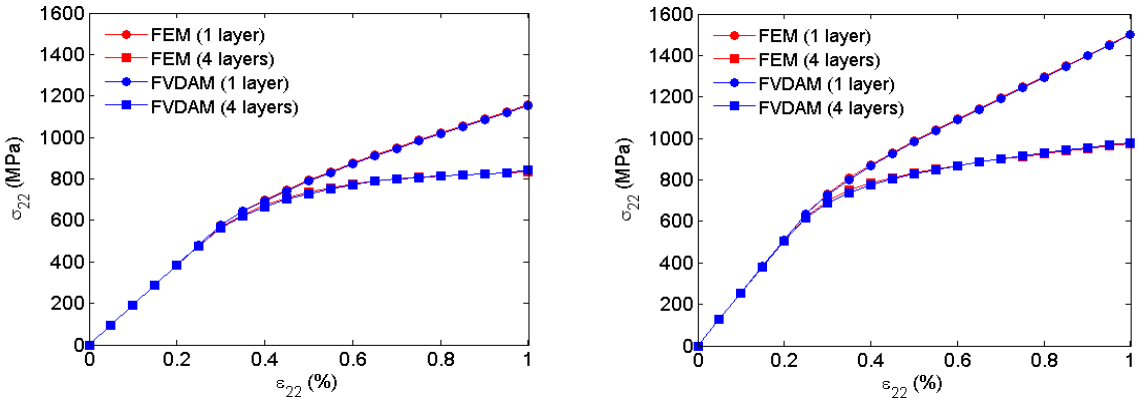

Figure 2.16. Macroscopic stress-strain response of wavy periodic multilayers with coarse and fine microstructures at the fixed hard phase volume fraction of 0.40 (left) and 0.60 (right) subjected to loading defined by $\sigma_{22} \neq 0$.

Figure 2.16 presents comparison of the response of these wavy periodic multilayers subjected to loading defined by $\sigma_{22} \neq 0$, with the macroscopic total and plastic strains adjusted at each load increment to ensure uniaxial macroscopic loading. While the

macroscopic response in the elastic region is not significantly affected by the microstructural refinement, the evolution of plasticity perhaps surprisingly alters the response in the post-yield region for this loading direction. Specifically, the response becomes substantially more compliant with increasing microstructural refinement, the extent of which also depends on the ceramic layer volume fraction.

The mechanism involves alteration of the load-bearing transverse stress component σ_{22} in the elastic ceramic plies due to thickness-controlled local bending in the trough regions of the ceramic layers and localized evolution of plasticity in the compliant elastic-plastic matrix layers. In the elastic region, the thicker ceramic layers experience greater tensile (as well as compressive) transverse stress across the crest-trough planes due to greater effective moment of inertia which controls localized bending. This difference, however, is not large enough to produce substantial changes in the homogenized response in the elastic region until localized evolution of plasticity, which is more pervasive in the unit cell with the refined four-ceramic layer microstructure. This is illustrated in Figure 2.17 which compares the effective plastic strain distributions in the single-ceramic and four-ceramic layer unit cells just past the onset of yielding in the off-trough and off-crest regions (FVDAM results for the ceramic phase with volume fraction of 0.40). The substantially greater plastic strain localization in the fine-microstructure unit cell further reduces the extent of transverse stress transferred into the load-bearing ceramic layers, leading to substantial degradation in the load bearing capacity of the ceramic layers observed at the macroscopic strain $\bar{\varepsilon}_{22} = 1\%$. Particularly significant is the reduction in transverse stress across crest-trough planes which is sufficiently high to initiate cracks in the coarse-microstructure unit cell. Hence, while the load-bearing capacity of the fine-

microstructure unit cell is substantially degraded by the localized evolution of plasticity, its toughness should be higher due to higher survivability of the brittle ceramic layers which carry more uniformly distributed transverse stress. Incorporation of the FVDAM theory into an optimization algorithm, facilitated by its closed-form analytical structure, will enable efficient identification of microstructures with targeted load-bearing capacity and toughness.

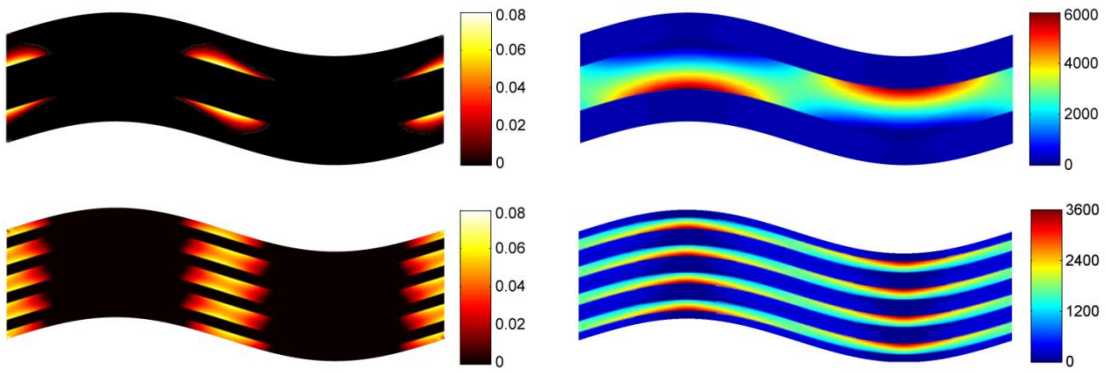

Figure 2.17. Plastic effective strain distributions at the applied homogenized strain $\bar{\varepsilon}_{22} = 0.3\%$ in unit cells with coarse and fine wavy microstuctures with 0.40 volume fraction of the hard phase (left), and σ_{22} stress distributions at $\bar{\varepsilon}_{22} = 1\%$ under loading defined by $\sigma_{22} \neq 0$ (right).

2.8. Interfacial Interpenetration and Discontinuity of the Non-Traction Stress Components in the Parametric FVDAM Theory

The current parametric FVDAM theory employs an incomplete second-order displacement field representation within quadrilateral subvolumes together with a surface-averaging framework which does not enforce displacement or traction continuity in a point-wise manner. This, in turn, produces relative rotations of adjacent subvolume faces which are not constrained, leading to interfacial interpenetrations, thereby

potentially causing problems in the context of finite-deformation applications involving very large deformations (Katham and Pindera, 2012). This is in stark contrast with conformable elements employed in the finite element method wherein the displacement field at the elemental level is defined in terms of nodal values obtained from interpolation functions which ensure interfacial displacement continuity. On the other hand, the use of a variational principle in the displacement-based finite element approach precludes the satisfaction of interfacial traction continuity between adjacent elements until the total potential energy is minimized, which occurs with sufficiently fine discretization. In contrast, the unknown coefficients $W_{i(mn)}^{(q)}$ in the parametric FVDAM theory are expressed in terms of surface-averaged displacements using the definitions for these quantities and the equilibrium equations satisfied in a surface-averaged sense. The incomplete second-order displacement field representation in conjunction with the use of quadrilateral subvolumes is sufficient to construct a local stiffness matrix using surface-averaged tractions, enabling enforcement of both surface-average interfacial displacement and traction continuity at any level of unit cell discretization, albeit at the expense of interfacial interpenetration and discontinuity of the non-traction stress components at common interfaces between subvolumes with the same elastic moduli.

The interfacial interpenetration phenomenon becomes very small with sufficient unit cell discretization as is demonstrated in Figure 2.18 for a hexagonal unit cell with a circular porosity subjected to transverse normal stress. The analysis, limited to elastic phases, is based on the elastic constants shown in Table 2.1. While face rotations and concomitant interfacial interpenetrations are noticeable for a unit cell discretized into 12x2 subvolumes, the interfacial interpenetrations become very small with further unit

cell refinement to 30x5 subvolumes, and practically vanish for the 60x10 subvolume unit cell. Comparison with Q8-based FEM predictions even for the 30x5 subvolume unit cell is favorable.

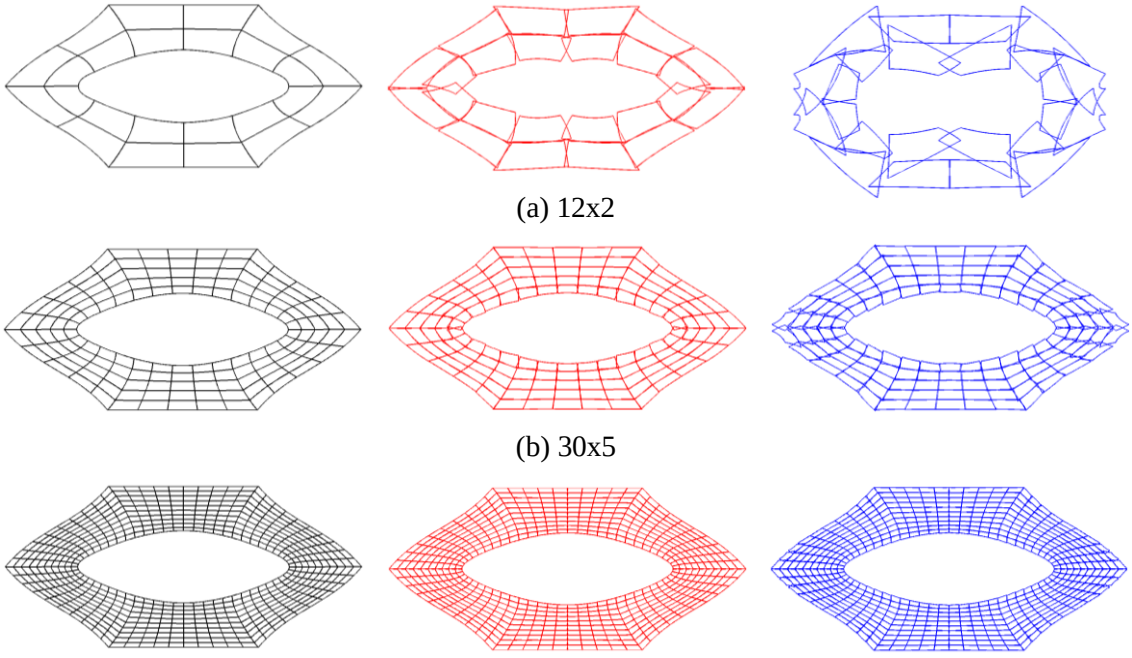

Figure 2.18. Comparison of deformed meshes (magnified 500 times) of unidirectionally loaded hexagonal arrays with 25% porosity by $\bar{\sigma}_{22} \neq 0$ at $\bar{\varepsilon}_{22} = 0.1\%$ as a function of mesh refinement.

The interfacial interpenetrations cannot be avoided within the present framework since the surface-averaging approach precludes the possibility of enforcing nodal displacement continuity using the current displacement field approximation and quadrilateral subvolumes. This is because the coefficients $W_{i(mn)}^{(q)}$ in the fluctuating displacement field approximation given in Equation (2.8) cannot be expressed uniquely in terms of the subvolume nodal displacements. In fact, multiple solutions are obtained only when the sums of surface-averaged displacements on opposite faces of a subvolume are set equal. This condition does not ensure that surface-averaged rotations of common faces shared

by adjacent subvolumes are equal. We demonstrate this for the reference square subvolume. Evaluating the inplane displacement field in Equation (2.8) at the four nodes, starting at the lower left corner and progressing counterclockwise, Figure 2.1, we obtain the following system of equations for the unknown coefficients $W_{i(mn)}^{(q)}$,

$$\begin{aligned} W_{i(00)}^{(q)} - W_{i(10)}^{(q)} - W_{i(01)}^{(q)} + W_{i(20)}^{(q)} + W_{i(02)}^{(q)} &= u'^{1(q)}_i \\ W_{i(00)}^{(q)} + W_{i(10)}^{(q)} - W_{i(01)}^{(q)} + W_{i(20)}^{(q)} + W_{i(02)}^{(q)} &= u'^{2(q)}_i \\ W_{i(00)}^{(q)} + W_{i(10)}^{(q)} + W_{i(01)}^{(q)} + W_{i(20)}^{(q)} + W_{i(02)}^{(q)} &= u'^{3(q)}_i \\ W_{i(00)}^{(q)} - W_{i(10)}^{(q)} + W_{i(01)}^{(q)} + W_{i(20)}^{(q)} + W_{i(02)}^{(q)} &= u'^{4(q)}_i \end{aligned} \tag{2.36}$$

Solution for the unknown coefficients in terms of the nodal displacements $u'^{p(q)}_i$, $p = 1, \dots, 4$, yields

$$\begin{aligned} W_{i(10)}^{(q)} &= \frac{1}{2}\left(u'^{1(q)}_i + u'^{2(q)}_i\right) \\ W_{i(01)}^{(q)} &= \frac{1}{2}\left(u'^{4(q)}_i - u'^{1(q)}_i\right) \\ W_{i(00)}^{(q)} + W_{i(20)}^{(q)} + W_{i(02)}^{(q)} &= \frac{1}{2}\left(u'^{2(q)}_i + u'^{4(q)}_i\right) \\ 0 &= \frac{1}{2}\left(u'^{1(q)}_i + u'^{3(q)}_i\right) - \frac{1}{2}\left(u'^{2(q)}_i + u'^{4(q)}_i\right) \end{aligned} \tag{2.37}$$

Hence, the existence of multiple solutions requires that

$$\left(u'^{1(q)}_i + u'^{3(q)}_i\right) = \left(u'^{2(q)}_i + u'^{4(q)}_i\right) \tag{2.38}$$

One potential way to mitigate the above problem is to employ a complete 2nd-order displacement field approximation by incorporating cross-product terms in Equation (2.8),

$$\begin{aligned} u'^{(q)}_i = W_{i(00)}^{(q)} + \eta W_{i(10)}^{(q)} + \xi W_{i(01)}^{(q)} + \eta\xi W_{i(11)}^{(q)} \\ + \frac{1}{2}(3\eta^2 - 1)W_{i(20)}^{(q)} + \frac{1}{2}(3\xi^2 - 1)W_{i(02)}^{(q)} \end{aligned} \tag{2.39}$$

In order to improve the non-traction stress component continuity, Cavalcante et al. (2008) suggested inclusion of cross-product terms in the incomplete second-order displacement

representation. Discontinuities in the non-traction stress component $\sigma_{22}(y_2, y_3)$ can be seen in Figure 2.19 on the horizontal interfaces of the subvolumes immediately above and below the circular porosity. However, introduction of such terms requires care, and may potentially lead to problems if done in an ad-hoc manner. In particular, complete 2nd-order displacement field representation does not ensure elimination of interfacial interpenetration and continuity of the non-traction stress components. In fact, an attempt to express the unknown coefficients $W_{i(mn)}^{(q)}$ in terms of nodal displacements also leads to multiple solutions as shown below

$$\begin{aligned} W_{i(10)}^{(q)} &= -\frac{1}{4}\left(u'^{1(q)}_i - u'^{2(q)}_i\right) + \frac{1}{4}\left(u'^{3(q)}_i - u'^{4(q)}_i\right) \\ W_{i(01)}^{(q)} &= -\frac{1}{4}\left(u'^{1(q)}_i + u'^{2(q)}_i\right) + \frac{1}{4}\left(u'^{3(q)}_i + u'^{4(q)}_i\right) \\ W_{i(00)}^{(q)} + W_{i(20)}^{(q)} + W_{i(02)}^{(q)} &= \frac{1}{4}\left(u'^{1(q)}_i + u'^{3(q)}_i\right) + \frac{1}{4}\left(u'^{2(q)}_i + u'^{4(q)}_i\right) \\ W_{i(11)}^{(q)} &= \frac{1}{4}\left(u'^{1(q)}_i + u'^{3(q)}_i\right) - \frac{1}{4}\left(u'^{2(q)}_i + u'^{4(q)}_i\right) \end{aligned} \tag{2.40}$$

Moreover, two additional equations besides the equilibrium equations are required to express the unknown coefficients in terms of the surface-averaged displacements.

Nonetheless, the above approach was recently proposed by Haj-Ali and Aboudi (2010) who followed the surface-averaging and parametric mapping framework of the FVDAM theory based on Equation (2.39) and the point-wise Jacobian of the parametric mapping transformation instead of the volume-averaged approximation in Equation (2.13). The two additional equations that these authors proposed to employ were so-called higher-order moments of the equilibrium equations chosen as follows,

$$\int_{V_{(q)}} y_2 y_3 \frac{\partial \sigma_{ji}^{(q)}}{\partial y_j} dV_{(q)} = \int_{S_{(q)}} y_2 y_3 t_i dS_{(q)} - \int_{V_{(q)}} (y_3 \sigma_{2i} + y_2 \sigma_{3i}) dV_{(q)} = 0 \tag{2.41}$$

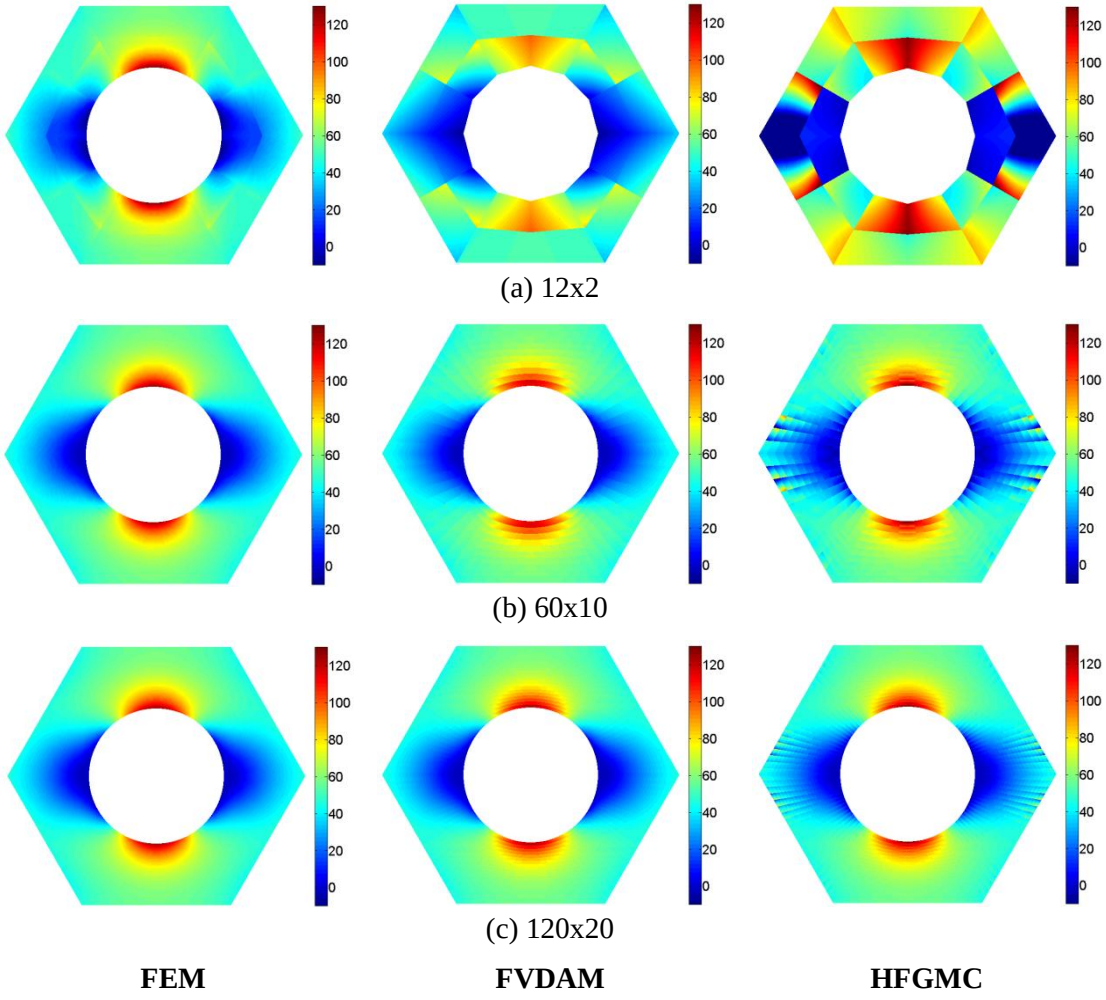

Figure 2.19. Comparison of σ_{22} stress fields in unidirectionally loaded hexagonal array with 25% porosity by $\bar{\sigma}_{22} \neq 0$ at $\bar{\varepsilon}_{22} = 0.1\%$ for increasingly greater unit cell discretizations.

The results of these modifications of the parametric FVDAM theory, which Haj-Ali and Aboudi (2010) renamed HFGMC without rational justification, are included in Figures 2.18 and 2.19. As observed in Figure 2.18, the interfacial interpenetrations predicted by the so-called HFGMC model are in fact amplified in the presence of cross-product terms at low unit cell discretizations. As in the case of the parametric FVDAM theory, these interpenetrations become negligibly small with increasing mesh refinement. However, substantially greater mesh discretizations are required relative to the parametric

FVDAM theory to achieve the same interfacial conformability. Similarly, the stress fields shown in Figure 2.19 are also degraded by the inclusion of cross-product terms and the use of additional higher-order moments of the equilibrium equations proposed by Haj-Ali and Aboudi (2010), where discontinuities of the non-traction stress component $\sigma_{22}(y_2, y_3)$ on the horizontal interfaces of the subvolumes are more noticeable, particularly for those subvolumes localized on the sides of the circular porosity. Even for highly discretized unit cells into 120x20 subvolumes, the HFGMC stress distributions are inferior to those predicted by the FVDAM and FEM methods.

The attempt by Haj-Ali and Aboudi (2010) to generalize the parametric FVDAM theory illustrates the potential pitfalls that may be encountered through an ad-hoc choice of additional equations for the determination of the unknown coefficients in the displacement field representation. This particular choice may also lead to violation of mechanics principles such as frame indifference (Cavalcante et al., 2012a).

One approach to mitigate these shortcomings, using a displacement representation of order higher than two, is proposed in our recently completed generalization of the original finite-volume theory, Cavalcante and Pindera (2012a,b). In order to preserve the finite-volume framework of the theory and its surface-averaging approach in satisfying equilibrium equations and continuity conditions between adjacent subvolumes, new surface-averaged kinematic and static variables are introduced based on elasticity considerations. The additional coefficients associated with higher-order terms in the displacement field representation are then expressed in terms of these kinematic variables which are required to be continuous across the adjacent subvolume faces together with

the concomitant static variables. This is the approach shown in the next chapter in the context of elastic stress analysis in solid mechanics.

2.9. Summary and Discussion

The predictive capabilities of the FVDAM and finite element approaches in the homogenization of elastic-plastic response of heterogeneous materials with periodic microstructures have been compared using the same theoretical framework, including displacement field decomposition, secant formulation of the elastic-plastic unit cell boundary-value problem, and iterative solution of the resulting nonlinear systems of equations. The unit cell discretizations were also virtually the same within the constraints of the employed Q8 elements used for comparison with the quadrilateral subvolumes. Two different classes of problems were investigated, characterized by large stress gradients and localized plastic strain fields, which provide a rigorous test bed for comparing the predictive capability of both approaches.

Detailed comparison of both the homogenized responses under radial stress ratios involving combinations of macroscopic normal and shear stresses in the perforated metallic sheets, and local stress and plastic strain fields, revealed no differences between the results obtained by the FVDAM and finite element approaches. These methods also produced virtually identical homogenized responses in the analyses of wavy multilayers, exhibiting the same microstructural effect recently reported by Khatam and Pindera (2010). The results for these two problems indicate that both the homogenized response and local stress and plastic strain fields can be predicted with comparable accuracy using FVDAM and finite element based unit cell homogenization with sufficient mesh

refinement, despite some fundamental differences in the two approaches' framework. While the FVDAM theory ensures local equilibrium satisfaction at any level of domain discretization, this only occurs with sufficient mesh refinement for the finite element approach based on the total potential energy minimization. On the other hand, the displacement field representation and the concomitant surface-averaging approach employed within the FVDAM framework does not ensure point-wise displacement continuity between adjacent subvolumes, in contrast with the Q8 elements employed herein. However, this is offset by the explicit satisfaction of interfacial traction continuity in a surface-average sense. Further, the FVDAM framework facilitates explicit derivation of the subvolume stiffness matrix elements, in contrast with the finite element framework wherein these elements are evaluated numerically, considerably slowing down the global stiffness matrix assembly, Cavalcante et al. (2008).

An improved displacement field representation through the inclusion of cross-product terms presents one approach in the continuing evolution and predictive capability improvement of the FVDAM theory, as suggested by Cavalcante et al. (2008). We note, however, that inclusion of cross-product terms requires the introduction of additional relations in light of the additional unknown coefficients associated with these terms. The additional relations should be introduced in a manner that is consistent with the fundamental principles of mechanics, including proper reduction and coordinate frame indifference, in order to ensure a consistent mechanics-based framework free of potential singularity problems (Cavalcante et al., 2012a). One way is to employ relations and quantities that have clearly defined physical meaning. This is the next step in the evolution of the FVDAM theory. Nonetheless, the evidence of the parametric FVDAM

theory's accuracy relative to the finite element method presented herein on the same footing firmly establishes our method in its current state as an attractive and efficient alternative for the analysis of heterogeneous materials with complex microstructures.

Chapter 3

Generalized Finite-Volume Theory for Elastic Stress Analysis in Solid Mechanics

3.1. Introduction

As the first step towards mitigating the limitations of the 0th order or parametric FVDAM theory, we generalize the original finite-volume theory for functionally graded materials based on rectangular subvolume discretization, Figure 3.1, and incomplete quadratic displacement field representation in the (β,γ) subvolume,

$$
\begin{aligned}
u_1'^{(\beta,\gamma)} &= x_1\bar{\varepsilon}_{11} \\
u_i'^{(\beta,\gamma)} &= W_{i(00)}^{(\beta,\gamma)} + \bar{x}_2^{(\beta)}W_{i(10)}^{(\beta,\gamma)} + \bar{x}_3^{(\gamma)}W_{i(01)}^{(\beta,\gamma)} + \frac{1}{2}\left(3\bar{x}_2^{(\beta)2} - \frac{h_\beta^2}{4}\right)W_{i(20)}^{(\beta,\gamma)} \\
&\quad + \frac{1}{2}\left(3\bar{x}_3^{(\gamma)2} - \frac{l_\gamma^2}{4}\right)W_{i(02)}^{(\beta,\gamma)}
\end{aligned}
\tag{3.1}
$$

$(i = 2,3)$ developed by Bansal and Pindera (2003) and Zhong et al. (2004), through the addition of higher-order terms. The higher-order terms require additional conditions which we choose on physical grounds motivated by elasticity considerations. This is the first step in generalizing our finite-volume approach without introducing the complication of parametric mapping which will be completed subsequently. The generalization is

accomplished in a systematic manner which, in fact, produces different orders of the finite-volume theory, with the 0th order corresponding to the original version. Each order corresponds to increasing complexity of the displacement field characterized by kinematic surface-averaged quantities motivated by elasticity considerations which possess mechanics significance. Comparison with the original finite-volume construction based on the displacement field representation given in Equation (3.1) is employed to gauge the advantages of the generalized approach.

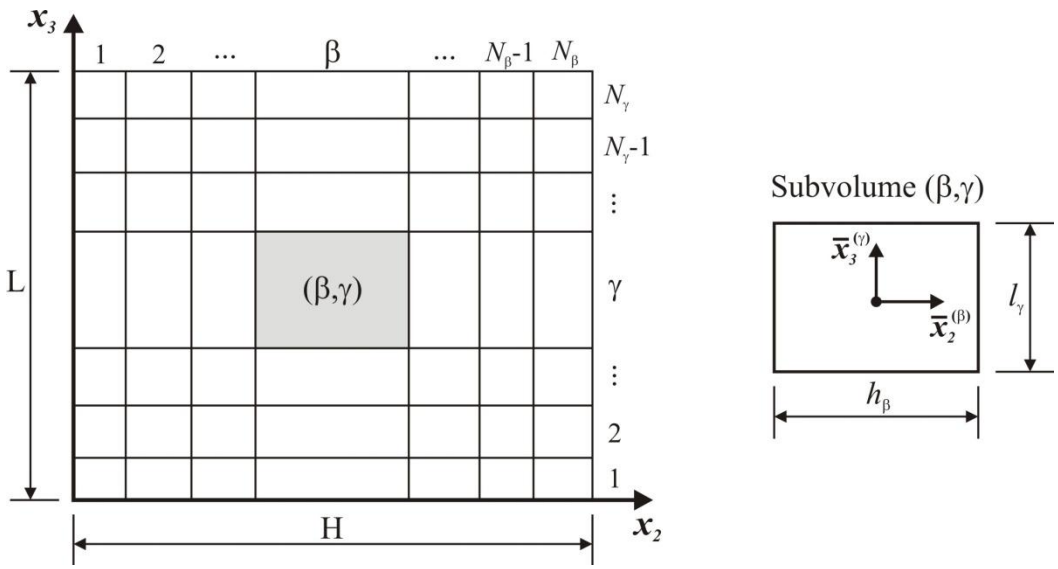

Figure 3.1. Discretization of the analysis domain into rectangular (β,γ) subvolumes (left), after Bansal and Pindera (2003). Note the local coordinate system $\bar{x}_2^{(\beta)} - \bar{x}_3^{(\gamma)}$ attached at the center of the (β,γ) subvolume (right).

In order to preserve the finite-volume framework of the theory and its surface-averaging approach in satisfying equilibrium equations and continuity conditions between adjacent subvolumes, we introduce new surface-averaged kinematic and static variables based on elasticity considerations. The additional coefficients associated with higher-order terms in the displacement field representation are then expressed in terms of these kinematic

variables which are required to be continuous across the adjacent subvolume faces together with the concomitant static variables.

3.2. Theoretical Framework

We consider a rectangular domain in the $x_2 - x_3$ plane occupying the region $0 \le x_2 \le H$ and $0 \le x_3 \le L$, and discretized into N_β and N_γ subvolumes denoted by pairs (β, γ), Figure 3.1. The inplane subvolume dimensions are h_β and l_γ (for $\beta = 1, \dots, N_\beta$ and $\gamma = 1, \dots, N_\gamma$) along the x_2 and x_3 axes, respectively. Each subvolume may contain different elastic material characterized by constant moduli. Hence the problem is solved under the generalized plane strain constraint such that $\bar{\varepsilon}_{11} = \varepsilon_{11}^{(\beta,\gamma)}$. The heterogeneous material microstructure in the $x_2 - x_3$ plane may be arbitrarily distributed, including statistically homogeneous, graded or ordered distributions. The loading applied in the $x_2 - x_3$ plane involves a combination of surface-averaged kinematic and/or static variables defined in the sequel along with uniform strain $\bar{\varepsilon}_{11}$.

The displacement field in the (β, γ) subvolume in the $x_2 - x_3$ plane is approximated by the incomplete fourth-order polynomial, subject to the constraint $u_1^{(\beta,\gamma)} = x_1 \bar{\varepsilon}_{11}$,

$$
\begin{aligned}
u'^{(\beta,\gamma)}_i = {} & W^{(\beta,\gamma)}_{i(00)} + \bar{x}_2^{(\beta)} W^{(\beta,\gamma)}_{i(10)} + \bar{x}_3^{(\gamma)} W^{(\beta,\gamma)}_{i(01)} + \bar{x}_2^{(\beta)} \bar{x}_3^{(\gamma)} W^{(\beta,\gamma)}_{i(11)} \\
& + \frac{1}{2}\left(3\bar{x}_2^{(\beta)2} - \frac{h_\beta^2}{4}\right) W^{(\beta,\gamma)}_{i(20)} + \frac{1}{2}\left(3\bar{x}_3^{(\gamma)2} - \frac{l_\gamma^2}{4}\right) W^{(\beta,\gamma)}_{i(02)} \\
& + \frac{1}{2}\left(3\bar{x}_2^{(\beta)2} - \frac{h_\beta^2}{4}\right) \bar{x}_3^{(\gamma)} W^{(\beta,\gamma)}_{i(21)} + \frac{1}{2}\left(3\bar{x}_3^{(\gamma)2} - \frac{l_\gamma^2}{4}\right) \bar{x}_2^{(\beta)} W^{(\beta,\gamma)}_{i(12)} \\
& + \frac{1}{4}\left(3\bar{x}_2^{(\beta)2} - \frac{h_\beta^2}{4}\right)\left(3\bar{x}_3^{(\gamma)2} - \frac{l_\gamma^2}{4}\right) W^{(\beta,\gamma)}_{i(22)}
\end{aligned}
\tag{3.2}
$$

where $i = 2, 3$ above and henceforth, and $W_{i(mn)}^{(\beta,\gamma)}$ are unknown coefficients. For plane strain $\bar{\varepsilon}_{11} = 0$ and for generalized plane strain, $\bar{\varepsilon}_{11}$ is either specified or determined from the condition

$$\sum_{\gamma=1}^{N_\gamma} \sum_{\beta=1}^{N_\beta} \int_{-l_\gamma/2}^{l_\gamma/2} \int_{-h_\beta/2}^{h_\beta/2} \sigma_{11}^{(\beta,\gamma)} \, d\bar{x}_2^{(\beta)} d\bar{x}_3^{(\gamma)} = 0 \tag{3.3}$$

Plane stress is obtained by leaving $u_1^{(\beta,\gamma)}$ unspecified with $\sigma_{11}^{(\beta,\gamma)} = 0$.

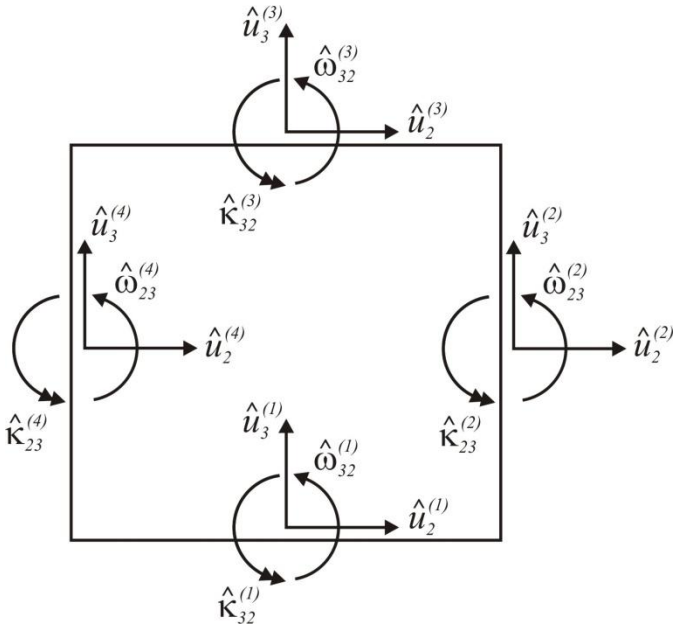

Figure 3.2. Surface-averaged kinematic variables on the four faces of (β, γ) subvolume.

The chosen displacement field is characterized by the total of 18 unknown coefficients in contrast with 10 employed in the original finite-volume theory based on the incomplete second-order polynomial given in Equation (3.1). The approach employed in the construction of the higher-order finite-volume theory is to define additional quantities with physical meaning which should be continuous across common subvolume faces in a surface-average sense, in addition to the surface-average displacements used in the 0th order theory. The 18 unknown coefficients $W_{i(mn)}^{(\beta,\gamma)}$ are then expressed in terms of these

physical quantities, facilitating construction of generalized stiffness matrix relations. The physical quantities are surface-averaged displacements, surface-averaged rotations and surface-averaged curvatures. Figure 3.2 illustrates these quantities associated with each face of the (β, γ) subvolume, with the face numbering convention starting at the bottom face and progressing counterclockwise. Hence the imposition of interfacial continuity requirement for these three sets of quantities will mitigate the interfacial interpenetration issue intrinsic to incomplete or complete second-order displacement field representation.

The surface-averaged interfacial displacements, rotations and curvatures are the major kinematic parameters that describe the deformation of a subvolume relative to its neighbors. This is one of the motivations for the choice of the displacement field in Equation (3.2). The introduction of related surface-averaged static variables derived from the displacement field, which are also required to satisfy interfacial continuity conditions, allows hierarchical construction of the local stiffness matrix in closed form for each subvolume which clearly delineates the contribution of each set of kinematic variables. This provides another motivation for the chosen displacement field representation. We note, however, that the continuity of interfacial tangential displacement gradients is not accommodated by the present construction as it appears to play a secondary role in the analyzed domain's interior. This limitation may become important on the boundaries of an analyzed domain subjected to concentrated normal loading and will be examined in an example given in the sequel. Nonetheless, such effects can be included in further development albeit at the expense of additional complexity.

We note that the chosen displacement field has the same functional form as that used in Q9 finite elements. No additional observations are readily apparent, however, given that

the solution approach employed in the finite element method based on the continuity of nodal displacements and force equilibrium within the energy minimization framework differs fundamentally from our surface-averaging based finite-volume method.

3.2.1. Kinematic Variables

Following the standard finite-volume theory developed by Bansal and Pindera (2003), we first define surface-averaged displacement components,

$$\begin{aligned}\hat{u}_i^{(1,3)} &= \frac{1}{h_\beta}\int_{-h_\beta/2}^{h_\beta/2} u_i\left(\bar{x}_2^{(\beta)}, \mp l_\gamma/2\right) d\bar{x}_2^{(\beta)},\\ \hat{u}_i^{(2,4)} &= \frac{1}{l_\gamma}\int_{-l_\gamma/2}^{l_\gamma/2} u_i\left(\pm h_\beta/2\,, \bar{x}_3^{(\gamma)}\right) d\bar{x}_3^{(\gamma)}\end{aligned} \tag{3.4}$$

where the superscripts indicate subvolume face number, noting that the superscripts (β,γ) which identify a given subvolume have been omitted for clarity. The next set of surface-averaged kinematic variables is motivated by point-wise continuity conditions on interfacial displacements between adjacent subvolumes. For the $u_3\left(\bar{x}_2^{(\beta)}, \bar{x}_3^{(\gamma)}\right)$ displacements on the 3rd face of (β,γ) subvolume and 1st face of $(\beta,\gamma+1)$ subvolume, we must have

$$u_3^{(3)}\left(\bar{x}_2^{(\beta)}, +l_\gamma/2\right) = u_3^{(1)}\left(\bar{x}_2^{(\beta)}, -l_{\gamma+1}/2\right) \tag{3.5}$$

for point-wise continuity. Hence, the following conditions must also apply for point-wise continuity

$$\begin{aligned}\frac{\partial u_3^{(3)}\left(\bar{x}_2^{(\beta)}, +l_\gamma/2\right)}{\partial \bar{x}_2^{(\beta)}} &= \frac{\partial u_3^{(1)}\left(\bar{x}_2^{(\beta)}, -l_{\gamma+1}/2\right)}{\partial \bar{x}_2^{(\beta)}}\\ \frac{\partial^2 u_3^{(3)}\left(\bar{x}_2^{(\beta)}, +l_\gamma/2\right)}{\partial \bar{x}_2^{2(\beta)}} &= \frac{\partial^2 u_3^{(1)}\left(\bar{x}_2^{(\beta)}, -l_{\gamma+1}/2\right)}{\partial \bar{x}_2^{2(\beta)}}\end{aligned} \tag{3.6}$$

with similar constraints on the $u_2\left(\bar{x}_2^{(\beta)}, \bar{x}_3^{(\gamma)}\right)$ displacements on the 2nd and 4th faces. Given the surface-averaging framework of our finite-volume theory, the above continuity conditions also must apply in a surface-averaged sense. Therefore, we next define surface-average rotation components,

$$\begin{aligned}\widehat{\omega}_{32}^{(1,3)} &= \frac{1}{h_\beta}\int_{-h_\beta/2}^{h_\beta/2}\frac{\partial u_3\left(\bar{x}_2^{(\beta)}, \mp l_\gamma/2\right)}{\partial \bar{x}_2^{(\beta)}}d\bar{x}_2^{(\beta)},\\ \widehat{\omega}_{23}^{(2,4)} &= -\frac{1}{l_\gamma}\int_{-l_\gamma/2}^{l_\gamma/2}\frac{\partial u_2\left(\pm h_\beta/2\,, \bar{x}_3^{(\gamma)}\right)}{\partial \bar{x}_3^{(\gamma)}}d\bar{x}_3^{(\gamma)}\end{aligned} \tag{3.7}$$

and finally surface-averaged curvature components,

$$\begin{aligned}\hat{\kappa}_{32}^{(1,3)} &= \frac{1}{h_\beta}\int_{-h_\beta/2}^{h_\beta/2}\frac{\partial^2 u_3\left(\bar{x}_2^{(\beta)}, \mp l_\gamma/2\right)}{\partial \bar{x}_2^{2(\beta)}}d\bar{x}_2^{(\beta)},\\ \hat{\kappa}_{23}^{(2,4)} &= -\frac{1}{l_\gamma}\int_{-l_\gamma/2}^{l_\gamma/2}\frac{\partial^2 u_2\left(\pm h_\beta/2\,, \bar{x}_3^{(\gamma)}\right)}{\partial \bar{x}_3^{2(\gamma)}}d\bar{x}_3^{(\gamma)}\end{aligned} \tag{3.8}$$

Substituting the expressions for the displacement field in the above definitions, the surface-averaged displacements are obtained in terms of the 0th, 1st and 2nd order coefficients,

$$\begin{aligned}\hat{u}_i^{(1,3)} &= W_{i(00)} \mp \frac{l_\gamma}{2}W_{i(01)} + \frac{l_\gamma^2}{4}W_{i(02)}\\ \hat{u}_i^{(2,4)} &= W_{i(00)} \pm \frac{h_\beta}{2}W_{i(10)} + \frac{h_\beta^2}{4}W_{i(20)}\end{aligned} \tag{3.9}$$

Similarly, the surface-averaged rotations are obtained in terms of the 1st, 2nd and 3rd order coefficients,

$$\begin{aligned}\widehat{\omega}_{32}^{(1,3)} &= W_{3(10)} \mp \frac{l_\gamma}{2}W_{3(11)} + \frac{l_\gamma^2}{4}W_{3(12)}\\ \widehat{\omega}_{23}^{(2,4)} &= -W_{2(01)} \mp \frac{h_\beta}{2}W_{2(11)} - \frac{h_\beta^2}{4}W_{2(21)}\end{aligned} \tag{3.10}$$

while the curvatures are obtained in terms of the 2nd, 3rd and 4th order coefficients,

$$\begin{aligned}\hat{\kappa}_{32}^{(1,3)} &= 3W_{3(20)} \mp \frac{3l_\gamma}{2} W_{3(21)} + \frac{3l_\gamma^2}{4} W_{3(22)} \\ \hat{\kappa}_{23}^{(2,4)} &= -3W_{2(02)} \mp \frac{3h_\beta}{2} W_{2(12)} - \frac{3h_\beta^2}{4} W_{2(22)}\end{aligned} \tag{3.11}$$

We note that the expressions for surface-averaged displacements are the same as those based on the incomplete second-order displacement representation (Equation 3.1), leading to the following relations between the unknown 1st and 2nd order coefficients and surface-averaged displacements and 0th order coefficients,

$$\begin{aligned}W_{i(10)} &= \frac{1}{h_\beta}\left(\hat{u}_i^{(2)} - \hat{u}_i^{(4)}\right) \\ W_{i(01)} &= \frac{1}{l_\gamma}\left(\hat{u}_i^{(3)} - \hat{u}_i^{(1)}\right) \\ W_{i(20)} &= \frac{2}{h_\beta^2}\left(\hat{u}_i^{(2)} + \hat{u}_i^{(4)}\right) - \frac{4}{h_\beta^2} W_{i(00)} \\ W_{i(02)} &= \frac{2}{l_\gamma^2}\left(\hat{u}_i^{(1)} + \hat{u}_i^{(3)}\right) - \frac{4}{l_\gamma^2} W_{i(00)}\end{aligned} \tag{3.12}$$

Similarly, the expressions for surface-averaged rotations lead to the following relations between the unknown 2nd and 3rd order coefficients and surface-averaged rotations and 1st order coefficients,

$$\begin{aligned}W_{2(11)} &= \frac{1}{h_\beta}\left(\hat{\omega}_{23}^{(4)} - \hat{\omega}_{23}^{(2)}\right) \\ W_{3(11)} &= \frac{1}{l_\gamma}\left(\hat{\omega}_{32}^{(3)} - \hat{\omega}_{32}^{(1)}\right) \\ W_{2(21)} &= -\frac{2}{h_\beta^2}\left(\hat{\omega}_{23}^{(2)} + \hat{\omega}_{23}^{(4)}\right) - \frac{4}{h_\beta^2} W_{2(01)} \\ W_{3(12)} &= \frac{2}{l_\gamma^2}\left(\hat{\omega}_{32}^{(1)} + \hat{\omega}_{32}^{(3)}\right) - \frac{4}{l_\gamma^2} W_{3(10)}\end{aligned} \tag{3.13}$$

Finally, the expressions for surface-averaged curvatures lead to the following relations between the unknown 3rd and 4th order coefficients and surface-averaged curvatures and 2nd order coefficients,

$$
\begin{aligned}
W_{2(12)} &= \frac{1}{3h_\beta}\left(\hat{\kappa}_{23}^{(4)} - \hat{\kappa}_{23}^{(2)}\right) \\
W_{3(21)} &= \frac{1}{3l_\gamma}\left(\hat{\kappa}_{32}^{(3)} - \hat{\kappa}_{32}^{(1)}\right) \\
W_{2(22)} &= -\frac{2}{3h_\beta^2}\left(\hat{\kappa}_{23}^{(2)} + \hat{\kappa}_{23}^{(4)}\right) - \frac{4}{h_\beta^2}W_{2(02)} \\
W_{3(22)} &= \frac{2}{3l_\gamma^2}\left(\hat{\kappa}_{32}^{(1)} + \hat{\kappa}_{32}^{(3)}\right) - \frac{4}{l_\gamma^2}W_{3(20)}
\end{aligned}
\tag{3.14}
$$

Examination of the above equations reveals that the sixteen 1st, 2nd, 3rd and 4th order coefficients $W_{i(mn)}^{(\beta,\gamma)}$ may be expressed in terms of the sixteen surface-averaged kinematic variables $\hat{u}_i^{(1,2,3,4)}$, $\hat{\omega}_{32}^{(1,3)}$, $\hat{\omega}_{23}^{(2,4)}$, $\hat{\kappa}_{32}^{(1,3)}$, $\hat{\kappa}_{23}^{(2,4)}$ and two 0th order coefficients $W_{i(00)}$. These remaining coefficients are obtained in terms of surface-averaged kinematic variables upon satisfaction of equilibrium equations in a surface-average sense. Relating these surface-averaged kinematic variables to appropriately defined static variables enables construction of the generalized local stiffness matrix based on the higher-order displacement field employed herein.

3.2.2. Static Variables

Following the standard finite-volume theory based on rectangular domain discretization, we first define surface-averaged traction components on each of the four subvolume faces, which are related to stresses through the Cauchy's relations $t_i^{(\beta,\gamma)} = \sigma_{ji}^{(\beta,\gamma)} n_j^{(\beta,\gamma)}$,

$$\hat{t}_i^{(1,3)} = \frac{1}{h_\beta}\int_{-h_\beta/2}^{h_\beta/2} t_i\left(\bar{x}_2^{(\beta)}, \mp l_\gamma/2\right) d\bar{x}_2^{(\beta)},$$
$$\hat{t}_i^{(2,4)} = \frac{1}{l_\gamma}\int_{-l_\gamma/2}^{l_\gamma/2} t_i\left(\pm h_\beta/2\,, \bar{x}_3^{(\gamma)}\right) d\bar{x}_3^{(\gamma)} \tag{3.15}$$

The surface-averaged tractions will be employed in the following section to ensure subvolume equilibrium in the integral sense. Since we are dealing with rectangular discretization of the analysis domain, the unit normal vectors to each face of a subvolume are either $\boldsymbol{n} = (\pm 1,0)$ or $\boldsymbol{n} = (0,\pm 1)$. Hence each local traction component is directly related to a single stress component as follows,

$$\begin{aligned} t_2^{(1,3)}\left(\bar{x}_2^{(\beta)}\right) &= \mp\sigma_{23}\left(\bar{x}_2^{(\beta)}, \mp l_\gamma/2\right) \\ t_3^{(1,3)}\left(\bar{x}_2^{(\beta)}\right) &= \mp\sigma_{33}\left(\bar{x}_2^{(\beta)}, \mp l_\gamma/2\right) \\ t_2^{(2,4)}\left(\bar{x}_3^{(\gamma)}\right) &= \pm\sigma_{22}\left(\pm h_\beta/2\,, \bar{x}_3^{(\gamma)}\right) \\ t_3^{(2,4)}\left(\bar{x}_3^{(\gamma)}\right) &= \pm\sigma_{23}\left(\pm h_\beta/2\,, \bar{x}_3^{(\gamma)}\right) \end{aligned} \tag{3.16}$$

The definition of the next set of static variables is motivated by the requirement that traction components must be continuous across common interfaces. For normal tractions acting on the 3rd face of (β,γ) subvolume and 1st face of $(\beta,\gamma+1)$ subvolume, we must have $t_3^{(3)}\left(\bar{x}_2^{(\beta)}\right)\Big|^{(\beta,\gamma)} + t_3^{(1)}\left(\bar{x}_2^{(\beta)}\right)\Big|^{(\beta,\gamma+1)} = 0$, or

$$\sigma_{33}\left(\bar{x}_2^{(\beta)}, +l_\gamma/2\right) = \sigma_{33}\left(\bar{x}_2^{(\beta)}, -l_{\gamma+1}/2\right) \tag{3.17}$$

for point-wise continuity. Hence, the following conditions must also apply for point-wise continuity

$$\frac{\partial\sigma_{33}\left(\bar{x}_2^{(\beta)}, +l_\gamma/2\right)}{\partial\bar{x}_2^{(\beta)}} = \frac{\partial\sigma_{33}\left(\bar{x}_2^{(\beta)}, -l_{\gamma+1}/2\right)}{\partial\bar{x}_2^{(\beta)}} \tag{3.18}$$

$$\frac{\partial^2 \sigma_{33}\left(\bar{x}_2^{(\beta)}, +l_\gamma/2\right)}{\partial \bar{x}_2^{2(\beta)}} = \frac{\partial^2 \sigma_{33}\left(\bar{x}_2^{(\beta)}, -l_{\gamma+1}/2\right)}{\partial \bar{x}_2^{2(\beta)}}$$

with similar requirements for shear traction components on the above faces, and normal and shear traction components on the 2nd and 4th faces.

Within the current theoretical framework, we satisfy interfacial traction continuity in a surface-average sense. Hence, given the higher-order displacement representation, we also require interfacial continuity of the appropriate 1st and 2nd derivatives of traction components to be satisfied in a surface-average sense. Because of the chosen displacement field representation, only the continuity of surface-averaged derivatives of normal traction components is enforced. Hence, the following corresponding surface-averaged normal traction derivatives are defined, Figure 3.3,

$$\begin{aligned}
\hat{t}_{3/2}^{(1,3)} &= \frac{1}{h_\beta}\int_{-h_\beta/2}^{h_\beta/2} \frac{\partial t_3\left(\bar{x}_2^{(\beta)}, \mp l_\gamma/2\right)}{\partial \bar{x}_2^{(\beta)}} d\bar{x}_2^{(\beta)} \\
\hat{t}_{2/3}^{(2,4)} &= -\frac{1}{l_\gamma}\int_{-l_\gamma/2}^{l_\gamma/2} \frac{\partial t_2\left(\pm h_\beta/2\,, \bar{x}_3^{(\gamma)}\right)}{\partial \bar{x}_3^{(\gamma)}} d\bar{x}_3^{(\gamma)} \\
\hat{t}_{3/22}^{(1,3)} &= \frac{1}{h_\beta}\int_{-h_\beta/2}^{h_\beta/2} \frac{\partial^2 t_3\left(\bar{x}_2^{(\beta)}, \mp l_\gamma/2\right)}{\partial \bar{x}_2^{2(\beta)}} d\bar{x}_2^{(\beta)} \\
\hat{t}_{2/33}^{(2,4)} &= -\frac{1}{l_\gamma}\int_{-l_\gamma/2}^{l_\gamma/2} \frac{\partial^2 t_2\left(\pm h_\beta/2\,, \bar{x}_3^{(\gamma)}\right)}{\partial \bar{x}_3^{2(\gamma)}} d\bar{x}_3^{(\gamma)}
\end{aligned} \tag{3.19}$$

For an orthotropic elastic material occupying (β, γ) subvolume, stress components are related to strain components through the familiar Hooke's law

$$\sigma_{ij}^{(\beta,\gamma)} = C_{ijkl}^{(\beta,\gamma)} \varepsilon_{kl}^{(\beta,\gamma)} \tag{3.20}$$

where $C_{ijkl}^{(\beta,\gamma)}$ are stiffness tensor elements of the material occupying the subvolume, and $\varepsilon_{ij}^{(\beta,\gamma)}$ are elastic strain components obtained from the strain-displacement relations,

$$\varepsilon_{ij}^{(\beta,\gamma)} = \frac{1}{2}\left(\frac{\partial u_j^{(\beta,\gamma)}}{\partial \bar{x}_i^{(\cdot)}} + \frac{\partial u_i^{(\beta,\gamma)}}{\partial \bar{x}_j^{(\cdot)}}\right) \tag{3.21}$$

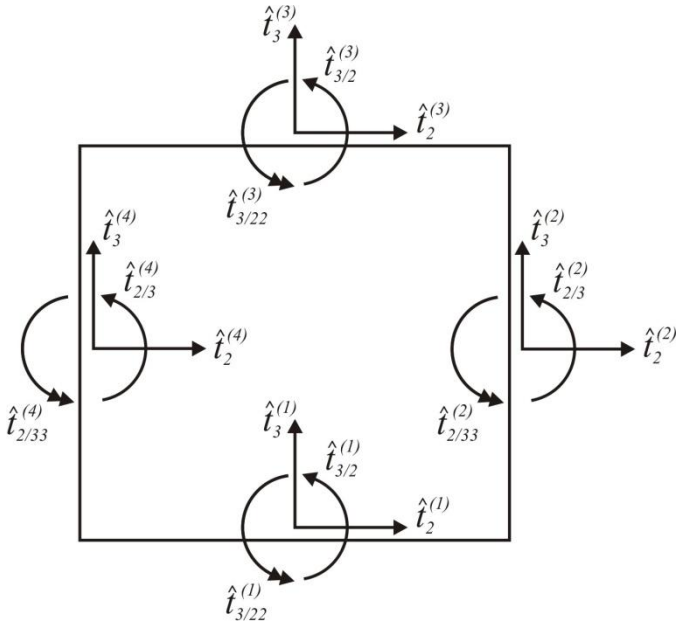

Figure 3.3. Surface-averaged static variables on the four faces of (β,γ) subvolume.

Use of the chosen displacement field in the strain-displacement relations, which are then used to express stress components in terms of the unknown coefficients $W_{i(mn)}^{(\beta,\gamma)}$, yields the following expressions for the surface-averaged static variables, starting with surface-averaged tractions,

$$\begin{aligned}
\hat{t}_2^{(1,3)} &= \mp C_{44}\left(W_{2(01)} \mp \frac{3}{2} l_\gamma W_{2(02)} + W_{3(10)} \mp \frac{1}{2} l_\gamma W_{3(11)} + \frac{1}{4} l_\gamma^2 W_{3(12)}\right) \\
\hat{t}_3^{(1,3)} &= \mp C_{23}\left(W_{2(10)} \mp \frac{1}{2} l_\gamma W_{2(11)} + \frac{1}{4} l_\gamma^2 W_{2(12)}\right) \mp C_{33}\left(W_{3(01)} \mp \frac{3}{2} l_\gamma W_{3(02)}\right) \\
\hat{t}_2^{(2,4)} &= \pm C_{22}\left(W_{2(10)} \pm \frac{3}{2} h_\beta W_{2(20)}\right) \pm C_{23}\left(W_{3(01)} \pm \frac{1}{2} h_\beta W_{3(11)} + \frac{1}{4} h_\beta^2 W_{3(21)}\right) \\
\hat{t}_3^{(2,4)} &= \pm C_{44}\left(W_{2(01)} \pm \frac{1}{2} h_\beta W_{2(11)} + \frac{1}{4} h_\beta^2 W_{2(21)} + W_{3(10)} \pm \frac{3}{2} h_\beta W_{3(20)}\right)
\end{aligned} \tag{3.22}$$

where reduced matrix notation is employed for the stiffness tensor elements. Next, we obtain surface-averaged first derivatives of normal traction components

$$\hat{t}_{3/2}^{(1,3)} = \mp C_{23}\left(3W_{2(20)} \mp \frac{3}{2} l_\gamma W_{2(21)} + \frac{3}{4} l_\gamma^2 W_{2(22)}\right) \mp C_{33}\left(W_{3(11)} \mp \frac{3}{2} l_\gamma W_{3(12)}\right)$$
$$\hat{t}_{2/3}^{(2,4)} = \mp C_{22}\left(W_{2(11)} \pm \frac{3}{2} h_\beta W_{2(21)}\right) \mp C_{23}\left(3W_{3(02)} \pm \frac{3}{2} h_\beta W_{3(12)} + \frac{3}{4} h_\beta^2 W_{3(22)}\right) \quad (3.23)$$

and finally the surface-averaged second derivatives of normal traction components

$$\hat{t}_{3/22}^{(1,3)} = \mp C_{33}\left(3W_{3(21)} \mp \frac{9}{2} l_\gamma W_{3(22)}\right)$$
$$\hat{t}_{2/33}^{(2,4)} = \mp C_{22}\left(3W_{2(12)} \pm \frac{9}{2} h_\beta W_{2(22)}\right) \quad (3.24)$$

The surface-averaged static variables are then expressed in terms of the surface-averaged kinematic variables and the remaining two 0th order coefficients $W_{i(00)}$ determined next.

3.2.3. Surface-Averaging of Equilibrium Equations

In the absence of body forces, the equilibrium equations that must be satisfied in the large are,

$$\int_{S_{(q)}} \sigma_{ji} n_j dS = \int_{S_{(q)}} t_i dS = \int_{-h_\beta/2}^{h_\beta/2} t_i^{(1)} d\bar{x}_2^{(\beta)} + \int_{-l_\gamma/2}^{l_\gamma/2} t_i^{(2)} d\bar{x}_3^{(\gamma)} + \int_{-h_\beta/2}^{h_\beta/2} t_i^{(3)} d\bar{x}_2^{(\beta)} + \int_{-l_\gamma/2}^{l_\gamma/2} t_i^{(4)} d\bar{x}_3^{(\gamma)} = 0 \quad (3.25)$$

or, upon use of the definitions for the surface-averaged tractions,

$$h_\beta \hat{t}_i^{(1)} + l_\gamma \hat{t}_i^{(2)} + h_\beta \hat{t}_i^{(3)} + l_\gamma \hat{t}_i^{(4)} = 0 \quad (3.26)$$

Substituting for the surface-averaged tractions given in terms of the coefficients $W_{i(mn)}^{(\beta,\gamma)}$, we obtain

$$3C_{22} W_{2(20)} + 3C_{44} W_{2(02)} + (C_{23} + C_{44}) W_{3(11)} = 0$$
$$3C_{33} W_{3(02)} + 3C_{44} W_{3(20)} + (C_{23} + C_{44}) W_{2(11)} = 0 \quad (3.27)$$

which upon use of Equations (3.12)-(3.13) yield,

$$W_{2(00)} = \frac{1}{2}\left(\hat{u}_2^{(1)} + \hat{u}_2^{(3)}\right)\alpha_2 + \frac{1}{2}\left(\hat{u}_2^{(2)} + \hat{u}_2^{(4)}\right)\beta_2 + \frac{1}{12}\left(\widehat{\omega}_{32}^{(3)} - \widehat{\omega}_{32}^{(1)}\right)l_\gamma\gamma_2$$
$$W_{3(00)} = \frac{1}{2}\left(\hat{u}_3^{(1)} + \hat{u}_3^{(3)}\right)\alpha_3 + \frac{1}{2}\left(\hat{u}_3^{(2)} + \hat{u}_3^{(4)}\right)\beta_3 + \frac{1}{12}\left(\widehat{\omega}_{23}^{(4)} - \widehat{\omega}_{23}^{(2)}\right)h_\beta\gamma_3 \quad (3.28)$$

where the dimensionless parameters α_i, β_i, γ_i are

$$\alpha_2 = \frac{h_\beta^2 C_{44}}{h_\beta^2 C_{44} + l_\gamma^2 C_{22}};\quad \beta_2 = \frac{l_\gamma^2 C_{22}}{h_\beta^2 C_{44} + l_\gamma^2 C_{22}};\quad \gamma_2 = \frac{h_\beta^2 (C_{23} + C_{44})}{h_\beta^2 C_{44} + l_\gamma^2 C_{22}}$$
$$\alpha_3 = \frac{h_\beta^2 C_{33}}{h_\beta^2 C_{33} + l_\gamma^2 C_{44}};\quad \beta_3 = \frac{l_\gamma^2 C_{44}}{h_\beta^2 C_{33} + l_\gamma^2 C_{44}};\quad \gamma_3 = \frac{l_\gamma^2 (C_{23} + C_{44})}{h_\beta^2 C_{33} + l_\gamma^2 C_{44}} \quad (3.29)$$

3.2.4. Local Stiffness Matrices

The developed framework enables systematic construction of local stiffness matrices of increasing order, each of which corresponds to a finite-volume theory of the particular order. The local stiffness matrices relate the surface-averaged static variables to the surface-averaged kinematic ones.

0th Order Finite-Volume Theory We start with the 0th order theory defined by the local stiffness matrix equation that relates surface-averaged tractions to surface-averaged displacements,

$$\hat{\boldsymbol{t}}^{(\beta,\gamma)} = \bar{\boldsymbol{K}}_{(00)}^{(\beta,\gamma)} \hat{\boldsymbol{u}}^{(\beta,\gamma)} \quad (3.30)$$

where the surface-averaged traction and displacement vectors are defined by ordering the respectively components as follows,

$$\hat{\boldsymbol{t}}^{(\beta,\gamma)} = \left[\hat{t}_2^{(1)}, \hat{t}_3^{(1)}, \hat{t}_2^{(2)}, \hat{t}_3^{(2)}, \hat{t}_2^{(3)}, \hat{t}_3^{(3)}, \hat{t}_2^{(4)}, \hat{t}_3^{(4)}\right]^{T(\beta,\gamma)} \quad (3.31)$$

$$\hat{\boldsymbol{u}}^{(\beta,\gamma)} = \left[\hat{u}_2^{(1)}, \hat{u}_3^{(1)}, \hat{u}_2^{(2)}, \hat{u}_3^{(2)}, \hat{u}_2^{(3)}, \hat{u}_3^{(3)}, \hat{u}_2^{(4)}, \hat{u}_3^{(4)}\right]^{T(\beta,\gamma)} \quad (3.32)$$

This is the finite-volume theory originally developed by Bansal and Pindera (2003), with differently arranged traction and displacement components. Hence the local stiffness matrix $\overline{\boldsymbol{K}}_{(00)}^{(\beta,\gamma)}$ is an 8x8 matrix containing 16 zero elements, with the remaining elements given in closed form which accelerates the global stiffness matrix assembly. This matrix may be obtained from the corresponding $\boldsymbol{K}_{(00)}^{(\beta,\gamma)}$ matrix of the second order theory given in the Appendix B by adding the following 8 nonzero elements,

$$\begin{aligned}(k_{14})_{(00)} = -(k_{18})_{(00)} = -(k_{54})_{(00)} = (k_{58})_{(00)} = \frac{-C_{44}}{h_\beta} \\ (k_{41})_{(00)} = -(k_{45})_{(00)} = -(k_{81})_{(00)} = (k_{85})_{(00)} = \frac{-C_{44}}{l_\gamma}\end{aligned} \tag{3.33}$$

with similar simple expressions for the remaining non-zero elements.

1st Order Finite-Volume Theory Inclusion of rotational degrees of freedom and corresponding static variables yields the 1st order finite-volume theory defined by the local stiffness matrix equation of the form

$$\begin{bmatrix}\hat{\boldsymbol{t}} \\ \hat{\boldsymbol{t}}_\nabla\end{bmatrix}^{(\beta,\gamma)} = \begin{bmatrix}\boldsymbol{K}_{(00)} & \boldsymbol{K}_{(01)} \\ \overline{\boldsymbol{K}}_{(10)} & \overline{\boldsymbol{K}}_{(11)}\end{bmatrix}^{(\beta,\gamma)} \begin{bmatrix}\widehat{\boldsymbol{u}} \\ \widehat{\boldsymbol{u}}_\nabla\end{bmatrix}^{(\beta,\gamma)} \tag{3.34}$$

where the additional surface-averaged static and kinematic variables are

$$\hat{\boldsymbol{t}}_\nabla = \left[\hat{t}_{3/2}^{(1)}, \hat{t}_{2/3}^{(2)}, \hat{t}_{3/2}^{(3)}, \hat{t}_{2/3}^{(4)}\right]^{T(\beta,\gamma)} \tag{3.35}$$

$$\widehat{\boldsymbol{u}}_\nabla = \left[\widehat{\omega}_{32}^{(1)}, \widehat{\omega}_{23}^{(2)}, \widehat{\omega}_{32}^{(3)}, \widehat{\omega}_{23}^{(4)}\right]^{T(\beta,\gamma)} \tag{3.36}$$

The additional sub-matrices $\boldsymbol{K}_{(01)}$, $\overline{\boldsymbol{K}}_{(10)}$ and $\overline{\boldsymbol{K}}_{(11)}$ of the local stiffness matrix are 8x4, 4x8 and 4x4, respectively, and they are also derived in closed form for quick global stiffness matrix assembly. The matrix $\boldsymbol{K}_{(01)}$ is the same as the corresponding matrix of the second order theory, while matrices $\overline{\boldsymbol{K}}_{(10)}$ and $\overline{\boldsymbol{K}}_{(11)}$ are obtained from the

corresponding $\boldsymbol{K}_{(10)}$ and $\boldsymbol{K}_{(11)}$ matrices of the second order theory, all three listed in the Appendix B, through additions similar to those for the $\overline{\boldsymbol{K}}_{(00)}^{(\beta,\gamma)}$ matrix.

2nd Order Finite-Volume Theory Finally, inclusion of curvature degrees of freedom completes the generalization of the finite-volume theory. The generalized local stiffness matrix equation takes the form

$$\begin{bmatrix} \hat{\boldsymbol{t}} \\ \hat{\boldsymbol{t}}_{\nabla} \\ \hat{\boldsymbol{t}}_{\nabla^2} \end{bmatrix}^{(\beta,\gamma)} = \begin{bmatrix} \boldsymbol{K}_{(00)} & \boldsymbol{K}_{(01)} & \boldsymbol{K}_{(02)} \\ \boldsymbol{K}_{(10)} & \boldsymbol{K}_{(11)} & \boldsymbol{K}_{(12)} \\ \boldsymbol{K}_{(20)} & \boldsymbol{K}_{(21)} & \boldsymbol{K}_{(22)} \end{bmatrix}^{(\beta,\gamma)} \begin{bmatrix} \hat{\boldsymbol{u}} \\ \hat{\boldsymbol{u}}_{\nabla} \\ \hat{\boldsymbol{u}}_{\nabla^2} \end{bmatrix}^{(\beta,\gamma)} \tag{3.37}$$

where the additional surface-averaged static and kinematic variables are

$$\hat{\boldsymbol{t}}_{\nabla^2} = \left[\hat{t}_{3/22}^{(1)}, \hat{t}_{2/33}^{(2)}, \hat{t}_{3/22}^{(3)}, \hat{t}_{2/33}^{(4)}\right]^{T(\beta,\gamma)} \tag{3.38}$$

$$\hat{\boldsymbol{u}}_{\nabla^2} = \left[\hat{\kappa}_{32}^{(1)}, \hat{\kappa}_{23}^{(2)}, \hat{\kappa}_{32}^{(3)}, \hat{\kappa}_{23}^{(4)}\right]^{T(\beta,\gamma)} \tag{3.39}$$

The additional sub-matrices $\boldsymbol{K}_{(02)}$, $\boldsymbol{K}_{(12)}$, $\boldsymbol{K}_{(20)}$, $\boldsymbol{K}_{(21)}$, $\boldsymbol{K}_{(22)}$ of the local stiffness matrix are 8x4, 4x4, 4x8, 4x4 and 4x4, respectively. They are also derived in closed form for quick global stiffness matrix assembly and listed in the Appendix B.

The structure of the local stiffness matrix of the generalized (2nd order) finite-volume theory reflects its systematic construction. This construction makes it possible to systematically generate lower-order versions without substantial effort at the analytical and code implementation levels. Moreover, each reduction in order relative to the generalized theory precisely indicates which kinematic and static features of the local subvolume response are abandoned, establishing clear connection between mathematics and physics of the subvolume's deformation characteristics relative to its neighbors.

3.2.5. Global Stiffness Matrix

The global stiffness matrix is assembled by applying interfacial continuity conditions on the surface-averaged kinematic and static variables, followed by the surface-averaged boundary conditions.

Continuity Conditions The continuity conditions on surface-averaged kinematic variables comprised of displacements, rotations and curvatures are,

$$\begin{aligned} \hat{u}_i^{(3)}\Big|^{(\beta,\gamma)} &= \hat{u}_i^{(1)}\Big|^{(\beta,\gamma+1)} \quad \text{and} \quad \hat{u}_i^{(2)}\Big|^{(\beta,\gamma)} = \hat{u}_i^{(4)}\Big|^{(\beta+1,\gamma)} \\ \widehat{\omega}_{32}^{(3)}\Big|^{(\beta,\gamma)} &= \widehat{\omega}_{32}^{(1)}\Big|^{(\beta,\gamma+1)} \quad \text{and} \quad \widehat{\omega}_{23}^{(2)}\Big|^{(\beta,\gamma)} = \widehat{\omega}_{23}^{(4)}\Big|^{(\beta+1,\gamma)} \\ \hat{\kappa}_{32}^{(3)}\Big|^{(\beta,\gamma)} &= \hat{\kappa}_{32}^{(1)}\Big|^{(\beta,\gamma+1)} \quad \text{and} \quad \hat{\kappa}_{23}^{(2)}\Big|^{(\beta,\gamma)} = \hat{\kappa}_{23}^{(4)}\Big|^{(\beta+1,\gamma)} \end{aligned} \tag{3.40}$$

Similarly, the continuity conditions on surface-averaged static variables are,

$$\begin{aligned} \hat{t}_i^{(3)}\Big|^{(\beta,\gamma)} + \hat{t}_i^{(1)}\Big|^{(\beta,\gamma+1)} &= 0 \quad \text{and} \quad \hat{t}_i^{(2)}\Big|^{(\beta,\gamma)} + \hat{t}_i^{(4)}\Big|^{(\beta+1,\gamma)} = 0 \\ \hat{t}_{3/2}^{(3)}\Big|^{(\beta,\gamma)} + \hat{t}_{3/2}^{(1)}\Big|^{(\beta,\gamma+1)} &= 0 \quad \text{and} \quad \hat{t}_{2/3}^{(2)}\Big|^{(\beta,\gamma)} + \hat{t}_{2/3}^{(4)}\Big|^{(\beta+1,\gamma)} = 0 \\ \hat{t}_{3/22}^{(3)}\Big|^{(\beta,\gamma)} + \hat{t}_{3/22}^{(1)}\Big|^{(\beta,\gamma+1)} &= 0 \quad \text{and} \quad \hat{t}_{2/33}^{(2)}\Big|^{(\beta,\gamma)} + \hat{t}_{2/33}^{(4)}\Big|^{(\beta+1,\gamma)} = 0 \end{aligned} \tag{3.41}$$

Boundary Conditions Any combination of kinematic or static surface-averaged quantities may be prescribed on the outer faces of the boundary subvolumes. For instance, on the left boundary of the rectangular analysis domain, see Figure 3.1, we may specify either one of the following three sets of quantities on each outer face of the boundary subvolumes,

$$\begin{aligned} \hat{u}_i^{(4)}\Big|^{(1,\gamma)} \quad &\text{or} \quad \hat{t}_i^{(4)}\Big|^{(1,\gamma)} \quad \text{for} \quad \gamma = 1, \dots, N_\gamma \\ \widehat{\omega}_{23}^{(4)}\Big|^{(1,\gamma)} \quad &\text{or} \quad \hat{t}_{2/3}^{(4)}\Big|^{(1,\gamma)} \quad \text{for} \quad \gamma = 1, \dots, N_\gamma \\ \hat{\kappa}_{23}^{(4)}\Big|^{(1,\gamma)} \quad &\text{or} \quad \hat{t}_{2/33}^{(4)}\Big|^{(1,\gamma)} \quad \text{for} \quad \gamma = 1, \dots, N_\gamma \end{aligned} \tag{3.42}$$

Similar boundary conditions are specified on the bottom, right and top boundaries.

Global Stiffness Matrix Assembly Application of the surface-averaged continuity and boundary conditions produces the global system of equations for the unknown surface-averaged kinematic variables.

$$\mathbb{K}\mathbb{U} = \mathbb{F} \tag{3.43}$$

where $\mathbb{K}$ is the global stiffness matrix comprised of the local subvolume stiffness matrices arranged and summed according to the manner of the application of continuity conditions, $\mathbb{U}$ contains all the interior and exterior surface-averaged kinematic variables that are not specified as boundary conditions, and $\mathbb{F}$ contains the specified boundary conditions in terms of kinematic and/or static variables. To eliminate rigid body translation and rotation, the analysis domain must be constrained by setting the appropriate surface-averaged boundary kinematic variables to zero at appropriate locations. The global stiffness matrix assembly may be done row-wise and column-wise as in Bansal and Pindera (2003) due to the employed rectangular discretization. Alternatively, assembly techniques developed by the finite element community may be exploited.

3.3. Testability and Verification

The generalized finite-volume theory was constructed in a manner that enables systematic specialization through reductions to lower-order versions. Hence the effect of including different-order terms, which enable definition of the three types of kinematic variables, on the interfacial displacements and local stress fields can be readily evaluated. The issues that are addressed in this section are the improvements in interfacial

displacement conformability and point-wise satisfaction of traction and non-traction stress component continuity across subvolume interfaces due to inclusion of the higher-order terms in the displacement field representation absent in the original or 0th order finite-volume theory. A related issue is convergence of the global unbalanced average stress as a function of mesh refinement, recently introduced by Cavalcante et al. (2011b) and presented in Chapter 2, which also provides a measure for comparison with finite element results.

The results of predictions of the different-order finite-volume theories are compared and verified with finite element results based on conformable Q9 elements and the same analysis domain discretizations, as well as with available elasticity solutions. The use of Q9 elements is consistent with the displacement field representation of the generalized finite-volume theory. Tendency of the unbalanced average subvolume stress to zero with mesh refinement is also included for comparison given the variational basis of the finite element technique, in contrast with the direct satisfaction of equilibrium equations in a surface-average sense which forms the basis of finite-volume methods.

The above issues are addressed through three illustrations, each chosen to critically test different aspects of the generalized finite-volume theory's predictive capabilities. In the first example, we consider a homogeneous rectangular strip constrained at one end and loaded by a shear resultant at the other. The large rotations of the strip's cross sections in the vicinity of the constrained end critically test the theory's ability to reproduce conformable interfacial displacements in this region. In the second example, we analyze the response of a rectangular strip with square cutouts under the same loading as in the first example. The cutouts produce a heterogeneous material with an infinite modulus

contrast which provides a critical test of the theory's ability to satisfy traction-free conditions at the cutout boundaries. In the third example we simulate the response of a long rectangular strip subjected to opposing uniform normal tractions distributed over a small surface interval, and compare finite-volume predictions with elasticity and finite element solutions. In this example, both large rotations and large stress gradients arise in the applied traction's vicinity, providing a critical test of predictive capabilities of the 0th, 1st and 2nd order theories vis-a-vis baseline elasticity and finite element solutions. Finally, comparison of the convergence characteristics of the finite-volume theories vis-a-vis finite element method based on the global unbalanced stress measure is presented for the second and third problems.

3.3.1. Cantilevered Homogeneous Rectangular Strip

The homogeneous rectangular strip constrained at left end and subjected to uniformly distributed shear tractions on the right end is shown in Figure 3.4(a). The classical solution for such homogeneous cantilevered strip under traction boundary conditions is given in terms of the Airy's stress function in standard elasticity textbooks, cf. Timoshenko and Goodier (1970). The stress field is valid for both plane stress and plane strain cases, while the displacement field depends on the manner of constraint at the left end. Herein, the plane stress case is chosen for comparison and the left end is constrained by pinning it at the center and preventing horizontal motion at the upper and lower corners. This boundary condition best mimics the fully constrained left end in the finite-volume and finite element simulations. The elastic constants used in the analysis were $E = 200GPa$ and $\nu = 0.32$. Both the finite-volume and finite element analyses were

performed using the same subvolume/element discretizations, with finite element analyses based on conformable Q9 elements. Subvolume and elemental dimensions were kept square at each level of mesh refinement.

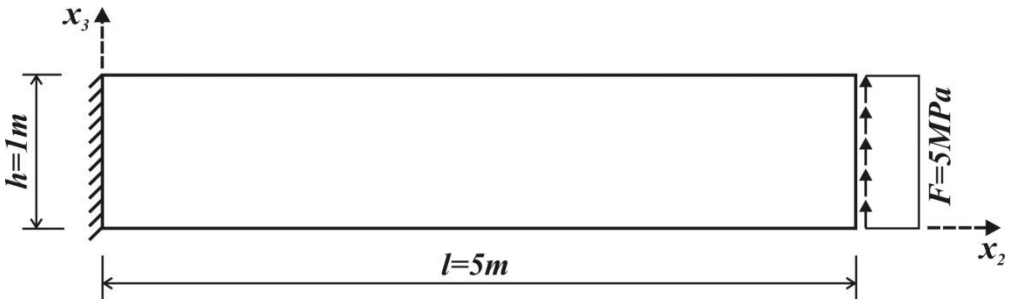

(a) Cantilevered homogeneous strip

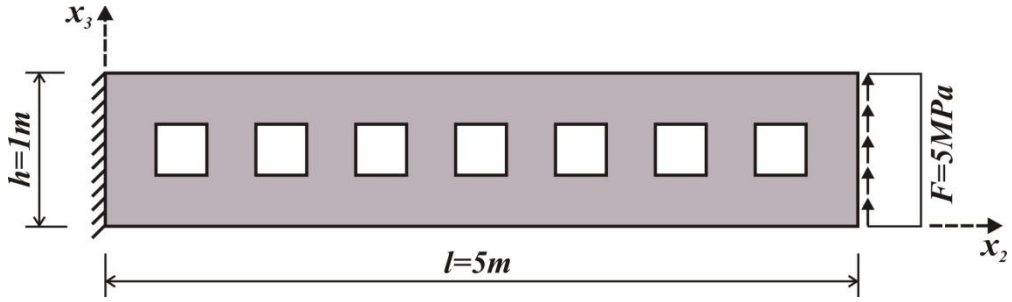

(b) Cantilevered strip with square cut-outs

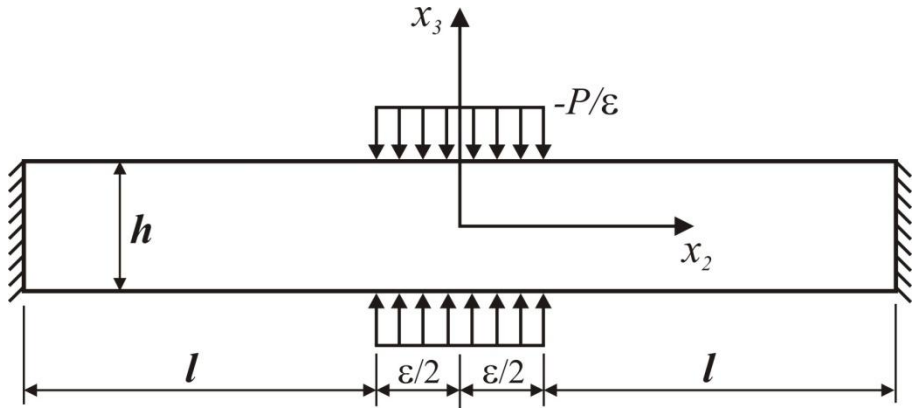

(c) Long rectangular strip subjected to concentrated, uniform normal tractions

Figure 3.4. Homogeneous and heterogeneous rectangular strips subjected to different loadings analyzed using the generalized finite-volume theory for verification with analytical and finite element results.

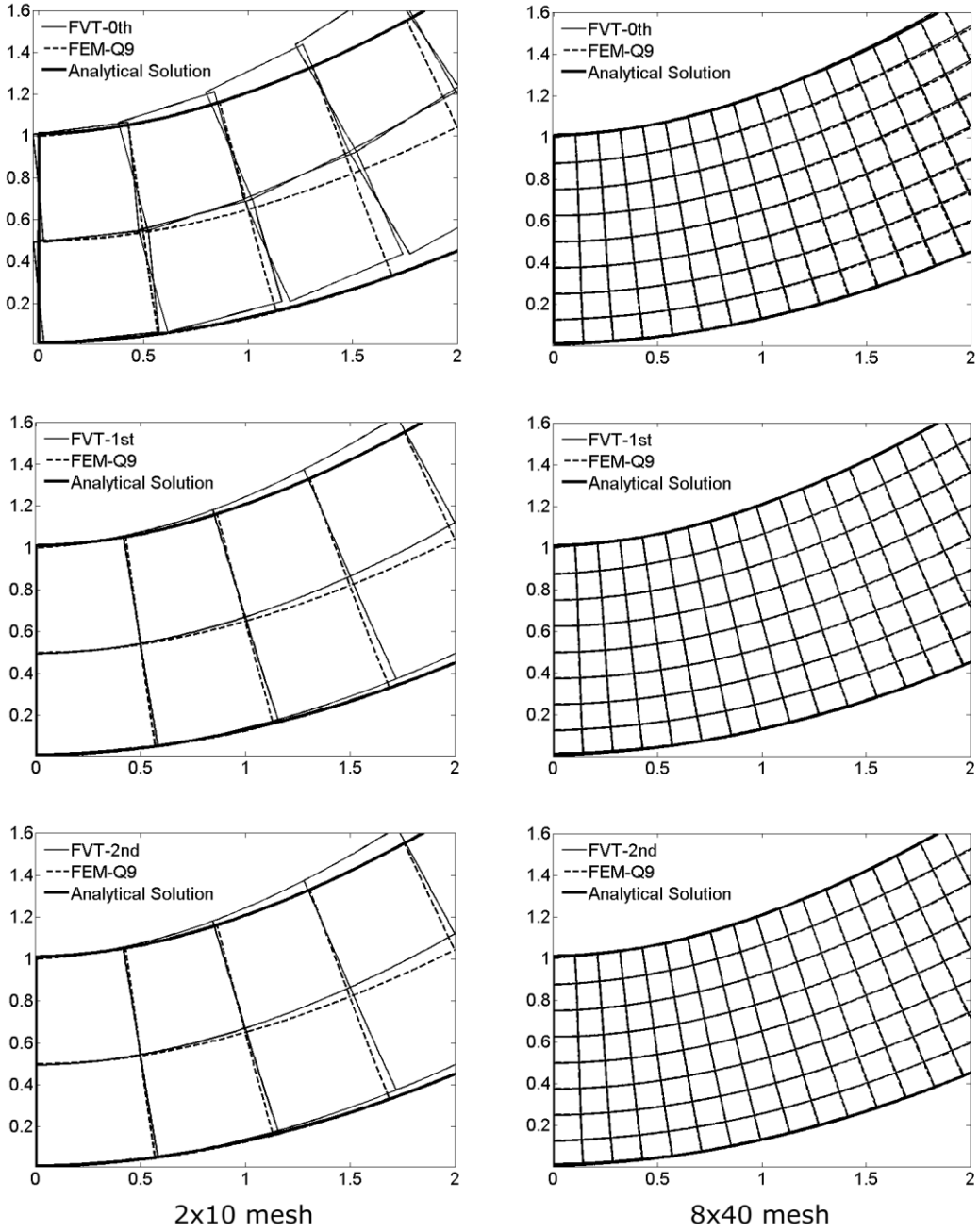

Figure 3.5. Deformed cantilevered strip under applied end load. Comparison amongst predictions of 0th, 1st and 2nd order (generalized) finite-volume theories, analytical and finite-element results.

Figure 3.5 compares the different-order finite-volume predictions of mesh deformations with the finite element results in the vicinity of the built-in end where rotation effects,

and hence propensity for interfacial interpenetration, are most pronounced. The deformed meshes were generated by amplifying the displacements 200 times. Interfacial interpenetrations are observed in the 0th order finite-volume theory predictions for the coarsest mesh comprised of 2x10 subvolumes, which become imperceptibly small at this level of magnification when the mesh size increases to 8x40 subvolumes. Conversely, interfacial interpenetrations are not readily observable in the case of the 1st and 2nd order (generalized) finite-volume theory predictions even for the coarsest mesh due to additional enforcement of surface-averaged rotation and curvature continuity across adjacent subvolume interfaces. All three versions of the finite-volume theory produce greater deflections relative to the finite element and analytical results when the mesh is coarse, with the 0th order theory producing the greatest deflection, and comparable but smaller deflections predicted by 1st and 2nd order theories. The differences relative to the finite element results vanish upon mesh refinement to 8x40 subvolumes in the case of the 1st and 2nd order theories, and become very small in the case of the 0th order theory. The analytical solution based on employed manner of constraint at the built-in end produces essentially the same deflection relative to the finest finite-volume and finite element meshes.

Quantification of the extent of interfacial interpenetration in support of the proposed generalized finite-volume theory will be presented in the context of the third problem, where substantial mesh distortions occur in the vicinity of the concentrated surface load. This problem provides a critical test of proposed theory's improvement relative to the original version given the substantial rotations, as well as relative sliding, of the adjacent subvolume interfaces due to the concentrated loading.

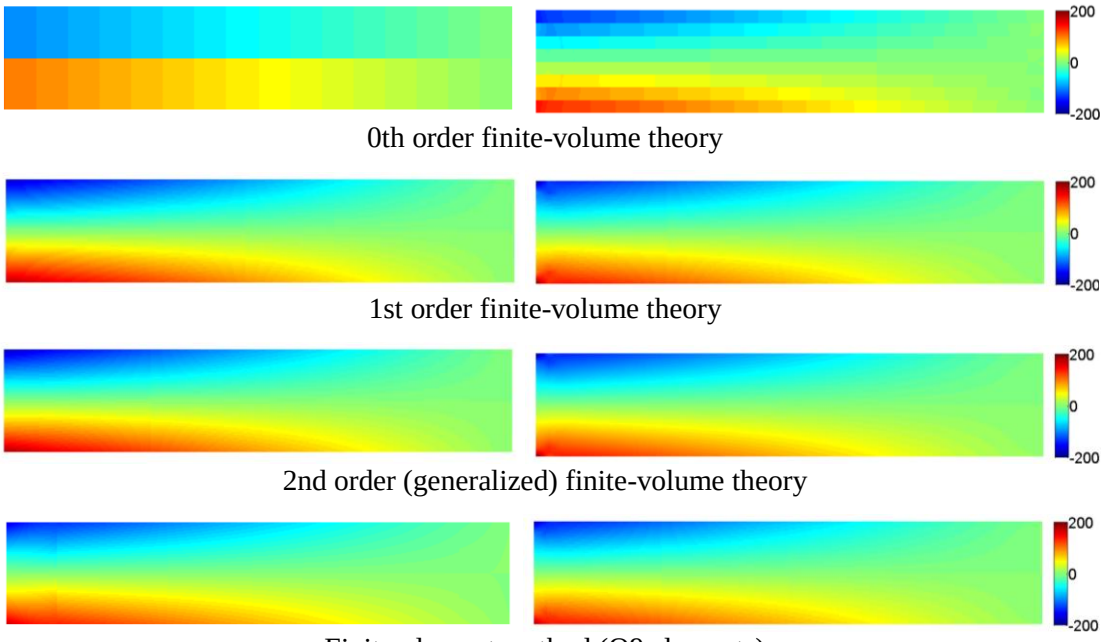

Figure 3.6. Normal stress distributions, $\sigma_{22}(x_2, x_3)$ (MPa), due to applied end load. Comparison amongst predictions of 0th, 1st and 2nd order (generalized) finite-volume theories and finite element results.

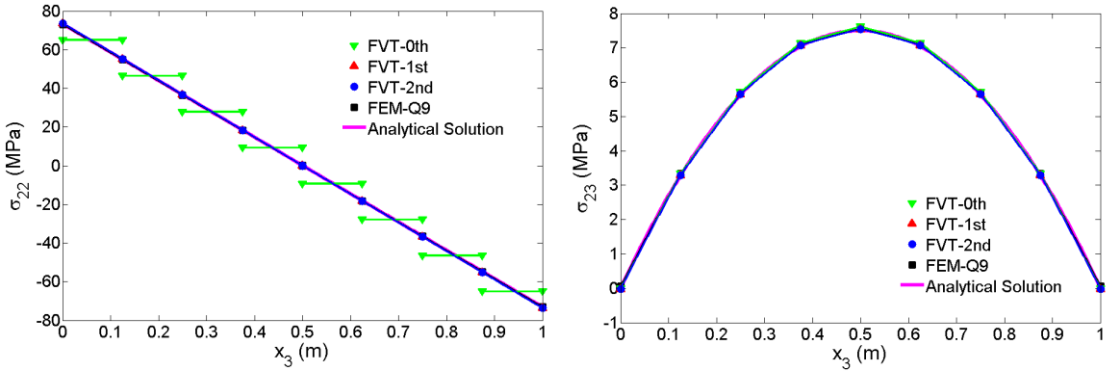

Figure 3.7. Normal (left) and shear (right) stress distributions, $\sigma_{22}(x_2^0, x_3)$, $\sigma_{23}(x_2^0, x_3)$ (MPa), in the $x_2^0 = 2.5625\, m$ cross section (in the middle of the 21th column) due to applied end load, generated using 8x40 mesh. Comparison amongst predictions of 0th, 1st and 2nd order (generalized) finite-volume theories, analytical and finite-element results.

The normal stress $\sigma_{22}(x_2, x_3)$ distributions are compared in Figure 3.6 for the two mesh discretizations. Substantial improvement in the normal stress distributions produced by

the inclusion of higher-order terms in the displacement field approximation is clearly evident in the 1st and 2nd order theory predictions even for the coarse mesh, characterized by smooth variations in both directions in the $x_2 - x_3$ plane and little observable difference with the finite element results. This contrasts with the 0th order theory results which capture only the length-wise stress variation with reasonable accuracy, with poor approximation of the through-thickness distribution due to the use of only two subvolumes along the x_3 coordinate. Increasing the mesh to 8x40 subvolumes improves substantially the 0th order theory results which now mimic stress variations in both directions with much greater fidelity. Nonetheless, the through-thickness $\sigma_{22}(x_2^0, x_3)$ variation exhibits visible discontinuities across horizontal subvolume interfaces since it is not a traction component required to be continuous along the x_3 coordinate. Inclusion of higher-order terms in the displacement fields of the constructed 1st and 2nd order finite-volume theories clearly mitigates this problem. Quantitative evidence of this is illustrated in Figure 3.7 where cross-sectional normal and shear stress distributions generated using the finest mesh are given at $x_2^0 = 2.5625\, m$ which passes through the middle of the 21st column. While the discontinuous character of the normal stress distribution predicted by the 0th order theory is clearly evident, the corresponding predictions of the 1st and 2nd order finite-volume theories are continuous as required and coincident with the analytical and finite element results. In contrast, the shear stress distributions are continuous for each version of the finite-volume theory given that this stress component also is a traction component along the x_3 coordinate. There are virtually no observable differences amongst the shear stress predictions of the finite-volume theories, analytical and finite element results for this mesh discretization.

3.3.2. Cantilevered Rectangular Strip with Square Cutouts

The overall geometry of the rectangular strip with square cutouts, Figure 3.4(b), is the same as that of the homogeneous strip investigated in the preceding section. Seven square cutouts with equal horizontal spacings are inserted, and the strip is constrained at the built-in end and subjected to loading at the right end in the same manner as before. The analysis was performed under plane strain conditions using the elastic constants $E = 420\ GPa$ and $\nu = 0.25$.

The coarsest discretization employed was based on 6x30 equally-dimensioned subvolumes which ensured that the cutouts were spanned by two subvolumes in each direction. At this level of discretization, the interfacial interpenetration in the vicinity of the built-in end is much smaller than in the case of the coarsest mesh used for the homogeneous slab. Hence the deformed meshes which exhibit similar trends vis-a-vis deflections predicted by the finite-volume theory relative to the finite element results are not shown.

Figure 3.8 presents comparison of the $\sigma_{22}(x_2, x_3)$ distributions generated using 6x30 and 18x90 meshes. While the 0th order theory captures the essential features of the normal stress field in both directions sufficiently well even at the coarsest discretization level, including traction-free condition at the vertical hole boundaries, the discontinuous nature of the stress field along the x_3 coordinate is evident. The discontinuities decrease with increasing mesh refinement, but remain observable upon mesh refinement to 18x90 subvolumes. In contrast, the 1st and 2nd order finite-volume theories produce smoothly varying normal stress distributions which are comparable to those obtained from the

finite element analysis. Smoother distributions are predicted by the 2nd order theory relative to the 1st order.

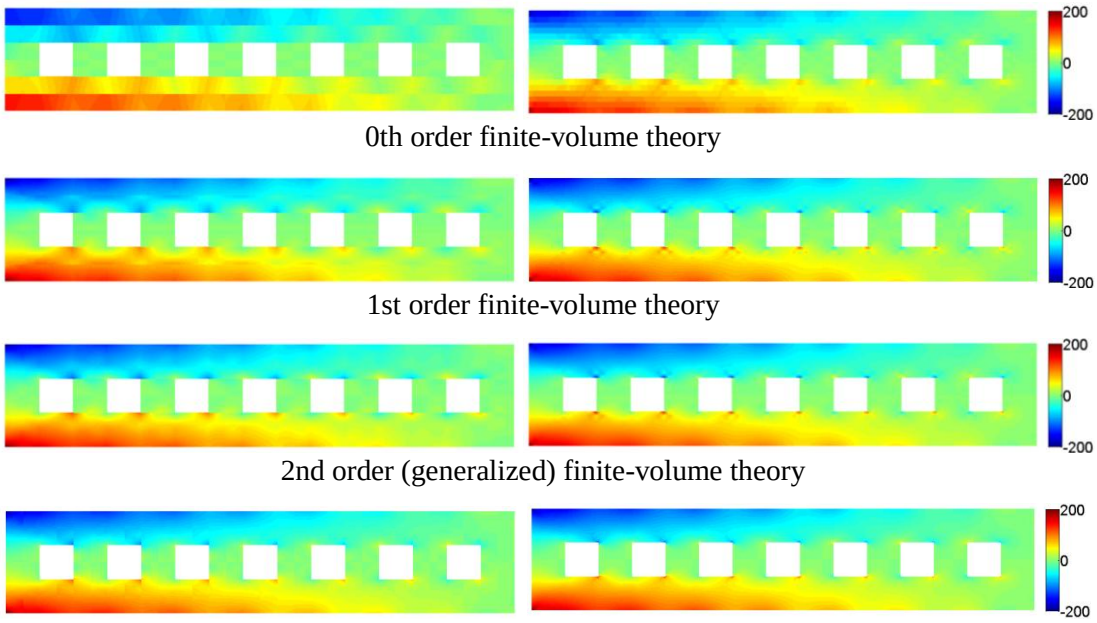

Figure 3.8. Normal stress distributions, $\sigma_{22}(x_2, x_3)$ (MPa), due to applied end load. Comparison amongst predictions of 0th, 1st and 2nd order (generalized) finite-volume theories and finite-element results.

The corresponding $\sigma_{23}(x_2, x_3)$ distributions are compared in Figure 3.9. Since this stress component is a traction component along the x_2 and x_3 axes, it should be continuous along both coordinate directions and hence satisfy traction-free conditions along the entire square hole boundary. As observed, even at the coarsest discretization level, the traction-free condition is satisfied by the shear stress fields generated using 0th, 1st and 2nd order finite-volume theories, in contrast with the finite element method where non-zero shear tractions are clearly visible along the hole boundary for the 6x30 element mesh. Moreover, at this discretization level, the overall character of the shear stress field is better captured by the finite-volume approach even when the 0th order theory is used,

despite the large stress gradients in regions between square cutouts. Increasing the mesh refinement to 18x90 subvolumes produces much smoother finite-volume shear stress distributions, with the 2nd order predictions being the smoothest and of better quality than the finite element results which exhibit localized checker-board patterns at the hole corners.

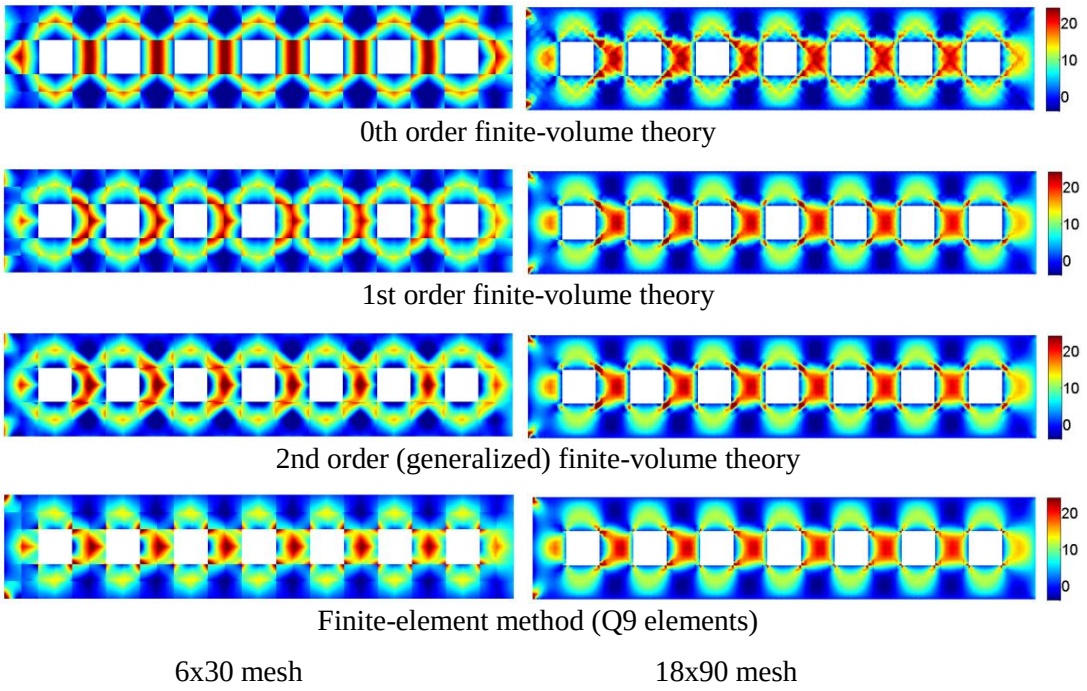

Figure 3.9. Shear stress distributions, $\sigma_{23}(x_2, x_3)$ (MPa), due to applied end load. Comparison amongst predictions of 0th, 1st and 2nd order (generalized) finite-volume theories and finite-element results.

More quantitative comparison of the normal and shear stress distributions is presented in Figure 3.10 at two x_2^0 cross sections generated for the 18x90 subvolume/element meshes. The $x_2^0 = 2.1944\, m$ cross section is situated halfway between the third and fourth square holes from the built-in end (middle of 40th column) along which continuous stress fields occur, while the $x_2^0 = 2.5278\, m$ cross section passes through the middle of the fourth square hole (middle of 46th column) along which the traction-free condition at the hole

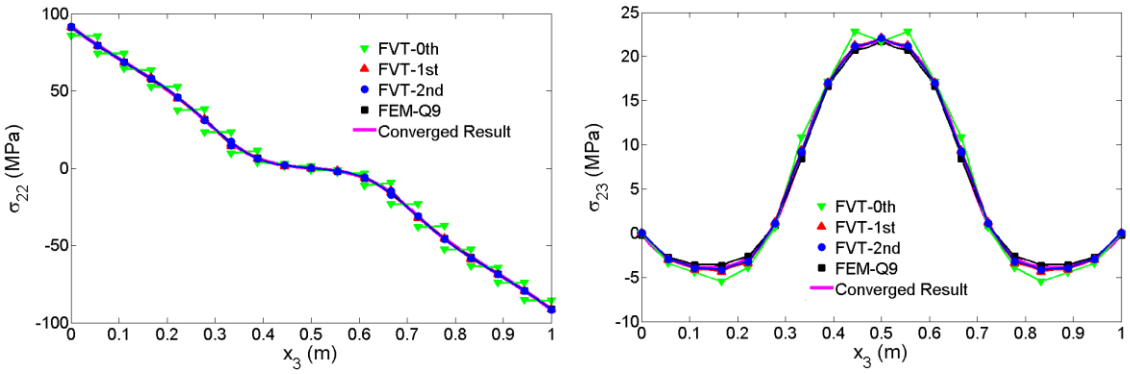

(a) $x_2^0 = 2.1944\ m$ (in the middle of the 40th column)

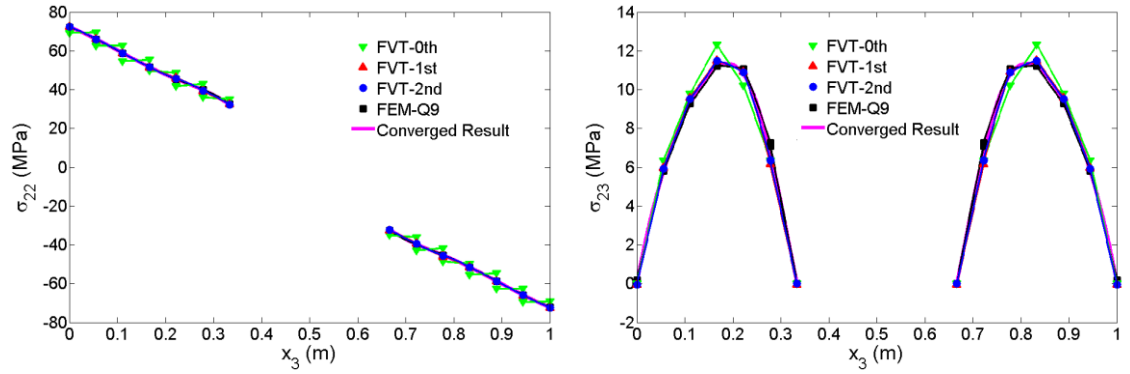

(b) $x_2^0 = 2.5278\ m$ (in the middle of the 46th column)

Figure 3.10. Normal (left) and shear (right) stress distributions, $\sigma_{22}(x_2^0, x_3)$, $\sigma_{23}(x_2^0, x_3)$ (MPa), at two cross sections due to applied end load, generated using 18x90 mesh. Comparison amongst predictions of 0th, 1st and 2nd order (generalized) finite-volume theories, finite-element method and a converged numerical result.

boundary must be satisfied in the case of shear stress. The normal stress distributions in both sections predicted by the 1st and 2nd order finite-volume theories coincide with the finite element results generated using both the 18x90 element mesh and a much more refined mesh which produces converged results included in the figure. These distributions are continuous along the x_3 direction in the respective regions even though the normal stress σ_{22} is not a traction component along this direction. In contrast, small discontinuities persist in the 0th order finite-volume theory predictions based on the quadratic displacement field approximation which does not ensure continuity of non-traction stress components across discretized subdomains with the same elastic materials.

Conversely, the shear stress distributions predicted by the three finite-volume theories are continuous along the two cross sections, but the 0th order predictions deviate from the 1st and 2nd order and finite element results in the regions of maximum shear stress values. Detailed examination of the results reveals that the 2nd order predictions are practically indistinguishable from the converged finite element results, while the finite element results based on the 18x90 element mesh exhibit small deviations.

3.3.3. Rectangular Strip under Concentrated Normal Tractions

The long rectangular strip subjected to concentrated normal tractions on the top and bottom surfaces is shown in Figure 3.4(c), where the overall length is $2l + \varepsilon = 205\, mm$, the height is $h = 20\, mm$, and the length over which the uniform normal traction is distributed is $\varepsilon = 5\, mm$. The total applied normal load is $P = 1000\, N$ per unit depth, and the end faces are fully constrained in the finite-volume and finite element simulations by eliminating all degrees of freedom on the kinematic variables. For the given aspect ratio and symmetric loading, the stress fields are highly localized and hence the end faces are practically traction-free despite the employed constraints. The material properties are $E = 200\, GPa$ and $\nu = 0.32$. Finite-volume and finite element analyses were conducted under plane stress conditions, noting that the inplane stress distributions do not depend on the plane condition for pure traction boundary value problems which the present case approximates in the vicinity of the concentrated surface tractions.

We start with the deformed meshes in the vicinity of the applied load on the upper surface shown in Figure 3.11, which have been generated from the displacements magnified 400 times for clarity. Three progressively finer mesh discretizations were

employed with the subdivisions 41x4, 123x12 and 287x28 which preserved square dimensions of the grid. Substantial interfacial interpenetrations are observed for the coarsest mesh in the 0th order theory predictions underneath the uniform normal traction and off to the sides where the rotations are greatest, which do not completely vanish when the mesh is further refined to 287x28 subvolumes. Even at this mesh refinement level, interpenetrations are still observed in the three subvolume rows directly below the applied surface traction. In contrast, interfacial interpenetrations for the coarsest mesh are much smaller in the case of the 1st order theory, and limited to the surface row of subvolumes. Moreover, they are further reduced with increasing mesh refinement. Imposition of interfacial continuity of surface-averaged displacements, rotations and curvatures in the 2nd order theory practically eliminates interfacial interpenetrations even in the case of the coarsest mesh. However, some relative tangential displacement along interfaces is observed given that the continuity of tangential interfacial displacement derivatives is not enforced in the surface-averaged sense in the present approach. The extent of the relative tangential displacement decreases with increasing mesh refinement, and practically vanishes in the case of the 287x28 mesh nearly everywhere except on the top surface just outside of the applied normal traction discontinuities. Comparison with the finite element results included in the figure illustrates that the 1st and 2nd order finite-volume theories with the additional constraints on interfacial continuity of surface-averaged rotations and curvatures mimic the locally deformed mesh very well with sufficient mesh refinement. The substantial improvement relative to the 0th order theory predictions for this particular loading well justifies the additional complexity introduced

through inclusion of the higher-order terms in the subvolume displacement field representation.

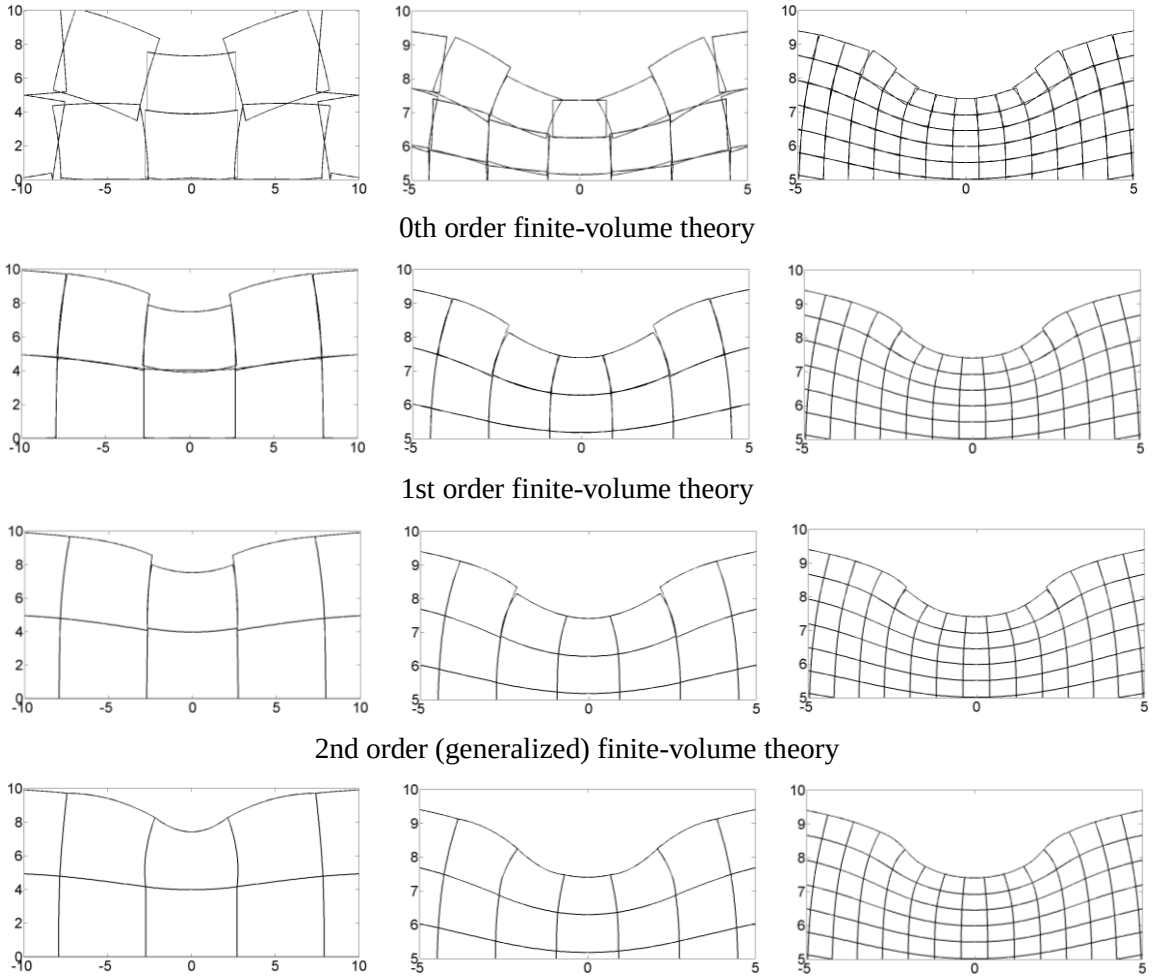

Figure 3.11. Deformed meshes in the vicinity of applied normal traction on the upper surface of rectangular strip magnified 400 times. Comparison amongst predictions of 0th, 1st and 2nd order (generalized) finite-volume theories and finite-element results.

The plane elasticity solution for the rectangular strip subjected to concentrated normal tractions on top and bottom surfaces is obtained in closed form when the strip is infinite along the x_2 axis, i.e., as $L \to \infty$. In the present case, this solution is applicable given the strip's large aspect ratio and concentrated surface loading by normal tractions which span

a very small portion of the overall strip's length. The inplane stress components are given in terms of the following integrals, Sneddon (1951),

$$\begin{aligned}
\sigma_{22}(x_2,x_3) &= \frac{2P}{\pi}\int_0^{+\infty}\frac{2}{\epsilon s}sin\left(\frac{\epsilon s}{2}\right)\frac{cos(sx_2)}{sh+sinh(sh)}\left\{\left[\frac{sh}{2}cosh\left(\frac{sh}{2}\right)\right.\right.\\
&\quad\left.\left.-sinh\left(\frac{sh}{2}\right)\right]cosh(sx_3)-sx_3sinh\left(\frac{sh}{2}\right)sinh(sx_3)\right\}ds\\
\sigma_{33}(x_2,x_3) &= -\frac{2P}{\pi}\int_0^{+\infty}\frac{2}{\epsilon s}sin\left(\frac{\epsilon s}{2}\right)\frac{cos(sx_2)}{sh+sinh(sh)}\left\{\left[\frac{sh}{2}cosh\left(\frac{sh}{2}\right)\right.\right.\\
&\quad\left.\left.+sinh\left(\frac{sh}{2}\right)\right]cosh(sx_3)-sx_3sinh\left(\frac{sh}{2}\right)sinh(sx_3)\right\}ds\\
\sigma_{23}(x_2,x_3) &= \frac{2P}{\pi}\int_0^{+\infty}\frac{2}{\epsilon s}sin\left(\frac{\epsilon s}{2}\right)\frac{sin(sx_2)}{sh+sinh(sh)}\left[\frac{sh}{2}cosh\left(\frac{sh}{2}\right)sinh(sx_3)\right.\\
&\quad\left.-sx_3sinh\left(\frac{sh}{2}\right)cosh(sx_3)\right]ds
\end{aligned} \tag{3.44}$$

which are readily evaluated numerically. Herein, Simpson's rule was employed with 500 subintervals and $s = 20$ for the upper integrand limit given that the integrands practically vanish for $s > 20$.

Figure 3.12 presents comparison of the three inplane stress distributions generated using the three versions of the finite-volume theory and finite element method based on the finest mesh discretization of 287x28 subvolumes/elements with the above elasticity solution. At this discretization level, discontinuities in the non-traction stress distributions are still apparent across subvolume interfaces along both coordinate directions for the 0th order theory. For the $\sigma_{22}(x_2,x_3)$ distributions, these discontinuities occur along the x_2^0 cross sections, and along the x_3^0 cross sections for the $\sigma_{33}(x_2,x_3)$ distributions. The $\sigma_{23}(x_2,x_3)$ distributions are continuous along both coordinate directions along which this stress component is a traction component. Inclusion of surface-averaged rotations and curvatures in the 1st and 2nd order theories eliminates normal stress discontinuities,

producing distributions practically indistinguishable from the finite element and analytical results.

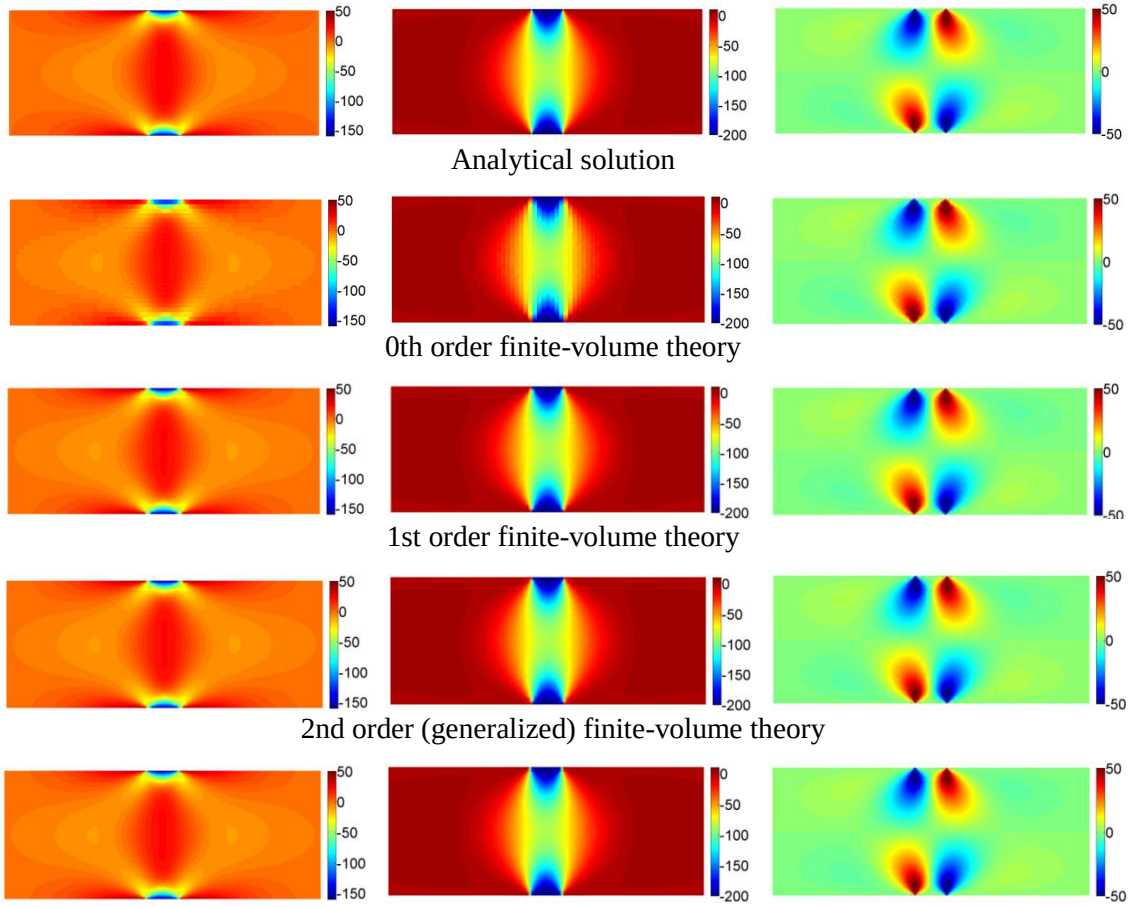

Figure 3.12. Normal and shear stress distributions, $\sigma_{22}(x_2, x_3)$, $\sigma_{33}(x_2, x_3)$, $\sigma_{23}(x_2, x_3)$ (MPa), in the vicinity of applied normal tractions on top and bottom surfaces of rectangular strip, generated using 287x28 mesh. Comparison amongst predictions of 0th, 1st and 2nd order (generalized) finite-volume theories, analytical and finite-element results.

Quantitative assessment of the above three stress fields is presented in Figure 3.13 in terms of quantities that characterize the global convergence of the stress distributions with mesh refinement. Towards this end, the global error function relative to the analytical solution is defined as follows,

$$E[\sigma_{ij}] = \frac{\int_V \left[\sigma_{ij}^{fvt,fem} - \sigma_{ij}^{analytical}\right]^2 dV}{\int_V \left[\sigma_{ij}^{analytical}\right]^2 dV} \tag{3.45}$$

which was calculated numerically for the finite-volume and finite element approaches using Gaussian integration based on 3x3 Gauss points for all employed mesh discretizations. The integral in the denominator was also calculated numerically using the finest 287x28 subvolume mesh. The results shown in Figure 3.13 demonstrate the substantial improvement of the stress convergence with mesh refinement to the analytical solution achieved by the 1st and 2nd order theory relative to the original version. Moreover, the convergence of the $\sigma_{23}(x_2, x_3)$ and $\sigma_{33}(x_2, x_3)$ distributions for the 2nd

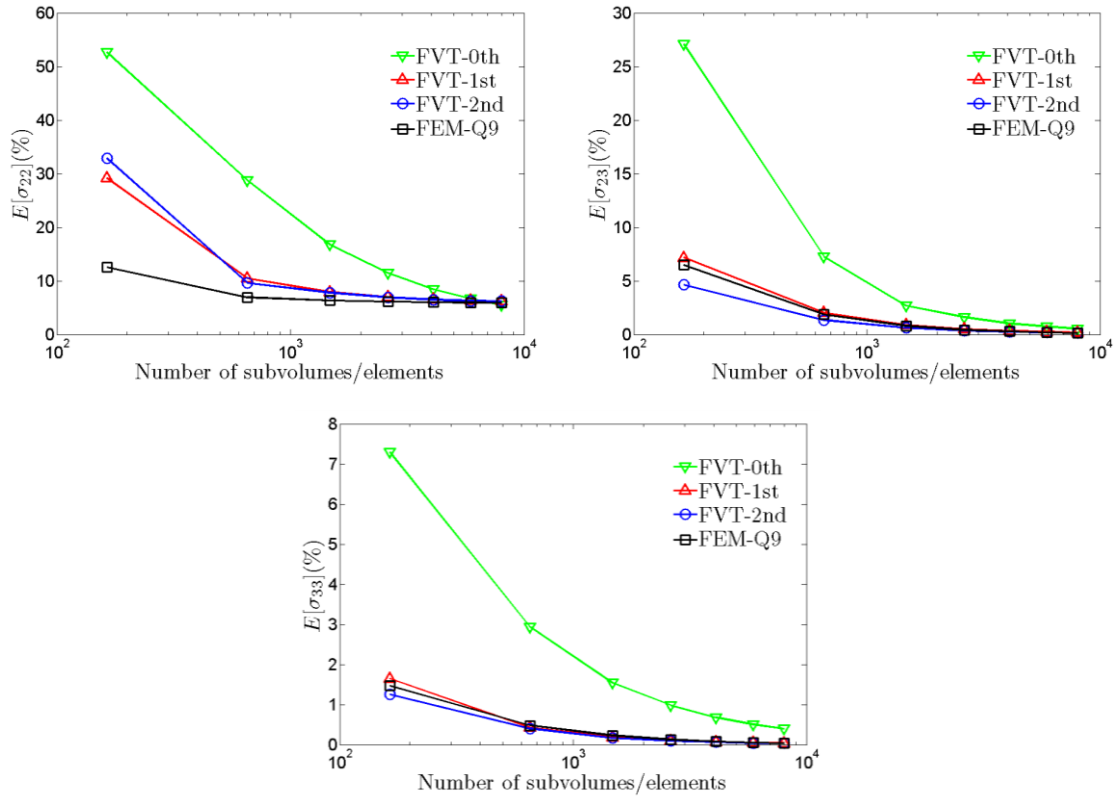

Figure 3.13. Global error measures relative to the analytical solution for the normal and shear stress fields $\sigma_{22}(x_2, x_3)$, $\sigma_{33}(x_2, x_3)$ and $\sigma_{23}(x_2, x_3)$ (MPa) as a function of mesh refinement. Comparison amongst predictions of 0th, 1st and 2nd order (generalized) finite-volume theories and finite element results.

order theory is a little better than the finite element results' convergence. The differences in the convergence of $\sigma_{22}(x_2, x_3)$ distributions predicted by the 1st and 2nd order theory and the finite element method vanishes with increasing mesh refinement, with the finite element results being more accurate at course mesh discretizations. While the error in the $\sigma_{23}(x_2, x_3)$ and $\sigma_{33}(x_2, x_3)$ distributions vanishes with increasing mesh refinement for the finite-volume and finite element approaches, the same small residual error remains in the case of the $\sigma_{22}(x_2, x_3)$ distribution predicted by the two approaches. This most likely indicates some influence of the boundary conditions on this stress component.

Examination of global convergence of the above integral stress field measure calculated at Gauss points leverages the strength of the finite element method, but does not provide a complete error measure for use in applications involving heterogeneous materials, and the concomitant importance of satisfying interfacial stress and displacement continuity. In order to assess the improvement in the continuity of these quantities achieved by the proposed generalization of our finite-volume theory as a function of mesh refinement, we define pointwise interfacial displacement and stress discontinuities along vertical and horizontal cross sections,

$$\begin{aligned} \Delta u_i(x_2, x_3) &= u_i^+(x_2, x_3) - u_i^-(x_2, x_3) \\ \Delta \sigma_{ij}(x_2, x_3) &= \sigma_{ij}^+(x_2, x_3) - \sigma_{ij}^-(x_2, x_3) \end{aligned} \tag{3.46}$$

In the case of the analyzed vertical cross section $x_2 = x_2^0$, the superscripts (-) and (+) represent values immediately to the left and to the right of the cross section, whereas in the case of the horizontal cross section $x_3 = x_3^0$ these respective superscripts represent values immediately below and above the cross section. These vertical and horizontal cross sections coincide with the interfaces of the subvolumes/elements for all the analyzed meshes. Using absolute values of these quantities, the following integral

measures of interfacial discontinuities are then defined along vertical and horizontal cross sections S_0,

$$\Delta\bar{u}_i|_{S_0} = \frac{1}{S_0}\int_{S_0} |\Delta u_i| dS \quad and \quad \Delta\bar{\sigma}_{ij}\big|_{S_0} = \frac{1}{S_0}\int_{S_0} |\Delta\sigma_{ij}| dS \tag{3.47}$$

The above interfacial discontinuities were then calculated along the vertical cross section $x_2^0 = 2.5\,mm$ which coincides with the discontinuity in the applied surface load, and the horizontal cross section $x_3^0 = 5.0\,mm$ which coincides with the first horizontal interface from the top surface of the rectangular strip of the coarsest mesh 41x4. Examination of the deformed meshes presented in Figure 3.11 indicates large interfacial rotations along both directions and relative slip along the vertical axis.

Figure 3.14 illustrates pointwise continuity satisfaction of the traction stress components $\sigma_{22}(x_2^0, x_3)$ and $\sigma_{23}(x_2^0, x_3)$, the non-traction stress component $\sigma_{33}(x_2^0, x_3)$, and the displacement components $u_2(x_2^0, x_3)$ and $u_3(x_2^0, x_3)$, as a function of mesh refinement along the cross section $x_2^0 = 2.5\,mm$. The improvement in the satisfaction of these quantities attained by the generalized finite-volume theory relative to the 0th order theory is notable. Moreover, the 2nd order finite-volume theory does a better job of satisfying pointwise interfacial traction continuity than the finite element method, particularly in the case of the normal component $\sigma_{22}(x_2^0, x_3)$. While conformable elements such as Q9 ensure pointwise interfacial displacement continuity at all levels of mesh discretization, the surface-averaging character of the finite-volume theory does not. Nonetheless, both the 1st and 2nd order theories dramatically improve pointwise continuity of the displacement component $u_2(x_2^0, x_3)$ through enforcement of surface-average rotation and curvature continuity, mimicking the finite element capability. In contrast, attainment of pointwise continuity of the displacement component $u_3(x_2^0, x_3)$ requires greater mesh

refinement because only this surface-averaged displacement component, and not its derivatives, is required to be continuous in the surface-average sense along the vertical direction.

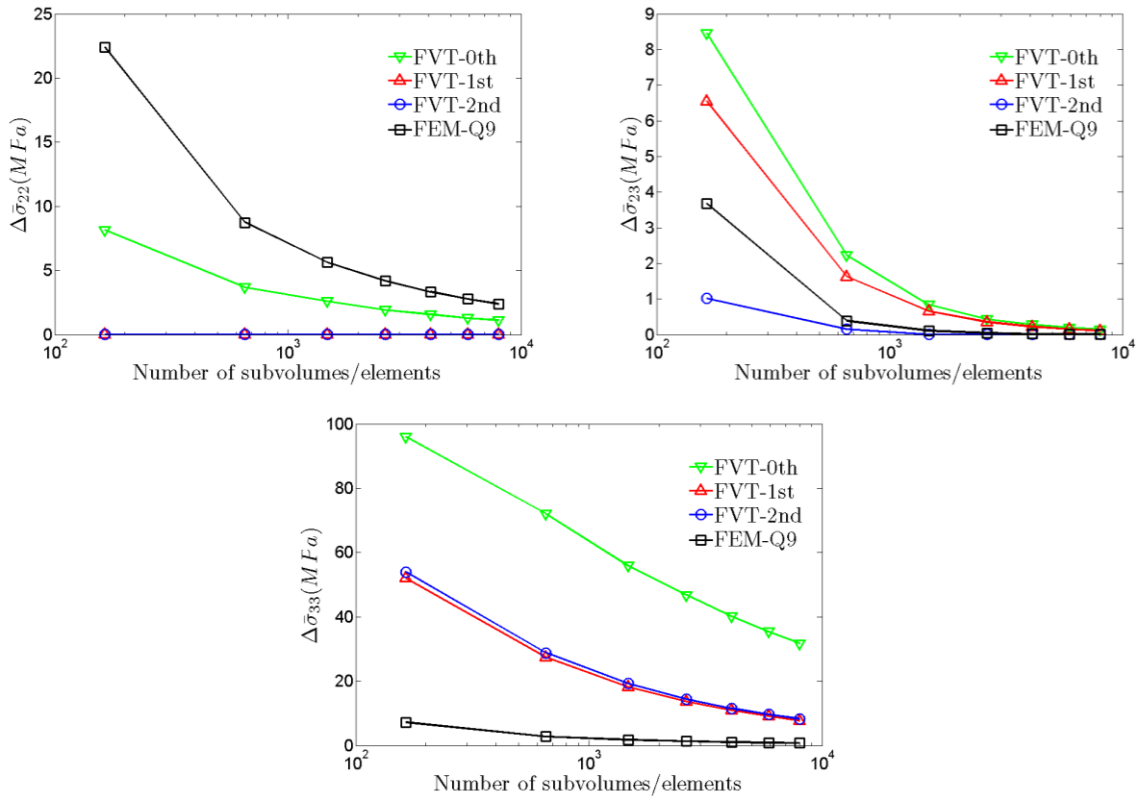

(a)

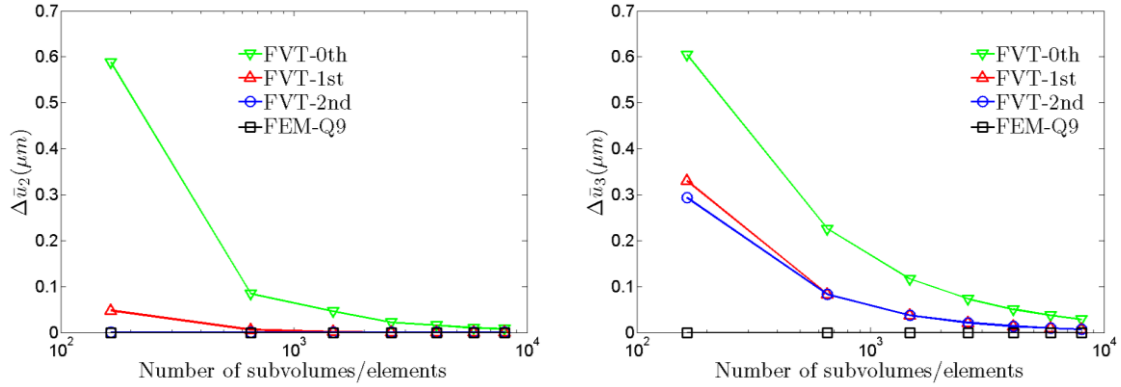

(b)

Figure 3.14. Interfacial stress (a) and displacement (b) difference measures at the cross section $x_2^0 = 2.5\ mm$ as a function of mesh refinement. Comparison amongst predictions of 0th, 1st and 2nd order (generalized) finite-volume theories and finite-element results.

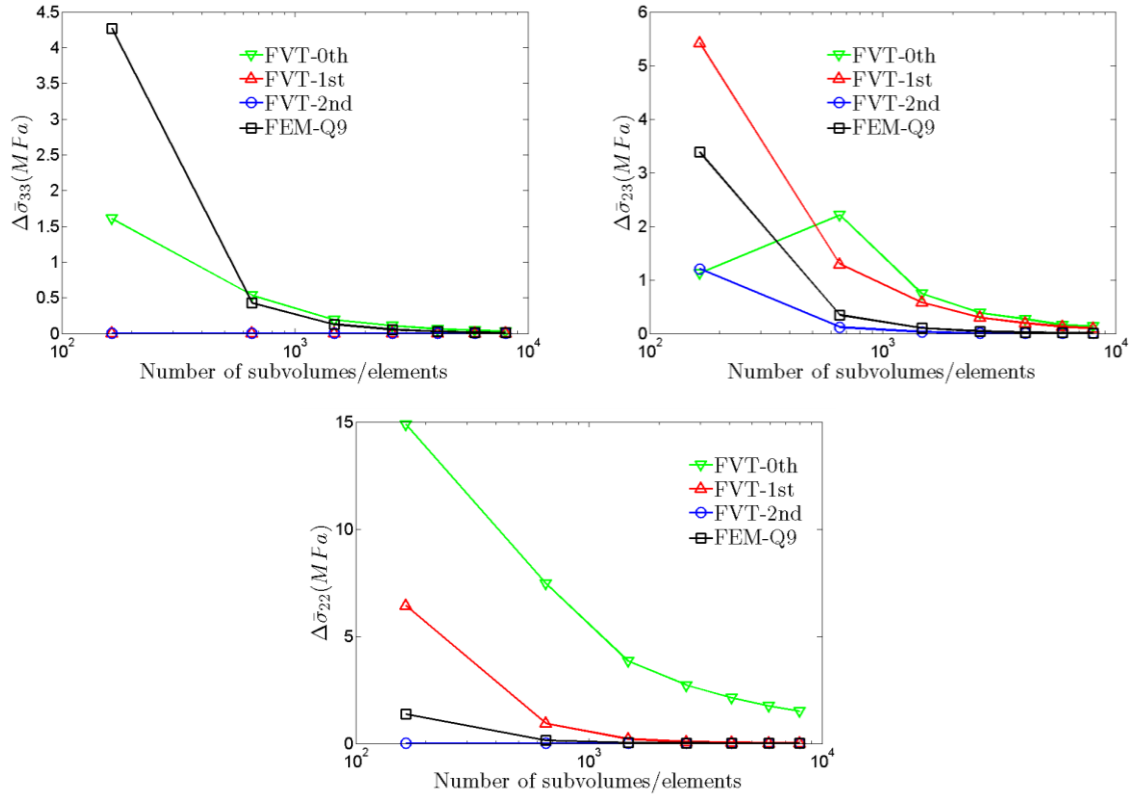

(a)

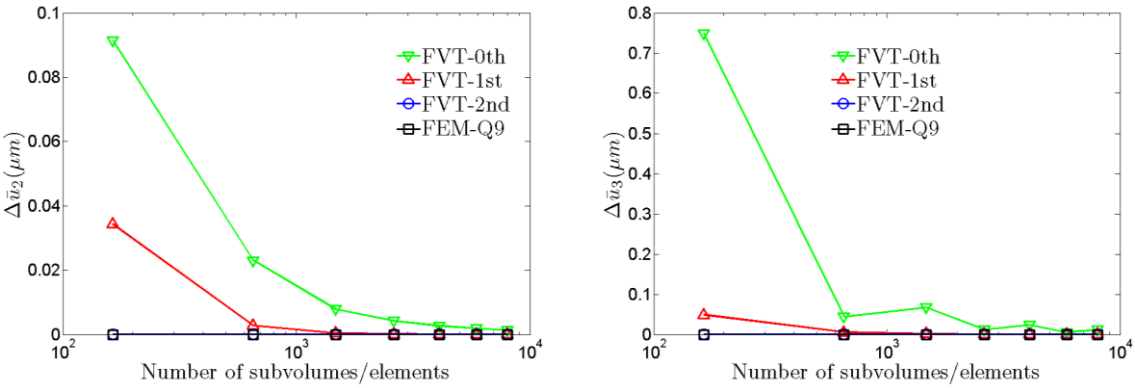

(b)

Figure 3.15. Interfacial stress (a) and displacement (b) difference measures at the cross section $x_3^0 = 5.0\,mm$ as a function of mesh refinement. Comparison amongst predictions of 0th, 1st and 2nd order (generalized) finite-volume theories and finite-element results.

Figure 3.15 illustrates the corresponding pointwise stress and displacement continuity satisfaction as a function of mesh refinement along the cross section $x_3^0 = 5.0\,mm$ in the interval $-22.5 \leq x_2 \leq +22.5\,mm$ where the stress gradients produced by the

concentrated load are greatest. In this case, the traction stress components are $\sigma_{33}(x_2, x_3^0)$ and $\sigma_{23}(x_2, x_3^0)$, whereas $\sigma_{22}(x_2, x_3^0)$ is the non-traction stress component. As in the vertical cross section, the improvement in the satisfaction of interfacial stress and displacement pointwise continuity made possible by the generalized finite-volume theory relative to the 0th order theory is significant. Moreover, the 2nd order theory outperforms the finite element method in satisfying interfacial traction and non-traction stress continuity, while also satisfying the continuity of both displacement components along this cross section.

Comparison of the interfacial stress discontinuity measures presented in Figures 3.14(a) and 3.15(a) along the two cross sections for the most refined mesh containing 287x28 subvolumes highlights the 0th order theory's inability to ensure continuity of non-traction stress components across interfaces between adjacent subvolumes containing the same material. In contrast, the traction stress components are continuous. Nonetheless, examination of the actual stress distributions (not shown) reinforces the known result that the average values of the non-traction stress components are accurate. Clearly, inclusion of higher-order terms in the displacement field representation, in conjunction with the newly introduced surface-averaged kinematic variables required being continuous across subvolume interfaces and sufficient mesh refinement, has eliminated the non-traction stress discontinuity problem in highly demanding situations characterized by large stress gradients produced by concentrated loading.

3.3.4. Unbalanced Average Stress Convergence

While each subvolume of the discretized domain is in a state of overall equilibrium due to satisfaction of equilibrium equations in a surface-average sense, the higher-order displacement fields of the 1st and 2nd order finite-volume theories produce a local, point-wise stress imbalance. In order to gauge how fast point-wise equilibrium equations tend to zero for comparison with finite element results, we employ the unbalanced average stress measure first introduced by Cavalcante et al. (2011b) in the context of the parametric FVDAM theory and presented in the previous chapter. At the subvolume level, using the Average Stress Theorem, the unbalanced average stress $\Delta\bar{\sigma}_{ij}^{(\beta,\gamma)}$ is defined as follows,

$$\Delta\bar{\sigma}_{ij}^{(\beta,\gamma)} = \hat{\sigma}_{ij}^{(\beta,\gamma)} - \bar{\sigma}_{ij}^{(\beta,\gamma)} = \frac{1}{V_{(\beta,\gamma)}} \int_{V_{(\beta,\gamma)}} \frac{\partial \sigma_{ki}}{\partial x_k} x_j dV \tag{3.48}$$

where

$$\hat{\sigma}_{ij}^{(\beta,\gamma)} = \frac{1}{V_{(\beta,\gamma)}} \int_{S_{(\beta,\gamma)}} t_i x_j dV, \quad \bar{\sigma}_{ij}^{(\beta,\gamma)} = \frac{1}{V_{(\beta,\gamma)}} \int_{V_{(\beta,\gamma)}} \sigma_{ij} dV \tag{3.49}$$

When the local equilibrium equations are satisfied in point-wise sense, i.e., $\partial\sigma_{ki}/\partial x_k = 0$, the same result for the subvolume average stress is obtained from surface averaging of traction components and volume averaging of stress components. This is true for the 0th order theory owing to the quadratic displacement field. However, the generalization of the finite-volume theory through the use of a higher-order displacement field violates point-wise equilibrium equations. For the 2nd order (generalized) finite-volume theory, we obtain the following unbalanced subvolume average stresses

$$\Delta\bar{\sigma}_{22}^{(\beta,\gamma)} = \frac{h_\beta^2}{4}\left[C_{44}W_{2(12)} + (C_{23}+C_{44})W_{3(21)}\right]^{(\beta,\gamma)}$$
$$\Delta\bar{\sigma}_{23}^{(\beta,\gamma)} = \frac{l_\gamma^2}{4}\left[C_{22}W_{2(21)} + (C_{23}+C_{44})W_{3(12)}\right]^{(\beta,\gamma)}$$
$$\Delta\bar{\sigma}_{32}^{(\beta,\gamma)} = \frac{h_\beta^2}{4}\left[(C_{23}+C_{44})W_{2(21)} + C_{33}W_{3(12)}\right]^{(\beta,\gamma)} \quad (3.50)$$
$$\Delta\bar{\sigma}_{33}^{(\beta,\gamma)} = \frac{l_\gamma^2}{4}\left[(C_{23}+C_{44})W_{2(12)} + C_{44}W_{3(21)}\right]^{(\beta,\gamma)}$$

while for the 1st order finite-volume theory we have,

$$\Delta\bar{\sigma}_{22}^{(\beta,\gamma)} = \Delta\bar{\sigma}_{33}^{(\beta,\gamma)} = 0 \quad \text{with} \quad \Delta\bar{\sigma}_{23}^{(\beta,\gamma)} \neq 0 \quad \text{and} \quad \Delta\bar{\sigma}_{32}^{(\beta,\gamma)} \neq 0 \quad (3.51)$$

Similarly, stress equilibrium equations are not satisfied locally in the finite element analysis until sufficient mesh discretization ensures that the total potential energy is minimized. Summing up all the subvolume unbalanced average stress contributions in the absolute value sense, we obtain the global measure for the entire analysis domain,

$$\Delta\bar{\sigma}_{ij} = \sum_{\gamma=1}^{N_\gamma}\sum_{\beta=1}^{N_\beta} c_{(\beta,\gamma)}\left|\Delta\bar{\sigma}_{ij}^{(\beta,\gamma)}\right| \quad (3.52)$$

where $c_{(\beta,\gamma)} = V_{(\beta,\gamma)}/V$ is the volume fraction of (β,γ) subvolume and $V = \sum_{\gamma=1}^{N_\gamma}\sum_{\beta=1}^{N_\beta} V_{(\beta,\gamma)}$.

Figure 3.16 presents comparison of the global unbalanced stress measures as a function of mesh discretization obtained from the 0th, 1st and 2nd order finite-volume theories with the corresponding finite element results for the rectangular cantilevered strip with square cutouts and the rectangular strip under concentrated normal tractions. We note that the finite element results have been computed relative to local coordinate systems centered in each element. Different results will be obtained relative to other coordinate

systems because element equilibrium is not explicitly satisfied in volumetric sense, in contrast with the finite-volume theory.

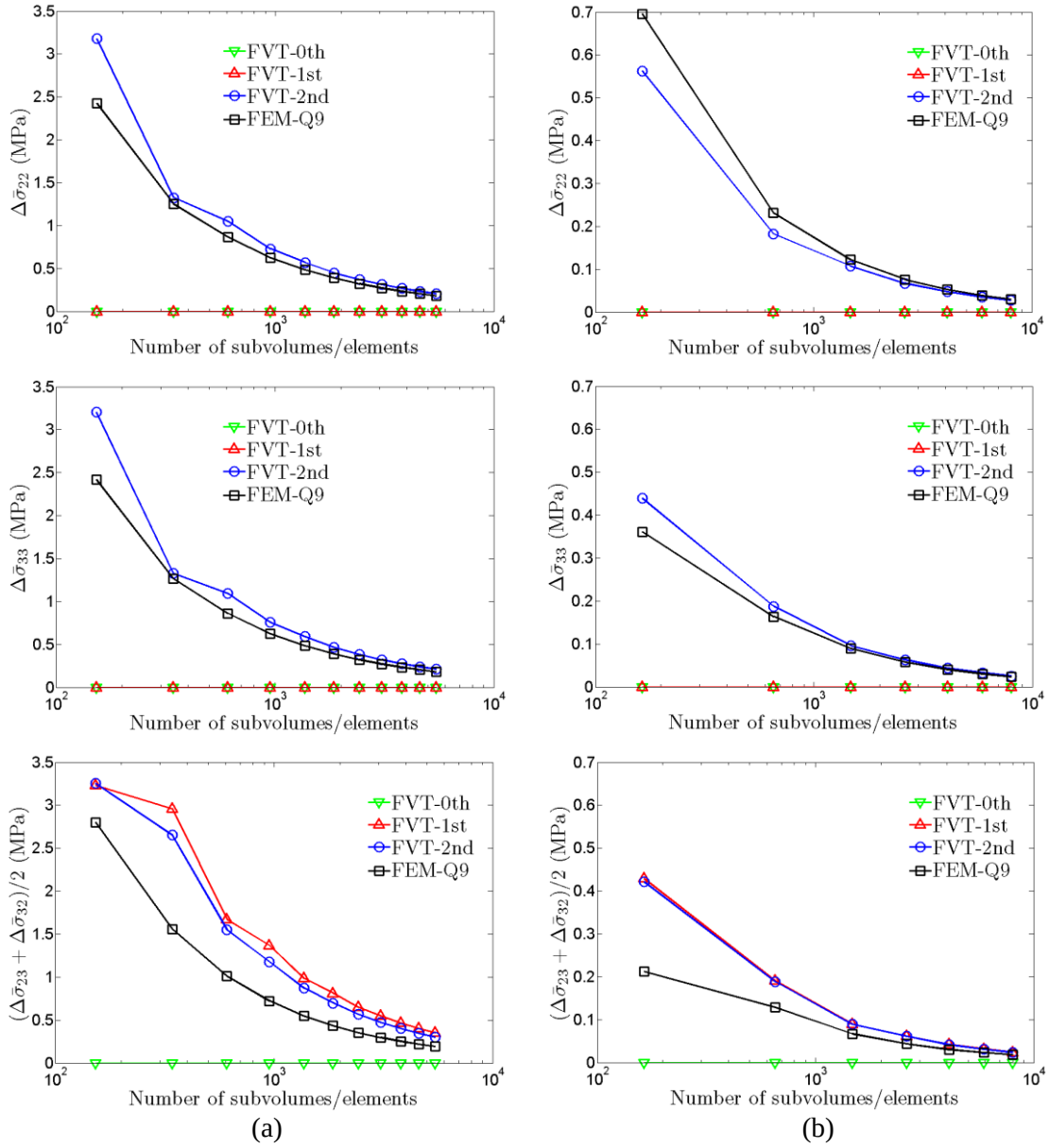

Figure 3.16. Convergence of the global unbalanced average stresses $\Delta\bar{\sigma}_{22}$, $\Delta\bar{\sigma}_{33}$, $(\Delta\bar{\sigma}_{23}+\Delta\bar{\sigma}_{32})/2$ (MPa) as a function of mesh refinement for: (a) cantilevered rectangular slab with square cutouts; (b) rectangular strip under concentrated normal tractions. Comparison amongst predictions of 0th, 1st and 2nd order (generalized) finite-volume theories and finite-element results.

In the first instance, the square cutouts produce local stress concentrations at the corners which are distributed throughout the entire analysis domain. Hence the magnitudes of the unbalanced stress measures are greater than in the second case where local stress gradients are limited to the region of the normal surface tractions. In both cases, the unbalanced normal stress measures of the 2nd order finite-volume theory and the finite element method tend to zero at comparable rates with mesh refinement, while the 0th and 1st order theories do not produce an unbalanced normal stress, see Equation (3.51). In contrast, the unbalanced shear stress measure $(\Delta\bar{\sigma}_{23} + \Delta\bar{\sigma}_{32})/2$ exhibits comparable magnitudes for both the 1st and 2nd order finite-volume theory as it tends to zero with mesh refinement, as do the corresponding finite element results. When the local stress concentrations are distributed throughout the analysis domain, as in the first instance involving cantilevered strip with square cutouts, the magnitudes of the unbalanced shear stress measure are greater relative to the finite element analysis for coarse meshes, while in the case of locally concentrated stress gradients the relative differences become magnified. In both cases, comparable mesh refinements are required to reduce the unbalanced shear stress measure to very small values. Hence overall, the unbalanced stress measure convergence characteristics of the 2nd order (generalized) finite-volume theory are comparable to those of the Q9 element-based finite element analysis.

The above convergence results demonstrate numerically the consistency of the proposed generalized finite-volume theory with mesh refinement. We do not make an attempt herein to derive convergence rates for the different order finite-volume theories explicitly as a function of mesh size for either pointwise or averaged stresses, or for the unbalanced stress measure. This is a topic for future study which will strengthen the proposed

theory's theoretical foundation. The presented results provide a strong motivation for such investigation.

3.4. Summary and Discussion

The previously developed finite-volume theory for heterogeneous materials based on rectangular analysis domains discretized into rectangular subvolumes characterized by quadratic displacement field representation has been generalized through the incorporation of cubic and quartic terms. The surface-averaging framework of the theory and its finite-volume foundation have been preserved through the introduction of elasticity-based, surface-averaged kinematic and static variables which facilitated construction of a generalized stiffness matrix governing the local subvolume response. The manner in which this matrix was constructed makes possible systematic reduction of the theory to lower-order versions, with the lowest order corresponding to the original construction by Bansal and Pindera (2003). Reductions to lower-order versions reveal precisely which characteristics of the subvolume response relative to its neighbors are abandoned, clearly establishing the connection between mathematics and physics of the subvolume's deformation features.

Verification of the generalized finite-volume theory was provided through three examples which critically test the theory's predictive capability under stringent loading conditions. Comparison with analytical and finite element results is the basis for this verification, while the recently introduced global unbalanced average stress measure provides one of the means for testing the method's convergence vis-a-vis that of the finite element method.

The results indicate that the addition of higher-order terms in the local displacement field representation, which provides the basis for the higher-order theory's framework, substantially improves the conformability of adjacent subvolumes by reducing and eliminating interfacial interpenetrations. This is a direct result of satisfying continuity of the newly introduced surface-averaged kinematic variables which represent interfacial rotations and curvatures. In loading situations by distributed tractions which produce large rotations, inclusion of surface-averaged rotations intrinsic to the 1st order finite-volume theory produces comparable results to those of the 2nd order (generalized) theory based on both surface-averaged rotations and curvatures. In more demanding situations involving concentrated tractions, however, the generalized (2nd order) theory is required to produce nearly continuous displacements across subvolume interfaces.

Inclusion of higher-order terms also largely eliminates, with sufficient mesh refinement, discontinuities in non-traction components across interfaces separating subvolumes with the same material properties. This shortcoming of the 0th order finite-volume theory had been recognized some time ago, Cavalcante et al. (2008), and provided the motivation for the construction of the proposed generalized (2nd order) finite-volume theory. The presented examples provide compelling evidence for the success of this generalized approach based on the novel surface-averaged kinematic and static variables which may find use in the development of new approaches to the solution of boundary-value problems in solid mechanics. The advantage of the generalized finite-volume theory's analytical framework, including the availability of closed-form expressions for the subvolume local stiffness matrix elements, offers both theoretical and computational advantages vis-a-vis the finite element method in the solution of elastic boundary-value

problems without deterioration of point-wise equilibrium convergence characteristics with mesh refinement. Incorporation of parametric mapping in order to mimic complex geometries and microstructures, Cavalcante et al. (2007a,b), and elements of homogenization theory, Gattu et al. (2008), Khatam and Pindera (2009b), Cavalcante et al. (2011b), is accomplished in the next chapter, taking account geometric and material nonlinearities, producing a powerful tool for the analysis of a wide range of problems in homogeneous and heterogeneous solids, including bio-inspired materials, Khatam and Pindera (2012).

Chapter 4

Generalized FVDAM Theory for Periodic Materials Undergoing Finite Deformations - Framework

4.1. Introduction

The generalization of the finite-volume theory for plane elastic problems on rectangular domains proposed by Cavalcante and Pindera (2012a,b), and presented in the previous chapter, offers several advantages with respect to the original version constructed by Bansal and Pindera (2003) and Zhong et al. (2004) for the analysis of functionally graded materials. These advantages include substantially improved adjacent subvolume conformability and continuity of non-traction stress components across subvolume interfaces in the absence of material discontinuities, as well as smaller domain discretization for the same stress field accuracy. They are a direct result of a higher-order displacement field representation within individual subvolumes employed in the analysis domain discretization, which enables satisfaction of continuity of a set of

elasticity-motivated kinematic and static interfacial variables between adjacent subvolumes in a surface-averaged sense. This generalizes the original idea of satisfying interfacial displacement continuity in a surface-averaged sense proposed by Achenbach (1975) in the context of a micromechanics theory based on unit cell analysis. The surface-averaged kinematic variables are displacements, rotations and curvatures which provide the necessary basis for minimizing interfacial relative rotations and maximizing conformability. However, consistent with the original finite-volume theory, the generalization has been carried out on rectangular domains and hence employs rectangular subvolume discretization. This in turn limits the type of material or geometric features within the analysis domain that may be considered, such as internal cutouts, inclusions, or different material phases. Moreover, the generalized finite-volume theory has been constructed under the infinitesimal deformation constraint.

Given the demonstrated success of the generalized finite-volume theory for linear plane elasticity problems, in this chapter we further extend its theoretical framework in order to enable analysis of periodic materials with complex microstructures undergoing large deformations. This is accomplished by formulating the governing equations in the finite-deformation domain based on the Lagrangian description of material deformation within the 0th order homogenization theory, and incorporating parametric mapping to enable efficient modeling of microstructural details of a periodic material such as inclusions and porosities with curved boundaries, amongst others. Parametric mapping was first incorporated into the original finite-volume theory for functionally graded materials by Cavalcante et al. (2007a,b), and the enhanced theory applied to technologically important thermal barrier coating problems

on curved surfaces, Cavalcante et al. (2009,2011a). Following this successful implementation, Gattu et al. (2008), Khatam and Pindera (2009a,b) and Khatam et al. (2009) incorporated parametric mapping into the finite-volume direct averaging micromechanics (FVDAM) theory constructed by Bansal and Pindera (2005,2006), and used the enhanced version to solve several technologically important problems. Subsequently, Khatam and Pindera (2012) incorporated finite deformation features into the parametric FVDAM theory which they used to simulate the response of biological tissues using bio-inspired material architectures. This contribution leads to a generalized parametric FVDAM theory with finite-deformation capabilities which offers similar advantages relative to the version developed by Khatam and Pindera (2012) as those enumerated in the foregoing in the context of plane elastic problems in solid mechanics.

4.2. Lagrangian Framework

In the Lagrangian description of material deformation, the position $\boldsymbol{x}$ of a particle in the deformed configuration is given as a function of the particle's location in the undeformed configuration specified by the coordinates $\boldsymbol{X}$

$$\boldsymbol{x}(\boldsymbol{X}) = \boldsymbol{X} + \boldsymbol{u}(\boldsymbol{X}) \tag{4.1}$$

where $\boldsymbol{u}(\boldsymbol{X})$ is the displacement vector of the material particle at the point $\boldsymbol{X}$. The components of the deformation gradient tensor $\boldsymbol{F}$ are defined as

$$F_{ij} = \frac{\partial x_i}{\partial X_j} = \frac{\partial u_i}{\partial X_j} + \delta_{ij} = H_{ij} + \delta_{ij} \tag{4.2}$$

where $H_{ij} = \partial u_i / \partial X_i$ is the definition of the displacement gradient tensor.

The symmetric right Cauchy-Green deformation tensor $\boldsymbol{C}$ used in the construction of potential based constitutive equations for a hyperelastic solid is defined in terms of $\boldsymbol{F}$ as follows

$$\boldsymbol{C} = \boldsymbol{F}^T\boldsymbol{F} \tag{4.3}$$

while the Green-Lagrange strain tensor $\boldsymbol{E}$, that reduces correctly to the engineering or infinitesimal strain tensor, is evaluated in terms of the Cauchy-Green deformation tensor $\boldsymbol{C}$ by the following expression

$$\boldsymbol{E} = \frac{1}{2}(\boldsymbol{C} - \boldsymbol{I}) = \frac{1}{2}(\boldsymbol{F}^T\boldsymbol{F} - \boldsymbol{I}) \tag{4.4}$$

or in terms of partial derivatives of the displacement field (using indicial notation)

$$E_{ij} = \frac{1}{2}\left(\frac{\partial u_i}{\partial X_j} + \frac{\partial u_j}{\partial X_i} + \frac{\partial u_k}{\partial X_i}\frac{\partial u_k}{\partial X_j}\right) \tag{4.5}$$

Hence the symmetric second Piola-Kirchhoff stress tensor $\boldsymbol{S}$ is obtained in terms of the Green-Lagrange strain tensor $\boldsymbol{E}$ or the Cauchy-Green deformation tensor $\boldsymbol{C}$ through the potential-based constitutive relations

$$S_{ij} = \frac{\partial W}{\partial E_{ij}} = 2\frac{\partial W}{\partial C_{ij}} \tag{4.6}$$

where W is the chosen strain-energy density function which, for isotropic materials, may be represented in terms of three invariants of the right Cauchy-Green deformation tensor $\boldsymbol{C}$

$$W = W(I_1, I_2, I_3) \tag{4.7}$$

where $I_1 = tr\boldsymbol{C}$, $I_2 = 1/2\,(tr^2\boldsymbol{C} - tr\boldsymbol{C}^2)$ and $I_3 = det\boldsymbol{C}$. In the case of incompressible materials $I_3 = 1$.

Particularly, for linearly elastic materials, W is a quadratic function of the Green-Lagrange strain tensor $\boldsymbol{E}$

$$W = \frac{1}{2}\mathbb{C}_{ijkl}E_{ij}E_{kl} \tag{4.8}$$

Thus, the second Piola-Kirchhoff stress tensor becomes

$$S_{ij} = \frac{\partial W}{\partial E_{ij}} = \mathbb{C}_{ijkl}E_{kl} \tag{4.9}$$

where $\mathbb{C}_{ijkl}$ are the components of the linear stiffness tensor related to the isotropic material constants, Young's modulus E, Poisson's ratio ν and shear modulus μ, as follows

$$\mathbb{C}_{1111} = \frac{(1-\nu)E}{(1-2\nu)(1+\nu)},\ \ \mathbb{C}_{1122} = \frac{\nu E}{(1-2\nu)(1+\nu)},\ \ \mathbb{C}_{2323} = \mu = \frac{E}{2(1+\nu)} \tag{4.10}$$

In general, for nonlinear elastic materials, we can define the following symmetric tensor (tangential stiffness tensor of the material)

$$\mathbb{C}_{ijkl} = \frac{\partial W^2}{\partial E_{ij}\partial E_{kl}} = 4\frac{\partial W^2}{\partial C_{ij}\partial C_{kl}} \tag{4.11}$$

The second Piola-Kirchhoff stress tensor has been frequently used in developing numerical methods for large deformation problems because of its symmetry despite lack of direct physical interpretation. In solving the unit cell boundary value problem, however, it is more convenient to formulate the problem using the first Piola-Kirchhoff stress tensor $\boldsymbol{T}$ in terms of which the equilibrium equations assume a simple form in the Lagrangian description,

$$\frac{\partial T_{1i}}{\partial X_1} + \frac{\partial T_{2i}}{\partial X_2} + \frac{\partial T_{3i}}{\partial X_3} = 0,\ \ i = 1,2,3 \tag{4.12}$$

where $\boldsymbol{T}$ is related to $\boldsymbol{S}$ as follows

$$\boldsymbol{T} = \boldsymbol{S}\boldsymbol{F}^T \tag{4.13}$$

The first Piola-Kirchhoff stress tensor is unsymmetric and sometimes called engineering or nominal stress in literature. It is related to the symmetric true or Cauchy stress

tensor $\boldsymbol{\sigma}$ defined with respect to the deformed configuration by $\boldsymbol{T} = J\boldsymbol{F}^{-1}\boldsymbol{\sigma}$, where J is the determinant of the deformation gradient tensor $\boldsymbol{F}$. Correspondingly simple equilibrium equations hold for the Cauchy stress tensor, albeit in terms of coordinates $\boldsymbol{x}$ in the deformed configuration using the Eulerian description not pursued herein.

The unit cell boundary value problem whose solution produces homogenized Hooke's law for a periodic multiphase material can be formulated using either the secant or tangential (incremental) formulation. The latter leads to a nonlinear system of equations which require iterative solution techniques such as Newton-Raphson, while the former provides a simpler framework at the expense of a computationally intensive solution procedure of the governing system of equations. Herein, the unit cell solution procedure is carried out using the tangential formulation. Hence an incremental form of the local (phase) material constitutive relations between the first Piola-Kirchhoff stress tensor and the deformation gradient tensor increments, $\Delta\boldsymbol{T}$ and $\Delta\boldsymbol{F}$, respectively, is employed in the solution of the unit cell boundary-value problem, Aboudi and Pindera (2004),

$$\Delta\boldsymbol{T} = \boldsymbol{R}\Delta\boldsymbol{F} \tag{4.14}$$

where $R_{ijkl} = \mathbb{C}_{imnl}F_{jm}F_{kn} + S_{il}\delta_{jk}$. The above incremental constitutive equation is obtained using the incremental form of Equation (4.6), $\Delta S_{ij} = \mathbb{C}_{ijkl}\Delta E_{kl}$, with the relationship between $\Delta\boldsymbol{E}$ and $\Delta\boldsymbol{F}$ obtained from Equation (4.4), leading to $\Delta S_{im} = \mathbb{C}_{imnl}F_{kn}\Delta F_{kl}$, which is then expressed in terms of $\Delta\boldsymbol{T}$ upon use of the incremental form of Equation (4.13). The form of the tangent stiffness matrix $\boldsymbol{R}$ depends on the particular potential-based constitutive equation for the local phase, Equation (4.7).

4.3. Unit Cell Boundary-Value Problem

The response of a periodic material subjected to macroscopically uniform deformation gradient is obtained by analyzing the response of a single unit cell under equivalent loading. Towards this end, two coordinate systems $\boldsymbol{X}$ and $\boldsymbol{Y}$ are introduced which describe global or macroscopic response of the entire array, and local or fluctuating response associated with the unit cell, respectively, Figure 4.1. As a first step, the microstructure of the unit cell is discretized into quadrilateral subvolumes, designated by (q), whose locations are specified by vertices referred to a fixed coordinate system. The *qth* quadrilateral subvolume is generated by mapping the reference subvolume in the $\eta - \xi$ plane bounded by $-1 \leq \eta \leq +1$ and $-1 \leq \xi \leq +1$, Figure 4.2, using the transformation,

$$Y_i^{(q)}(\eta, \xi) = \sum_{p=1}^{4} N_p\,(\eta, \xi) Y_i^{(p,q)}, \quad i = 2,3 \tag{4.15}$$

first introduced by Cavalcante et al. (2007a) into the structural version of the finite-volume theory of Bansal and Pindera (2003). The vertices $Y_i^{(p,q)}$ correspond to the vertices of the reference subvolume, and $N_p(\eta, \xi)$ are given by

$$\begin{aligned} N_1(\eta, \xi) &= \frac{1}{4}(1-\eta)(1-\xi), \quad N_2(\eta, \xi) = \frac{1}{4}(1+\eta)(1-\xi), \\ N_3(\eta, \xi) &= \frac{1}{4}(1+\eta)(1+\xi), \quad N_4(\eta, \xi) = \frac{1}{4}(1-\eta)(1+\xi). \end{aligned} \tag{4.16}$$

This is the same mapping as that employed for the Q4 element which ensures that the sides of the mapped element remain straight.

Following the 0th-order asymptotic homogenization theory framework, cf. Bensoussan et al. (1978), Sanchez-Palancia (1980), the displacement field increment in the *qth*

subvolume is represented by the two-scale expansion involving macroscopic and fluctuating components

$$\Delta u_i^{(q)}\big(\boldsymbol{X}, \boldsymbol{Y}(\eta,\xi)\big) = \Delta \bar{F}_{ij} X_j + \Delta u_i'^{(q)}(\eta,\xi) \tag{4.17}$$

where the fluctuating components induced by the microstructure are given by,

$$\begin{aligned}
\Delta u_1'^{(q)} &= \Delta W_{1(00)}^{(q)} + \eta \Delta W_{1(10)}^{(q)} + \xi \Delta W_{1(01)}^{(q)} + \frac{1}{2}(3\eta^2 - 1)\Delta W_{1(20)}^{(q)} \\
&\quad + \frac{1}{2}(3\xi^2 - 1)\Delta W_{1(02)}^{(q)} \\
\Delta u_i'^{(q)} &= \Delta W_{i(00)}^{(q)} + \eta \Delta W_{i(10)}^{(q)} + \xi \Delta W_{i(01)}^{(q)} + \eta\xi \Delta W_{i(11)}^{(q)} + \frac{1}{2}(3\eta^2 - 1)\Delta W_{i(20)}^{(q)} \\
&\quad + \frac{1}{2}(3\xi^2 - 1)\Delta W_{i(02)}^{(q)} + \frac{1}{2}(3\eta^2 - 1)\xi \Delta W_{i(21)}^{(q)} \\
&\quad + \frac{1}{2}(3\xi^2 - 1)\eta \Delta W_{i(12)}^{(q)} + \frac{1}{4}(3\eta^2 - 1)(3\xi^2 - 1)\Delta W_{i(22)}^{(q)}
\end{aligned} \tag{4.18}$$

where $i = 2, 3$ in the second equation and $\Delta W_{i(mn)}^{(q)}$ are unknown coefficients.

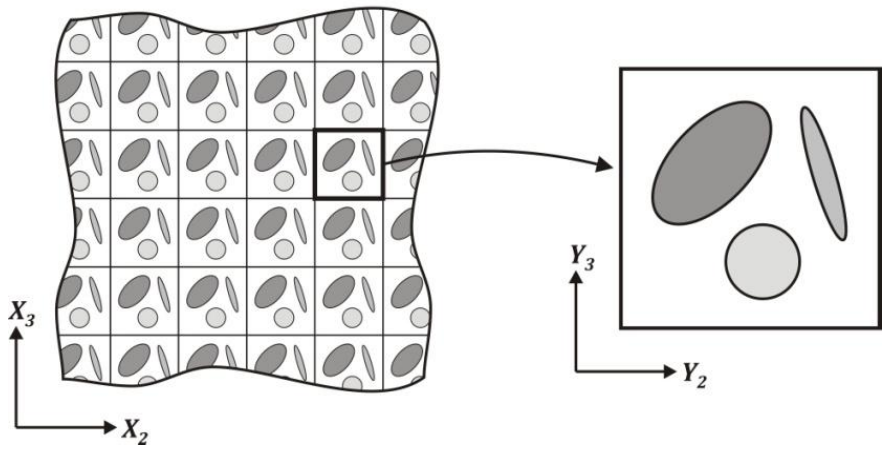

Figure 4.1. Material with periodic microstructure characterized by a repeating unit cell (RUC).

The chosen displacement field increment which reflects continuous reinforcement along Y_1 direction is characterized by the total of 18 unknown coefficients that describe the local displacement field increment in the $Y_2 - Y_3$ plane, and 5 unknown coefficients that describe the displacement field increment and the corresponding axial shear response in the $Y_1 - Y_2$ and $Y_1 - Y_3$ planes. This is in contrast with 15 coefficients employed in the

original FVDAM theory based on the incomplete second-order polynomial given in the first of the above equations. The 23 unknown coefficients $\Delta W_{i(mn)}^{(q)}$ are expressed solely in terms of surface-averaged kinematic variables upon satisfaction of the equilibrium equations of each subvolume in a surface-averaged sense following the standard finite-volume method practice. These kinematic variables, which are required to be continuous across common subvolume faces, are increments of surface-averaged fluctuating displacements used in the standard theory and newly defined increments of surface-averaged fluctuating rotations and curvatures. Figure 4.3 illustrates these quantities associated with each face of the *qth* subvolume, with the face numbering convention progressing counterclockwise. The imposition of interfacial continuity requirement for these three sets of quantities mitigates the interfacial interpenetration issue intrinsic to incomplete or complete second-order displacement field representation employed in the standard FVDAM theory.

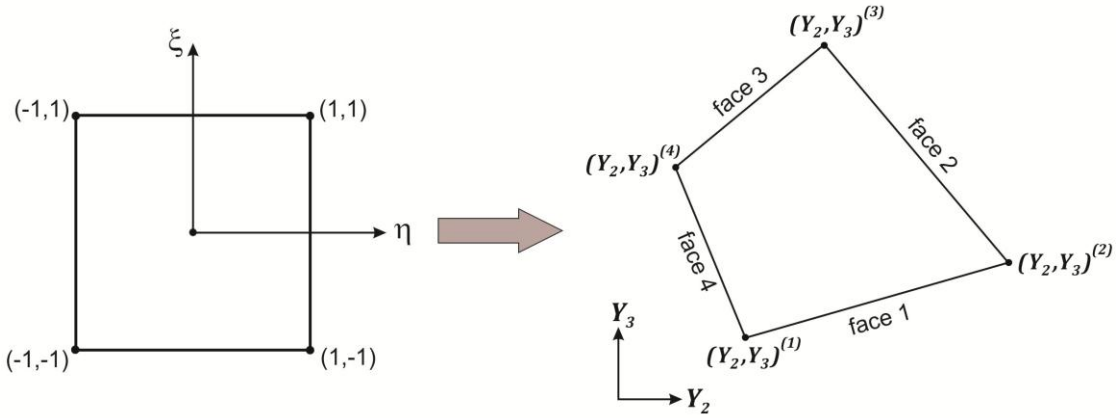

Figure 4.2. Mapping of the reference square subvolume in the $\eta - \xi$ coordinate system onto the corresponding quadrilateral subvolume in the actual microstructure defined in the $Y_2 - Y_3$ coordinate system.

Definition of corresponding surface-averaged static variables motivated by subvolume interfacial traction continuity considerations makes possible the construction of

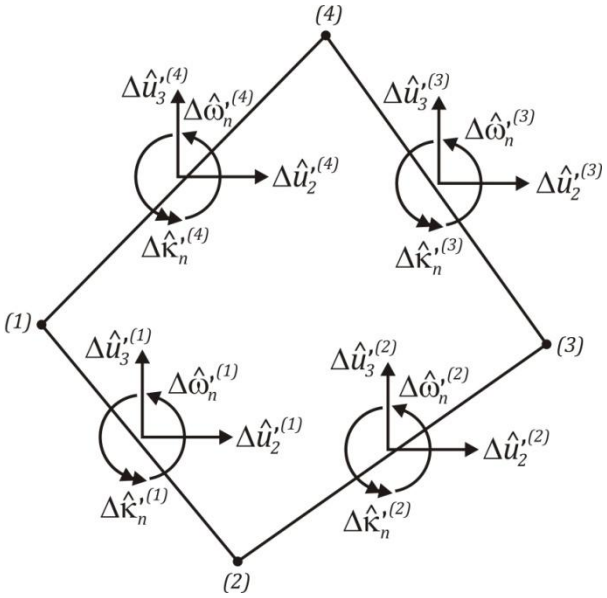

Figure 4.3. Surface-averaged kinematic variables on the four faces of (q) subvolume.

generalized stiffness matrix relations that govern the response of individual subvolumes. Assembly of the local stiffness matrix relations in a manner that ensures continuity of static and kinematic surface-averaged variables produces a global system of equations for the unknown surface-averaged kinematic variables whose solution at each macroscopic deformation gradient increment establishes the localization relations for the *qth* subvolume, Hill (1963),

$$\Delta \boldsymbol{F}^{(q)} = \mathbb{A}^{(q)} \Delta \overline{\boldsymbol{F}} \tag{4.19}$$

where $\mathbb{A}^{(q)}$ is the elastic deformation gradient concentration tensor calculated at each point along the loading path for the specified macroscopic increment $\Delta\overline{\boldsymbol{F}}$. Using these relations in the definition for the volume-averaged first Piola-Kirchhoff stress increment expressed in terms of corresponding subdomain stress increments,

$$\Delta \overline{\boldsymbol{T}} = \frac{1}{V}\int_V \Delta \boldsymbol{T}(\boldsymbol{X}) dV = \frac{1}{V}\sum_{q=1}^{N_q}\int_{V_q} \Delta \boldsymbol{T}^{(q)}(\boldsymbol{X}) dV_q = \sum_{q=1}^{N_q} c_{(q)} \Delta \overline{\boldsymbol{T}}^{(q)} \tag{4.20}$$

and hence deformation gradient increments through the local constitutive equations, the

homogenized Hooke's law for the periodic array represented by the unit cell is constructed in the form,

$$\Delta\overline{\boldsymbol{T}} = \boldsymbol{R}^{*}\Delta\overline{\boldsymbol{F}} \tag{4.21}$$

where the homogenized tangent stiffness matrix $\boldsymbol{R}^{*}$ is given by,

$$\boldsymbol{R}^{*} = \frac{1}{V}\sum_{q=1}^{N_q}\int_{V_q}\boldsymbol{R}^{(q)}\mathbb{A}^{(q)}dV_q = \sum_{q=1}^{N_q} c_{(q)}\,\overline{[\boldsymbol{R}^{(q)}\mathbb{A}^{(q)}]} \tag{4.22}$$

and $c_{(q)}$ is the volume fraction of the *qth* subvolume.

4.3.1. Kinematic Variables

Following the standard FVDAM theory, we first define increments of surface-averaged fluctuating displacements on each face of the reference subvolume, and then perform the integration to obtain these in terms of the unknown 0th, 1st and 2nd order coefficients $\Delta W_{i(mn)}^{(q)}$. This yields,

$$\begin{aligned}
\Delta\hat{u}_i^{\prime(1,3)} &= \frac{1}{2}\int_{-1}^{+1}\Delta u_i'(\eta,\mp 1)d\eta = \Delta W_{i(00)} \mp \Delta W_{i(01)} + \Delta W_{i(02)} \\
\Delta\hat{u}_i^{\prime(2,4)} &= \frac{1}{2}\int_{-1}^{+1}\Delta u_i'(\pm 1,\xi)d\xi = \Delta W_{i(00)} \pm \Delta W_{i(10)} + \Delta W_{i(20)}
\end{aligned} \tag{4.23}$$

where the superscripts $(p = 1, 2, 3\ or\ 4)$ indicate subvolume face number, noting that the superscripts (q) which identify a given subvolume have been omitted for clarity. Next, we employ increments of fluctuating displacement components normal to an inclined face (p) of the *qth* subvolume with the unit normal vectors $\boldsymbol{n}^{(p)} = (0, n_2, n_3)^{(p)}$

$$\begin{aligned}
\Delta u_n^{\prime(1,3)}(\eta,\mp 1) &= n_2^{(1,3)}\Delta u_2'(\eta,\mp 1) + n_3^{(1,3)}\Delta u_3'(\eta,\mp 1) \\
\Delta u_n^{\prime(2,4)}(\pm 1,\xi) &= n_2^{(2,4)}\Delta u_2'(\pm 1,\xi) + n_3^{(2,4)}\Delta u_3'(\pm 1,\xi)
\end{aligned} \tag{4.24}$$

to define increments of normal surface-averaged fluctuating rotation components, following Cavalcante and Pindera (2012a), which are obtained in terms of the 1st, 2nd and 3rd order coefficients $\Delta W_{i(mn)}^{(q)}$,

$$\begin{aligned}\Delta\widehat{\omega}_n'^{(1,3)} &= \mp\frac{1}{2}\int_{-1}^{+1}\frac{\partial\Delta u_n'^{(1,3)}(\eta,\mp1)}{\partial\eta}d\eta \\ &= \mp\Big[n_2^{(1,3)}\big(\Delta W_{2(10)}\mp\Delta W_{2(11)}+\Delta W_{2(12)}\big) \\ &+ n_3^{(1,3)}\big(\Delta W_{3(10)}\mp\Delta W_{3(11)}+\Delta W_{3(12)}\big)\Big] \\ \Delta\widehat{\omega}_n'^{(2,4)} &= \mp\frac{1}{2}\int_{-1}^{+1}\frac{\partial\Delta u_n'^{(2,4)}(\pm1,\xi)}{\partial\xi}d\xi \\ &= \mp\Big[n_2^{(2,4)}\big(\Delta W_{2(01)}\pm\Delta W_{2(11)}+\Delta W_{2(21)}\big) \\ &+ n_3^{(2,4)}\big(\Delta W_{3(01)}\pm\Delta W_{3(11)}+\Delta W_{3(21)}\big)\Big]\end{aligned} \tag{4.25}$$

and finally increments of normal surface-averaged fluctuating curvature components obtained in terms of the 2nd, 3rd and 4th order coefficients $\Delta W_{i(mn)}^{(q)}$,

$$\begin{aligned}\Delta\hat{\kappa}_n'^{(1,3)} &= \mp\frac{1}{2}\int_{-1}^{+1}\frac{\partial^2\Delta u_n'^{(1,3)}(\eta,\mp1)}{\partial\eta^2}d\eta \\ &= \mp3\Big[n_2^{(1,3)}\big(\Delta W_{2(20)}\mp\Delta W_{2(21)}+\Delta W_{2(22)}\big) \\ &+ n_3^{(1,3)}\big(\Delta W_{3(20)}\mp\Delta W_{3(21)}+\Delta W_{3(22)}\big)\Big] \\ \Delta\hat{\kappa}_n'^{(2,4)} &= \mp\frac{1}{2}\int_{-1}^{+1}\frac{\partial^2\Delta u_n'^{(2,4)}(\pm1,\xi)}{\partial\xi^2}d\xi \\ &= \mp3\Big[n_2^{(2,4)}\big(\Delta W_{2(02)}\pm\Delta W_{2(12)}+\Delta W_{2(22)}\big) \\ &+ n_3^{(2,4)}\big(\Delta W_{3(02)}\pm\Delta W_{3(12)}+\Delta W_{3(22)}\big)\Big]\end{aligned} \tag{4.26}$$

We note that the expressions for surface-averaged fluctuating displacement increments are the same as those based on the incomplete second-order fluctuating displacement increment representation, leading to the same relations between the unknown 1st and 2nd

order coefficients and surface-averaged fluctuating displacement increments and 0th order coefficients. Defining the vector of the unknown 1st and 2nd order coefficients $\Delta W_{i(mn)}^{(q)}$

$$\Delta \boldsymbol{W}_i^{(q)} = \left[\Delta W_{i(10)}, \Delta W_{i(01)}, \Delta W_{i(20)}, \Delta W_{i(02)}\right]^{(q)T} \tag{4.27}$$

these coefficients are obtained in terms of the surface-averaged fluctuating displacement increments

$$\Delta \widehat{\boldsymbol{u}}_i'^{(q)} = \left[\Delta \hat{u}_i'^{(1)}, \Delta \hat{u}_i'^{(2)}, \Delta \hat{u}_i'^{(3)}, \Delta \hat{u}_i'^{(4)}\right]^{(q)T} \tag{4.28}$$

and the 0th order coefficient in the form

$$\Delta \boldsymbol{W}_i^{(q)} = \boldsymbol{A} \Delta \widehat{\boldsymbol{u}}_i'^{(q)} - \boldsymbol{a} \Delta W_{i(00)}^{(q)} \tag{4.29}$$

where the matrix $\boldsymbol{A}$ and vector $\boldsymbol{a}$ are given in the Appendix C, and the above relations hold in all the planes (i.e., for $i = 1, 2, 3$).

Similarly, the expressions for increments of surface-averaged fluctuating rotations and curvatures in the $Y_2 - Y_3$ plane lead to coupled relations amongst the remaining unknown 2nd, 3rd and 4th order coefficients. These relations may be expressed compactly upon defining the following vector quantities in this plane (for $i = 2, 3$)

$$\Delta \overline{\boldsymbol{W}}_i^{(q)} = \left[\Delta W_{i(11)}, \Delta W_{i(21)}, \Delta W_{i(12)}, \Delta W_{i(22)}\right]^{(q)T} \tag{4.30}$$

$$\Delta \widehat{\boldsymbol{\omega}}_n'^{(q)} = \left[\Delta \hat{\omega}_n'^{(1)}, \Delta \hat{\omega}_n'^{(2)}, \Delta \hat{\omega}_n'^{(3)}, \Delta \hat{\omega}_n'^{(4)}\right]^{(q)T} \tag{4.31}$$

$$\Delta \widehat{\boldsymbol{\kappa}}_n'^{(q)} = \left[\Delta \hat{\kappa}_n'^{(1)}, \Delta \hat{\kappa}_n'^{(2)}, \Delta \hat{\kappa}_n'^{(3)}, \Delta \hat{\kappa}_n'^{(4)}\right]^{(q)T} \tag{4.32}$$

to obtain the following expressions for $\Delta \overline{\boldsymbol{W}}_i^{(q)}$ in terms of $\Delta \boldsymbol{W}_i^{(q)}$, $\Delta \widehat{\boldsymbol{\omega}}_n'^{(q)}$ and $\Delta \widehat{\boldsymbol{\kappa}}_n'^{(q)}$

$$\begin{bmatrix} \Delta \overline{\boldsymbol{W}}_2^{(q)} \\ \Delta \overline{\boldsymbol{W}}_3^{(q)} \end{bmatrix} = \overline{\boldsymbol{Q}}^{(q)} \begin{bmatrix} \Delta \widehat{\boldsymbol{\omega}}_n'^{(q)} \\ \Delta \widehat{\boldsymbol{\kappa}}_n'^{(q)} \end{bmatrix} - \boldsymbol{Q}_2^{(q)} \Delta \boldsymbol{W}_2^{(q)} - \boldsymbol{Q}_3^{(q)} \Delta \boldsymbol{W}_3^{(q)} \tag{4.33}$$

where the matrices $\overline{\boldsymbol{Q}}^{(q)}$, $\boldsymbol{Q}_2^{(q)}$ and $\boldsymbol{Q}_3^{(q)}$ given in the Appendix C involve unit normal

components to the four faces of quadrilateral subvolumes in the actual microstructure. Hence the twenty 1st, 2nd, 3rd and 4th order coefficients $\Delta W_{i(mn)}^{(q)}$ that define the fluctuating displacement field increment of the *qth* subvolume are expressed in terms of the twenty surface-averaged kinematic variables $\Delta\widehat{\boldsymbol{u}}_i'^{(q)}$, $\Delta\widehat{\boldsymbol{\omega}}_n'^{(q)}$, $\Delta\widehat{\boldsymbol{\kappa}}_n'^{(q)}$ and three 0th order coefficients $\Delta W_{i(00)}^{(q)}$. These remaining coefficients are obtained in terms of surface-averaged kinematic variables upon satisfaction of equilibrium equations in a surface-average sense. Relating these surface-averaged kinematic variables to appropriately defined static variables enables construction of the generalized local stiffness matrix based on the higher-order fluctuating displacement field increment employed herein that will be described in the sequel.

Unlike the generalized finite-volume theory constructed by Cavalcante and Pindera (2012a,b), and presented in the previous chapter, for the solution of linearly elastic plane problems on rectangular domains, the generalized FVDAM theory couples rotational and curvature effects due to parametric mapping. Hence, a local stiffness matrix involving exclusively surface-averaged fluctuating displacement and rotation increments cannot be developed without additional assumptions. Herein, for completeness, we introduce one such assumption which decouples rotational and curvature effects, and makes possible construction of a local stiffness matrix for a 1st order FVDAM theory. Specifically, the assumption is chosen such that the ensuing local stiffness matrix reduces correctly to that of the 1st order theory on rectangular domains. Namely, we propose the following relations which reduce the number of unknown coefficients through the following coupled relations defined in terms of the common coefficients $\Delta W_{(12)}^{*}$ and $\Delta W_{(21)}^{*}$

$$\Delta W_{i(21)} = d_{i(21)}\Delta W^{*}_{(21)}, \quad \Delta W_{i(12)} = d_{i(12)}\Delta W^{*}_{(12)} \tag{4.34}$$

for $i = 2, 3$, where

$$d_{i(21)} = \left(n_i^{(2)} - n_i^{(4)}\right)/2, \quad d_{i(12)} = \left(n_i^{(3)} - n_i^{(1)}\right)/2 \tag{4.35}$$

For a rectangular subvolume in the correspondingly oriented Cartesian coordinate system, $n_2^{(1,3)} = 0$, $n_2^{(2,4)} = \pm 1$, $n_3^{(1,3)} = \mp 1$ and $n_3^{(2,4)} = 0$, and thus the above relations reduce to

$$d_{2(21)} = d_{3(12)} = 1, \quad d_{2(12)} = d_{3(21)} = 0 \tag{4.36}$$

Therefore, we obtain the following relations for the higher-order coefficients

$$\Delta W_{2(21)} = \Delta W^{*}_{(21)}, \quad \Delta W_{3(12)} = \Delta W^{*}_{(12)}, \quad \Delta W_{2(12)} = \Delta W_{3(21)} = 0 \tag{4.37}$$

which leads to the following expressions for the surface-averaged fluctuating rotational increments,

$$\begin{aligned} \Delta\widehat{\omega}_n^{\prime(1,3)} &= \Delta W_{3(10)} \mp \Delta W_{3(11)} + \Delta W^{*}_{(12)} \\ \Delta\widehat{\omega}_n^{\prime(2,4)} &= -\Delta W_{2(01)} \mp \Delta W_{2(11)} - \Delta W^{*}_{(21)} \end{aligned} \tag{4.38}$$

similar to those obtained in the previous chapter for rectangular subvolumes.

Using the above assumptions, we obtain the expressions below for $\Delta\overline{\boldsymbol{W}}_i^{(q)}$ solely in terms of $\Delta\boldsymbol{W}_i^{(q)}$ and $\Delta\widehat{\boldsymbol{\omega}}_n^{\prime(q)}$

$$\begin{bmatrix} \Delta\overline{\boldsymbol{W}}_2^{(q)} \\ \Delta\overline{\boldsymbol{W}}_3^{(q)} \end{bmatrix} = \overline{\mathbb{Q}}^{(q)}\Delta\widehat{\boldsymbol{\omega}}_n^{\prime(q)} - \mathbb{Q}_2^{(q)}\Delta\boldsymbol{W}_2^{(q)} - \mathbb{Q}_3^{(q)}\Delta\boldsymbol{W}_3^{(q)} \tag{4.39}$$

where the matrices $\overline{\mathbb{Q}}^{(q)}$, $\mathbb{Q}_2^{(q)}$ and $\mathbb{Q}_3^{(q)}$ are also given in the Appendix C and involve unit normal components to the four faces of quadrilateral subvolumes in the actual microstructure.

4.3.2. Static Variables

Following the standard FVDAM theory, we first define increments of surface-averaged traction components on each of the four subvolume faces,

$$\Delta\hat{t}_i^{(1,3)} = \frac{1}{2}\int_{-1}^{+1} \Delta t_i(\eta, \mp 1)d\eta, \quad \Delta\hat{t}_i^{(2,4)} = \frac{1}{2}\int_{-1}^{+1} \Delta t_i(\pm 1, \xi)d\xi \tag{4.40}$$

which are related to stresses through the Cauchy's relations given in terms of the first Piola-Kirchhoff stress increments $\Delta t_i^{(p)} = \Delta T_{ji}^{(p)} n_j^{(p)}$. The superscript p denotes the face number and $n_j^{(p)}$ are the corresponding unit normal components. Within the standard theoretical framework, we satisfy interfacial traction continuity in a surface-average sense. Hence, given the higher-order fluctuating displacement increment representation, we also require interfacial continuity of the appropriate 1st and 2nd derivatives of increments of traction components to be satisfied in a surface-average sense as discussed in the previous chapter. Because of the chosen incremental fluctuating displacement field representation, only the continuity of surface-averaged derivatives of normal increments of traction components is enforced. Thus, we employ increments of traction components normal to an inclined face of the *qth* subvolume,

$$\begin{aligned} \Delta t_n^{(1,3)}(\eta, \mp 1) &= n_2^{(1,3)}\Delta t_2(\eta, \mp 1) + n_3^{(1,3)}\Delta t_3(\eta, \mp 1) \\ \Delta t_n^{(2,4)}(\pm 1, \xi) &= n_2^{(2,4)}\Delta t_2(\pm 1, \xi) + n_3^{(2,4)}\Delta t_3(\pm 1, \xi) \end{aligned} \tag{4.41}$$

to define surface-averaged derivatives of these components acting on each face of the *qth* subvolume, Figure 4.4, following Cavalcante and Pindera (2012a),

$$\begin{aligned} \Delta\hat{t}_{n/\eta}^{(1,3)} &= \mp\frac{1}{2}\int_{-1}^{+1} \frac{\partial \Delta t_n^{(1,3)}(\eta, \mp 1)}{\partial \eta} d\eta, \quad \Delta\hat{t}_{n/\xi}^{(2,4)} = \mp\frac{1}{2}\int_{-1}^{+1} \frac{\partial \Delta t_n^{(2,4)}(\pm 1, \xi)}{\partial \xi} d\xi \\ \Delta\hat{t}_{n/\eta\eta}^{(1,3)} &= \mp\frac{1}{2}\int_{-1}^{+1} \frac{\partial^2 \Delta t_n^{(1,3)}(\eta, \mp 1)}{\partial \eta^2} d\eta, \quad \Delta\hat{t}_{n/\xi\xi}^{(2,4)} = \mp\frac{1}{2}\int_{-1}^{+1} \frac{\partial^2 \Delta t_n^{(2,4)}(\pm 1, \xi)}{\partial \xi^2} d\xi \end{aligned} \tag{4.42}$$

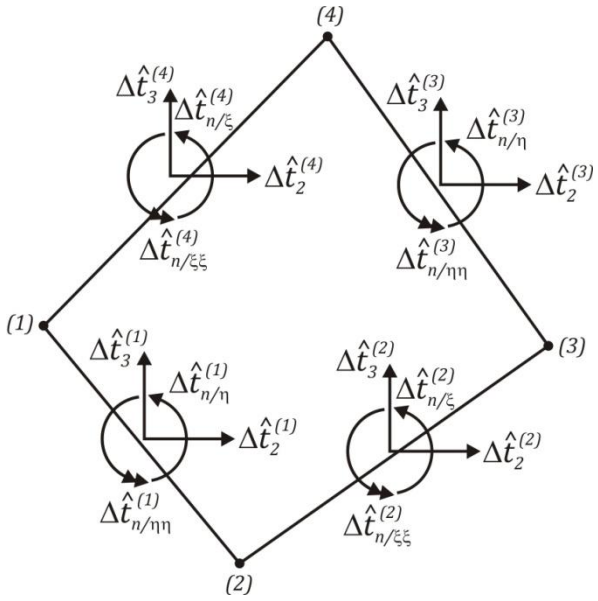

Figure 4.4. Surface-averaged static variables on the four faces of (q) subvolume.

The above-defined surface-averaged increments of tractions and derivatives of normal traction increments are then expressed in terms of the unknown coefficients appearing in the fluctuating displacement field increment representation using the tangential form of the local constitutive equations

$$\Delta \boldsymbol{T}^{(q)} = \boldsymbol{R}^{(q)} \Delta \boldsymbol{F}^{(q)} \tag{4.43}$$

where

$$\Delta F_{ij}^{(q)} = \Delta \bar{F}_{ij} + \frac{\partial \Delta u_i'^{(q)}}{\partial Y_j} \tag{4.44}$$

Given the different representations of the incremental fluctuating displacement components in the three planes in Equation (4.18), the displacement gradient tensor increments in the $Y_1 - Y_2$ and $Y_1 - Y_3$ planes are obtained in the following form ($i = 1$)

$$\begin{bmatrix} \dfrac{\partial \Delta u_1'^{(q)}}{\partial Y_2} \\ \dfrac{\partial \Delta u_1'^{(q)}}{\partial Y_3} \end{bmatrix} = \boldsymbol{J}^{-1}(\eta, \xi) \begin{bmatrix} \dfrac{\partial \Delta u_1'^{(q)}}{\partial \eta} \\ \dfrac{\partial \Delta u_1'^{(q)}}{\partial \xi} \end{bmatrix} = \boldsymbol{B}(\eta, \xi) \Delta \boldsymbol{W}_1^{(q)} \tag{4.45}$$

where, in light of the employed parametric mapping transformation, the Jacobian $\boldsymbol{J}$ is a linear function of the (η, ξ) coordinates, and

$$\boldsymbol{B}(\eta,\xi) = \boldsymbol{J}^{-1}(\eta,\xi)\begin{bmatrix} 1 & 0 & 3\eta & 0 \\ 0 & 1 & 0 & 3\xi \end{bmatrix} \tag{4.46}$$

In contrast, the displacement gradient tensor increments in the $Y_2 - Y_3$ plane contain higher-order coefficients as follows $(i = 2, 3)$

$$\begin{bmatrix} \dfrac{\partial \Delta u_i'^{(q)}}{\partial Y_2} \\ \dfrac{\partial \Delta u_i'^{(q)}}{\partial Y_3} \end{bmatrix} = \boldsymbol{J}^{-1}(\eta,\xi)\begin{bmatrix} \dfrac{\partial \Delta u_i'^{(q)}}{\partial \eta} \\ \dfrac{\partial \Delta u_i'^{(q)}}{\partial \xi} \end{bmatrix} = \boldsymbol{B}(\eta,\xi)\Delta \boldsymbol{W}_i^{(q)} + \overline{\boldsymbol{B}}(\eta,\xi)\Delta \overline{\boldsymbol{W}}_i^{(q)} \tag{4.47}$$

where

$$\overline{\boldsymbol{B}}(\eta,\xi) = \boldsymbol{J}^{-1}(\eta,\xi)\begin{bmatrix} \xi & 3\eta\xi & (3\xi^2-1)/2 & 3/2\,(3\xi^2-1)\eta \\ \eta & (3\eta^2-1)/2 & 3\eta\xi & 3/2\,(3\eta^2-1)\xi \end{bmatrix} \tag{4.48}$$

Use of the chosen displacement field increment in the deformation gradient tensor increment relations, which are then used to express incremental stress components in terms of the unknown coefficients $\Delta W_{i(mn)}^{(q)}$, yields the following expressions for the surface-averaged static variables, starting with surface-averaged increments of tractions,

$$\Delta \hat{\boldsymbol{t}}^{(p,q)} = \widehat{\boldsymbol{R}}_0^{(p,q)}\Delta \overline{\boldsymbol{F}} + \widehat{\boldsymbol{Y}}_0^{(p,q)}\Delta \boldsymbol{W}^{(q)} + \widehat{\boldsymbol{Z}}_0^{(p,q)}\Delta \overline{\boldsymbol{W}}^{(q)} \tag{4.49}$$

where

$$\Delta \boldsymbol{W}^{(q)} = \left[\Delta \boldsymbol{W}_1^{(q)T}, \Delta \boldsymbol{W}_2^{(q)T}, \Delta \boldsymbol{W}_3^{(q)T}\right]^T \tag{4.50}$$

$$\Delta \overline{\boldsymbol{W}}^{(q)} = \left[\Delta \overline{\boldsymbol{W}}_2^{(q)T}, \Delta \overline{\boldsymbol{W}}_3^{(q)T}\right]^T \tag{4.51}$$

Next, we obtain increments of surface-averaged first derivatives of normal traction components

$$\Delta \hat{t}_{n/i}^{(p,q)} = \widehat{\boldsymbol{R}}_1^{(p,q)}\Delta \overline{\boldsymbol{F}} + \widehat{\boldsymbol{Y}}_1^{(p,q)}\Delta \boldsymbol{W}^{(q)} + \widehat{\boldsymbol{Z}}_1^{(p,q)}\Delta \overline{\boldsymbol{W}}^{(q)} \tag{4.52}$$

and finally the increments of surface-averaged second derivatives of normal traction components

$$\Delta\hat{t}_{n/ii}^{(p,q)} = \widehat{\boldsymbol{R}}_2^{(p,q)}\Delta\overline{\boldsymbol{F}} + \widehat{\boldsymbol{Y}}_2^{(p,q)}\Delta\boldsymbol{W}^{(q)} + \widehat{\boldsymbol{Z}}_2^{(p,q)}\Delta\overline{\boldsymbol{W}}^{(q)} \tag{4.53}$$

where for $p = 1{,}3 \rightarrow n/i = n/\eta\,, n/ii = n/\eta\eta$ and $p = 2{,}4 \rightarrow n/i = n/\xi\,, n/ii = n/\xi\xi$. In the above equations, $\widehat{\boldsymbol{R}}_i^{(p,q)}$, $\widehat{\boldsymbol{Y}}_i^{(p,q)}$ and $\widehat{\boldsymbol{Z}}_i^{(p,q)}$ $(i = 0, 1, 2)$ are numerically evaluated and defined in Appendix D.

The surface-averaged static variables are then expressed in terms of the surface-averaged kinematic variables and the remaining three 0th order coefficients $\Delta W_{i(00)}^{(q)}$ determined next.

4.3.3. Surface-Averaging of Equilibrium Equations

In the absence of body forces, the equilibrium equations that must be satisfied in the volumetric or surface-averaged sense for each subvolume are,

$$\int_{S_q} \Delta T_{ji} n_j dS = \int_{S_q} \Delta t_i dS = \sum_{p=1}^{4} \int_{L_p} \Delta t_i^{(p)} dL_p = \sum_{p=1}^{4} L_p\, \Delta\hat{t}_i^{(p)} = 0 \tag{4.54}$$

Substituting for the surface-averaged increments of tractions given in terms of the coefficients $\Delta W_{i(mn)}^{(q)}$ and the applied deformation gradient increment $\Delta\overline{\boldsymbol{F}}$, we obtain

$$\widehat{\mathbb{R}}_0^{(q)}\Delta\overline{\boldsymbol{F}} + \widehat{\mathbb{Y}}_0^{(q)}\Delta\boldsymbol{W}^{(q)} + \widehat{\mathbb{Z}}_0^{(q)}\Delta\overline{\boldsymbol{W}}^{(q)} = \boldsymbol{0} \tag{4.55}$$

where

$$\widehat{\mathbb{R}}_0^{(q)} = \sum_{p=1}^{4} L_p\, \widehat{\boldsymbol{R}}_0^{(p,q)}, \quad \widehat{\mathbb{Y}}_0^{(q)} = \sum_{p=1}^{4} L_p\, \widehat{\boldsymbol{Y}}_0^{(p,q)}, \quad \widehat{\mathbb{Z}}_0^{(q)} = \sum_{p=1}^{4} L_p\, \widehat{\boldsymbol{Z}}_0^{(p,q)} \tag{4.56}$$

Substituting for $\Delta \boldsymbol{W}^{(q)}$ and $\Delta \overline{\boldsymbol{W}}^{(q)}$ using equations (4.29), (4.33) or (4.39), we obtain expressions for the 0th order coefficients $\Delta W_{i(00)}^{(q)}$ in terms of the surface-averaged kinematic variables and the applied deformation gradient increment $\Delta \overline{\boldsymbol{F}}$.

4.3.4. Local Stiffness Matrices

The developed framework enables systematic construction of local stiffness matrices of increasing order, each of which corresponds to a finite-volume direct averaging micromechanics (FVDAM) theory of the particular order. The local stiffness matrices relate the surface-averaged static variables to the surface-averaged kinematic ones.

0th Order FVDAM Theory We start with the 0th order FVDAM theory defined by the local stiffness matrix equation that relates surface-averaged increments of tractions to surface-averaged increments of fluctuating displacements. Expressing the surface-averaged increments of tractions in Equation (4.49) solely in terms of $\Delta \boldsymbol{W}^{(q)}$ and the applied deformation gradient increment $\Delta \overline{\boldsymbol{F}}$, and satisfying the local equilibrium equations (4.55) also considering only the contributions of $\Delta \boldsymbol{W}^{(q)}$ and $\Delta \overline{\boldsymbol{F}}$, we obtain the following form of the local stiffness matrix relation,

$$\Delta \hat{\boldsymbol{t}}^{(q)} = \boldsymbol{K}_{(00)}^{(q)} \Delta \hat{\boldsymbol{u}}'^{(q)} + \overline{\mathbb{R}}_0^{(q)} \Delta \overline{\boldsymbol{F}} \tag{4.57}$$

where the local stiffness matrix $\boldsymbol{K}_{(00)}^{(q)}$ is an 8x8 matrix and the incremental surface-averaged traction and fluctuating displacement vectors are defined by ordering the respectively components as follows,

$$\Delta \hat{\boldsymbol{t}}^{(q)} = \left[\Delta \hat{t}_1^{(1)}, \Delta \hat{t}_2^{(1)}, \Delta \hat{t}_3^{(1)}, \dots, \Delta \hat{t}_1^{(4)}, \Delta \hat{t}_2^{(4)}, \Delta \hat{t}_3^{(4)}\right]^{(q)T} \tag{4.58}$$

$$\Delta\hat{\boldsymbol{u}}'^{(q)} = \left[\Delta\hat{u}_1'^{(1)}, \Delta\hat{u}_2'^{(1)}, \Delta\hat{u}_3'^{(1)}, \ldots, \Delta\hat{u}_1'^{(4)}, \Delta\hat{u}_2'^{(4)}, \Delta\hat{u}_3'^{(4)}\right]^{(q)T} \tag{4.59}$$

This is the FVDAM theory originally developed by Khatam and Pindera (2012), albeit with two approximations involved in the calculation of the local stiffness matrix.

The first approximation originally introduced by Cavalcante et al. (2007a,b) in the context of the parametric finite-volume theory for solid mechanics applications relates surface averages of the partial derivatives of fluctuating displacement increments in the reference and actual coordinate systems through the volume-averaged Jacobian $\bar{\boldsymbol{J}}$. The second approximation involves the use of a spatially constant tangential stiffness tensor $\boldsymbol{R}^{(q)} = \boldsymbol{R}_0^{(q)}$ in the incremental constitutive equations. These approximations facilitate analytical construction of the local stiffness matrix but require sufficiently fine unit cell discretizations in order to be valid, particularly in the presence of large deformations. In the present construction, these approximations are abandoned at the expense of additional numerical effort in calculating the local stiffness matrices.

1st Order FVDAM Theory Expressing $\Delta\overline{\boldsymbol{W}}^{(q)}$ solely in terms of the incremental surface-averaged fluctuating displacements and rotations, based on the additional assumptions used to construct Equation (4.39), which decouple rotational and curvature effects, we obtain the following form of the local stiffness matrix equation for the 1st order FVDAM theory

$$\begin{bmatrix}\Delta\hat{\boldsymbol{t}}\\ \Delta\hat{\boldsymbol{t}}_\nabla\end{bmatrix}^{(q)} = \begin{bmatrix}\boldsymbol{K}_{(00)} & \boldsymbol{K}_{(01)}\\ \boldsymbol{K}_{(10)} & \boldsymbol{K}_{(11)}\end{bmatrix}^{(q)} \begin{bmatrix}\Delta\hat{\boldsymbol{u}}'\\ \Delta\hat{\boldsymbol{\omega}}_n'\end{bmatrix}^{(q)} + \begin{bmatrix}\overline{\mathbb{R}}_0\\ \overline{\mathbb{R}}_1\end{bmatrix}^{(q)} \Delta\overline{\boldsymbol{F}} \tag{4.60}$$

where the additional surface-averaged static variable is defined as follows

$$\Delta\hat{\boldsymbol{t}}_{\nabla}^{(q)} = \left[\Delta\hat{t}_{n/\eta}^{(1)}, \Delta\hat{t}_{n/\xi}^{(2)}, \Delta\hat{t}_{n/\eta}^{(3)}, \Delta\hat{t}_{n/\xi}^{(4)}\right]^{(q)T} \tag{4.61}$$

The additional sub-matrices $\boldsymbol{K}_{(01)}$, $\boldsymbol{K}_{(10)}$ and $\boldsymbol{K}_{(11)}$ of the local stiffness matrix are 8x4, 4x8 and 4x4, respectively.

2nd Order FVDAM Theory In the absence of the additional assumptions which decouple rotational and curvature effects, employing Equation (4.33) to evaluate $\Delta\overline{\boldsymbol{W}}^{(q)}$ we obtain the 2nd order or generalized FVDAM theory which reduces directly to the 0th order or standard version upon discarding the higher-order coefficients of the fluctuating displacement field increment. The generalized local stiffness matrix equation takes the following form, upon expressing $\Delta\boldsymbol{W}^{(q)}$ and $\Delta\overline{\boldsymbol{W}}^{(q)}$ in Equations (4.49), (4.52) and (4.53) solely in terms of the incremental surface-averaged fluctuating displacements, rotations and curvatures,

$$\begin{bmatrix} \Delta\hat{\boldsymbol{t}} \\ \Delta\hat{\boldsymbol{t}}_{\nabla} \\ \Delta\hat{\boldsymbol{t}}_{\nabla^2} \end{bmatrix}^{(q)} = \begin{bmatrix} \boldsymbol{K}_{(00)} & \boldsymbol{K}_{(01)} & \boldsymbol{K}_{(02)} \\ \boldsymbol{K}_{(10)} & \boldsymbol{K}_{(11)} & \boldsymbol{K}_{(12)} \\ \boldsymbol{K}_{(20)} & \boldsymbol{K}_{(21)} & \boldsymbol{K}_{(22)} \end{bmatrix}^{(q)} \begin{bmatrix} \Delta\hat{\boldsymbol{u}}' \\ \Delta\hat{\boldsymbol{\omega}}_n' \\ \Delta\hat{\boldsymbol{\kappa}}_n' \end{bmatrix}^{(q)} + \begin{bmatrix} \overline{\mathbb{R}}_0 \\ \overline{\mathbb{R}}_1 \\ \overline{\mathbb{R}}_2 \end{bmatrix}^{(q)} \Delta\overline{\boldsymbol{F}} \tag{4.62}$$

where the additional surface-averaged static variable is defined as follows

$$\Delta\hat{\boldsymbol{t}}_{\nabla^2}^{(q)} = \left[\Delta\hat{t}_{n/\eta\eta}^{(1)}, \Delta\hat{t}_{n/\xi\xi}^{(2)}, \Delta\hat{t}_{n/\eta\eta}^{(3)}, \Delta\hat{t}_{n/\xi\xi}^{(4)}\right]^{(q)T} \tag{4.63}$$

The additional sub-matrices $\boldsymbol{K}_{(02)}$, $\boldsymbol{K}_{(12)}$, $\boldsymbol{K}_{(20)}$, $\boldsymbol{K}_{(21)}$, $\boldsymbol{K}_{(22)}$ of the local stiffness matrix are 8x4, 4x4, 4x8, 4x4 and 4x4, respectively.

The structure of the local stiffness matrix of the generalized (2nd order) FVDAM theory reflects its systematic construction. This construction makes it possible to systematically generate lower-order versions without substantial effort at the analytical and code implementation levels. Moreover, each reduction in order

relative to the generalized FVDAM theory precisely indicates which kinematic and static features of the local subvolume response are abandoned, establishing clear connection between mathematics and physics of the subvolume's deformation characteristics relative to its neighbors.

4.3.5. Global Stiffness Matrix

The global stiffness matrix is assembled by applying interfacial continuity conditions on the surface-averaged kinematic and static variables, followed by the surface-averaged periodicity conditions. The boundary conditions are specified in terms of the macroscopic or average displacement gradient tensor increment $\Delta\overline{\boldsymbol{F}}$ appearing in the local stiffness matrix relations and thus the global system of equations. Its components are defined by the specified loading path and can be adjusted to produce unidirectional or multidirectional loading along radial paths in the homogenized stress space.

Continuity Conditions The surface-averaged kinematic variables comprised of incremental fluctuating displacements, rotations and curvatures are required to be continuous across common interfaces separating adjacent subvolumes. The designation of common faces of adjacent subvolumes depends on the manner of unit cell discretization, including the ordered discretization into rows and columns originally employed by Bansal and Pindera (2003, 2005) on rectangular domains. Alternatively, the different discretization approaches developed by the finite-element community may be profitably exploited in our approach as well. Hence for two adjacent subvolumes (q) and $(q+1)$ with common faces p and p^*, respectively, the following continuity conditions for the kinematic variables must hold,

$$\begin{aligned}
\Delta\hat{u}_i'^{(p)}\Big|^{(q)} &= \Delta\hat{u}_i'^{(p^*)}\Big|^{(q+1)} \\
\Delta\,\widehat{\omega}_n'^{(p)}\Big|^{(q)} &= \Delta\widehat{\omega}_n'^{(p^*)}\Big|^{(q+1)} \\
\Delta\hat{\kappa}_n'^{(p)}\Big|^{(q)} &= \Delta\hat{\kappa}_n'^{(p^*)}\Big|^{(q+1)}
\end{aligned} \tag{4.64}$$

Similarly, the following continuity conditions on surface-averaged static variables must hold,

$$\begin{aligned}
\Delta\hat{t}_i^{(p)}\Big|^{(q)} + \Delta\hat{t}_i^{(p^*)}\Big|^{(q+1)} &= 0 \\
\Delta\hat{t}_{n/i}^{(p)}\Big|^{(q)} + \Delta\hat{t}_{n/i}^{(p^*)}\Big|^{(q+1)} &= 0 \\
\Delta\hat{t}_{n/ii}^{(p)}\Big|^{(q)} + \Delta\hat{t}_{n/ii}^{(p^*)}\Big|^{(q+1)} &= 0
\end{aligned} \tag{4.65}$$

Global Stiffness Matrix Assembly Application of the surface-averaged continuity and periodicity conditions produces the global system of equations for the unknown surface-averaged kinematic variables.

$$\mathbb{K}\Delta\mathbb{U} = \mathbb{R}\Delta\overline{\boldsymbol{F}} \tag{4.66}$$

where $\mathbb{K}$ is the global stiffness matrix comprised of the local subvolume stiffness matrices arranged and summed according to the manner of the application of continuity conditions, $\Delta\mathbb{U}$ contains the common surface-averaged kinematic variables associated with subvolume interfaces (including the common mirror image boundaries), $\Delta\overline{\boldsymbol{F}}$ contains the specified proportions of deformation gradient tensor increments, and the global $\mathbb{R}$ matrix results from the arrangement and summation of the local $\overline{\mathbb{R}}_i^{(q)}$ subvolume matrices. To eliminate rigid body translation and rotation, the analysis domain is constrained by setting the appropriate surface-averaged boundary kinematic variables to zero at appropriate locations. The global stiffness matrix assembly depends on the unit cell discretization, including row-wise and column-wise as in Gattu et al.

(2008) discretization based on quadrilateral subvolumes. Alternatively, assembly techniques developed by the finite-element community may be exploited.

4.3.6. Unbalanced Static Variables

The use of the tangential form of the local constitutive relations, Equation (4.43), in the calculation of the surface-averaged static variables, incorporates linearities to the unit cell boundary value problem which originally do not exist, demanding a very small displacement gradient tensor increment $\Delta\overline{\boldsymbol{F}}$ to obtain a converged solution. We can guarantee or define the accuracy of the results only using an error controlling iterative scheme, based herein on the Newton-Raphson approach. To accomplish this, we need to quantify the error in the evaluation of static variables at subvolume interfaces. This is done upon employing Cauchy's relations expressed in the total form $t_i^{(p)} = T_{ji}^{(p)} n_j^{(p)}$ in conjunction with Equation (4.13) in the calculation of tractions acting on subvolume faces, which takes account of the nonlinearities and produces the following unbalanced surface-averaged static variables

$$\begin{aligned} \hat{t}_i^{(p)}\Big|^{(q)} + \hat{t}_i^{(p^*)}\Big|^{(q+1)} &= \Delta\hat{t}_i^{(p-p^*)} \\ \hat{t}_{n/i}^{(p)}\Big|^{(q)} + \hat{t}_{n/i}^{(p^*)}\Big|^{(q+1)} &= \Delta\hat{t}_{n/i}^{(p-p^*)} \\ \hat{t}_{n/ii}^{(p)}\Big|^{(q)} + \hat{t}_{n/ii}^{(p^*)}\Big|^{(q+1)} &= \Delta\hat{t}_{n/ii}^{(p-p^*)} \end{aligned} \tag{4.67}$$

The surface-averaged static variables $\hat{t}_i^{(p)}$, $\hat{t}_{n/i}^{(p)}$ and $\hat{t}_{n/ii}^{(p)}$ are evaluated following Equations (4.40), (4.41) and (4.42) with the increments replaced by the total quantities. These unbalanced surface-averaged static variables at subvolume interfaces quantify the

error and make possible the implementation of an iterative scheme based on the Newton-Raphson approach.

4.4. Locally-Applied Average Stress Theorem

Cavalcante et al. (2011b) introduced a stress measure based on the Average Stress Theorem in order to gauge the rate of convergence of the parametric FVDAM theory vis-a-vis the finite-element method for infinitesimal deformations. This same measure was employed by Cavalcante and Pindera (2012b) to assess the performance of the generalized finite-volume theory vis-a-vis the finite-element method. In this section, the same stress measure will be used to assess the proposed generalized FVDAM theory in the finite-deformation domain based on the first Piola-Kirchhoff stress. In this case, the Average Stress Theorem is re-stated below

$$\begin{aligned}\hat{T}_{ij} &= \frac{1}{V}\int_S t_j X_i dS = \frac{1}{V}\int_S T_{kj} n_k X_i dS \\ &= \frac{1}{V}\int_V \frac{\partial}{\partial X_k}\left(T_{kj} X_i\right) dV = \bar{T}_{ij} + \frac{1}{V}\int_V \frac{\partial T_{kj}}{\partial X_k} X_i dV\end{aligned} \tag{4.68}$$

where $\hat{T}_{ij}$ and $\bar{T}_{ij}$ denote average stress calculated from the integral of surface tractions and from the volume integral of point-wise stresses, respectively. When the local equilibrium equations are satisfied in point-wise sense, i.e., $\partial T_{kj}/\partial X_k = 0$, the two definitions are identical. The stress equilibrium equations are not satisfied locally in the finite-element analysis until sufficient mesh discretization ensures that the total potential energy is minimized. Similarly, the generalization of the FVDAM theory through the use of a higher-order fluctuating displacement field increment does violate point-wise (but not surface-averaged) equilibrium equations.

In order to gauge how fast point-wise equilibrium equations tend to zero in the case of the generalized FVDAM theory relative to the finite-element method, following Cavalcante et al. (2011b) we employ locally unbalanced average stress in any subvolume of the discretized domain,

$$\Delta\bar{T}_{ij}^{(q)} = \hat{T}_{ij}^{(q)} - \frac{1}{V_q}\int_{V_q} T_{ij}^{(q)} dV = \hat{T}_{ij}^{(q)} - \bar{T}_{ij}^{(q)} = \frac{1}{V_q}\int_{V_q} \frac{\partial T_{kj}}{\partial X_k} X_i|^{(q)} dV_q \tag{4.69}$$

In contrast with the infinitesimal FVDAM theory where closed-form expressions are available for the unbalanced averaged subvolume stresses in terms of the displacement field coefficients, no such expressions are readily available in the presence of finite-deformation effects.

The unbalanced average stress measure applied at the subvolume level will be employed in the sixth chapter of this dissertation to gauge how fast the finite-volume analysis produces point-wise equilibrated stress fields relative to the finite-element results.

4.5. Summary and Discussion

The previously developed generalized finite-volume theory for plane linear elasticity problems on rectangular domains has been extended to the finite-deformation domain within the 0th order homogenization theory applicable to materials with arbitrary periodic microstructures characterized by one continuous reinforcement direction. This significant extension, which in effect generalizes the previously developed FVDAM theory of Khatam and Pindera (2012), enables simulation of the response of periodic materials with nonlinear elastic constituent potentials undergoing very large deformations such as certain types of biological tissues. As will be

demonstrated in Chapter 6, the additional terms in the incremental fluctuating displacement field representation practically eliminate interfacial interpenetrations between adjacent subvolumes, dramatically improving subvolume conformability, as well as discontinuity in the non-traction stress components between subvolumes with the same elastic moduli. This is particularly important in the finite-deformation domain where significant mesh distortions accompanied by the concomitant subvolume face rotations may produce ill-conditioning of the global governing system of equations in the absence of interfacial conformability between adjacent subvolumes.

In Chapter 6, verification of the generalized FVDAM theory is provided through examples which critically test the generalized theory's capability for unit cell microstructures with large constituent moduli contrast. Comparison with analytical and finite-element results is the basis for this verification, while the newly defined unbalanced averaged stress measure provides a means for testing the method's convergence vis-a-vis that of the finite-element method.

Chapter 5

Finite Element Method Applied to Periodic Materials Subjected to Large Deformation

5.1. Introduction

In order to verify the proposed extension of the generalized finite-volume theory to enable modeling of heterogeneous materials with periodic microstructures (Drago and Pindera, 2007) in the finite-deformation domain by independent means, the finite element based approach for periodic materials undergoing infinitesimal deformations described in Chapter 2 is extended by incorporating large strain capability based on nonlinear elastic potentials. A *Total Lagrangian Formulation* is adopted, where all the measures are defined relative to the undeformed configuration (initial configuration), as well as the *Principle of Virtual Displacements* (Bathe, 1996), the basis of a finite element approach. The use of numerical techniques such as the finite element method enables analyses of problems with complex geometries which cannot be tackled using analytical techniques.

In the sequel, the finite element based homogenization approach is described in a concise way, and applied to problems with analytical solutions for verification.

5.2. Measures used in a Total Lagrangian Formulation

The measures used in a *Total Lagrangian Formulation* are defined using the undeformed configuration. The deformation gradient tensor F_{ij} is a basic kinematic measure which describes pointwise variation of the current position x_i relative to the initial position X_j.

$$F_{ij} = \frac{\partial x_i}{\partial X_j} \tag{5.1}$$

The next quantity describes the variation of the displacement field u_i relative to the initial position X_j, and is called displacement gradient tensor defined as follows,

$$H_{ij} = \frac{\partial u_i}{\partial X_j} \tag{5.2}$$

The other two kinematic quantities are the right Cauchy-Green deformation tensor (Equation 5.3) and the Green-Lagrange strain tensor (Equation 5.4), where δ_{ij} is the Kronecker delta.

$$C_{ij} = F_{ki}F_{kj} \tag{5.3}$$

$$E_{ij} = \frac{1}{2}\left(C_{ij} - \delta_{ij}\right) = \frac{1}{2}\left(\frac{\partial u_i}{\partial X_j} + \frac{\partial u_j}{\partial X_i} + \frac{\partial u_k}{\partial X_i}\frac{\partial u_k}{\partial X_j}\right) \tag{5.4}$$

The basic static quantity is the Second Piola-Kirchhoff stress tensor (Equation 5.5), derived from the strain energy density W, which defines material response in the large deformation domain. Although the Second Piola-Kirchhoff stress tensor does not have physical meaning, it is a symmetric stress measure used to quantify strain energy for problems in the large deformation domain.

$$S_{ij} = \frac{\partial W}{\partial E_{ij}} = 2\frac{\partial W}{\partial C_{ij}} \tag{5.5}$$

The next two static quantities have physical interpretation, unlike the Second Piola-Kirchhoff stress tensor which is directly related to the strain energy density. The first Piola-Kirchhoff stress tensor (Equation 5.6), also called engineering stress, is related to undeformed configuration, and is usually the stress measure used in experimental work. The last one is the Cauchy stress tensor (Equation 5.7), also called true stress, and theoretically, is a static measure with greater physical meaning as it is related to the deformed configuration. In Equation (5.7), J is the determinant of the gradient deformation tensor (Equation 5.1).

$$T_{ij} = S_{ik}F_{jk} \tag{5.6}$$

$$\sigma_{ij} = \frac{1}{\mathrm{J}}F_{ik}S_{kl}F_{jl} \tag{5.7}$$

5.3. Principle of Virtual Displacements for Nonlinear Analysis

The Principle of Virtual Displacements for Nonlinear Analysis can be expressed in terms of the deformed or the undeformed configurations, with the latter used in the Total Lagrangian Formulation. The internal virtual work δW_{in} is evaluated as shown below, where δ denotes variation. In addition, the superscripts *0* and *t* appearing in the following relations refer to undeformed (initial) and deformed (current) configurations, respectively.

$$\delta W_{in} = \int_{V^t} \sigma_{ij}\delta e_{ij} dV^t = \int_{V^0} S_{ij}\delta E_{ij} dV^0 \tag{5.8}$$

In the first integral of Equation (5.8) appears the strain tensor δe_{ij} defined in terms of the virtual displacement components δu_i as follows,

$$\delta e_{ij} = \frac{1}{2}\left(\frac{\partial \delta u_i}{\partial x_j} + \frac{\partial \delta u_j}{\partial x_i}\right) \tag{5.9}$$

The external virtual work δW_{ext}, without considering body forces, can be evaluated as shown in Equation (5.10), where τ_i and t_i are tractions acting on the surfaces S^t and S^0, which are related to Cauchy and first Piola-Kirchhoff stress tensors, respectively.

$$\delta W_{ext} = \int_{S^t} \tau_i \delta u_i dS^t = \int_{S^0} t_i \delta u_i dS^0 \tag{5.10}$$

It can be shown that the external virtual work for homogenized problems with periodic boundary conditions is zero (Appendix E), resulting in the following *equation of motion* using measures associated with the initial configuration, once $\delta W_{in} = \delta W_{ext}$.

$$\int_{V^0} S_{ij} \delta E_{ij} dV^0 = 0 \tag{5.11}$$

5.4. Homogenized Unit Cell Problem

In the 0th-order homogenization theory, the displacement field u_i is decomposed into two parts, one related to homogenized response ($\bar{u}_i$) and another associated with fluctuations caused by the presence of heterogeneities (u_i'). Hence, using the definition for the homogenized displacement gradient tensor $\bar{H}_{ij}$, we have

$$u_i = \bar{u}_i + u_i' = \bar{H}_{ij} X_j + u_i' \quad where \quad H_{ij} = \bar{H}_{ij} + H_{ij}' \tag{5.12}$$

Using the same idea, the first Piola-Kirchhoff and Cauchy stress tensors can be decomposed as shown below, where the homogenized part is evaluated in a way consistent with the Average Stress Theorem (Nemat-Nasser and Hori, 1999).

$$T_i = \bar{T}_i + T_i' \;\; with \;\; \bar{T}_i = \frac{1}{V^0}\int_{V^0} T_i \, dV^0 \tag{5.13}$$

$$\sigma_i = \bar{\sigma}_i + \sigma_i' \;\; with \;\; \bar{\sigma}_i = \frac{1}{V^t}\int_{V^t} \sigma_i \, dV^t \tag{5.14}$$

The linearization of the equation of motion (Appendix F), applied in an incremental total Lagrangian formulation (Bathe, 1996), results in

$$\begin{aligned} &\int_{V^0} \mathbb{C}^t_{ijkl}\epsilon'^t_{kl}\delta\epsilon'^t_{ij}dV^0 + \int_{V^0} S^t_{ij}\delta\eta'_{ij}dV^0 \\ &= -\int_{V^0} S^t_{ij}\delta\epsilon'^t_{ij}dV^0 - \int_{V^0} \mathbb{C}^t_{ijkl}F^t_{mk}\delta\epsilon'^t_{ij}dV^0\Delta\bar{H}_{ml} \end{aligned} \tag{5.15}$$

where $\mathbb{C}^t_{ijkl}$ is the tangential stiffness tensor of the material in the current configuration (Equation 5.16) and ϵ_{ij} and η_{ij} are the linear (Equation 5.17) and non-linear (Equation 5.18) contributions of the current Green-Lagrange strain tensor E^t_{ij}, respectively.

$$\mathbb{C}^t_{ijkl} = \frac{\partial^2 W}{\partial E^t_{ij}\partial E^t_{kl}} = 4\frac{\partial^2 W}{\partial C^t_{ij}\partial C^t_{kl}} \tag{5.16}$$

$$\epsilon'^t_{ij} = \frac{1}{2}\left(\Delta H'_{ij} + \Delta H'_{ji} + \bar{H}^t_{ki}\Delta H'_{kj} + \Delta H'_{ki}\bar{H}^t_{kj} + H'^t_{ki}\Delta H'_{kj} + \Delta H'_{ki}H'^t_{kj}\right) \tag{5.17}$$

$$\eta'_{ij} = \frac{1}{2}\Delta H'_{ki}\Delta H'_{kj} \tag{5.18}$$

In the above relations, we have an incremental decomposition of the equation of motion, defined by $\Delta\bar{H}_{ij} = \bar{H}^{t+\Delta t}_{ij} - \bar{H}^t_{ij}$ and $\Delta H'_{ij} = H'^{t+\Delta t}_{ij} - H'^t_{ij}$, where the superscript $t + \Delta t$ is associated with the following step at which equilibrium configuration is achieved, and the

superscript t is associated with the current equilibrium configuration. In Equation (5.17), the terms related to $\bar{H}_{ij}^{t}$ and $H_{ij}^{\prime t}$ represent the current homogenized and fluctuating displacement field effects, respectively.

The error due the linearization of the equation of motion is evaluated by Equation (5.19), and represents the "out-of-balance virtual work". The evaluation of the error allows the use of an iterative scheme based on Newton-Raphson approach, in order to achieve a desirable error level, resulting in converged and more reliable results.

$$Error = -\int_{V^0} S_{ij}^{t+\Delta t}\delta\epsilon_{ij}^{\prime t+\Delta t}dV^0 \tag{5.19}$$

Equations (5.15) and (5.19) are used to evaluate the tangential stiffness matrices and the incremental force vector that appear in the finite element formulation, which can be done following the procedure suggested by Bathe (1996), resulting in

$$(\boldsymbol{K_L} + \boldsymbol{K_{NL}})\Delta\boldsymbol{u}' = \Delta\boldsymbol{f} \tag{5.20}$$

where $\boldsymbol{K_L}$ and $\boldsymbol{K_{NL}}$ are the linear and nonlinear tangential stiffness matrices, respectively, $\Delta\boldsymbol{u}'$ is the vector with the incremental fluctuating nodal displacements, and $\Delta\boldsymbol{f}$ is the incremental force vector resulting from the incremental macroscopic loading $\Delta\bar{H}_{ij}$ or the error evaluated during the iterative procedure.

5.5. Verification with Analytical Solutions

The next set of results illustrates the capability of this approach to model mechanical response of periodic materials subjected to large deformation, where verifications are carried out using available analytical solutions.

5.5.1. Biaxial and Simple Shear Loadings of Blatz-Ko Material

The Blatz-Ko model for compressible materials is a simplified form of the expression suggested by Blatz and Ko (1962), and it can be used to model the deformation of a highly compressible polyurethane foam rubber, where the Poisson's ratio is assumed to be 0.25 ($\nu = 0.25$), and the shear modulus μ can be evaluated in terms of the Young's modulus E using the expression $\mu = E/2.5$. The strain energy density function for the Blatz-Ko model in terms of the invariants of the right Cauchy-Green deformation tensor (I_i) and the shear modulus (μ) is the following

$$W = \frac{\mu}{2}\left(\frac{I_2}{I_3} + 2\sqrt{I_3} - 5\right) \tag{5.21}$$

In this section we analyze the Blatz-Ko material subjected to two types of homogenous deformations for which analytical solutions are available. This problem represents a good test for the constitutive part of the numerical approach, since this material exhibits a highly nonlinear behavior at large stretches. In the finite element analysis, 100 load increments were employed using a square mesh with just 2x2 Q9 elements.

The homogeneous deformations caused by biaxial and simple shear loadings are characterized by the following final configurations in terms of λ and κ, respectively.

$$x_1 = X_1; x_2 = \lambda X_2 \; and \; x_3 = \lambda X_3 \tag{5.22}$$

$$x_1 = X_1; x_2 = X_2 + \kappa X_3 \; and \; x_3 = X_3 \tag{5.23}$$

The normalized first Piola-Kirchhoff and Cauchy stress components relative to the shear modulus μ are shown in Figures 5.1 and 5.2, where we see perfect agreement between the analytical and numerical results, illustrating the capability of the developed numerical approach to model materials with highly nonlinear behavior.

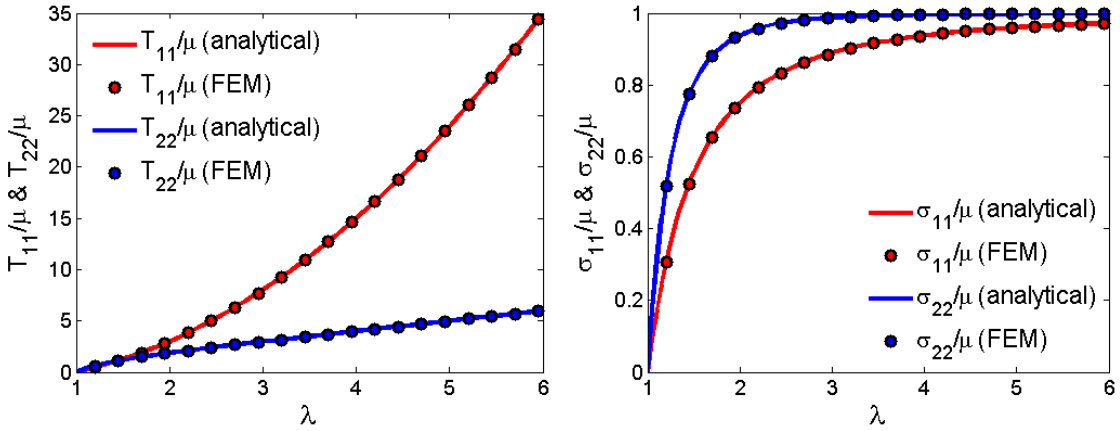

Figure 5.1 – Normalized first Piola-Kischhoff (left) and Cauchy (right) stress components for the homogenous deformation caused by biaxial loading of Blatz-Ko material.

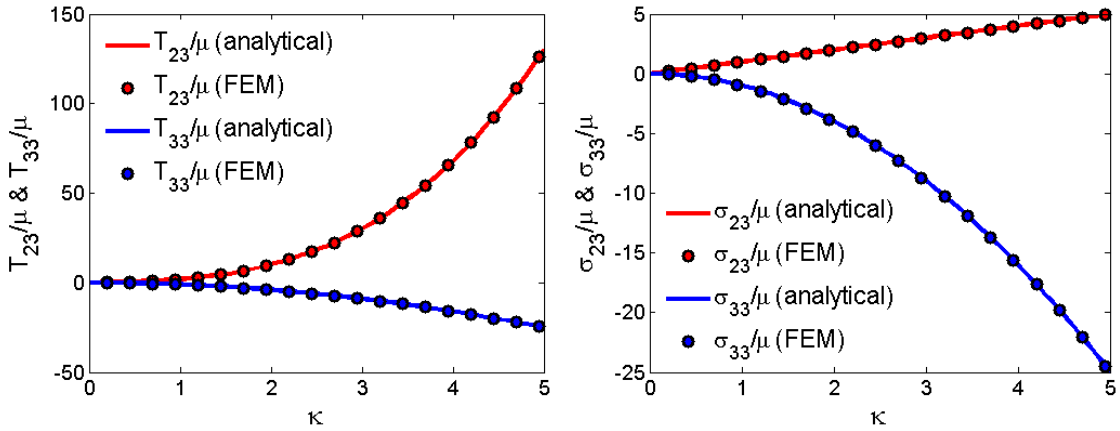

Figure 5.2 – Normalized first Piola-Kischhoff (left) and Cauchy (right) stress components for the homogenous deformation caused by simple shear loading of Blatz-Ko material.

5.5.2. The Cylindrical Model: Axisymmetric Loading

For this problem, a Blatz-Ko material with a hole (5% of porosity) is subjected to biaxial loading, defined by equal stretches in the two in-plane directions ($\lambda_2 = \lambda_3$) and unit stretch in the out-of-plane direction ($\lambda_1 = 1$). An incremental-iterative scheme based on Newton-Raphson approach was employed, and the numerical results obtained using 100 increments and a mesh of quadrilateral Q9 elements shown in Figure 5.3 are compared with the analytical solution obtained by Chung et al. (1986) in the context of internally pressurized hollow cylinder. This comparison is valid for a small porosity volume

fraction and a limited stretch, where, in this case, the normal homogenized first Piola-Kirchhoff stress components in the two in-plane directions ($\bar{T}_{22}$ and $\bar{T}_{33}$) obtained from the numerical approach are equivalent to the radial homogenized first Piola-Kirchhoff stress component ($\bar{T}_{RR}$) generated by the analytical solution. Figure 5.4 shows a comparison of the homogenized first Piola-Kirchhoff stress components and the inner radius deformation obtained from the numerical and analytical approaches, and an excellent agreement between these two solutions is observed. In Figures 5.5 and 5.6, the normalized Cauchy stress components σ_{22}/μ and σ_{23}/μ are presented for several stretch values λ_2, showing the capability of the proposed numerical approach to capture local response.

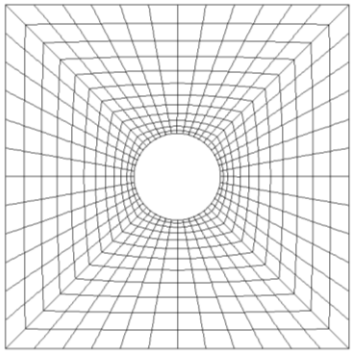

Figure 5.3 – Mesh used in the numerical solution for the cylindrical model.

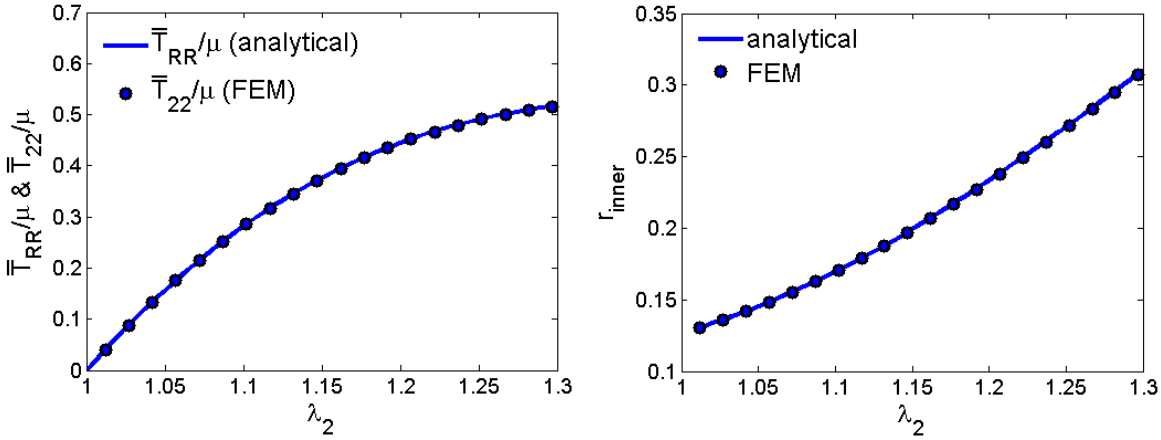

Figure 5.4 –Normalized homogenized first Piola-Kirchhoff stress components (left) and inner radius (right) obtained from the numerical and analytical solutions.

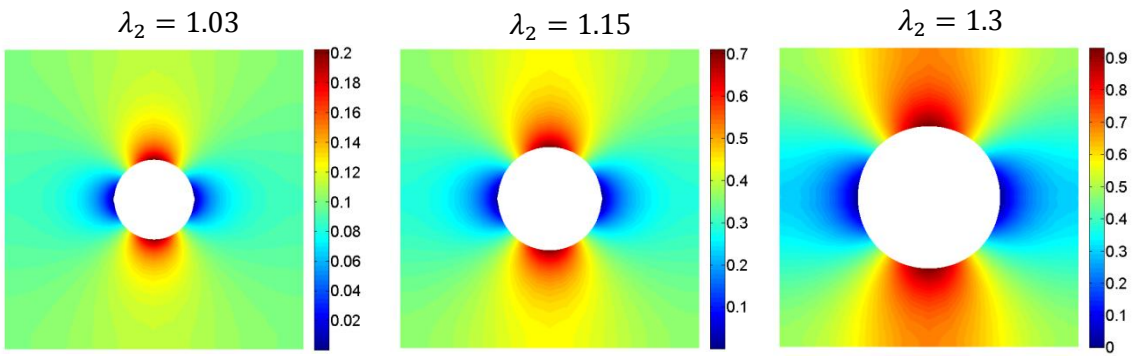

Figure 5.5 – Normalized Cauchy stress σ_{22}/μ fields for some stretches λ_2.

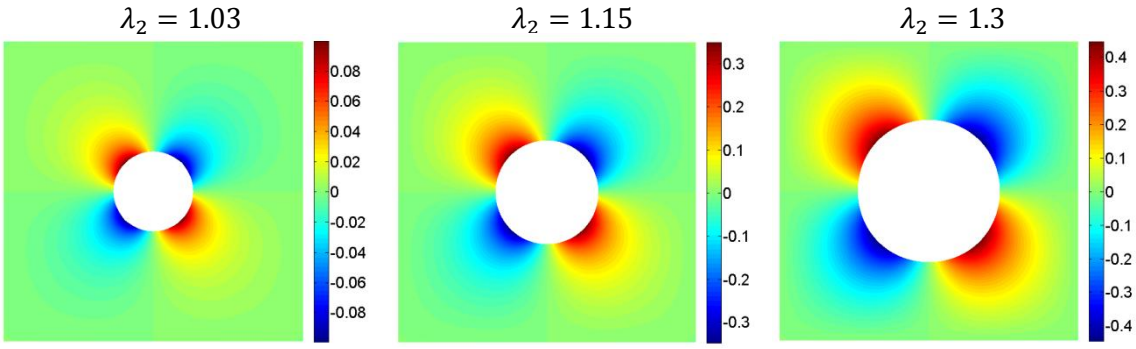

Figure 5.6 – Normalized Cauchy stress σ_{23}/μ fields for some stretches λ_2.

5.6. Summary and Discussion

In this chapter, a finite element based homogenization approach was described for modeling heterogeneous materials subjected to periodic boundary conditions, considering geometric and material nonlinearities. The finite element method formulation for homogenized problems in the large deformation domain yielded excellent agreement with the analytical solutions for two types of homogeneous deformations of Blatz-Ko material and a hollow cylinder with a small inner radius subjected to axisymmetric loading. Thus, this numerical approach based on an incremental total Lagrangian formulation is appropriate for modeling heterogeneous periodic materials subjected to large amount of

stretches, and can be used as a numerical verification tool for comparison with the generalized FVDAM theory, which will be done in the next chapter.

Chapter 6

Generalized FVDAM Theory for Periodic Materials Undergoing Finite Deformations - Results

6.1. Introduction

The objective of the FVDAM theory's generalization described in Chapter 4 was to enhance both the kinematic and static responses across common interfaces separating adjacent subvolumes through inclusion of higher-order terms in the fluctuating displacement field representation within individual subvolumes. This approach ensures continuity of surface-averaged displacements, rotations and curvatures across common interfaces, which is expected to enhanced conformability between adjacent subvolumes. This is particularly important in the finite-deformation domain where relative rotations at the interfaces of adjacent subvolumes may be very large, requiring rotational compatibility to ensure preservation of domain discretization integrity. The higher-order terms also enable enforcement of the continuity of surface-averaged

derivatives of interfacial tractions along tangential directions, which is expected to produce smoother stress fields across subvolume interfaces for both traction and non-traction stress components.

In this chapter, the results of predictions of the different-order FVDAM theories are verified and compared with finite element results based on conformable Q9 elements and the same analysis domain discretizations, as well as with available elasticity solutions. The use of Q9 elements is consistent with the fluctuating displacement field representation of the generalized FVDAM theory. A major focus is to demonstrate that the above goals, that is improvements in interfacial displacement conformability and point-wise continuity of tractions and non-traction stress components across subvolume interfaces, have been achieved through the inclusion of higher-order terms in the fluctuating displacement field representation absent in the original or 0th order FVDAM theory. Towards this end, the following integral measures of interfacial discontinuities are introduced which are used to test whether the objective has been attained, which is carried out as a function of mesh refinement

$$\Delta\bar{u}|_{S_0} = \frac{1}{S_0}\int_{S_0} \|\Delta u'\| dS, \quad \|\Delta u'\| = \sqrt{\Delta u_1'^2 + \Delta u_2'^2 + \Delta u_3'^2} \tag{6.1}$$

$$\Delta\bar{\mathrm{t}}|_{\mathrm{S_0}} = \frac{1}{\mathrm{S_0}}\int_{\mathrm{S_0}} \|\Delta \mathrm{t}\| \mathrm{dS}, \quad \|\Delta \mathrm{t}\| = \sqrt{\Delta \mathrm{t}_1^2 + \Delta \mathrm{t}_2^2 + \Delta \mathrm{t}_3^2} \tag{6.2}$$

where $\Delta \mathrm{t_i}$ and $\Delta u_i'$ are discontinuities of the traction and fluctuating displacement components at the common interfaces separating adjacent subvolumes or elements, respectively. The above calculations are carried out along all the interfaces separating adjacent subvolumes or elements, using a numerical integration based on the Newton-Cotes formula assuming a parabolic approximation (Simpson's Rule). In the case of the

finite element method, the first Piola-Kirchhoff stresses at the boundaries or faces of the elements are extrapolated from their values at the Gauss points using the respective interpolation functions, following the procedure shown in Chen et al. (1996) and discussed in Chapter 2.

A related issue is convergence of the global unbalanced average stress as a function of mesh refinement, recently introduced by Cavalcante et al. (2011b), which also provides a measure for comparison with finite element results, given the variational basis of the finite element technique, in contrast with the direct satisfaction of equilibrium equations in a surface-average sense which forms the basis of the finite-volume method used within the FVDAM framework for the unit cell problem. At the subvolume or elemental level, using the Average Stress Theorem, the unbalanced average first Piola-Kirchhoff stress $\Delta\bar{T}_{ij}^{(q)}$ is defined as follows

$$\Delta\bar{T}_{ij}^{(q)} = \hat{T}_{ij}^{(q)} - \bar{T}_{ij}^{(q)} = \frac{1}{V_q}\int_{V_q} \frac{\partial T_{kj}}{\partial X_k} X_i|^{(q)} dV_q \tag{6.3}$$

where

$$\hat{T}_{ij}^{(q)} = \frac{1}{V_q}\int_{S_q} t_j X_i|^{(q)} dS, \quad \bar{T}_{ij}^{(q)} = \frac{1}{V_q}\int_{V_q} T_{ij}^{(q)} dV \tag{6.4}$$

Summing up all the subvolume unbalanced average stress contributions in the absolute value sense, we obtain the global measure for the entire analysis domain,

$$\Delta\bar{T}_{ij} = \sum_{q=1}^{N_q} c_{(q)} \left|\Delta\bar{T}_{ij}^{(q)}\right| \tag{6.5}$$

where $c_{(q)} = V_q/V$ is the volume fraction of the *qth* subvolume or element and $V = \sum_{q=1}^{N_q} V_q$.

The unbalanced average first Piola-Kirchhoff stresses $\Delta\bar{T}_{ij}^{(q)}$ at the subvolume or elemental level are evaluated using numerical integration techniques, Gauss quadrature for the finite element method and Simpson's Rule for the FVDAM theories. Once again, the first Piola-Kirchhoff stresses at the boundaries of the finite elements are extrapolated from their values at the Gauss points using the respective interpolation functions, Chen et al. (1996).

We note that the unbalanced average first Piola-Kirchhoff stresses $\Delta\bar{T}_{ij}^{(q)}$ at the subvolume or elemental level are computed relative to local translated coordinate systems centered in each subvolume or element, with the origin defined by $(\eta, \xi) = (0,0)$ using the corresponding parametric mapping. Different results will be obtained relative to other coordinate systems because element equilibrium is not satisfied in volumetric sense for the finite element method, and the subvolume equilibrium is approximately satisfied for the FVDAM theories given that a numerical integration technique is employed in the evaluation of static variables. The influence of the adopted coordinate system in this calculation is especially noticeable in the finite deformation domain.

The above issues are tested through two illustrations, each chosen to critically test different aspects of the generalized FVDAM theory's predictive capabilities. In the first problem, we consider a dilute case of cylindrical porosities in a square array subjected to uniform far-field loading by transverse stress which is small enough to produce infinitesimal deformations. Exact elasticity solution is available for this problem which makes it possible to verify that the finite-deformation solution reduces correctly to the exact result. In the second problem, a hexagonal array of circular porosities with non-dilute volume fraction is analyzed under transverse loading, and the issues of interfacial

interpenetrations, stress continuity and convergence with mesh refinement are examined in a wide range of applied stretches. Finally, an application of the generalized FVDAM theory to the modeling of the response of bio-inspired wavy multilayers as a function of microstructural refinement is presented, in order to verify recently generated predictions by the 0th order FVDAM theory that revealed interesting layer-thickness effects, Khatam and Pindera (2012).

6.2. Cylindrical Porosity in a Dilute Square Array

As a first step, we consider a square array of cylindrical porosities with a volume fraction of 0.785% subjected to far-field transverse loading, Figure 6.1, which well approximates the dilute case or a single cylindrical cavity in an infinite slab. For the latter case, which is the celebrated Kirsch problem discussed in standard elasticity books, Timoshenko and Goodier (1970), exact linear elasticity solution valid for small strains is available under plane stress or plane strain assumption. Generalized plane strain solution can be readily adapted by suitable superposition of uniform axial strain.

For this case, we consider the surrounding slab to be made of isotropic linearly elastic material with the following Young's modulus and Poisson's ratio: $E = 70\,GPa$, $\nu = 0.33$. For such a material, the strain energy density function is a quadratic function of the Green-Lagrange strain tensor $\boldsymbol{E}$, Equation (4.8), employed in the determination of the local tangent stiffness tensor $\boldsymbol{R}$ appearing in the incremental constitutive relations, Equation (4.14).

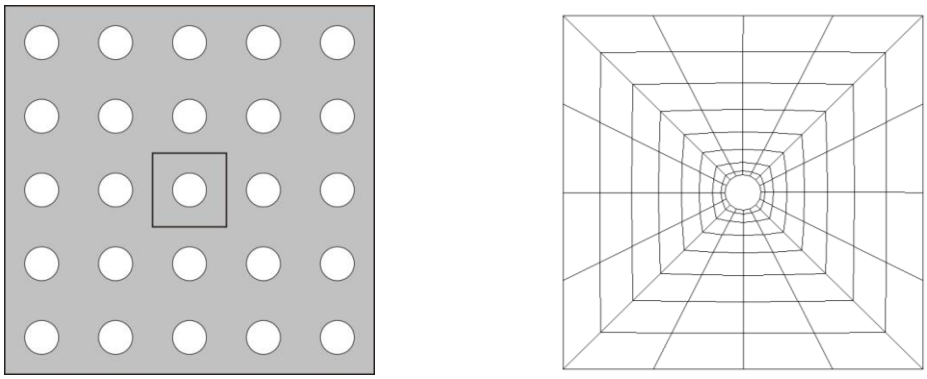

(a) (b)

Figure 6.1. Square array of circular porosities (a) and the coarsest mesh used in the analysis with 16x8 circumferential and radial subvolumes/elements (b).

For the FVDAM and FEM analyses, the unit cell of the porous array was discretized in the circumferential and radial manner, shown in Figure 6.1 for the 16x8 subvolume/element mesh which is the coarsest mesh employed. The applied uniaxial far-field loading is $\sigma_{22}^{\infty} = 1\,MPa$ which produces very small deformations, making comparison with the exact linear elasticity solution valid.

First, we compare convergence of pointwise traction and displacement continuity across adjacent subvolume/element faces with mesh refinement for the 0th, 1st and 2nd order (generalized) FVDAM theories and the Q9-based FEM in Figure 6.2. As observed, traction continuity is substantially improved through inclusion of higher-order terms in the fluctuating displacement field representation of the generalized FVDAM theory relative to the 0th version. In fact, all of the terms are required as the 1st order theory produces a modest improvement. Nonetheless, both lower-order versions are superior to the Q9-based FEM at coarse mesh discretizations, with the differences vanishing with mesh refinement. In contrast, the 2nd order FVDAM theory satisfies pointwise interfacial traction continuity very well even for coarse meshes. Pointwise displacement continuity is identically satisfied for the conformable Q9 elements which provide the reference

standard which is very well approximated by the predicted 2nd order FVDAM displacement fields. The pointwise interfacial displacement continuity predicted by the 1st order theory is also substantially improved relative to the 0th order predictions, highlighting the importance of the rotational term contribution to the minimization of interfacial interpenetration phenomenon suffered by the 0th order theory.

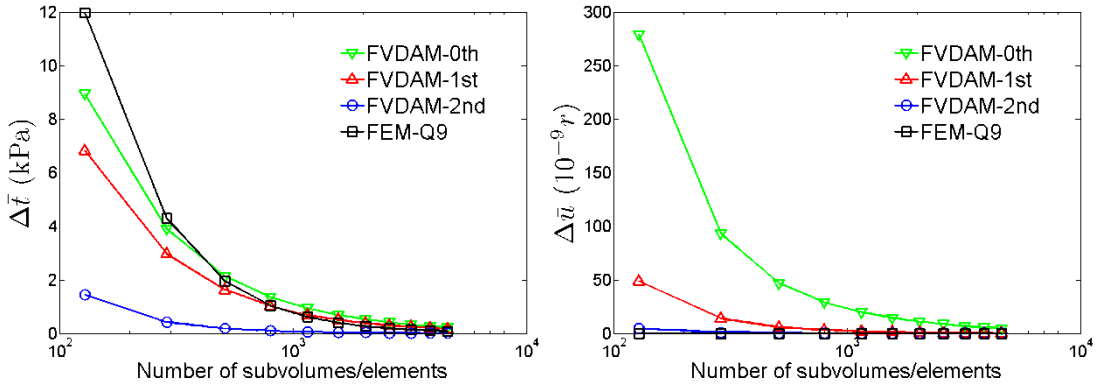

Figure 6.2. Interfacial traction and displacement difference measures as a function of the mesh refinement (r is the radius of the circular porosity, which can have any value or measure).

Next, we examine convergence of the global unbalanced average first Piola-Kirchhoff stresses as a function of mesh refinement, shown in Figure 6.3 for $\Delta\overline{T}_{22}$ and $(\Delta\overline{T}_{23} + \Delta\overline{T}_{32})/2$. In the presence of spatially variable Jacobian matrix and local stiffness tensor within individual subvolumes, the equilibrium equations are satisfied in a surface-average but not pointwise sense, even for the 0th order FVDAM theory, ensuring only overall subvolume equilibrium. This leads to discrepancy between average subvolume stress calculated from the surface and volumetric averaging procedures whose magnitude decreases with mesh refinement as observed in Figure 6.3 due to smaller spatial local property and hence stress variations with decreasing subvolume size. The differences in the global unbalanced stresses amongst the different-order FVDAM theories and the finite element method at each mesh refinement are ordered

according to the order of the displacement field approximation, with the 2nd order FVDAM theory and the finite element method yielding comparable results characterized by the largest differences due to the same displacement field representation. The 0th order theory produces the smallest differences followed by the 1st order theory.

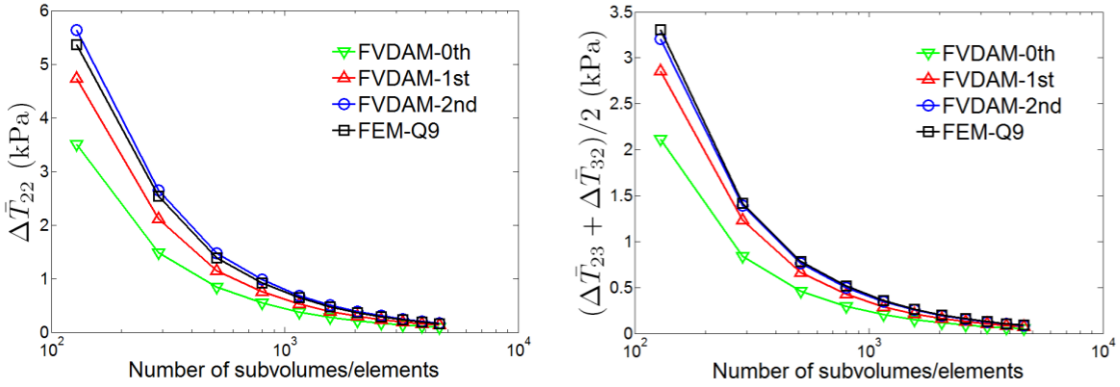

Figure 6.3. Convergence of the global unbalanced average first Piola-Kirchhoff stresses as a function of mesh refinement.

The local Cauchy stress fields $\sigma_{22}(Y_2, Y_3)$, $\sigma_{33}(Y_2, Y_3)$ and $\sigma_{23}(Y_2, Y_3)$ in the vicinity of the cylindrical porosity predicted by the different-order FVDAM theories are compared with the exact elasticity solution in Figure 6.4 for the unit cell mesh comprised of 64x32 subvolumes along circumferential and radial directions, respectively. At this level of mesh refinement, the 1st and 2nd order FVDAM theories produce very smoothly varying distributions for both the traction and non-traction stress components as suggested by the results of Figure 6.2. Some small irregularities in the stress fields predicted by the 0th order theory are identifiable in Figure 6.4, which are also suggested by the result in Figure 6.2, but these are very small at the given applied load level.

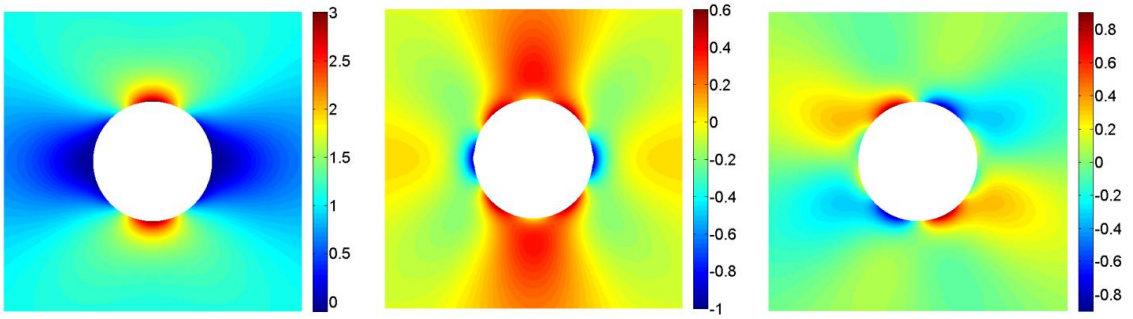

(a) Exact elasticity solution

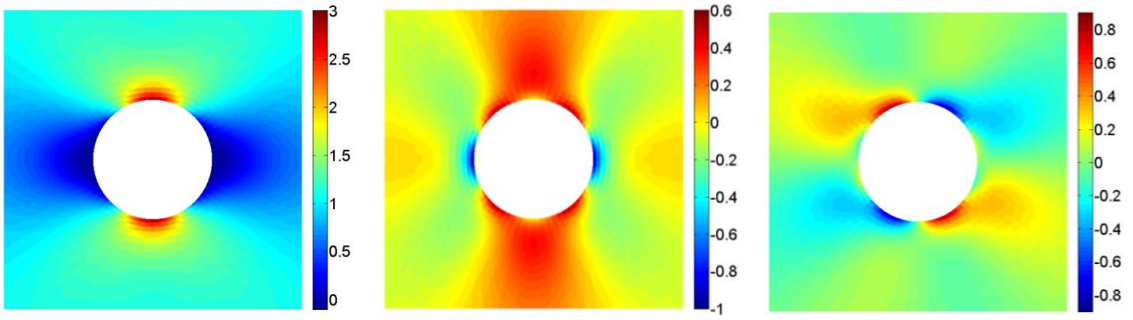

(b) 0th order FVDAM theory

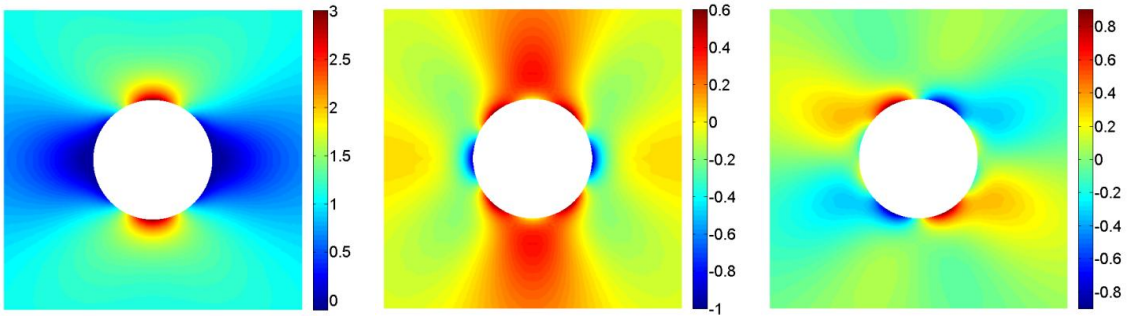

(c) 1st order FVDAM theory

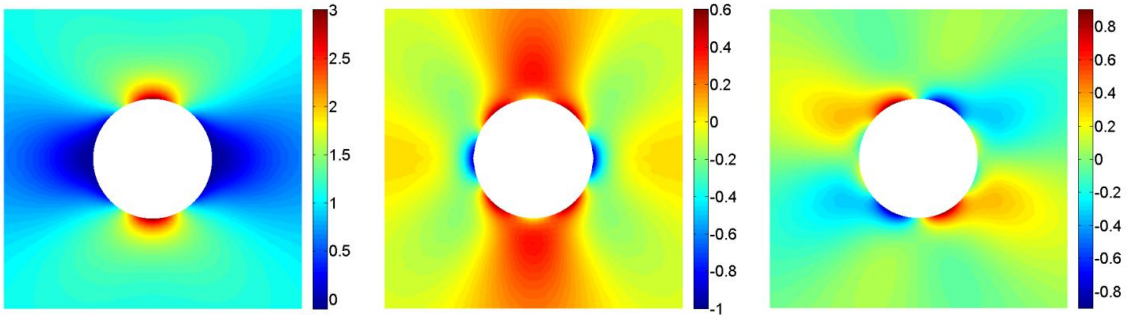

(d) 2nd order (generalized) FVDAM theory

$\sigma_{22}(Y_2, Y_3)$ $\sigma_{33}(Y_2, Y_3)$ $\sigma_{23}(Y_2, Y_3)$

Figure 6.4. Comparison of Cauchy stress fields obtained from the analytical and FVDAM solutions for the dilute cylindrical porosity array under uniaxial far-field transverse stress $\sigma_{22}^{\infty} = 1\ MPa$ and unit cell discretization of 64x32 subvolumes.

The last set of results addresses the issue of adjacent subvolume conformability. Deformed meshes have been generated as a function of mesh refinement by calculating new nodal subvolume displacement coordinates from the solution of the unit cell problem at the given load. For illustration purposes, the displacements have been magnified 50,000 times and the corresponding deformed meshes are shown in Figure 6.5 for the different-order FVDAM theory predictions and the analytical solution. The deformed meshes obtained from the analytical solution were generated by using the same unit cell coordinates for the calculation of nodal displacements as the nodal coordinates of the subvolumes used in different mesh discretizations. At coarse unit cell discretizations the 0th order FVDAM results exhibit substantial differences in the common face rotations between adjacent subvolumes in the vicinity of the pore boundary, leading to interfacial interpenetrations. These rotation differences vanish away from the pore boundary where the stress gradients decrease. Moreover, the interfacial interpenetrations become increasingly smaller with increasing mesh refinement at this level of applied macroscopic strain. Inclusion of rotational surface-averaged kinematic variables in the fluctuating displacement field representation substantially reduces the interfacial interpenetrations at coarse discretizations, as observed in the results of the 1st order FVDAM theory in the figure. The adjacent subvolume conformability is further enhanced at coarse mesh discretizations by the inclusion of surface-averaged curvature kinematic variables included in the 2nd order or generalized FVDAM theory.

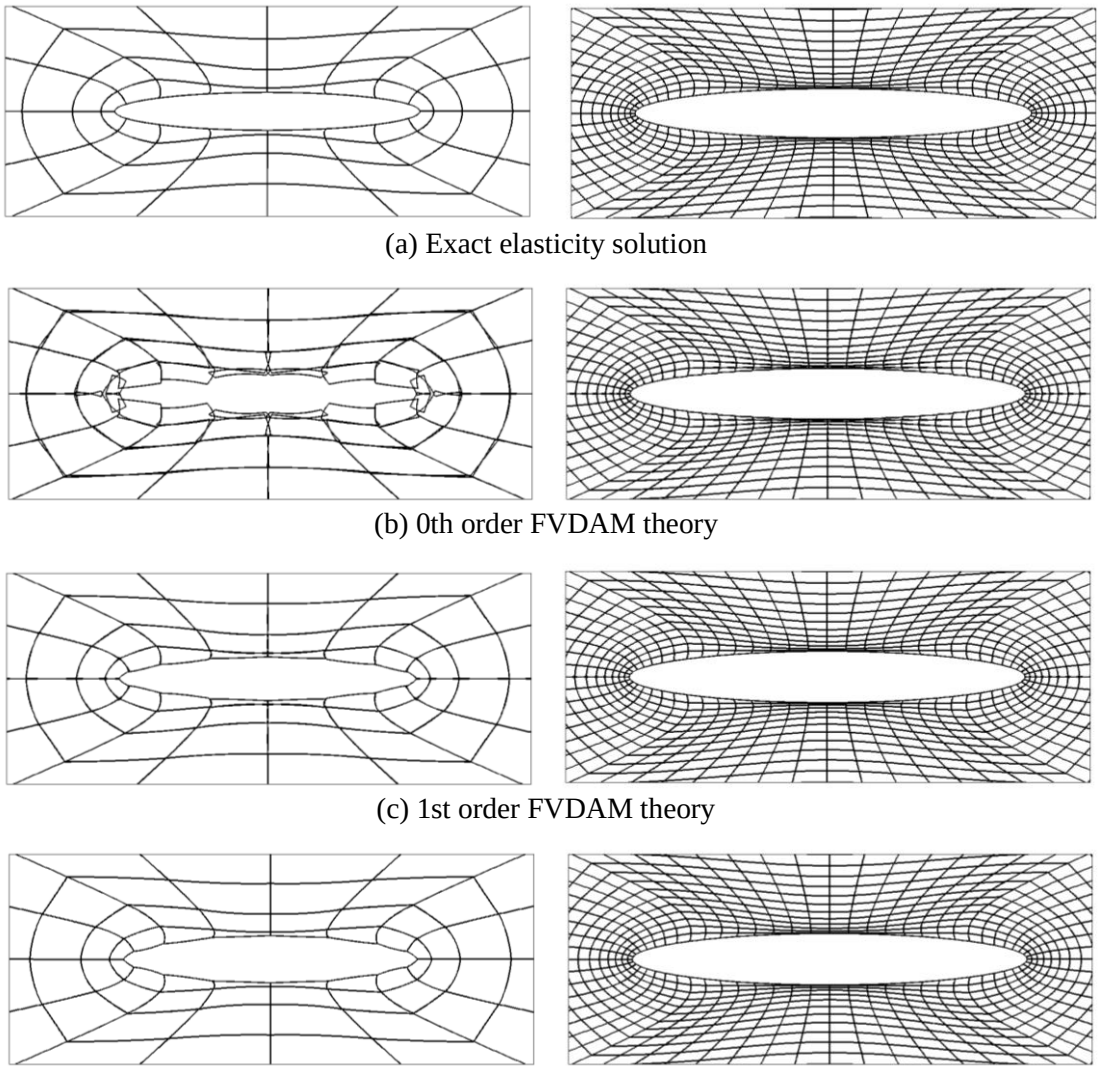

(a) Exact elasticity solution

(b) 0th order FVDAM theory

(c) 1st order FVDAM theory

(d) 2nd order (generalized) FVDAM theory

16x8 subvolumes 64x32 subvolumes

Figure 6.5. Deformed meshes generated by the displacements amplified 50,000 times obtained from the analytical and FVDAM solutions using coarse and fine mesh discretizations.

The above results indicate that interfacial interpenetrations, which are an intrinsic feature of the 0th order FVDAM theory, may be minimized in the linearly elastic region through suitable mesh refinement. This issue is addressed in the next section in the presence of finite deformations where adjacent subvolume face rotation differences in regions of high stress gradients are expected to be substantially greater. A similar problem exists close to singular stress fields produced by cracks within the

framework of linear elastic analysis as demonstrated by Bansal and Pindera (2005) which at present remains an open issue.

6.3. Cylindrical Porosity in a Non-Dilute Hexagonal Array

In this section we examine the effect of the higher-order displacement field variables which represent surface-averaged rotational and curvature effects for a hexagonal array of cylindrical porosities with 25% volume content, Figure 6.6, subjected to a sufficient large transverse stress to produce finite deformations. Mesh discretizations employed in this study ranged from 18x3 to 66x11 subvolumes along circumferential and radial directions, respectively. As no analytical solution is available for this case, the Q9-based finite element formulation developed in Chapter 5 is employed for verification and comparison. An incremental-iterative scheme based on Newton-Raphson approach was employed for both the generalized FVDAM theory and finite element method.

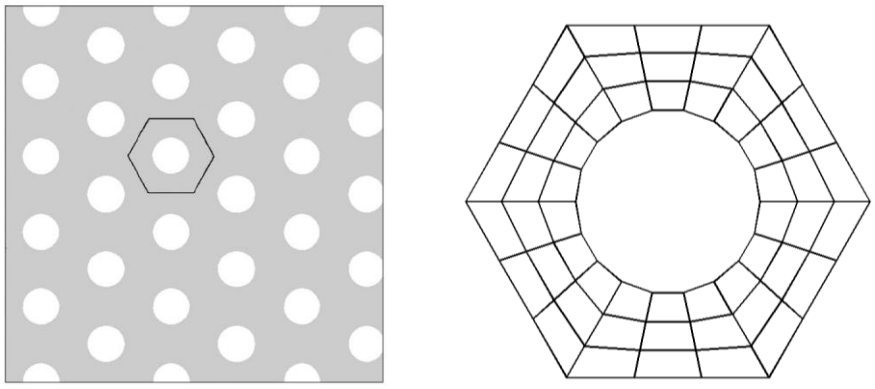

(a) (b)

Figure 6.6. Hexagonal array of circular porosities (a) and one of the coarsest meshes used in the analysis with 18x3 subvolumes/elements (b).

The matrix is modeled by the compressible Mooney-Rivlin material with the strain

energy density function given in terms of the three invariants of the right-Cauchy deformation tensor $\boldsymbol{C}$,

$$W = c_1\left(\frac{I_1}{I_3^{1/3}} - 3\right) + c_2\left(\frac{I_2}{I_3^{2/3}} - 3\right) + c_3(J-1)^2 \tag{6.6}$$

where I_1, I_2 and I_3 are defined in Chapter 4 below Equation (4.7) and $J = det\boldsymbol{F} = \sqrt{I_3}$. For consistency with linear elasticity in the limit of small strains, $c_1 + c_2 = \mu/2$ and $c_3 = \kappa/2$, where μ and κ are shear and bulk moduli, respectively. The original Mooney-Rivlin material is incompressible, yielding Poisson's ratio equal to 0.5. This modified strain energy density function for compressible materials was suggested by Sussman and Bathe (1987), where the compressibility or Poisson's ratio may be changed by assigning different values for $\kappa = 2\mu(1+\nu)/3(1-2\nu)$. The compressible Money-Rivlin is particularly popular in modeling soft materials because of the control of the amount of compressibility. It should be noted that when c_2 is set to zero, the material is reduced to compressible neo-Hookean. The matrix phase parameters are listed in Table 6.1.

Table 6.1 – Elastic parameters of the compressible Mooney-Rivlin material.

Material	***E (MPa)***	**ν**	***κ (MPa)***	***μ (MPa)***	***c_1 (MPa)***	***c_2 (MPa)***
Rubber matrix	4.00	0.45	13.3333	1.3793	0.6897	0.00

The applied pure transverse loading was carried out using 200 increments until a maximum transverse stretch of $\lambda_2 = 2.0$ was attained. The resulting homogenized $\bar{T}_{22} - \lambda_2$ stress-stretch response predicted by the FVDAM theories and the finite element analysis is shown in Figure 6.7 for three mesh discretizations ranging from 18x3 to 54x9 which were sufficient to produce converged homogenized response. As observed, converged homogenized response is obtained for the coarsest mesh with the finite

element approach whereas 30x5 subvolumes were required for the FVDAM theories, with very little difference observed between this and the coarsest mesh, however. Hence no essential difference could be detected in the homogenized responses generated using finite-volume and finite element approaches.

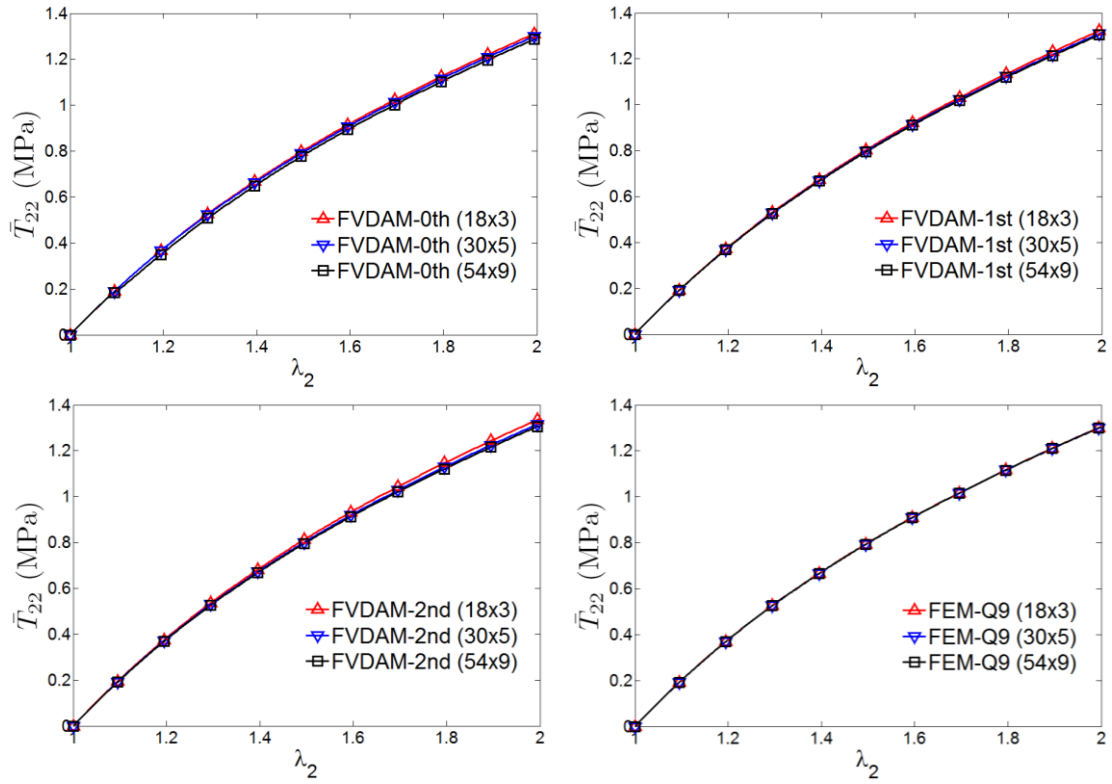

Figure 6.7. Homogenized response obtained from the numerical solutions using different mesh discretizations for a uniaxial macroscopic transverse loading $\bar{T}_{22} \neq 0$.

Despite quick convergence of the homogenized response with mesh refinement for the 0th order theory, the interfacial interpenetrations due to rotational differential of adjacent subvolume faces become substantial at large stretches, and do not completely vanish with mesh refinement, thereby affecting the local stress fields. This is seen in Figure 6.8 which compares the local transverse Cauchy stress $\sigma_{22}(Y_2, Y_3)$ distributions predicted by the FVDAM and finite element approaches and plotted in the deformed configurations at the final stretch of $\lambda_2 = 2.0$ for the two mesh discretizations of 18x3 and 54x9

subvolumes/elements. In contrast, smooth distributions are observed for the 1st and 2nd order FVDAM theories which converge to the finite element results with sufficient mesh refinement, which in this case is the 54x9 subvolume mesh.

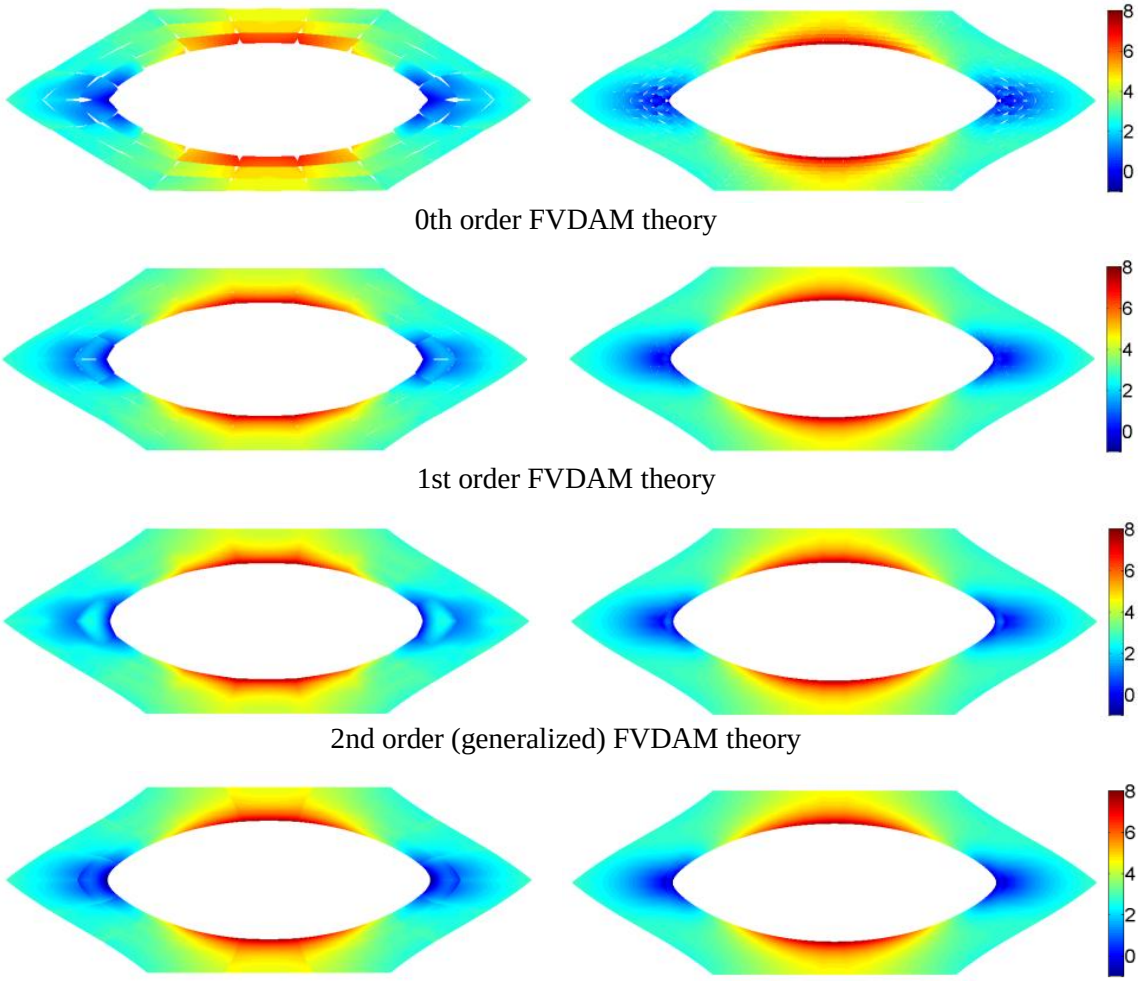

Figure 6.8. Comparison of the Cauchy stress fields $\sigma_{22}(Y_2, Y_3)$ obtained from the numerical solutions using different mesh discretizations for a uniaxial macroscopic transverse loading $\bar{T}_{22} \neq 0$ at the macroscopic stretch $\lambda_2 = 2.0$.

The question of adjacent subvolume conformability with applied macroscopic stretch is addressed in detail in Figure 6.9 which compares local mesh deformations predicted by the three FVDAM theory versions at low and maximum stretches for the finest mesh of

66x11 subvolumes. As observed, the initially small subvolume face interpenetrations at the porosity boundary at the stretch of $\lambda_2 = 1.01$ predicted by the 0th order FVDAM theory increase substantially when the stretch is increased to $\lambda_2 = 2.0$. In this case, the homogenized response remains stable and the local stress fields exhibit correctly the basic features despite the non-smooth distributions seen in Figure 6.8 for a slightly smaller mesh. Nonetheless, such uncontrolled interfacial interpenetrations may very well become problematic leading to ill-conditioning or singularity issues of the global system of equations for the unknown surface-averaged kinematic variables, Equation (4.66) in Chapter 4. These potential problems are eliminated by the inclusion of the surface-averaged rotational and curvature features in the local fluctuating displacement field representation as observed in the deformed meshes predicted by the 1st and 2nd order versions of the FVDAM theory. Moreover, the separation of the coupling between the surface-averaged rotational and curvature variables in the manner described in Chapter 4 clearly delineates the relative contribution of each effect in enhancing the adjacent subvolume conformability.

Quantitative comparison of the effect of higher-order terms in the fluctuating displacement field representation on pointwise stress continuity satisfaction is given in Figure 6.10 at the applied transverse stretches of $\lambda_2 = 1.01$ and $\lambda_2 = 2.0$ as a function of mesh refinement. In the linearly elastic regime when $\lambda_2 = 1.01$ the results of the different-order FVDAM theories follow those of the dilute case presented in Figure 6.2, and the finite element results are close to the 1st order results. As the applied stretch is increased to its maximum value, the 2nd order FVDAM results remain by far the best for all mesh discretizations, with the 1st order predictions exhibiting fluctuations with mesh

refinement which exceed the 0th order results at several mesh sizes. In contrast with the dilute case results, the finite element predictions are below those of the 0th and 1st order theories.

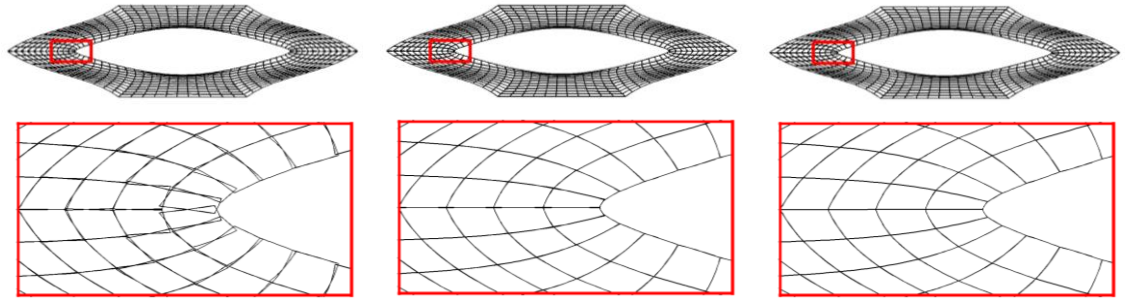

(a)

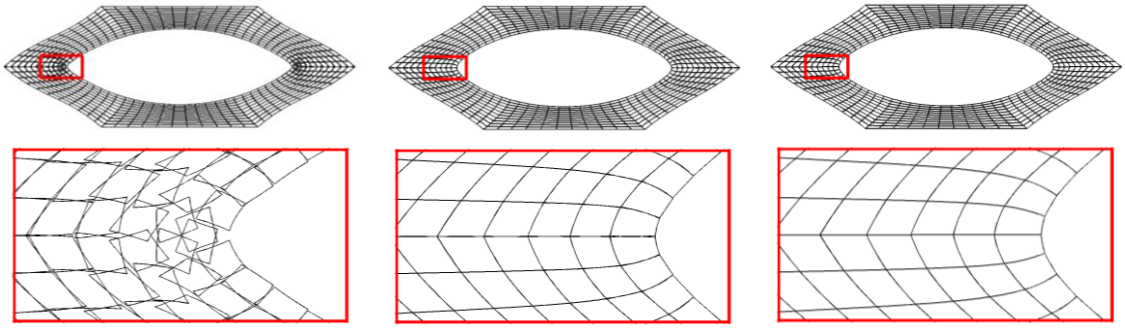

(b)

Figure 6.9. Deformed meshes with 66x11 subvolumes (the finest mesh used in the analysis) for a uniaxial macroscopic transverse loading $\bar{T}_{22} \neq 0$ at the macroscopic stretch of $\lambda_2 = 1.01$ (generated by the displacements amplified 100 times) (a) and $\lambda_2 = 2.0$ (b).

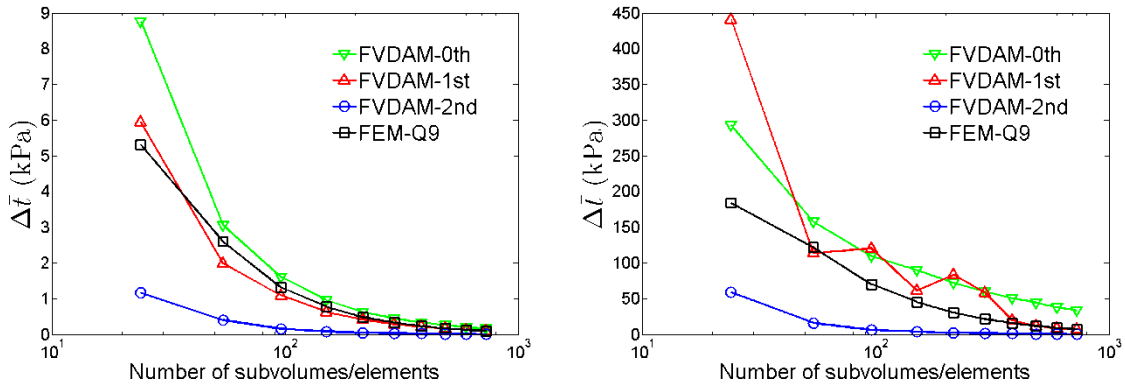

(a) (b)

Figure 6.10. Interfacial traction difference measure as a function of the mesh refinement at $\lambda_2 = 1.01$ (a) and $\lambda_2 = 2.0$ (b).

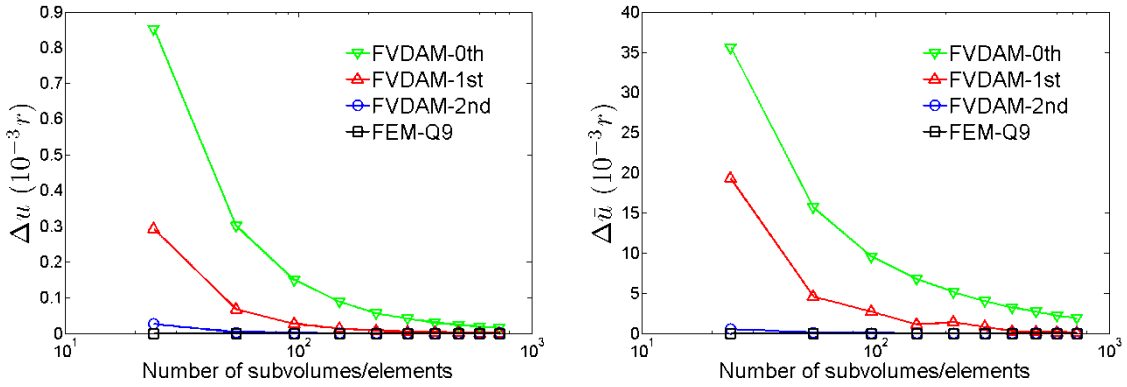

(a) (b)

Figure 6.11. Interfacial displacement difference measure as a function of the mesh refinement at $\lambda_2 = 1.01$ (a) and $\lambda_2 = 2.0$ (b) (r is the radius of the circular porosity, which can have any value or measure).

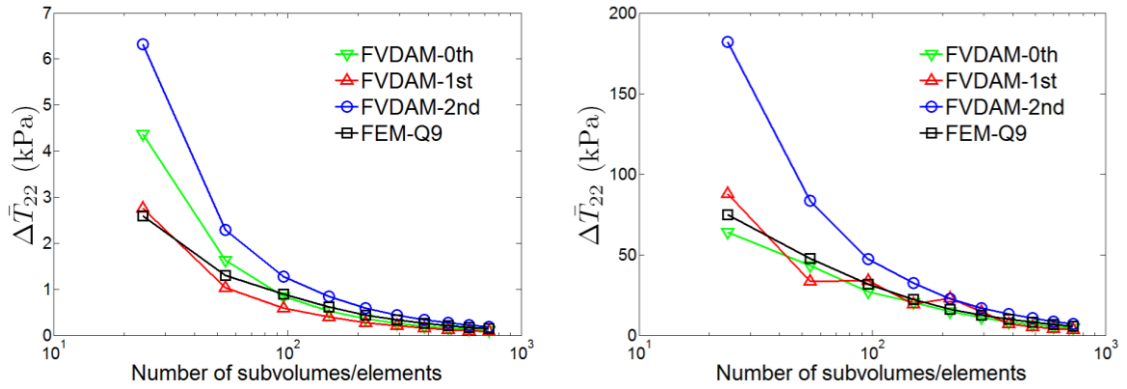

(a) (b)

Figure 6.12. Convergence of the global unbalanced average first Piola-Kirchhoff stress component $\Delta\overline{T}_{22}$ as a function of the mesh refinement at $\lambda_2 = 1.01$ (a) and $\lambda_2 = 2.0$ (b).

The corresponding pointwise interfacial displacement difference measures as a function of mesh refinement are illustrated in Figure 6.11. In both the small and finite deformation regions the trends exhibit the same features with the same ranking of the different-order FVDAM theory predictions as those already seen in Figure 6.2 for the dilute porosity case. Remarkably, the subvolume conformability obtained from the 2nd order theory remains almost as good as that of the fully comfortable Q9 elements as the applied stretch increases to very large values. Moreover, the importance of surface-averaged curvature

variables in the local fluctuating displacement field representation is observed to increase with increasing deformation.

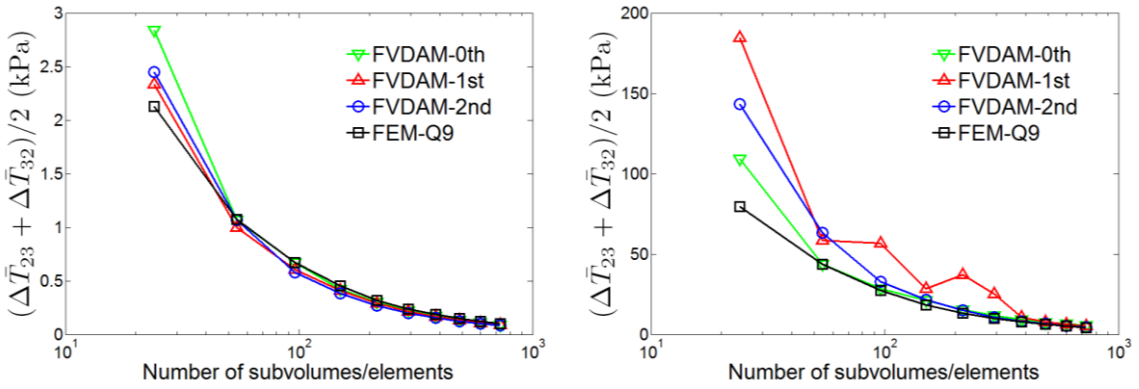

Figure 6.13. Convergence of the global unbalanced average first Piola-Kirchhoff stress components $(\Delta\overline{T}_{23}+\Delta\overline{T}_{32})/2$ as a function of the mesh refinement at $\lambda_2 = 1.01$ (a) and $\lambda_2 = 2.0$ (b).

Finally, the global unbalanced average first Piola-Kirchhoff stresses for $\Delta\overline{T}_{22}$ and $(\Delta\overline{T}_{23}+\Delta\overline{T}_{32})/2$ as a function of mesh refinement are given in Figures 6.12 and 6.13, respectively, at the two stretches $\lambda_2 = 1.01$ and $\lambda_2 = 2.0$. The trends in the manner of convergence of this stress measure to zero with increasing mesh refinement, which ensures pointwise satisfaction of the equilibrium equations, are not as clearly defined as in the case of materials with linearly elastic strain energies. The convergence depends on the stress component and the stretch level, and moreover no discernible rankings amongst the three versions of the FVDAM theory can be discerned. The finite element method appears to produce the fastest overall convergence with mesh refinement relative to any particular version of the FVDAM theory, but this may be a function of the employed strain energy density function, requiring further investigation. Nonetheless, all three versions of the FVDAM theory and the finite element method produce unbalanced average stresses that tend to zero with sufficient and not excessively large mesh refinement.

6.4. Some Aspects of Bio-Inspired Wavy-Multilayer Mechanics

In this section we verify the previously established stiffening effect observed by Khatam and Pindera (2012) in bio-inspired wavy-multilayers, Figure 6.14, whose response mimics certain types of biological tissues such as chordae tendineae. The microstructure consists of stiff wavy layers with an amplitude-to-wavelength ratio of 0.135 embedded in substantially softer matrix material, Table 6.2, and stiff layer volume fraction of 0.50. The soft matrix substance does not produce much resistance as the wavy crimp pattern unfolds due to applied transverse load, producing a stiffening effect. This stiffening effect characterized by a knee in the stress-stretch curve as the wavy layers unfold was shown to depend on the layer thickness which controls the local bending stiffness (or moment of inertia) in the crest and trough regions of the wavy microstructure.

Herein, we first compare the predictive capability of the different-order FVDAM theories in capturing the stiffening effect as a function of mesh refinement of the unit cell relative to the finite element predictions, and then illustrate the microstructural effect in controlling the unfolding process of the crimped microstructure. Once again, an incremental-iterative scheme based on Newton-Raphson approach was employed for both generalized FVDAM theory and finite element method.

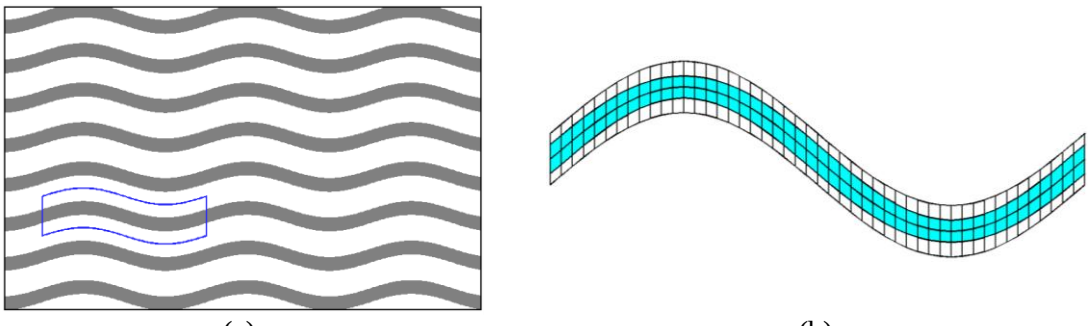

(a) (b)

Figure 6. 14. A wavy lamellar material with a highlighted unit cell of the periodic microstructure (a) and the coarsest mesh used in the analysis with 48x4 subvolumes/elements (b).

Table 6.2 – Elastic parameters of the compressible Mooney-Rivlin materials employed in modeling the response of chordae tendineae.

Layer	*E (MPa)*	ν	*κ (MPa)*	*μ (MPa)*	c_1 *(MPa)*	c_2 *(MPa)*
Stiff	125.00	0.3	104.167	48.076	24.038	0.0
Soft	0.1	0.3	0.083	0.038	0.019	0.0

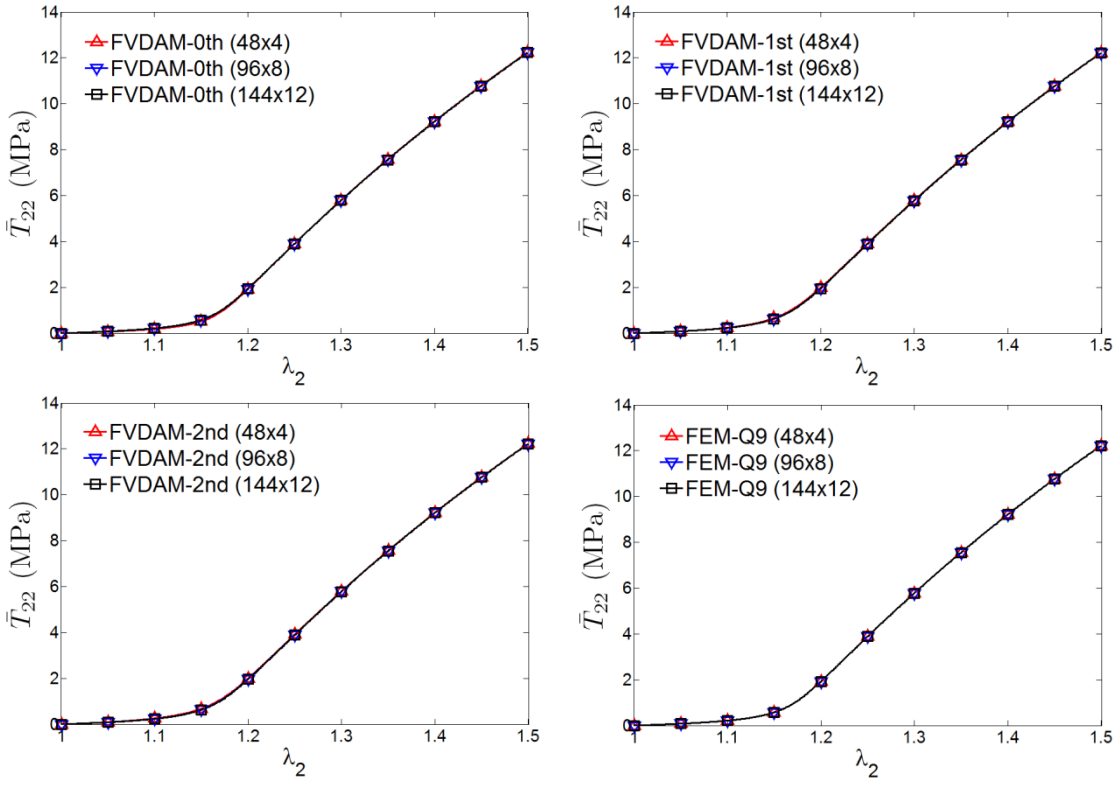

Figure 6.15. Homogenized response due to transverse load $\bar{T}_{22} \neq 0$ obtained from FVDAM theories and finite element method for different unit cell discretizations.

Figure 6.15 compares the stress-stretch response of the wavy microstructure subjected to uniaxial loading by $\bar{T}_{22} \neq 0$ only up to the final transverse stretch of $\lambda_2 = 1.5$ predicted by the FVDAM theories and the finite element analysis, using 500 increments, for three unit cell mesh discretizations of 48x4, 96x8 and 144x12 subvolumes/elements. As observed, converged homogenized response has been obtained even with the coarsest mesh of 48x4 subvolumes for the three versions of the FVDAM theory which compare very well with the corresponding finite element results. As expected from previous

experience, the local stress resolution increases with mesh refinement for the 0th order FVDAM theory as observed in the Cauchy stress fields $\sigma_{22}(Y_2, Y_3)$ plotted in the deformed configurations in Figures 6.16 and 6.17 at the applied stretches of $\lambda_2 = 1.05$ and $\lambda_2 = 1.25$, respectively. In contrast, inclusion of the higher-order terms in the displacement field representations employed in the 1st and 2nd order FVDAM theories smoothes out the stress distributions substantially even for the coarsest mesh, which compare very well with the corresponding finite element distributions. Nonetheless, even the 0th order theory captures the microstructural unfolding process very well, confirming the previously generated results of Khatam and Pindera (2012).

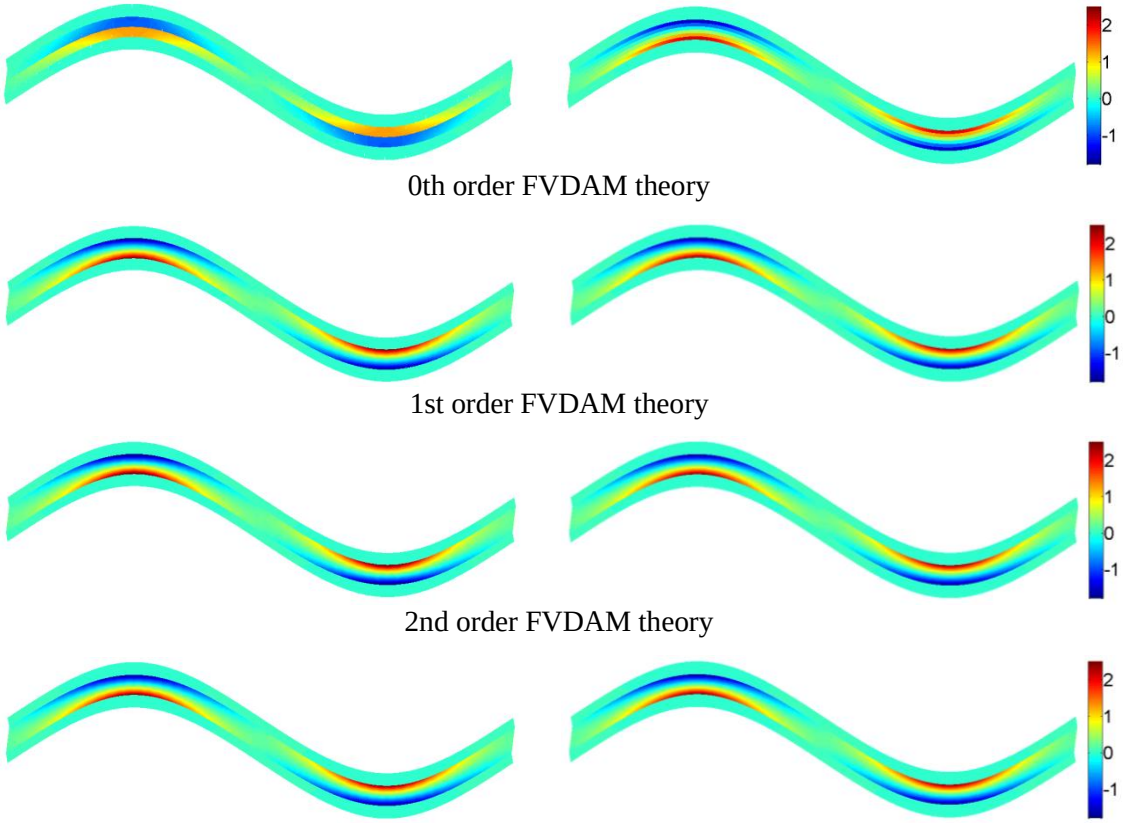

Figure 6.16. Comparison of Cauchy stress fields $\sigma_{22}(Y_2, Y_3)$ due to transverse load $\bar{T}_{22} \neq 0$ at $\lambda_2 = 1.05$ obtained from the FVDAM theories and finite element method for two different mesh discretizations.

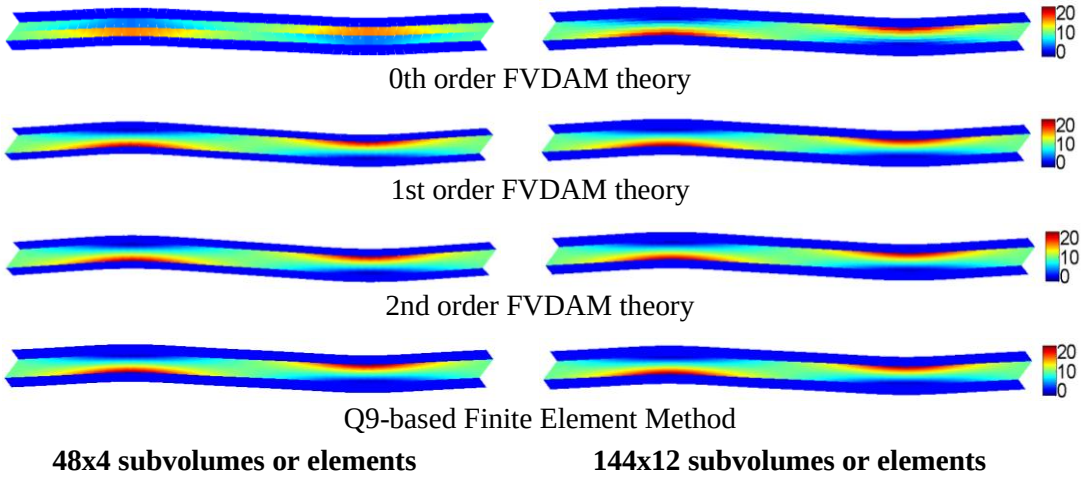

Figure 6.17. Comparison of Cauchy stress fields $\sigma_{22}(Y_2, Y_3)$ due to transverse load $\bar{T}_{22} \neq 0$ at $\lambda_2 = 1.25$ obtained from the FVDAM theories and finite element method for two different mesh discretizations.

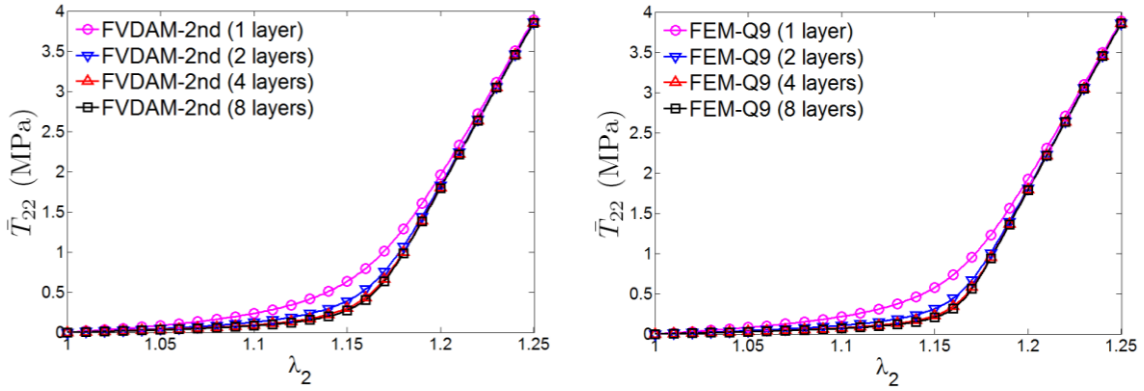

Figure 6.18. Homogenized response due to transverse load $\bar{T}_{22} \neq 0$ obtained from 2nd order FVDAM theory and finite element method for unit cells with progressively finer microstructures (thinner layers).

Finally, we illustrate the effect of microstructural refinement on the homogenized and local responses which involves subdividing a single thick layer into several layers without altering the amplitude-to-wavelength ratio and the stiff layer volume fraction. For this study, unit cell discretization of 144x12 subvolumes/elements was employed to analyze the response of unit cells containing one and two stiff layers, and 256x8 subvolumes/elements were employed for unit cells with four and eight stiff layers. Figure

6.18 compares the transverse responses of the four unit cells with progressively finer microstructures characterized by thinner stiff layers that were generated by the 2nd order FVDAM theory and Q9-based finite element analysis. As observed, there are no significant differences in the microstructure-dependent responses obtained from the two methods.

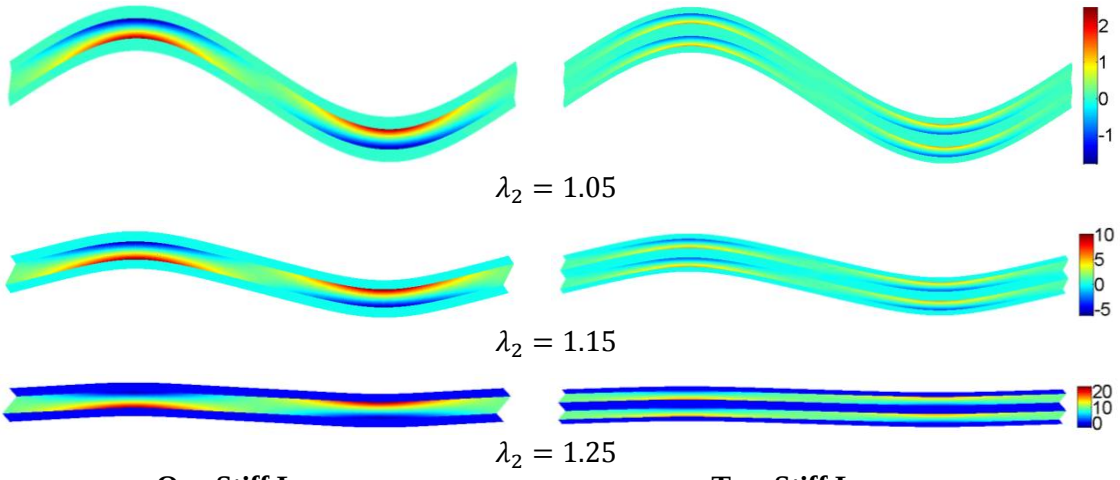

Figure 6.19. Comparison of Cauchy stress fields $\sigma_{22}(Y_2, Y_3)$ at three transverse stretch values obtained by the 2nd order FVDAM theory for two unit cells with one and two stiff layers subjected to transverse load $\bar{T}_{22} \neq 0$.

Comparison of the local Cauchy stress fields $\sigma_{22}(Y_2, Y_3)$ obtained from the FVDAM analysis at three stretch levels for unit cells with one and two stiff layers is presented in Figure 6.19 where the finer microstructure characterized by smaller local bending stiffness of the initially wavy layers produces normal stress field characterized by smaller through-thickness gradients. These smaller gradients produce less resistance to the unfolding process of the initially crimped microstructure, offering less initial resistance and a sharper knee in the homogenized stress-stretch curve observed in Fig. 6.18 as the unit cell microstructure transitions to a nearly fully straight configuration.

6.5. Summary and Discussion

In this chapter, verification of the generalized FVDAM theory was provided through examples which critically test the theory's predictive capability. Comparison with analytical and finite element results was the basis for this verification, while the recently introduced global unbalanced average stress measure provides one of the means for testing the method's convergence vis-a-vis that of the finite element method.

The results indicate that the addition of higher-order terms in the local fluctuating displacement field representation, which provides the basis for the higher-order theory's framework, substantially improves the conformability of adjacent subvolumes by reducing and eliminating interfacial interpenetrations. This is a direct result of satisfying continuity of the newly introduced surface-averaged kinematic variables which represent interfacial rotations and curvatures, and it is particularly important in situations involving large deformations. In these situations, the preservation of mesh integrity is an important consideration in the calculation of local stress fields as well as in the solution of the global system of equations that govern the unit cell response.

Inclusion of higher-order terms also largely eliminates, with sufficient mesh refinement, discontinuities in non-traction stress components across interfaces separating subvolumes with the same material properties. This shortcoming of the 0th order finite-volume theory had been recognized some time ago by Cavalcante et al. (2008), and provided the motivation for the construction of the generalized (2nd order) finite-volume theory.

The incorporation of parametric mapping into the generalized finite-volume theory, which allows to mimic complex geometries and microstructures, within the homogenization framework, resulting in the proposed generalized FVDAM theory,

represents a powerful micromechanics tool for the analysis, design and optimization of periodic materials undergoing large deformations, including bio-inspired materials.

Chapter 7

Conclusions and Future Work

7.1. Summary and Conclusions

Micromechanics of heterogeneous materials is a very rich area of research, characterized by different approaches developed during the last decades based either on simplified geometries of constituent phases amenable to analytical treatment, or on numerical techniques for the analysis of complex geometries subjected to particular boundary conditions, depending on the employed concept for the smallest subdomain representative of the material-at-large, Drago and Pindera (2007). The finite element method has been the standard numerical approach in the mechanics community for the analysis of wide range of problems, including micromechanics of heterogeneous materials. The displacement based finite element formulation is most commonly used because of its simplicity, where the minimization of the total potential energy or the satisfaction of the principle of virtual displacements guarantees reliable solutions with sufficiently fine meshes.

In contrast, the use of the finite-volume method by the scientific mechanics community has been more recent, with several advantages pointed out, such as stability in the solution of fluid and mechanics problems, even when coarse meshes are employed, due to the local satisfaction of the governing field equations. Amongst the different versions of the finite-volume approaches, this dissertation focused on the recently developed parametric finite-volume direct averaging micromechanics (FVDAM) theory, applied to the analysis of heterogeneous periodic materials, and based on the satisfaction of local equilibrium equations in a volume-averaged sense and continuity of both surface-averaged traction and displacement components at the common interfaces separating adjacent subvolumes.

The FVDAM theory has been developed independently of other finite-volume approaches, and has its roots in the so-called High-Fidelity Generalized Method of Cells proposed by Aboudi et al. (2002), but employs a simplified discretization of the analysis domain, and uses surface-averaged displacements at subvolume faces as the unknown variables in the resulting system of equations. This made possible re-examination of this approach, Bansal and Pindera (2005), and subsequently a name change which reflected its fundamental character as a finite-volume technique, i.e., the local satisfaction of equilibrium equations in a volume-averaged sense, Bansal and Pindera (2006).

The substantially simplified framework led to several key improvements and incorporation of different thermo-mechanical modeling capabilities, such as the parametric mapping originally proposed by Cavalcante et al. (2007a,b) in the context of the finite-volume theory for the analysis of functionally graded materials. These new capabilities enabled application of the method to a wide range of problems in a sequence

of papers by Gattu et al. (2008), Khatam and Pindera (2009a,b), Khatam et al. (2009) and Khatam and Pindera (2010, 2011, 2012).

However, two important shortcomings of the parametric FVDAM theory based on the incomplete second order polynomial representation of the displacement field were pointed out and discussed by Cavalcante et al. (2008, 2012a,b). These shortcomings are the interfacial interpenetration and discontinuity of non-traction stress components at the interfaces separating adjacent subvolumes with the same mechanical properties. One possible solution suggested by Cavalcante et al. (2008) was the incorporation of cross-product terms into the displacement field, resulting in a complete second order polynomial representation. This was the approach taken by Haj-Ali and Aboudi (2010), where additional relations for the solution of the resulting system of equations were proposed, named higher-order moments of the equilibrium equations. Unfortunately, this approach produced poorer displacement and stress fields, amplifying the shortcomings cited above, Cavalcante et al. (2012a,b).

As the main focus and contribution of this dissertation, a generalization of the parametric FVDAM theory for the analysis of heterogeneous periodic materials undergoing finite-deformations was developed based on a higher-order fluctuating displacement field representation, wherein additional kinematic and static variables are defined from elasticity considerations involving pointwise continuity of displacement and traction stress components at the interfaces separating adjacent subvolumes, Cavalcante and Pindera (2012a,b). Enforcement of the continuity of these new kinematic and static variables, together with the local satisfaction of equilibrium equations in a volume-averaged sense, the basis of a finite-volume approach, made possible construction of

different orders of the generalized FVDAM theory, with each reduction in order precisely indicating which kinematic and static features of the local subvolume response are abandoned, establishing clear connection between mathematics and physics of the subvolume's deformation characteristics relative to its neighbors. Verification and comparison with analytical and finite element solutions have illustrated the success of this generalized approach in obtaining better conformability and continuity of traction and non-traction stress components relative to the standard parametric FVDAM theory. This is especially important in the finite-deformation domain where big relative rotations present in the 0th order version can seriously compromise the integrity of the deformed mesh, even when a very refined mesh is employed, potentially producing ill-conditioning of the global system of equations, thereby negatively impacting solution convergence.

As a result, wide range of micromechanics analyses can be carried out using the developed generalized FVDAM theory, facilitating discovery and in-depth discussion of new effects such as the thickness effect in wavy multilayers, Khatam and Pindera (2010, 2012). Alternatives to the finite element method will continue to be sought, focusing on the discussion of the advantages of theoretical and computational features, illustrating which characteristics of a proposed approach are more important for a given application. These include a proposed technique’s stability, facility to incorporate different modeling capabilities, and a better understanding of mathematical and physical aspects of the formulation. In terms of computational efficiency, we must take into account the facility to formulate and implement these different techniques, and the execution time necessary to produce converged and reliable results. The constructed generalization of the finite-volume theory applied to heterogeneous periodic materials, and named generalized finite-

volume direct averaging micromechanics (FVDAM) theory, has been shown to be very well suited and efficient for the analysis of heterogeneous materials. This sets the stage for continuing development of this method by independent research groups in order to identify different features and widen its application.

7.2. Proposed Future Work

The main focus of this dissertation were the theoretical aspects of the generalized FVDAM theory and its consistent and systematic construction. Computational features such as execution time relative to other techniques, including different versions of the finite-volume method, were not investigated in depth. Although convergence studies demonstrated numerically the consistency of the developed generalized FVDAM theory with mesh refinement, no attempt was made to derive convergence rates for the different order FVDAM theories explicitly as a function of mesh size for either pointwise or averaged stresses or for the unbalanced stress measure proposed by Cavalcante et al. (2011b). This is a topic for future study that will strengthen the proposed theory's theoretical foundation. The presented results provide a strong motivation for such investigation.

Another feature of the generalized FVDAM theory that must be explored is the enforcement of continuity of both displacement and traction components at the interfaces separating adjacent subvolumes. This feature, not present in the displacement based formulations of the finite element method and other finite-volume techniques, makes possible study of damage at material interfaces using explicit relations between relative displacements and incremental traction components at the interfaces separating adjacent

subvolumes. Moreover, the substantially improved conformability and continuity of traction and non-traction stress components of this generalized approach relative to the standard or 0th order FVDAM theory makes possible a more reliable investigation of damage caused by cracks than the investigation conducted by Bansal and Pindera (2005) using the standard approach. Therein, the crack tip deformation was not predicted accurately due to relative interfacial interpenetrations of the subvolume faces directly adjacent to the crack tips along the crack plane. Consequently, the singular nature of the crack-tip stress field could not be captured accurately.

Incorporation of different modeling capabilities into the generalized FVDAM theory will also provide a wider range of applications, for instance, incorporation of constitutive models for the analysis of periodic heterogeneous materials with elastic-plastic and viscoelastic phases.

This dissertation represents one more and very important step in the evolution of the finite-volume theory applied to the analysis of periodic heterogeneous materials, named generalized FVDAM theory, and through a set of investigations provides the necessary motivation for the continuing evolution of this approach.

REFERENCES

Aboudi, J., Pindera, M.-J. and Arnold, S. M. (1999). Higher-order theory for functionally graded materials. *Composites: Part B*, 30 (8), 777-832.

Aboudi, J., Pindera, M.-J. and Arnold, S. M. (2001). Linear thermoelastic higher-order theory for periodic multiphase materials. *Journal of Applied Mechanics*, 68 (5), 697-707.

Aboudi, J., Pindera, M.-J. and Arnold, S. M. (2002). High-fidelity generalized method of cells for inelastic periodic multiphase materials. *NASA Technical Memorandum 2002-211469*. NASA-Glenn Research Center, Cleveland, OH. March 2002.

Aboudi, J. and Pindera, M.-J., (2004). High-fidelity micromechanical modeling of continuously reinforced elastic multiphase materials undergoing finite deformation. *Mathematics & Mechanics of Solids*, 9 (6), 599-628.

Achenbach, J. D. (1975). *A Theory of Elasticity with Microstructure for Directionally Reinforced Composites*. Springer-Verlag, New York.

Bailey, C. and Cross, M. (1995). A finite volume procedure to solve elastic solid mechanics problems in three dimensions on an unstructured mesh. *International Journal for Numerical Methods in Engineering*, 38, 1757-1776.

Bansal, Y. and Pindera, M.-J. (2003). Efficient reformulation of the thermoelastic higher-order theory for fgms. *Journal of Thermal Stresses*, 26 (11-12), 1055-1092.

Bansal, Y. and Pindera, M.-J. (2005). A second look at the higher-order theory for periodic multiphase materials. *Journal of Applied Mechanics*, 72 (2), 177-195. See also: NASA CR2004-213043.

Bansal, Y. and Pindera, M.-J. (2006). Finite-volume direct averaging micromechanics of heterogeneous materials with elastic-plastic phases. *International Journal of Plasticity*, 22 (5), 775-825.

Basic, H., Demirdzic, I. and Muzaferija, S. (2005). Finite volume method for simulation of extrusion processes. *International Journal for Numerical Methods in Engineering*, 62, 475-494.

Bathe, K. J. (1996). *Finite Element Procedures*. London, Prentice-Hall.

Bensoussan, A., Lions, J.-L. and Papanicolaou, G. (1978). *Asymptotic Analysis for Periodic Structures*. North Holland, Amsterdam.

Bijelonja, I., Demirdzic, I. and Muzaferija, S. (2006). A finite volume method for incompressible linear elasticity. *Computer Methods in Applied Mechanics and Engineering*, 195, 6378-6390.

Birman, V. and Byrd, L. W. (2007). Modeling and analysis of functionally graded materials and structures. *Applied Mechanics Reviews*, 60, 195-215.

Blatz, P. J. and Ko, W. L. (1962). Application of finite elasticity theory to deformation of rubbery materials. *Transaction of the Society of Rheology*, 6, 223-251.

Bufler, H. (1971). Theory of elasticity of a multilayered medium. *Journal of Elasticity*, 1, 125-143.

Buryachenko, V. A. (2007). *Micromechanics of Heterogeneous Materials*. Springer, New York.

Cavalcante, M. A. A. (2006). *Modelling of the Transient Thermo-Mechanical Behavior of Composite Material Structures by the Finite-Volume Theory*. MS Thesis, Federal University of Alagoas, Maceio, Alagoas, Brazil.

Cavalcante, M. A. A., Marques, S. P. C. and Pindera, M.-J. (2007a). Parametric formulation of the finite-volume theory for functionally graded materials. Part I: Analysis. *Journal of Applied Mechanics*, 74 (5), 935-945.

Cavalcante, M. A. A., Marques, S. P. C. and Pindera, M.-J. (2007b). Parametric formulation of the finite-volume theory for functionally graded materials. Part II: Numerical Results. *Journal of Applied Mechanics*, 74 (5), 946-957.

Cavalcante, M. A. A., Marques, S. P. C. and Pindera, M.-J. (2008). Computational aspects of the parametric finite-volume theory for functionally graded materials. *Journal of Computational Materials Science*, 44 (2), 422-438.

Cavalcante, M. A. A., Marques, S. P. C. and Pindera, M.-J. (2009). Transient thermo-mechanical analysis of a layered cylinder by the parametric finite-volume theory. *Journal of Thermal Stresses*, 32 (1), 112-134.

Cavalcante, M. A. A., Marques, S. P. C., and Pindera, M.-J. (2011a). Transient finite-volume analysis of a graded cylindrical shell under thermal shock loading. *Mechanics of Advanced Materials and Structures*, 18 (1), 53-67.

Cavalcante, M. A. A., Khatam, H. and Pindera, M.-J. (2011b). Homogenization of elastic-plastic periodic materials by FVDAM and FE approaches - An assessement. *Composites: Part B*, 42, 1713-1730.

Cavalcante, M. A. A, Lages, E. N., Marques, S. P. C. and Pindera, M.-J. (2012a). The High-fidelity Generalized Method of Cells with arbitrary cell geometry and its relationship to the Parametric Finite-Volume Micromechanics. *International Journal of Solids and Structures*, 49 (15-16), 2037-2050.

Cavalcante, M. A. A., Pindera, M.-J. and Khatam, H. (2012b). Finite-volume micromechanics of periodic materials: Past, present and future. *Composites: Part B*, 43, 2521-2543.

Cavalcante, M. A. A. and Pindera, M.-J. (2012a). Generalized finite-volume theory for elastic stress analysis in solid mechanics. Part I: framework. *Journal of Applied Mechanics*, 79, 051006-1.

Cavalcante, M. A. A. and Pindera, M.-J. (2012b). Generalized finite-volume theory for elastic stress analysis in solid mechanics. Part II: Results. *Journal of Applied Mechanics*, 79, 051007-1.

Charalambakis, N. (2010). Homogenization techniques and micromechanics. A survey and perspectives. *Applied Mechanics Reviews*, 63, 030803, 1-10.

Charalambakis, N. and Murat, F. (2006). Homogenization of stratified thermoviscoplastic materials. *Quarterly of Applied Mathematics*, 64 (2), 359-399.

Chatzigeorgiou, G., Charalambakis, N., and Murat, F. (2008). Homogenization problems of a hollow cylinder made of elastic materials with discontinuous properties. *International Journal of Solids and Structures*, 45 (18-19), 5165-5180.

Chen, D. J., Shah, D. K. and Chan, W. S. (1996). Interfacial stress estimation using least-square extrapolation and local stress smoothing in laminated composites. *Computers and Structures*, 58, 765-774.

Chung, D. T., Horgan, C. O. and Abeyaratne, R. (1986). The finite deformation of internally pressurized hollow cylinders and spheres for a class of compressible elastic materials. *International Journal of Solids & Structures*, 22, 1557-1570.

Demirdzic, I., Martinovic, D. and Ivankovic, A. (1988). Numerical simulation of thermomechanical deformation processes in a welded work-piece. *Zavarivanje*, 31, 209-219 (in Serbo-Croat).

Demirdzic, I. and Martinovic, D. (1993). Finite volume method for thermo-elastic-plastic stress analysis. *Computer Methods in Applied Mechanics and Engineering*, 109, 331-349.

Demirdzic, I. and Muzaferija, S. (1994). Finite volume method for stress analysis in complex domains. *International Journal for Numerical Methods in Engineering*, 37, 3751-3766.

Demirdzic, I., Horman, I. and Martinovic, D. (2000). Finite volume analysis of stress and deformation in hygro-thermo-elastic orthotropic body. *Computer Methods in Applied Mechanics and Engineering*, 190, 1221-1232

Drago, A. S. and Pindera, M.-J. (2007). Micro-macromechanical analysis of heterogeneous materials: macroscopically homogeneous vs periodic microstructures. *Composites Science and Technology*, 67 (6), 1243-1263.

Fallah, N., Bailey, C., Cross, M. and Taylor, G.A. (2000). Comparison of finite element and finite volume methods application in geometrically nonlinear stress analysis. *Applied Mathematical Modelling*, 24, 439-455

Fallah, N. (2004). A cell vertex and cell centred finite volume method for plate bending analysis. *Computer Methods in Applied Mechanics and Engineering*, 193, 3457-3470.

Fallah, N. (2005a). A new approach in cell centred finite volume formulation for plate bending analysis. *Lecture Series on Computer and Computational Sciences*, 4, 187-190.

Fallah, N. (2005b). Using shape function in cell centred finite volume formulation for two dimensional stress analysis. *Lecture Series on Computer and Computational Sciences*, 4, 183-186.

Fallah, N. (2006). On the use of shape functions in the cell centered finite volume formulation for plate bending analysis based on Mindlin-Reissner plate theory. *Computers and Structures*, 84, 1664-1672.

Fallah, N. (2008). A method for the calculation of face gradients in the two-dimensional, cell centred, finite volume formulation for stress analysis in solid problems. *Scientia Iranica* (*International Journal of Science and Technology*), 15 (3), 286-294.

Fedele, R., Maier, G. and Whelan, M. (2006). Stochastic calibration of local constitutive models through measurements at the macroscale in heterogeneous media. *Computer Methods in Applied Mechanics and Engineering*, 195, 4971-4990.

Fryer, Y. D., Bailey, C., Cross, M. and Lai, C.-H. (1991). A control volume procedure for solving the elastic stress-strain equations on an unstructured mesh. *Applied Mathematical Modelling*. 15, 639-645.

Gao, X., Song, Y. and Sun, Z. (2009). Quadrilateral subcell based finite volume micromechanics theory for multiscale analysis of elastic periodic materials. *Journal of Applied Mechanics*, 76, 011013-1.

Gattu, M., Khatam, H., Drago, A. S. and Pindera, M.-J. (2008). Parametric finite-volume micromechanics of uniaxial, continuously-reinforced periodic materials with elastic phases. *Journal of Engineering Materials and Technology*, 130 (3), 031015-15.

Haj-Ali, R. and Aboudi, J. (2010). Formulation of the high-fidelity generalized method of cells with arbitrary cell geometry for refined micromechanics and damage in composites. *International Journal of Solids and Structures*, 47, 3447-3461.

Hill, R. (1963). Elastic properties of reinforced solids: some theoretical principles. *Journal of the Mechanics and Physics of Solids*, 11, 357-372.

Khatam, H. and Pindera, M.-J. (2009a). Thermo-elastic moduli of lamellar composites with wavy architectures. *Composites: Part B*, 40 (1), 50-64.

Khatam, H. and Pindera, M.-J. (2009b). Parametric finite-volume micromechanics of periodic materials with elastoplastic phases. *International Journal of Plasticity*, 25 (7), 1386-1411.

Khatam, H., Chen, L. and Pindera, M.-J. (2009). Elastic and Plastic Response of Perforated Plates with Different Porosity Architectures. *Journal of Engineering Materials and Technology*, 131 (3), 031015-14.

Khatam, H. and Pindera, M.-J. (2010). Plasticity-triggered architectural effects in periodic multilayers with wavy microstructures. *International Journal of Plasticity*, 26 (2), 273-287.

Khatam, H. and Pindera, M.-J. (2011). Plastic deformation modes in perforated sheets and their relation to yield and limit surfaces. *International Journal of Plasticity*, 27 (10) 1537-1559.

Khatam, H. and Pindera, M.-J. (2012). Microstructural scale effects in the nonlinear elastic response of bio-inspired wavy multilayers undergoing finite deformation. *Composites: Part B*, 43 (3), 869-884.

Leveque, R.J. (2002). *Finite Volume Methods for Hyperbolic Problems*. Cambridge University Press, Cambridge, UK.

Mendelson, A. (1986). *Plasticity: Theory and Application*. Krieger Publishing Co., Malabar, FL (*reprint edition*).

Nemat-Nasser, S. and Hori, M. (1999). *Micromechanics: Overall Properties of Heterogeneous Materials* (2nd edition). North-Holand.

Paley, M. and Aboudi, J. (1992). Micromechanical analysis of composites by the generalized method of cells. *Mechanics of Materials*, 14, 127-139.

Pan, W., Wheel, M. A. and Qin, Y. (2010). Six-node triangle finite volume method for solids with a rotational degree of freedom for incompressible material. *Computers & Structures*, 88, 1506-1511.

Paulino, G. H., Pindera, M.-J., Dodds, R. H., Rochinha, F. E., Dave, E. V. and Chen, L. (Ed.). (2008). Multiscale and Functionally Graded Materials. *AIP Conference Proceedings 973*. Melville, New York.

Pindera, M.-J. (1991). Local/global stiffness matrix formulation for composite materials and structures. *Composites Engineering*, 1 (2), 69-83.

Pindera, M.-J., Khatam, H., Drago, A. S. and Bansal, Y. (2009). Micromechanics of spatially uniform heterogeneous media: A critical review and emerging approaches. *Composites: Part B*, 40 (5), 349-378.

Sanchez-Palencia, E. (1980). Non-Homogeneous Media and Vibration Theory. *Lecture Notes in Physics*, 127, Springer-Verlag, Berlin (New York).

Sneddon, I. N. (1951). *Fourier Transforms*. McGraw-Hill, New York.

Suquet, P. M. (1987). Elements of homogenization for inelastic solid mechanics. *Lecture Notes in Physics*, 272, 193-278. Springer-Verlag, Berlin (New York).

Sussman, T. and Bathe, K. J. (1987). A finite element deformation of nonlinear incompressible elastic and inelastic analysis. *Computers and Structures*, 26, 357-409.

Taylor, G. A., Bailey, C., and Cross, M. (1995). Solutions of the elastic/visco-plastic constitutive equations: A finite volume approach. *Applied Mathematics Modelling*, 19, 746-760.

Taylor, G. A., Bailey, C. and Cross, M. (2003). A vertex-based finite volume method applied to non-linear material problems in computational solid mechanics. *International Journal for Numerical Methods in Engineering*, 56, 507-529.

Timoshenko, S. P. and Goodier, N. J. (1970). *Theory of Elasticity* (3rd edition). McGraw-Hill, New York.

Versteeg, H. K. and Malalasekera, W. (2007). *An Introduction to Computational Fluid Dynamics: The Finite Volume Method*. Prentice-Hall, New York.

Wenke, P. and Wheel, M. A. (2003). A finite volume method for solid mechanics incorporating rotational degrees of freedom. *Computers and Structures*, 81, 321-329.

Wheel, M. A. (1996). A finite-volume approach to the stress analysis of pressurized axisymmetric structures. *International Journal of Pressure Vessels and Piping*, 68, 311-317.

Wheel, M. A. (1999). A mixed finite volume formulation for determining the small strain deformation of incompressible materials. *International Journal for Numerical Methods in Engineering*, 44, 1843-1861.

Wheel, M. A. (2008). A control volume-based finite element method for plane micropolar elasticity. *International Journal for Numerical Methods in Engineering*, 75, 992-1006.

Williams, T. O. and Pindera, M.-J. (1997). An analytical model for the inelastic axial shear response of unidirectional metal matrix composites. *International Journal of Plasticity*, 13 (3), 261-289.

Zhong, Y., Bansal, Y. and Pindera, M.-J. (2004). Efficient reformulation of the thermal higher-order theory for FGM's with variable thermal conductivity. *International Journal of Computational Science and Engineering*, 5 (4), 795-831. See also: NASA CR 2002-211910, November 2002.

Appendix A

Total Potential Energy for Infinitesimal Elasto-Plastic Analysis of Periodic Materials

Derivation of the elastic strain energy using indicial notation:

$$U = \int_V \frac{1}{2}\left(\varepsilon_{ij} - \varepsilon_{ij}^p\right) C_{ijkl} \left(\varepsilon_{kl} - \varepsilon_{kl}^p\right) dV$$

$$= \frac{1}{2}\int_V \left(\bar{\varepsilon}_{ij} + \varepsilon'_{ij} - \varepsilon_{ij}^p\right) C_{ijkl} \left(\bar{\varepsilon}_{kl} + \varepsilon'_{kl} - \varepsilon_{kl}^p\right) dV$$

$$= \frac{1}{2}\int_V \bar{\varepsilon}_{ij} C_{ijkl}\, \bar{\varepsilon}_{kl} dV + \frac{1}{2}\int_V \varepsilon'_{ij} C_{ijkl}\, \varepsilon'_{kl} dV + \int_V \varepsilon'_{ij} C_{ijkl}\, \bar{\varepsilon}_{kl} dV$$

$$- \int_V \varepsilon'_{ij} C_{ijkl}\, \varepsilon_{kl}^p dV - \int_V \bar{\varepsilon}_{ij} C_{ijkl}\, \varepsilon_{kl}^p dV + \frac{1}{2}\int_V \varepsilon_{ij}^p C_{ijkl}\, \varepsilon_{kl}^p dV$$

Derivation of the work of tractions using indicial notation:

$$\Omega = \int_S t_i u_i \, dS = \int_S \sigma_{ji} n_j u_i \, dS = \int_S \left(\sigma_{ji} u_i\right) n_j \, dS$$

$$= \int_V \frac{\partial}{\partial x_j}\left(\sigma_{ji} u_i\right) dV = \int_V \left(\frac{\partial \sigma_{ji}}{\partial x_j} u_i + \sigma_{ji} \frac{\partial u_i}{\partial x_j}\right) dV$$

From equilibrium

$$\frac{\partial \sigma_{ji}}{\partial x_j} = 0$$

and taking into account kinematic considerations, follows

$$\frac{\partial u_i}{\partial x_j} = \frac{1}{2}\left(\frac{\partial u_i}{\partial x_j} + \frac{\partial u_j}{\partial x_i}\right) + \frac{1}{2}\left(\frac{\partial u_i}{\partial x_j} - \frac{\partial u_j}{\partial x_i}\right) = \varepsilon_{ij} + \omega_{ij}$$

then

$$\Omega = \int_V \sigma_{ji}\left(\varepsilon_{ij} + \omega_{ij}\right) dV = \int_V \sigma_{ji}\varepsilon_{ij}\, dV + \int_V \sigma_{ji}\omega_{ij}\, dV$$

As $\sigma_{ji} = \sigma_{ij}$ and $\omega_{ij} = -\omega_{ji}$, we have $\sigma_{ji}\varepsilon_{ij} = \sigma_{ij}\varepsilon_{ij}$ and $\sigma_{ji}\omega_{ij} = 0$, thus

$$\Omega = \int_V \sigma_{ij}\varepsilon_{ij}\, dV$$

From Hill's Lemma

$$\frac{1}{V}\int_V \sigma_{ij}\varepsilon_{ij}\, dV = \left(\frac{1}{V}\int_V \sigma_{ij}\, dV\right)\left(\frac{1}{V}\int_V \varepsilon_{ij}\, dV\right) = \bar{\sigma}_{ij}\bar{\varepsilon}_{ij}$$

which implies

$$\Omega = \bar{\sigma}_{ij}\bar{\varepsilon}_{ij}V$$

Finally, the total potential energy using indicial notation for infinitesimal elasto-plastic analysis of periodic materials is

$$\Pi = U - \Omega = \frac{1}{2}\int_V \bar{\varepsilon}_{ij}C_{ijkl}\,\bar{\varepsilon}_{kl}dV + \frac{1}{2}\int_V \varepsilon'_{ij}C_{ijkl}\,\varepsilon'_{kl}dV + \int_V \varepsilon'_{ij}C_{ijkl}\,\bar{\varepsilon}_{kl}dV$$
$$- \int_V \varepsilon'_{ij}C_{ijkl}\,\varepsilon^p_{kl}dV - \int_V \bar{\varepsilon}_{ij}C_{ijkl}\,\varepsilon^p_{kl}dV + \frac{1}{2}\int_V \varepsilon^p_{ij}C_{ijkl}\,\varepsilon^p_{kl}dV - \bar{\sigma}_{ij}\bar{\varepsilon}_{ij}V$$

Appendix B

Local Stiffness Matrices of the Generalized Finite-Volume Theory

The non-zero elements of the $\boldsymbol{K}_{(00)}$ matrix are

$$k_{11} = \frac{C_{44}(4-3\alpha_2)}{l_\gamma}, \quad k_{13} = \frac{-3C_{44}\beta_2}{l_\gamma}, \quad k_{15} = \frac{C_{44}(2-3\alpha_2)}{l_\gamma},$$

$$k_{22} = \frac{C_{33}(4-3\alpha_3)}{l_\gamma}, \quad k_{23} = \frac{-C_{23}}{h_\beta}, \quad k_{24} = \frac{-3C_{33}\beta_3}{l_\gamma}, \quad k_{26} = \frac{C_{33}(2-3\alpha_3)}{l_\gamma},$$

$$k_{31} = \frac{-3C_{22}\alpha_2}{h_\beta}, \quad k_{32} = \frac{-C_{23}}{l_\gamma}, \quad k_{33} = \frac{C_{22}(4-3\beta_2)}{h_\beta}, \quad k_{37} = \frac{C_{22}(2-3\beta_2)}{h_\beta},$$

$$k_{42} = \frac{-3C_{44}\alpha_3}{h_\beta}, \quad k_{44} = \frac{C_{44}(4-3\beta_3)}{h_\beta}, \quad k_{48} = \frac{C_{44}(2-3\beta_3)}{h_\beta},$$

$$k_{17} = k_{13}, \quad k_{27} = -k_{23}, \quad k_{28} = k_{24}, \quad k_{35} = k_{31}, \quad k_{36} = -k_{32}, \quad k_{46} = k_{42},$$

$$k_{51} = k_{15}, \quad k_{53} = k_{13}, \quad k_{55} = k_{11}, \quad k_{57} = k_{13},$$

$$k_{62} = k_{26}, \quad k_{63} = -k_{23}, \quad k_{64} = k_{24}, \quad k_{66} = k_{22}, \quad k_{67} = k_{23}, \quad k_{68} = k_{24},$$

$$k_{71} = k_{31}, \quad k_{72} = -k_{32}, \quad k_{73} = k_{37}, \quad k_{75} = k_{31}, \quad k_{76} = k_{32}, \quad k_{77} = k_{33},$$

$$k_{82} = k_{42}, \quad k_{84} = k_{48}, \quad k_{86} = k_{42}, \quad k_{88} = k_{44}.$$

The non-zero elements of the $\boldsymbol{K}_{(10)}$ matrix are

$$k_{11} = \frac{12C_{23}}{h_\beta^2}, \quad k_{13} = \frac{-6C_{23}}{h_\beta^2}, \quad k_{14} = \frac{-6C_{33}}{h_\beta l_\gamma},$$

$$k_{21} = \frac{-6C_{22}}{h_\beta l_\gamma}, \quad k_{22} = \frac{-6C_{23}}{l_\gamma^2}, \quad k_{24} = \frac{12C_{23}}{l_\gamma^2},$$

$$k_{17} = k_{13}, \quad k_{18} = -k_{14}, \quad k_{25} = -k_{21}, \quad k_{26} = k_{22},$$

$$k_{33} = -k_{13}, \quad k_{34} = k_{14}, \quad k_{35} = -k_{11}, \quad k_{37} = -k_{13}, \quad k_{38} = -k_{14},$$

$$k_{41} = k_{21}, \quad k_{42} = -k_{22}, \quad k_{45} = -k_{21}, \quad k_{46} = -k_{22}, \quad k_{48} = -k_{24}.$$

The non-zero elements of the $\boldsymbol{K}_{(20)}$ matrix are

$$k_{12} = \frac{36C_{33}\alpha_3}{h_\beta^2 l_\gamma}, \quad k_{14} = \frac{36C_{33}(\beta_3 - 1)}{h_\beta^2 l_\gamma}, \quad k_{21} = \frac{36C_{22}(1-\alpha_2)}{h_\beta l_\gamma^2}, \quad k_{23} = \frac{-36C_{22}\beta_2}{h_\beta l_\gamma^2},$$

$$k_{16} = k_{12}, \quad k_{18} = k_{14}, \quad k_{25} = k_{21}, \quad k_{27} = k_{23},$$

$$k_{32} = k_{12}, \quad k_{34} = k_{14}, \quad k_{36} = k_{12}, \quad k_{38} = k_{14},$$

$$k_{41} = k_{21}, \quad k_{43} = k_{23}, \quad k_{45} = k_{21}, \quad k_{47} = k_{23}.$$

The non-zero elements of the $\boldsymbol{K}_{(01)}$ matrix are

$$k_{11} = \frac{C_{44}(\gamma_2 - 2)}{2}, \quad k_{13} = \frac{-C_{44}\gamma_2}{2}, \quad k_{22} = \frac{C_{33}\gamma_3 h_\beta^2 - C_{23} l_\gamma^2}{2h_\beta l_\gamma},$$

$$k_{31} = \frac{C_{22}\gamma_2 l_\gamma^2 - C_{23} h_\beta^2}{2h_\beta l_\gamma}, \quad k_{42} = \frac{C_{44}(\gamma_3 - 2)}{2}, \quad k_{44} = \frac{-C_{44}\gamma_3}{2},$$

$$k_{24} = -k_{22}, \quad k_{33} = -k_{31}, \quad k_{51} = -k_{13}, \quad k_{53} = -k_{11}, \quad k_{62} = k_{22}, \quad k_{64} = -k_{22},$$

$$k_{71} = k_{31}, \quad k_{73} = -k_{31}, \quad k_{82} = -k_{44}, \quad k_{84} = -k_{42}.$$

The non-zero elements of the $\boldsymbol{K}_{(11)}$ matrix are

$$k_{11} = \frac{4C_{33}}{l_\gamma}, \quad k_{12} = \frac{-3C_{23}l_\gamma}{h_\beta^2}, \quad k_{13} = \frac{2C_{33}}{l_\gamma},$$

$$k_{21} = \frac{-3C_{23}h_\beta}{l_\gamma^2}, \quad k_{22} = \frac{4C_{22}}{h_\beta}, \quad k_{24} = \frac{2C_{22}}{h_\beta},$$

$k_{14} = k_{12}, \quad k_{23} = k_{21}, \quad k_{31} = k_{13}, \quad k_{32} = k_{12}, \quad k_{33} = k_{11}, \quad k_{34} = k_{12},$

$k_{41} = k_{21}, \quad k_{42} = k_{24}, \quad k_{43} = k_{21}, \quad k_{44} = k_{22}.$

The non-zero elements of the $\boldsymbol{K}_{(21)}$ matrix are

$$k_{12} = \frac{-6C_{33}\gamma_3}{h_\beta l_\gamma}, \quad k_{21} = \frac{6C_{22}\gamma_2}{h_\beta l_\gamma},$$

$k_{14} = -k_{12}, \quad k_{23} = -k_{21}, \quad k_{32} = k_{12}, \quad k_{34} = -k_{12}, \quad k_{41} = k_{21}, \quad k_{43} = -k_{21}.$

The non-zero elements of the $\boldsymbol{K}_{(02)}$ matrix are

$$k_{22} = \frac{C_{23}l_\gamma^2}{12h_\beta}, \quad k_{31} = \frac{-C_{23}h_\beta^2}{12l_\gamma},$$

$k_{24} = -k_{22}, \quad k_{33} = -k_{31}, \quad k_{62} = -k_{22}, \quad k_{64} = k_{22}, \quad k_{71} = -k_{31}, \quad k_{73} = k_{31}.$

The non-zero elements of the $\boldsymbol{K}_{(12)}$ matrix are

$$k_{12} = \frac{C_{23}l_\gamma^2}{2h_\beta^2}, \quad k_{21} = \frac{-C_{23}h_\beta^2}{2l_\gamma^2},$$

$k_{14} = k_{12}, \quad k_{23} = k_{21}, \quad k_{32} = -k_{12}, \quad k_{34} = -k_{12}, \quad k_{41} = -k_{21}, \quad k_{43} = -k_{21}.$

The non-zero elements of the $\boldsymbol{K}_{(22)}$ matrix are

$$k_{11} = \frac{4C_{33}}{l_\gamma}, \quad k_{13} = \frac{2C_{33}}{l_\gamma}, \quad k_{22} = \frac{4C_{22}}{h_\beta}, \quad k_{24} = \frac{2C_{22}}{h_\beta},$$

$k_{31} = k_{13}, \quad k_{33} = k_{11}, \quad k_{42} = k_{24}, \quad k_{44} = k_{22}.$

Appendix C

Kinematic Matrices of the Generalized FVDAM Theory

The following matrices are employed in the kinematic relations of the generalized FVDAM theory:

$$\boldsymbol{A} = \begin{bmatrix} 0 & 1/2 & 0 & -1/2 \\ -1/2 & 0 & 1/2 & 0 \\ 0 & 1/2 & 0 & 1/2 \\ 1/2 & 0 & 1/2 & 0 \end{bmatrix} \quad \text{and} \quad \boldsymbol{a} = \begin{bmatrix} 0 \\ 0 \\ 1 \\ 1 \end{bmatrix} \tag{C.1}$$

$$\overline{\boldsymbol{Q}}^{(q)} = \begin{bmatrix} \overline{\boldsymbol{D}}_2^{(q)} & \overline{\boldsymbol{D}}_3^{(q)} \\ \overline{\boldsymbol{E}}_2^{(q)} & \overline{\boldsymbol{E}}_3^{(q)} \end{bmatrix}^{-1} \quad \text{and} \quad \boldsymbol{Q}_i^{(q)} = \overline{\boldsymbol{Q}}^{(q)} \begin{bmatrix} \boldsymbol{D}_i^{(q)} & \boldsymbol{0} \\ \boldsymbol{0} & \boldsymbol{E}_i^{(q)} \end{bmatrix} \tag{C.2}$$

$$\overline{\mathbb{Q}}^{(q)} = \mathbb{D}\left(\begin{bmatrix} \overline{\boldsymbol{D}}_2^{(q)} & \overline{\boldsymbol{D}}_3^{(q)} \end{bmatrix}\mathbb{D}\right)^{-1} \quad \text{and} \quad \mathbb{Q}_i^{(q)} = \overline{\mathbb{Q}}^{(q)} \begin{bmatrix} \boldsymbol{D}_i^{(q)} & \boldsymbol{0} \end{bmatrix} \tag{C.3}$$

for $i = 2, 3$, where we used auxiliary matrices defined as follows

$$\boldsymbol{D}_i^{(q)} = \begin{bmatrix} -n_i^{(1)} & 0 & n_i^{(3)} & 0 \\ 0 & -n_i^{(2)} & 0 & n_i^{(4)} \end{bmatrix}^{(q)T} \tag{C.4}$$

$$\boldsymbol{E}_i^{(q)} = 3\begin{bmatrix} -n_i^{(1)} & 0 & n_i^{(3)} & 0 \\ 0 & -n_i^{(2)} & 0 & n_i^{(4)} \end{bmatrix}^{(q)T} \tag{C.5}$$

$$\bar{\boldsymbol{D}}_i^{(q)} = \begin{bmatrix} n_i^{(1)} & 0 & -n_i^{(1)} & 0 \\ -n_i^{(2)} & -n_i^{(2)} & 0 & 0 \\ n_i^{(3)} & 0 & n_i^{(3)} & 0 \\ -n_i^{(4)} & n_i^{(4)} & 0 & 0 \end{bmatrix}^{(q)} \tag{C.6}$$

$$\bar{\boldsymbol{E}}_i^{(q)} = 3\begin{bmatrix} 0 & n_i^{(1)} & 0 & -n_i^{(1)} \\ 0 & 0 & -n_i^{(2)} & -n_i^{(2)} \\ 0 & n_i^{(3)} & 0 & n_i^{(3)} \\ 0 & 0 & -n_i^{(4)} & n_i^{(4)} \end{bmatrix}^{(q)} \tag{C.7}$$

$$\mathbb{D} = \begin{bmatrix} 1 & 0 & 0 & 0 \\ 0 & 0 & d_{2(21)} & 0 \\ 0 & 0 & 0 & d_{2(12)} \\ 0 & 0 & 0 & 0 \\ 0 & 1 & 0 & 0 \\ 0 & 0 & d_{3(21)} & 0 \\ 0 & 0 & 0 & d_{3(12)} \\ 0 & 0 & 0 & 0 \end{bmatrix}^{(q)} \tag{C.8}$$

In the above definitions, $n_i^{(p)}$ are the unit normal components to the four faces of quadrilateral subvolumes in the actual microstructure, and $d_{i(mn)}$ are defined in Equation (4.35), as a result of the assumption used to decouple rotational and curvature effects, making possible the construction of a local stiffness matrix for a 1st order FVDAM theory.

Appendix D

Static Matrices of the Generalized FVDAM Theory

From the tangential form of the local constitutive equations, we have

$$\Delta \boldsymbol{T}^{(q)} = \boldsymbol{R}^{(q)}(\eta,\xi)\Delta\overline{\boldsymbol{F}} + \boldsymbol{Y}^{(q)}(\eta,\xi)\Delta\boldsymbol{W}^{(q)} + \boldsymbol{Z}^{(q)}(\eta,\xi)\Delta\overline{\boldsymbol{W}}^{(q)} \tag{D.1}$$

where

$$\boldsymbol{Y}^{(q)}(\eta,\xi) = \boldsymbol{R}^{(q)}(\eta,\xi)\begin{bmatrix}\boldsymbol{L} & \boldsymbol{0} & \boldsymbol{0}\\ \boldsymbol{0} & \boldsymbol{L} & \boldsymbol{0}\\ \boldsymbol{0} & \boldsymbol{0} & \boldsymbol{L}\end{bmatrix}\begin{bmatrix}\boldsymbol{B}(\eta,\xi) & \boldsymbol{0} & \boldsymbol{0}\\ \boldsymbol{0} & \boldsymbol{B}(\eta,\xi) & \boldsymbol{0}\\ \boldsymbol{0} & \boldsymbol{0} & \boldsymbol{B}(\eta,\xi)\end{bmatrix} \tag{D.2}$$

and

$$\boldsymbol{Z}^{(q)}(\eta,\xi) = \boldsymbol{R}^{(q)}(\eta,\xi)\begin{bmatrix}\boldsymbol{0} & \boldsymbol{0}\\ \boldsymbol{L} & \boldsymbol{0}\\ \boldsymbol{0} & \boldsymbol{L}\end{bmatrix}\begin{bmatrix}\overline{\boldsymbol{B}}(\eta,\xi) & \boldsymbol{0}\\ \boldsymbol{0} & \overline{\boldsymbol{B}}(\eta,\xi)\end{bmatrix} \quad \text{with} \quad L = \begin{bmatrix}0 & 0\\ 1 & 0\\ 0 & 1\end{bmatrix} \tag{D.3}$$

In the above relations, the incremental first Piola-Kirchhoff stress and macroscopic deformation gradient vectors are defined by ordering the respectively components as follows,

$$\Delta \boldsymbol{T}^{(q)} = [\Delta T_{11} \quad \Delta T_{12} \quad \Delta T_{13} \quad \Delta T_{21} \quad \Delta T_{22} \quad \Delta T_{23} \quad \Delta T_{31} \quad \Delta T_{32} \quad \Delta T_{33}]^{(q)T} \tag{D.4}$$

$$\Delta \overline{\boldsymbol{F}} = [\Delta \bar{F}_{11} \quad \Delta \bar{F}_{12} \quad \Delta \bar{F}_{13} \quad \Delta \bar{F}_{21} \quad \Delta \bar{F}_{22} \quad \Delta \bar{F}_{23} \quad \Delta \bar{F}_{31} \quad \Delta \bar{F}_{32} \quad \Delta \bar{F}_{33}]^{T} \tag{D.5}$$

This yields the expressions in Equations (4.49), (4.52) and (4.53) for the surface-averaged static variables, where

$$\widehat{\boldsymbol{R}}_0^{(p,q)} = \boldsymbol{N}^{(p,q)} \sum_{j=1}^{3} \boldsymbol{R}^{(q)}\left(\eta_j^{(p)}, \xi_j^{(p)}\right) w_{j(0)} \tag{D.7}$$

$$\widehat{\boldsymbol{Y}}_0^{(p,q)} = \boldsymbol{N}^{(p,q)} \sum_{j=1}^{3} \boldsymbol{Y}^{(q)}\left(\eta_j^{(p)}, \xi_j^{(p)}\right) w_{j(0)} \tag{D.8}$$

$$\widehat{\boldsymbol{Z}}_0^{(p,q)} = \boldsymbol{N}^{(p,q)} \sum_{j=1}^{3} \boldsymbol{Z}^{(q)}\left(\eta_j^{(p)}, \xi_j^{(p)}\right) w_{j(0)} \tag{D.9}$$

and

$$\widehat{\boldsymbol{R}}_i^{(p,q)} = \boldsymbol{n}^{(p,q)} \boldsymbol{N}^{(p,q)} \sum_{j=1}^{3} \boldsymbol{R}^{(q)}\left(\eta_j^{(p)}, \xi_j^{(p)}\right) w_{j(i)}^{(p)} \tag{D.10}$$

$$\widehat{\boldsymbol{Y}}_i^{(p,q)} = \boldsymbol{n}^{(p,q)} \boldsymbol{N}^{(p,q)} \sum_{j=1}^{3} \boldsymbol{Y}^{(q)}\left(\eta_j^{(p)}, \xi_j^{(p)}\right) w_{j(i)}^{(p)} \tag{D.11}$$

$$\widehat{\boldsymbol{Z}}_i^{(p,q)} = \boldsymbol{n}^{(p,q)} \boldsymbol{N}^{(p,q)} \sum_{j=1}^{3} \boldsymbol{Z}^{(q)}\left(\eta_j^{(p)}, \xi_j^{(p)}\right) w_{j(i)}^{(p)} \tag{D.12}$$

for $i = 1, 2$. In the above calculations, we have $\boldsymbol{n}^{(p,q)} = \begin{bmatrix} 0 & n_2^{(p)} & n_3^{(p)} \end{bmatrix}^{(q)}$ and

$$\boldsymbol{N}^{(p,q)} = \begin{bmatrix} 0 & 0 & 0 & n_2^{(p)} & 0 & 0 & n_3^{(p)} & 0 & 0 \\ 0 & 0 & 0 & 0 & n_2^{(p)} & 0 & 0 & n_3^{(p)} & 0 \\ 0 & 0 & 0 & 0 & 0 & n_2^{(p)} & 0 & 0 & n_3^{(p)} \end{bmatrix}^{(q)} \tag{D.13}$$

The matrices $\widehat{\boldsymbol{R}}_i^{(p,q)}$, $\widehat{\boldsymbol{Y}}_i^{(p,q)}$ and $\widehat{\boldsymbol{Z}}_i^{(p,q)}$ are numerically evaluated, where we assume a parabolic distribution of the traction increments at the subvolume faces, which implies $\boldsymbol{w}_0 = (1/6\,, 2/3\,, 1/6)$, $\boldsymbol{w}_1^{(1,2)} = (1/2\,, 0, -1/2)$, $\boldsymbol{w}_1^{(3,4)} = (-1/2\,, 0, 1/2)$, $\boldsymbol{w}_2^{(1,2)} = (-1, 2, -1)$ and $\boldsymbol{w}_2^{(3,4)} = (1, -2, 1)$, for $\boldsymbol{\eta}^{(1,3)} = (-1, 0, 1)$, $\boldsymbol{\eta}^{(2,4)} = (\pm 1, \pm 1, \pm 1)$, $\boldsymbol{\xi}^{(1,3)} = (\mp 1, \mp 1, \mp 1)$ and $\boldsymbol{\xi}^{(2,4)} = (-1, 0, 1)$.

Appendix E

External Virtual Work for Nonlinear Elastic Analysis of Periodic Materials

Derivation of the external virtual work using the deformed configuration:

$$\delta W_{ext} = \int_{S^t} \tau_i \delta u_i dS^t = \int_{S^t} \sigma_{ji} n_j^t \delta u_i dS^t = \int_{S^t} (\sigma_{ji} \delta u_i) n_j^t dS^t$$
$$= \int_{V^t} \frac{\partial}{\partial x_j} (\sigma_{ji} \delta u_i) dV^t = \int_{V^t} \left(\frac{\partial \sigma_{ji}}{\partial x_j} \delta u_i + \sigma_{ji} \frac{\partial \delta u_i}{\partial x_j} \right) dV^t$$

From equilibrium

$$\frac{\partial \sigma_{ji}}{\partial x_j} = 0$$

and taking into account kinematic considerations, follows

$$\frac{\partial \delta u_i}{\partial x_j} = \frac{1}{2} \left(\frac{\partial \delta u_i}{\partial x_j} + \frac{\partial \delta u_i}{\partial x_i} \right) + \frac{1}{2} \left(\frac{\partial \delta u_i}{\partial x_j} - \frac{\partial \delta u_i}{\partial x_i} \right) = \delta e_{ij} + \delta \omega_{ij}$$

then

$$\delta W_{ext} = \int_{V^t} \sigma_{ji} (\delta e_{ij} + \delta \omega_{ij}) \, dV^t = \int_{V^t} \sigma_{ji} \delta e_{ij} \, dV^t + \int_{V^t} \sigma_{ji} \delta \omega_{ij} \, dV^t$$

As $\sigma_{ji} = \sigma_{ij}$ and $\delta \omega_{ij} = -\delta \omega_{ji}$, we have $\sigma_{ji} \delta e_{ij} = \sigma_{ij} \delta e_{ij}$ and $\sigma_{ji} \delta \omega_{ij} = 0$, thus

$$\delta W_{ext} = \int_{V^t} \sigma_{ij} \delta e_{ij} \, dV^t$$

From Hill's Lemma

$$\frac{1}{V^t}\int_{V^t}\sigma_{ij}\delta e_{ij}\,dV^t = \left(\frac{1}{V^t}\int_{V^t}\sigma_{ij}\,dV^t\right)\left(\frac{1}{V^t}\int_{V^t}\delta e_{ij}\,dV^t\right) = \bar{\sigma}_{ij}\delta\bar{e}_{ij}$$

which implies

$$\delta W_{ext} = \bar{\sigma}_{ij}\delta\bar{e}_{ij}V^t$$

Once we are working with a displacement based formulation, where the macroscopic loading is defined in terms of average displacement gradient increments $\Delta\overline{H}_{ij}$, the tensor $\bar{e}_{ij}$ does not vary in the analysis, resulting in $\delta\bar{e}_{ij} = 0$, and, consequently, $\delta W_{ext} = 0$.

Appendix F

Linearization of the Equation of Motion for Nonlinear Elastic Analysis of Periodic Materials

Equation of motion at the time $t + \Delta t$:

$$\int_{V^0} S_{ij}^{t+\Delta t} \delta E_{ij}^{t+\Delta t} dV^0 = 0$$

Incremental decomposition of the Green-Lagrange strain tensor:

$$\delta E_{ij}^{t+\Delta t} = \delta\left(E_{ij}^t + \Delta E_{ij}\right) = \underbrace{\delta E_{ij}^t}_{=0} + \delta \Delta E_{ij} = \delta \Delta E_{ij}$$

Following Bathe (1996), we can decompose the incremental Green-Lagrange strain tensor in linear ($\bar{\epsilon}_{ij}^t$ and $\epsilon_{ij}'^t$) and nonlinear ($\bar{\eta}_{ij}$ and η_{ij}') contributions, as follows

$$\delta \Delta E_{ij} = \delta\left(\bar{\epsilon}_{ij}^t + \epsilon_{ij}'^t + \bar{\eta}_{ij} + \eta_{ij}'\right) = \underbrace{\delta \bar{\epsilon}_{ij}^t}_{=0} + \delta \epsilon_{ij}'^t + \underbrace{\delta \bar{\eta}_{ij}}_{=0} + \delta \eta_{ij}' = \delta \epsilon_{ij}'^t + \delta \eta_{ij}'$$

where

$$\bar{\epsilon}_{ij}^t = \frac{1}{2}\left(\Delta \bar{H}_{ki} F_{kj}^t + F_{ki}^t \Delta \bar{H}_{kj}\right), \quad \epsilon_{ij}'^t = \frac{1}{2}\left(\Delta H_{ki}' F_{kj}^t + F_{ki}^t \Delta H_{kj}'\right),$$

$$\bar{\eta}_{ij} = \frac{1}{2} \Delta \bar{H}_{ki} \Delta \bar{H}_{kj}, \quad \eta_{ij}' = \frac{1}{2} \Delta H_{ki}' \Delta H_{kj}'$$

Incremental decomposition of the equation of motion:

$$\int_{V^0} S_{ij}^{t+\Delta t}\delta E_{ij}^{t+\Delta t}dV^0 = 0 \therefore \int_{V^0} S_{ij}^{t+\Delta t}\delta\Delta E_{ij}dV^0 = 0 \therefore \int_{V^0} \left(S_{ij}^{t} + \Delta S_{ij}\right)\delta\Delta E_{ij}dV^0 = 0$$

$$\therefore \int_{V^0} S_{ij}^{t}\delta\Delta E_{ij}dV^0 + \int_{V^0} \Delta S_{ij}\delta\Delta E_{ij}dV^0 = 0$$

$$\therefore \int_{V^0} \Delta S_{ij}\delta\Delta E_{ij}dV^0 + \int_{V^0} S_{ij}^{t}\delta\eta'_{ij}dV^0 = -\int_{V^0} S_{ij}^{t}\delta\epsilon'^{t}_{ij}dV^0$$

Linearization of the equation of motion:

$$\int_{V^0} \Delta S_{ij}\delta\Delta E_{ij}dV^0 \approx \int_{V^0} \left(\frac{\partial S_{ij}^{t}}{\partial E_{kl}^{t}}\Delta E_{kl}\right)\delta\Delta E_{ij}dV^0 = \int_{V^0} \mathbb{C}_{ijkl}^{t}\Delta E_{kl}\delta\Delta E_{ij}dV^0$$

$$= \int_{V^0} \mathbb{C}_{ijkl}^{t}\left(\bar{\epsilon}_{kl}^{t} + \epsilon'^{t}_{kl} + \underbrace{\bar{\eta}_{kl} + \eta'_{kl}}_{neglected}\right)\delta\left(\epsilon'^{t}_{ij} + \underbrace{\eta'_{ij}}_{neg.}\right)dV^0 \approx \int_{V^0} \mathbb{C}_{ijkl}^{t}(\bar{\epsilon}_{kl}^{t} + \epsilon'^{t}_{kl})\delta\epsilon'^{t}_{ij}dV^0$$

Thus

$$\int_{V^0} \mathbb{C}_{ijkl}^{t}\epsilon'^{t}_{kl}\delta\epsilon'^{t}_{ij}dV^0 + \int_{V^0} S_{ij}^{t}\delta\eta'_{ij}dV^0 = -\int_{V^0} S_{ij}^{t}\delta\epsilon'^{t}_{ij}dV^0 - \int_{V^0} \mathbb{C}_{ijkl}^{t}\bar{\epsilon}_{kl}^{t}\delta\epsilon'^{t}_{ij}dV^0$$

Finally, using the symmetry of the tangential stiffness tensor $\mathbb{C}_{ijkl}^{t}$, follows

$$\int_{V^0} \mathbb{C}_{ijkl}^{t}\epsilon'^{t}_{kl}\delta\epsilon'^{t}_{ij}dV^0 + \int_{V^0} S_{ij}^{t}\delta\eta'_{ij}dV^0 = -\int_{V^0} S_{ij}^{t}\delta\epsilon'^{t}_{ij}dV^0 - \int_{V^0} \mathbb{C}_{ijkl}^{t}F_{mk}^{t}\delta\epsilon'^{t}_{ij}dV^0\,\Delta\bar{H}_{ml}$$